Dissertation

submitted to the

Combined Faculties of the Natural Sciences and Mathematics

of Heidelberg University, Germany

for the degree of

Doctor of Natural Sciences

Put forward by

M.Sc. Janko Nauta

born in: Leeuwarden, the Netherlands

Oral examination: 29.07.2020

An extreme-ultraviolet frequency comb enabling frequency metrology with highly charged ions

Referees: PD Dr. José R. Crespo López-Urrutia
Prof. Dr. Andreas Wolf

An extreme ultraviolet frequency comb for highly charged ion metrology
Highly charged ions (HCI) have been proposed as extremely sensitive probes for physics beyond the Standard Model, such as a possible α-variation, and as novel frequency standards, due to their insensitivity to external fields. We aim at performing ultra-high precision spectroscopy of HCI in the extreme ultraviolet (XUV) region, where many transitions are located. Therefore, we have developed an XUV frequency comb. Femtosecond pulses from a 100 MHz phase-stabilized near-infrared comb are amplified and fed into an enhancement cavity inside an ultra-high vacuum chamber. In the tight focus ($w_0 = 15\,\mu$m) of the astigmatism-compensated cavity, intensities $\sim 10^{14}\,\mathrm{W/cm^2}$ are reached. As a first application, we perform multi-photon ionization of xenon using the velocity-map imaging technique. The high repetition rate facilitates fast data acquisition even at low intensities, enabling future precision tests in nonlinear physics. Finally, we have observed outcoupled XUV radiation, produced in the cavity focus, up to the 35th harmonic order (42 eV; 30 nm). No signs of mirror degradation were observed during five hours of continuous operation. Using He:Xe gas mixtures, improved phase-matching conditions led to 49 μW output power at 16 eV. This is sufficient to drive HCI transitions with kHz excitation rates and is an important step towards XUV frequency metrology with HCI.

Ein ultravioletter Frequenzkamm für die Metrologie mit hochgeladenen Ionen
Hochgeladene Ionen (HCI) gelten als vielversprechende Kandidaten für hochempfindliche Messungen, die über das Standardmodell hinausgehen, wie beispielsweise bei der Suche nach einer möglichen α-Variation. Aufgrund ihrer hohen Unempfindlichkeit gegenüber externen Störungen wurden sie außerdem für zukünftige Atomuhren vorgeschlagen. Unser Ziel ist die Ultrahochpräzisionsspektroskopie mit HCI im extrem ultravioletten (XUV) Spektralbereich, in welchem HCI viele Übergänge aufweisen. Um diese anzuregen wurde ein XUV Frequenzkamm entwickelt. Femtosekundenpulse aus einem 100 MHz phasenstabilen Kamm im nahen Infrarotbereich werden verstärkt und in einem Überhöhungsresonator in einer Ultrahochvakuumkammer überlagert. Im kleinen Fokus ($w_0 = 15\,\mu$m) der Astigmatismus-kompensierten Kavität werden Intensitäten von $\sim 10^{14}\,\mathrm{W/cm^2}$ erreicht. Als erste Anwendung haben wir Multiphotonenionisation von Xenon mithilfe der 'velocity-map imaging' Technik realisiert. Die hohe Repetitionsrate erlaubt auch bei niedrigen Intensitäten eine sehr schnelle Datenaufnahme und ermöglicht zukünftige Präzisionstests in der nichtlinearen Physik. Wir konnten im Fokus der Verstärkungskavität XUV Strahlung bis zur 35. harmonischen Ordnung (42 eV; 30 nm) beobachten. Während des kontinuierlichen Betriebs über fünf Stunden war keine Spiegeldegradation feststellbar. Durch die Verwendung von He:Xe Gasmischungen konnte eine Verbesserung der Phasenanpassung im Fokus erzielt werden und die gemessene Ausgangsleistung auf 49 μW bei 16 eV erhöht werden. Dies genügt um HCI mit kHz Raten anzuregen und ist ein wichtiger Schritt in Richtung XUV Frequenzmetrologie mit HCI.

Contents

List of Figures

List of Tables

Abbreviations

ADK	Ammosov, Delone and Krainov
AOI	Angle Of Incidence
AR	Anti-Reflection
ATI	Above-Threshold Ionization
a. u.	arbitrary units
BBO	Beta-Barium Borate
CEO	Carrier-to-Envelope Offset
CEP	Carrier-to-Envelope Phase
CERN	Conseil Européen pour la Recherche Nucléaire
CF	ConFlat
CNC	Computer Numerical Control
CPA	Chirped Pulse Amplification
CryPTEx	Cryogenic Paul Trap Experiment
CW	Continuous Wave
DDS	Direct Digital Synthesizer
EBIT	Electron Beam Ion Trap
EC	Enhancement Cavity
EDM	Clectric Dipole Moment
EOM	Electro-Optic Modulator
FEL	Free-Electron Laser
FROG	Frequency-Resolved Optical Gating
fsEC	femtosecond Enhancement Cavity
FSR	Free Spectral Range
FWHM	Full-Width Half-Maximum
GDD	Group Delay Dispersion
GIP	Grazing Incidence Plate
GR	General Relativity
GRISM	Grating Prism
HC	Hänsch-Couillaud
HCI	Highly Charged Ions
HHG	High Harmonic Generation

HV	High Voltage
IC	Input Coupler
IR	InfraRed
LIDT	Laser-Induced Damage Threshold
LLI	Local Lorentz Invariance
LMA	Large Mode Area
MCP	Micro-Channel Plate
MPI	Muti-Photon Ionization
MPIK	Max-Planck-Institut für Kernphysik
NIR	Near-InfraRed
PAD	Photo-electron Angular Distributions
PDH	Pound-Drever-Hall
PID	Proportional-Integral-Derivative
PLO	Phase-Locked Oscillator
ppm	parts per million
PPT	Perelomov, Popov and Terent'ev
PTB	Physikalisch-Technische Bundesanstalt
PZT	lead Zirconate Titanate
QLS	Quantum Logic Spectroscopy
RF	Radio Frequency
ROC	Radius Of Curvature
SHG	Second Harmonic Generation
SM	Standard Model
SPM	Self Phase Modulation
TOD	Third Order Dispersion
TSM	Three-Step Model
UHV	Ultra-High Vacuum
VMI	Velocity-Map Imaging
VUV	Vacuum Ultraviolet
WOMOC	Wedge-On-Mirror Output Coupler
XUV	Extreme UltraViolet

List of Symbols

A	amplitude distribution factor, Gaussian beam ABCD matrix parameter
$\mathbf{A}$	laser field vector potential
α	fine-structure constant, empirical fitting parameter
α_j	proportionality constant
B	Gaussian beam ABCD matrix parameter
β	cavity enhancement, PAD anisotropy parameter
β_c	cavity coupling efficiency
c	speed of light
C	Gaussian beam ABCD matrix parameter
$\mathcal{C}$	cavity contrast
ϵ_0	vacuum permittivity
d	dipole transition matrix element
D	Gaussian beam ABCD matrix parameter
Δf	frequency bandwidth
$\Delta\mathbf{k}$	phase mismatch
$\Delta\mathbf{k_d}$	dipole phase mismatch
$\Delta\mathbf{k_g}$	Gouy phase mismatch
$\Delta\mathbf{k_n}$	neutral gas dispersion phase mismatch
$\Delta\mathbf{k_p}$	plasma dispersion phase mismatch
$\Delta\phi_{cav}$	cavity round-trip phase
$\Delta\phi_{\mathrm{CE}}$	carrier-to-envelope phase
$\Delta\omega_{\mathrm{FSR}}$	free spectral range
$\Delta\omega_{1/2}$	cavity linewidth
e	elementary charge
E	energy, electric field
E_c	circulating electric field
E_{in}	incident electric field
E_{kin}	kinetic energy
E_{max}	cutoff energy
E_{refl}	reflected electric field
ϵ	mode matching factor

η	ionization fraction
η_{crit}	critical ionization fraction
η_{pulse}	ionization fraction after a single laser pulse
θ	angle
f	frequency, focal length, 3D signal density
f_{CEO}	offset frequency
f_{rep}	repetition frequency
F	laser field strength, observed intensity
$\mathcal{F}$	cavity finesse
$\mathscr{F}$	Fourier transform
γ	Keldysh parameter
h	Planck constant
I	laser intensity
I_{cav}	cavity intensity
I_{in}	incident intensity
I_{refl}	reflected intensity
j	electronic angular momentum
k	wave number
K	sensitivity factor for variation of α
κ	sensitivity factor for variation of light quark masses, constant equal to $\sqrt{2U_{\text{ion}}}$
l	orbital angular momentum quantum number momentum
L	path length
L_0	cavity length for maximum enhancement
L_{med}	medium length
L_{abs}	absorption length
$\mathcal{L}_{\text{cav}}$	cavity losses except input coupler transmission
$\mathcal{L}_{\text{tot}}$	total cavity losses
λ_0	laser wavelength
Λ_{QCD}	quantum chromo-dynamic energy scale
m	magnetic momentum quantum number, resonance fringe number
m_{e}	electron mass
M	ABCD ray transfer matrix
M_{avg}	average molar mass
M_{cav}	cavity ABCD ray transfer matrix
μ	proton-to-electron mass ratio
μ_0	vacuum permeability
n	principle quantum number, FC mode number,

	number of absorbed photons
n_0	refractive index for fundamental radiation
n_q	refractive index for harmonic radiation
n_2	intensity-dependent refractive index
N	number of atoms, number of pulses
N_a	atomic number density
N_q	fitting parameter for harmonic order q
p	cavity mode number
P	pressure
P_l	Legendre polynomial
P_0	standard pressure
P_{match}	phase-matching pressure
$\mathbf{p}$	canonical momentum
q	sensitivity parameter for variation of α, harmonic order,
	Gaussian beam propagation parameter
q_0	Gaussian beam propagation parameter at the focus
Q	ionization charge state
σ_y	Alan deviation
ρ	gas density
r	radial coordinate
r_e	classical electron radius
r_i	field reflectivity coefficient of the IC
R	radius of curvature, mirror reflectivity, ideal gas constant
R_i	IC mirror reflectivity
R_∞	Rydberg constant
S	quasi-classical action
S_q	yield of the q-th harmonic
S_ϕ	phase-matching and absorption factor
σ	ionization cross-section
σ_{FWHM}	FWHM of laser intensity profile
t	time, field transmission coefficient
t_i	field transmission coefficient of the IC
t_π	duration of a π pulse (Rabi flop)
T	mirror transmission, round-trip time, temperature
T_c	cavity transmission except IC
T_i	IC transmission
τ	pulse duration
τ_{beam}	atom flight time through FWHM of laser focal volume

τ_c	cavity decay time
τ_{ion}	ion flight time through FWHM of ion generation volume
T_m	clock interrogation time
T_{rep}	repetition time
u	complex scalar transverse amplitude
U_{pond}	ponderomotive potential
U_{ion}	ionization potential
v	velocity
v_{gas}	target gas velocity
V	atomic potential
ϕ	phase
ϕ_{circ}	circulating steady-state phase
ϕ_d	dispersion phase shift
ϕ_j	dipole phase
ϕ_0	constant phase shift
ϕ_1	group delay
ϕ_2	group delay dispersion
x	position, dipole moment
X_q	strong interaction parameter
y	transverse coordinate
ψ	atomic wavefuntion, total nonlinear phase
w_0	focus waist size
w	Gaussian beam waist
z	longitudinal direction
z_R	Rayleigh range
Z	nuclear charge
ω	angular frequency
ω_{ADK}	ionization rate according to ADK theory
ω_c	carrier angular frequency
ω_{CEO}	angular offset frequency
ω_{lock}	angular locking frequency
ω_{rep}	angular repetition frequency
Ω	Rabi frequency

Chapter 1

Introduction

In this chapter we cover the background and motivation of the research performed in the scope of this thesis. First, in Section 1.1, a general introduction to today's open questions in physics is provided and some approaches for searches of new physics are discussed, followed by a brief introduction of the frequency comb, in Section 1.2, that has enabled a tremendous increase in the measurement precision of laboratory experiments. Section 1.3 focuses on one of these approaches; the possible variation of fundamental constants, and how such an effect could be detected. Next, in Section 1.4, highly charged ions (HCI) are introduced as sensitive probes for new physics. Subsequently, in Section 1.5, we discuss how high-precision spectroscopy could be extended from the optical into the extreme ultraviolet regime. Section 1.6 provides an overview of how this new concept is implemented experimentally. Finally, a brief outline of this thesis is given in Section 1.7.

1.1 Probing fundamental physics

Over the course of the last century, our understanding of the physical universe has greatly improved: from processes at the smallest scales, where interactions of fundamental particles take place, to the largest scales in the visible universe, where superclusters form massive structures of galaxies. The former is described by the Standard Model (SM) of particle physics [1], while the latter is governed by the predictions of the theory of general relativity (GR) [2]. The SM has proven to be exceptionally successful in describing fundamental interactions to a high precision. Numerous experiments have confirmed its validity and the level of correspondence between theoretically predicted and experimentally measured values is astonishing. Despite its overwhelming success, there are important cases where the SM does not correspond to reality. It cannot, for instance, explain the apparent imbalance between *matter* and *antimatter*. Nor does it account for the existence of *dark matter* (DM) and *dark energy*, for which a large amount of evidence has been found. Furthermore, although numerous attempts have been made, so far the SM has not successfully been unified with GR to form a consistent theory of gravitation and fundamental

interactions.

As for the first point, the most easily observable parts of our universe, namely stars and gases, are almost completely made up of ordinary matter in the form of protons, neutrons and electrons. The *baryon* content of the universe thus largely outweighs its antibaryonic counterpart, of which almost nothing is observed. This asymmetry is believed to arise from fundamental interaction laws in the early stages of the universe [3]. However, within the SM, baryon number, and also lepton number, is conserved to a very good approximation, since no renormalizable interaction terms exist which violate either conservation of baryon number or the individual lepton numbers [4]. Several theoretical mechanisms have been proposed to induce the observed asymmetry, but so far none of these have been confirmed by experimental observations.

The first experimental evidence for the second problem of the SM, the fact that baryonic matter only makes up a small part of our universe, originates from observations of galaxy rotation curves in 1932 [5]. Since then, many experiments have searched for the nature of the mysterious dark matter [6]. This type of matter seems only to interact with baryonic matter through gravitational interactions and makes up 26% of the universe according to a recent study of the cosmic microwave background [7]. Despite numerous investigations in a variety of directions, the origin of dark matter remains unclear to date, although the parameter space for possible dark matter candidates has been constrained considerably over the last decades. Where the nature of dark matter is already mysterious, we have even less of a clue of what makes up the largest part of our universe. Astronomical observations of type I supernovae in distant galaxies have revealed that the expansion of the universe is accelerating [8], a result that can only be explained by the presence of some kind of dark energy. The origin of dark energy, acting like a repulsive gravitational force, is completely unclear, although it makes up 69% of our universe.

In conclusion, despite major scientific breakthroughs and many important discoveries, we have essentially no idea what makes up 95% of our universe. Nor is it clear why it is almost solely made up of matter and how this has survived annihilation with antimatter shortly after the big bang. These big open questions show that our understanding of the underlying fundamental processes which have formed the present universe is still far from complete and are a strong motivation to look for new physics beyond the SM.

When it comes to experimental searches for new physics, two distinct but complementary approaches can be identified. On the one hand, large-scale collider experiments running at $\sim$ TeV energies, such as the Large Hadron Collider at CERN, can be used to search for new particles by directly producing and detecting them. This recently led to the discovery of the Higgs boson, along with many other subatomic particles over the past decades. The disadvantage of this type of experiments is the large scale, and thus costs, of the facilities that are required to reach ever increasing energies to produce new particles. On the other

hand, there are *table-top* experiments which operate at much lower energies $\sim$ eV but can achieve a very high precision [9, 10]. Even though possible new particles or fields are not expected to be produced at these energies, their existence can be detected indirectly by looking for tiny deviations from the SM predictions for known quantities. Very good control over the atomic or molecular system under observation, mainly enabled by the development of laser technology since the 1960s, permits high-accuracy measurements of their transition energies. In this way, table-top experiments can be sensitive to new physics at large energy scales, while these kinds of experiments take place at low energies, in small-scale laboratories at modest costs.

Since the SM is based on symmetry principles, one suitable method of testing its predictions is to measure if the underlying symmetries really hold or if they are slightly broken. The three discrete symmetries of the SM are *charge conjugation* (C), *parity* (P) and *time reversal* (T) and their combinations. The combined CPT symmetry is conserved for any relativistic quantum field theory. Its conservation has also been confirmed by experiments to a very high precision [11]. Although the SM includes a small amount of T violation, this is by far insufficient to explain the observed matter-antimatter imbalance. Violation of T can manifest itself as a permanent electric dipole moment (EDM) in a fundamental particle, which can be measured in experiments. The electron EDM, for instance, has recently been measured using ThO molecules to be $< 1.1 \times 10^{-29}\, e$cm [12], putting constraints on new T-violating physics at the multi-TeV level [13]. A measurement of P violation in Cs atoms [14] provides the most accurate low-energy tests to date on the electroweak sector of the SM [10]. Violation of the fundamental principle of local Lorentz invariance (LLI), which has been suggested by some theoretical developments in quantum gravity, is also being experimentally tested, with one of the most stringent limits originating from experiments with atomic dysprosium [15]. These are just a few examples of how the SM can be tested using high-precision, table-top experiments. In the following section, we will discuss one of the major technological breakthroughs that has enabled substantial improvements in the precision of such experiments: the *frequency comb* (FC).

1.2 Invention of the frequency comb

With the first development of tunable, monochromatic laser sources and Doppler-free spectroscopy techniques in the 1970s, rapid advances were made in the field of precision spectroscopy. To measure frequencies in an absolute sense, comparison with a reference is necessary [16]. Since 1967, the definition of the second is provided by the frequency of the cesium clock transition at 9.2 GHz [17]. Optical frequencies, however, are in the range of several hundred THz, much higher than what can be counted electronically. As a consequence, this large frequency gap needed to be overcome, which was done using

a chain of frequency links consisting of a high number of different types oscillators with electronically controlled frequencies relative to neighboring oscillators in the chain. Due to their size, high level of complexity and difficult operation, only a few of such systems have been employed, mainly at national laboratories.

Already in the late 1970s the use of pulsed lasers for frequency measurements was demonstrated [18]. The comb lines of the phase-coherent pulse train were used as a frequency ruler, with a line interval equal to the repetition rate f_{rep} of the pulsed laser, to measure fine-structure energy differences. However, the unknown phase-slips between consecutive pulses, which shift the entire frequency spectrum, prevented absolute measurements. This changed in the late 1990s, when techniques for broadening the comb spectrum became available. In work which was honored by the Nobel-prize, Theodor Hänsch, John Hall and coworkers developed a self-referencing method to extract the carrier-to-envelope offset frequency f_{CEO} for the first time [19, 20].

With a stabilized repetition rate and offset frequency, a train of femtosecond pulses thus turns into a FC. The frequency of the *comb tooth* with mode number n can then be described by [21]

$$f_{\mathrm{n}} = f_{\mathrm{CEO}} + n f_{\mathrm{rep}}. \tag{1.1}$$

The comb can be thought of as a ruler for optical frequencies which can be used to measure large frequency differences. Since the frequency of each individual mode is fully determined by two radio-frequency (RF) signals and the tooth number n, the FC provides a direct link between the optical (THz) range and the MHz domain, where frequencies can be counted electronically. The introduction of the FC has thus made the cumbersome frequency chains superfluous since optical frequencies could now be counted with standard RF electronics, with fractional uncertainties as small as 10^{-21} [22].

Soon after its invention, a frequency comb at even higher frequencies was generated via the production of high harmonics. In 2005, the groups of Thomas Udem in Garching and Jun Ye in Boulder reported the generation of coherent radiation below 100 nm [23, 24], extending the frequency comb techniques to the extreme ultraviolet range.

In conclusion, the frequency comb has revolutionized frequency metrology by enabling frequency determinations with unprecedented precision. It has proven to be an indispensable tool for the development of optical clocks [25], and has found numerous other applications, for instance in the fields of molecular spectroscopy [26], exoplanet observations [27], attosecond science [28] and optical communication [29]. In the next section, we will discuss how such precise frequency measurements can be used to search for possible variation of fundamental constants.

1.3 Variation of fundamental constants

The SM contains a set of dimensionless parameters, 19 in its minimal version, of which the values need to be determined by experiments. These *fundamental* constants have been measured extensively [30] and within the SM their values are unchanging. However, in many proposed theories unifying gravity with other interactions, these constants become dynamical fields that can vary in time or space. The values of the fundamental constants could thus be different in distant regions of the universe. Since the value of many fundamental constants, such as the Planck constant h or speed of light c, depends on the unit definition that is used, it is reasonable to only consider variation of dimensionless constants. Since they are most important for atoms, molecules, chemistry and life, most of the recent studies have been focusing on possible variation of the proton-to-electron mass ratio $\mu = m_p/m_e$ and the fine structure constant α, which is defined as

$$\alpha = \frac{1}{4\pi\epsilon_0}\frac{e^2}{\hbar c}, \tag{1.2}$$

where ϵ_0 is the vacuum permittivity and e is the elementary charge.

These types of searches are conducted in a diverse range of systems, such as meteorite dating, cosmic microwave background, big bang nucleosynthesis and the Oklo natural nuclear reactor [31]. The first experimental evidence for varying fundamental constants originates from quasar absorption spectra and hinted towards a dipole-like space variation of α on cosmological distances [32]. Although there is an ongoing debate about the influence of instrument distortions on the measurement result [33, 34], the discovery of the so-called *Australian dipole* has triggered many laboratory searches for α variation.

From Dirac's theory of the hydrogen atom it becomes clear that atomic spectroscopy enables the detection of possible variation of α. The energy levels $E_{n,j}$ of an electron bound to an infinite-mass, point-like nucleus are given by [10]

$$E_{n,j} = m_e c^2 \left[1 + \frac{(Z\alpha)^2}{[n - j - (1/2) + \sqrt{(j+1/2)^2 - (Z\alpha)^2}]^2}\right]^{-1/2}, \tag{1.3}$$

where Z is the charge of the nucleus in units of the elementary charge, n the principle quantum number and j the electronic angular momentum in units of $\hbar$. When $E_{n,j}$ is expanded in powers of α, it becomes clear that for electronic states with different n, the energy splitting scales as α^2, whereas for states with different j but the same n, it scales as α^4. Therefore, frequency ratios between these different types of transitions are sensitive to a variation of α. In more complicated atomic systems, the dependence of the energy

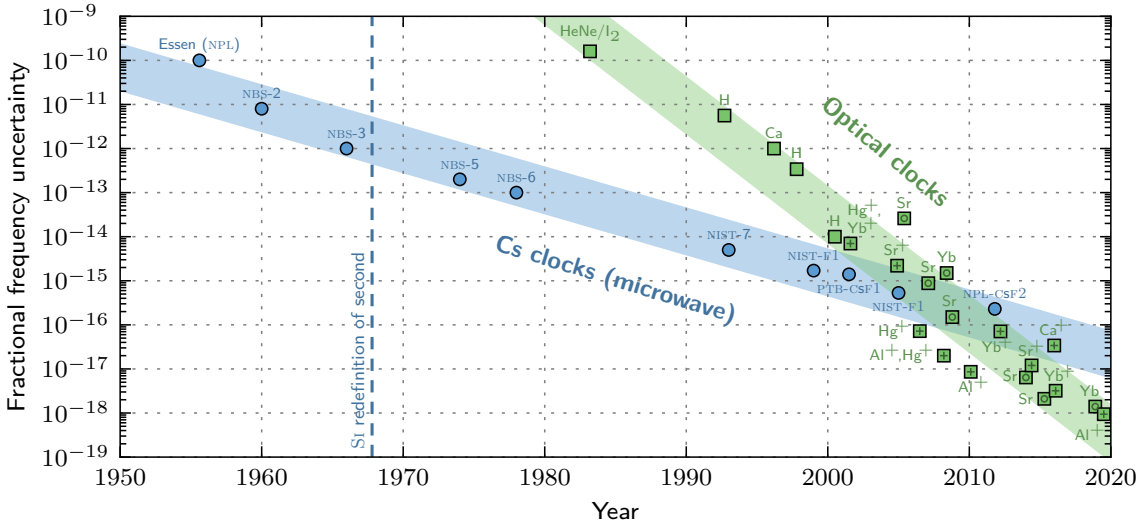

Figure 1.1: Recent progress in the accuracy of optical atomic clocks and microwave frequency standards. The trends for both clock types are indicated by colored bands as guides to the eye. Since a little over one decade, the systematic uncertainty of optical clocks have surpassed the uncertainty of cesium clocks. Figure from E. A. Dijck [36].

level E on α can be parametrized by the coefficient q [35]:

$$E(\alpha) = E_0 + q\left[\left(\frac{\alpha}{\alpha_0}\right)^2 - 1\right], \tag{1.4}$$

where α_0 is the current value of α and E_0 the corresponding energy. Since the value of q depends only weakly on electron correlations, it can be determined from atomic structure calculations with a higher accuracy than the absolute energy level values. The q parameter can then be linked to variation of the transition frequency $f = E/h$ via

$$\frac{\dot{f}}{f_0} = \frac{2q}{f_0}\frac{\dot{\alpha}}{\alpha_0} \equiv K\frac{\dot{\alpha}}{\alpha_0}, \tag{1.5}$$

such that variation of α can be expressed in terms of a dimensionless sensitivity factor $K = 2q/f_0$. The sensitivity of a frequency comparison between two different atomic frequencies to α variation is then given by the difference in their respective K values: $\Delta K = |K_2 - K_1|$. The larger this difference, the more sensitive the measurement is to variation of α. It is therefore advantageous to select a set of transitions with a large ΔK, ideally with opposite signs of K.

The accuracy of frequency determinations in the optical region has increased tremendously over the course of the past decades, and *optical atomic clocks* can now measure electronic transitions with fractional uncertainties in the 10^{-19} range [37]. This level of

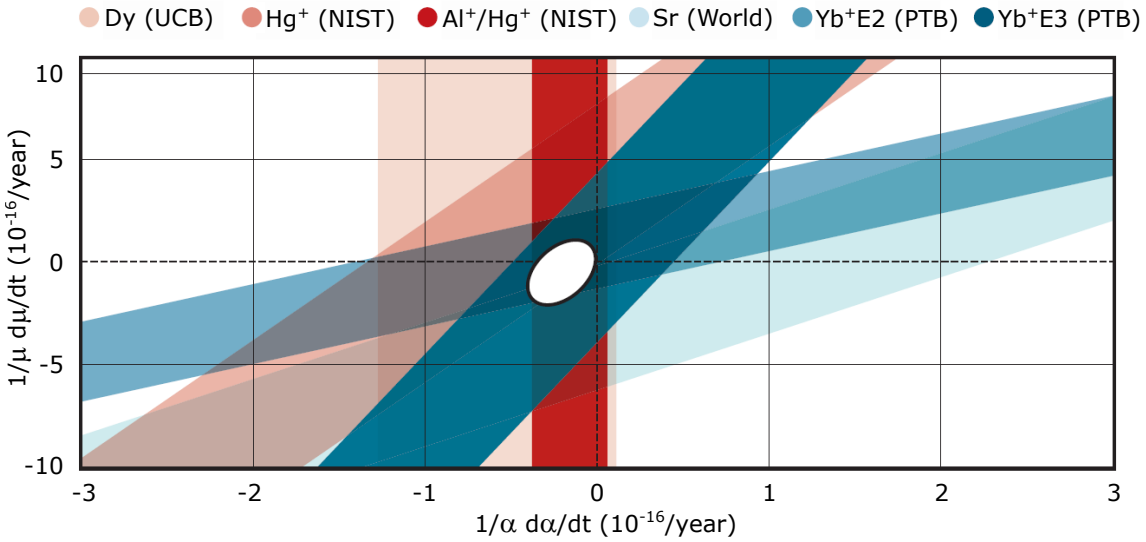

Figure 1.2: Overview of constraints from different optical clocks measurements on the variation of α and μ. The bands show 1σ uncertainty regions. Figure from DeMille et al. [9], original from Huntemann et al. [42].

accuracy surpasses that of the best Cs microwave frequency standards, which is on the order of 10^{-16}, and thereby the definition of the second [38]. This is illustrated in Figure 1.1, where the recent development of the fractional frequency uncertainty of optical and microwave clocks is shown. Due to their superior performance, optical clocks are considered for a potential future redefinition of the second [39]. Until then, only relative measurements can be performed beyond fractional uncertainties of 10^{-16} by measuring the frequency ratios between different optical clocks.

At such high accuracy levels, optical clocks have become very sensitive probes for different types of physics. It is therefore not surprising that they find applications in a wide range of fields, including navigation, telecommunication, radio astronomy, geodesy, metrology and fundamental physics. In the field of geodesy, for instance, clocks can be used as very accurate references for geodetic measurements of the Earth's surface [40]. A height difference of 1 cm at sea level causes, due to the relativistic effect of the gravitational potential, a fractional frequency shift of 1×10^{-18} in the measured atomic transition. In a recent proposal, it was suggested that optical clocks could be used to search for topological defect dark matter [41]. Light dark matter fields could form macroscopic structures, which could be detected when the Earth passes through a domain wall, as a transient effect on the frequency measured of atomic clocks.

Now let us return to the possible variation of fundamental constants and examine the sensitivity of the current generation of atomic clocks to α. For most of these, the aforementioned K factors lie between zero and one and are therefore relatively small, except

for the octupole transitions in Hg^+ ($K = -3$) and Yb^+ ($K = -6$). Using a combination of one of the octupole transitions together with one of the other transitions therefore results in a good candidate to measure α variation. To date, the most accurate limit from a single clock comparison was set by a combination of Al^+ and Hg^+ and resulted in a standard error of $2.3 \times 10^{-17}\,\mathrm{yr}^{-1}$ [43].

Hyperfine transitions, as are used in microwave clocks, are sensitive to both α, μ and the strong interaction parameter X_q, which equals the ratio between the average light quark mass and the quantum chromo-dynamic energy scale Λ_{QCD}. Extraction of X_q, however, requires nuclear structure calculations, which depend on a particular theoretical model [10]. Utilizing a combination of different microwave and optical clocks, the variations in α, μ and X_q can be measured independently, as is illustrated in Figure 1.2 for the former two. The present day best limits are given by [42, 44]

$$\begin{aligned} \kappa_{Cs}\frac{\dot{X}_q}{X_q} &= (0.14 \pm 0.09) \times 10^{-16}\,\mathrm{yr}^{-1} \\ \frac{\dot{\alpha}}{\alpha} &= (-2.0 \pm 2.0) \times 10^{-17}\,\mathrm{yr}^{-1} \\ \frac{\dot{\mu}}{\mu} &= (0.2 \pm 1.1) \times 10^{-16}\ \mathrm{yr}^{-1}, \end{aligned} \tag{1.6}$$

where κ_{Cs}, is the dimensionless sensitivity factor of the Cs hyperfine transition to the variation of the light quark masses.

1.4 Highly charged ions

The set of atomic and ionic species that can be employed as an atomic clock is very limited due to both technical constraints and the limited number of elements to choose from in the periodic table. As a result, there are only a handful of K factors available for measuring α variation. To further increase the sensitivity of such a measurement, atomic systems with larger K factors need to be used. By utilizing HCI, atomic species in higher charge states, systems with much larger K factor become available. The charge state can be used as a third degree of freedom, apart from proton and neutron number, in the periodic table for selecting a species with optimal properties. The electronic energy levels of a HCI scale proportional to $(Q+1)^2 R_\infty$, where Q is the ionization charge and R_∞ the Rydberg constant [45]. Since q scales as $\alpha^2 Z^2 (Q+1)^2$ in general, K does not directly scale with charge state Q. However, in optical transitions that occur close to level crossings in HCI, where the filling order of the electron shells changes from the Madelung rule to Coulomb with increasing ion charge [46], the scaling of the transition frequency is suppressed, such

that

$$K \propto 2\alpha^2 Z^2 (Q+1)^2. \tag{1.7}$$

The sensitivity of these optical transitions in HCI to α variation is thus enhanced by a factor $(Q+1)^2$, which is on the order of 100, as compared to neutral atomic systems.

Several theoretical studies have identified a number of suitable HCI candidates possessing K factors up to several hundred [47–50]. Although the energy levels of HCI scale with the charge state squared towards higher energies, forbidden transitions in the optical regime can be found, due to level crossings between states with accidental near degeneracy.

Apart from an increased sensitivity to α variation, HCI have more advantages compared to neutral or singly charged systems. Due to their strong binding energies, the electronic cloud shrinks and the HCI are therefore much more insensitive to external electric and magnetic fields, leading to significantly smaller systematic perturbations. This is particularly relevant for determining transition energies with a very high accuracy. The uncertainty budgets of the current generation of optical clocks are limited by systematic effects like Stark shifts, black-body radiation shifts and Zeeman shifts. These all originate from external perturbations to the electronic wavefunction and are significantly lower in HCI [51]. Therefore, HCI have been proposed as promising candidates for novel high-accuracy atomic clocks [45, 52]. Furthermore, the strong binding energies induce large fractional energy contributions from nuclear, quantum electrodynamic and special relativity effects. They form an ideal platform for benchmarking theory calculations with experimental observations [53]. Finally, recent investigations have shown that HCI are also very sensitive probes to other fundamental physics effects, for instance violation of LLI [54, 55].

Although HCI offer many advantages as probes for fundamental physics, their production and handling is much more challenging compared to singly charged ions. To reach the desired charge state, a large amount of energy is required to strip off the electrons from the neutral atom. Therefore, these ions are usually produced in an electron beam ion trap (EBIT) [57], where a high-intensity electron beam is focused by a strong magnetic field from a pair of coils in Helmholtz configuration, as it is shown in Figure 1.3. Neutral atoms are fed to the focus region and are ionized by the impact of the electron beam. Once ionized, the particles are radially trapped by the negative space charge of the electron beam. Longitudinal confinement is provided by a set of *drift tubes*, electrodes surrounding the trap region. The ions, trapped in the vicinity of the electron beam, are further ionized by electron impact ionization. Their charge state increases until the energy of the incoming electrons is no longer sufficient to reach the next charge state. The continuous electron bombardment of the electron beam populates highly excited states and induces a steady-state emission of photons via many different decay channels. This fluorescence

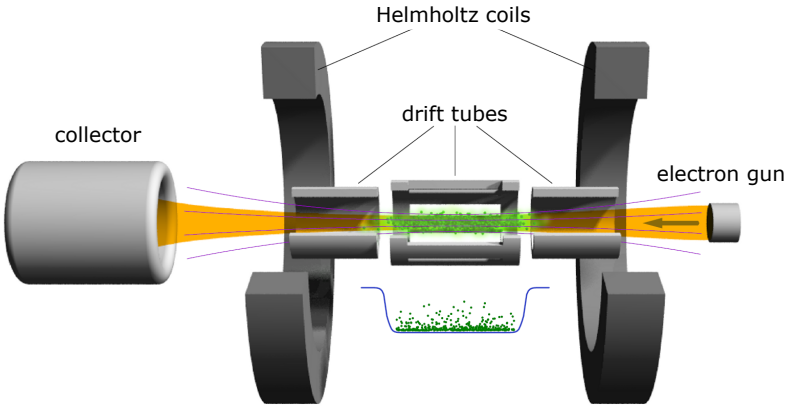

Figure 1.3: Schematic overview of an EBIT. Electrons (orange) are emitted by the electron gun and travel towards the collector. The magnetic field lines (violet), generated by a pair of Helmholtz coils, compress the electron beam. The produced ions (green) are radially confined by its space charge. By lowering the (relative) potential on the central drift tube, axial confinement of the ions is ensured, as illustrated by the blue potential curve. Figure from S. Bernitt [56].

light can then be used to monitor the charge state and identify transition energies.

Spectroscopy inside an EBIT is a task of crucial importance, since there is an enormous scarcity of experimental data. Many possible ions have never been explored and therefore reside in the so-called *spectral desert* [45]. Due to the continuous supply of energy by the electron beam, typical temperatures of the ion cloud in an EBIT are of the order of MK. This can be reduced by roughly one order of magnitude by lowering the electrode potentials and evaporatively cooling the HCI cloud. Still, at such high temperatures the linewidths of the observed transitions are Doppler broadened by tens of GHz, severely limiting the attainable spectroscopic accuracy to a few parts per million (ppm) at most. In contrast, singly charged ion traps routinely achieve temperatures below μK enabling accuracies on the order of 10^{-18}, as discussed in the previous section. To bridge this enormous gap, the HCI need to be extracted from the EBIT and subsequently cooled and stored in a more controllable environment.

Direct laser cooling, the standard tool for neutrals and singly charged ions, is not available for most HCI due to the lack of fast-cycling optical transitions. The fast electric-dipole (E1) transitions are shifted towards the x-ray domain and the remaining optical lines are usually forbidden and therefore have long lifetimes. To overcome this difficulty, sympathetic cooling of the HCI by a different, singly charged ionic species can be employed. This technique was experimentally realized a few years ago at the Max-Planck-Institut für Kernphysik (MPIK) in the Cryogenic Paul Trap Experiment (CryPTEx) [58]. Ar^{13+} ions were extracted from the EBIT, decelerated and subsequently retrapped in a cryogenic Paul trap. A crystal of Be^{+} ions was used for sympathetic cooling of the HCI and

brought down their temperature to the mK region. In a more recent follow-up experiment at the Physikalisch-Technische Bundesanstalt (PTB), HCI were cooled to below 50 μK [59]. Quantum logic spectroscopy (QLS), where one HCI is co-trapped with a single cooling ion, was implemented on the forbidden $^2P_{1/2} \rightarrow {}^2P_{3/2}$ transition in Ar^{13+} at 441 nm. The strong Coulomb coupling between both ions enables reading out the state of the HCI via the logic ion [60]. Although the systematic shifts are not yet fully evaluated, the observed fractional uncertainty of 3×10^{-15} is seven orders of magnitude smaller than that of previous measurements in EBITs. This result demonstrates that HCI can be used for ultrahigh precision spectroscopy, enabling novel high-accuracy atomic clocks and new tests of fundamental physics based on HCI.

1.5 Extreme ultraviolet spectroscopy

The performance of an optical clock is often expressed in terms of the *Allan deviation* σ_y, which provides a measure of the statistical errors during a frequency determination [61]. For a Ramsey interrogation scheme of the clock transition frequency f_0 with the $\pi/2$ pulses being short compared to the probe time T_m and perfect detection efficiency, the Allan deviation is given by [25]

$$\sigma_y(t) = \frac{1}{2\pi\nu_0\sqrt{NT_m t}}. \tag{1.8}$$

Here, N is the number of uncorrelated atoms or ions and t is the total averaging time. Clearly, a large atom number, long probe time and high transition frequency result in a lower instability and thus better resolution within a given averaging time. Increasing the atom number can dramatically lower the averaging times, which is ~ 10 minutes for the best Sr lattice clocks [62], but also leads to additional systematic shifts originating from the trapping potentials. The probe time is limited either by the lifetime of the excited state or by the coherence of the clock laser. The current most stable lasers with a flicker noise floor of 4×10^{-17} achieve phase coherence times of a few tens of seconds [63]. Increasing the transition frequency is the final possibility of improving the stability of the clock. It is mainly for this reason that optical atomic clocks, with transition frequencies in the THz region, outperform the Cs microwave frequency standards at 9 GHz.

It would therefore make sense to further increase the clock frequency in order to improve on its stability. However, clock operation at higher frequencies is not that easy and has so far been prevented by two main issues. First, lack of a suitable atomic system, since most neutrals and singly charged ions are ionized when exposed to extreme ultraviolet (XUV) or x-ray radiation. Narrow linewidth clock transitions with considerably higher frequencies are therefore scarce among these systems. Second, the lack of coherent light sources in the

XUV and x-ray domains limits the attainable frequency determination accuracy outside the infrared (IR) and optical regions. We will now briefly discuss both issues and their possible solutions in more detail.

The first limitation can be overcome by using clock transitions at higher frequencies in HCI, since they are robust against the high energy photons from XUV and x-ray radiation. In recent theoretical studies, many possible clock transitions have been identified with long lifetimes and low sensitivity to external perturbations [45, 46, 64]. Although most of the suggested forbidden lines lie in the optical or near-infrared (NIR) region such that they are easily accessible by standard laser technology, the vast majority of HCI transitions are located in the XUV and x-ray regions due to the $\sim (Q+1)^2 R_\infty$ scaling. Among these, many suitable clock transitions can be found, of which the properties can be carefully fine-tuned by selecting the appropriate charge state, atomic number and isotope. Apart from HCI, there is also the possibility to use a nuclear excitation as a clock transition. Many investigations have been performed towards the *thorium isomer*, the first excited state of the ^{229}Th nucleus. At an energy of $7.8 \pm 0.5\,\mathrm{eV}$, this unique nuclear transition has been proposed as an ideal clock candidate with a very long excited state lifetime [65]. Recently also a different nuclear transition in ^{235}U at 76 eV was proposed as an alternative [66]. It was shown that using a specific charge state, $^{235}\mathrm{U}^{7+}$, the electronic bridge mechanism greatly enhances the probability of a nuclear excitation. Also for the thorium isomer, using certain charge states might increase the transition probability via this mechanism. It thus becomes evident that highly charged systems are crucial for the development of XUV or even x-ray clocks.

The second limitation, the lack of coherent light sources for driving narrow transitions beyond the optical region, stems from the fact that almost all solid materials start to absorb electromagnetic radiation below $\sim$200 nm, limiting the choice of gain media to gases. The scarcity of highly reflective mirrors in this spectral region further complicates the development of this type of lasers. Beams of high energy photos can be delivered by large-scale facilities such as synchrotrons or free-electron lasers (FEL). Where the emitted radiation is incoherent in the case of a synchrotron, self-amplified spontaneous emission in an FEL leads to microbunching of the electrons in the undulator. The outgoing photons within one bunch are likely to be emitted in phase, producing a quasi-coherent photon beam with much higher brilliance compared to a synchrotron. Although radiation from such facilities can be used for spectroscopy of HCI [67–69], the lack of coherence limits the attainable fractional uncertainty to >1 ppm. An alternative method to generate XUV radiation is the upconversion of laser radiation from optical or NIR wavelengths. Techniques such as second-harmonic generation (SHG), third-harmonic generation and four-wave mixing are widely used in frequency metrology laboratories in order to obtain coherent light at the desired wavelengths. By cascading several of such frequency conversions, radiation

in the vacuum ultraviolet region can be produced [70, 71].

To reach even higher energies and obtain XUV wavelengths, high harmonic generation (HHG) can be used. This highly non-linear process produces odd harmonics of the fundamental radiation via the interaction of a high intensity laser field with a dense gas cloud [72–74]. Photon energies up to keV can be produced [75], requiring very high laser intensities in the range of $10^{13} - 10^{15}\,\mathrm{W/cm^2}$. These can be reached by strongly focusing ultrashort laser pulses. Since such short pulses posses a broad spectrum of frequencies, they are usually not suitable for precise frequency determinations. One solution is the use of longer pulses in the ns range, which provide still enough power to drive the non-linear conversion process, but also have a sufficiently narrow bandwidth to allow for XUV frequency spectroscopy [76, 77]. A different approach is to produce harmonics with a stabilized train of femtosecond pulses and utilize its comb structure, as introduced in Section 1.2.

The resulting *XUV comb* has been rapidly evolving since its first introduction in 2005. The generated power has increased by roughly six orders of magnitude, from initial nW power levels to the current generation of several mW per harmonic [78–80]. The development of fiber laser technology has enabled switching from Ti:sapph sources to more robust fiber-based systems [81, 82]. Subsequently, the maximum generated photon energies have increased from $\sim 20\,\mathrm{eV}$ in the first experiments, to over $100\,\mathrm{eV}$ in recent years [83, 84]. Furthermore, in an experiment of crucial importance, it was shown that such combs can generate radiation with long coherence times $> 1\,\mathrm{s}$ [85]. XUV combs can thus be used for direct frequency spectroscopy in the XUV [86], while exploiting the standard, well-developed laser stabilization techniques that are available in the optical and NIR. In this way, the XUV comb principally allows for reaching fractional accuracies in the XUV that are similar to that of modern optical clocks.

In conclusion, the development of XUV comb technology enables ultra-high precision spectroscopy in the XUV and HCI are very robust and suitable targets in this spectral region. So far, no spectroscopy with a precision exceeding a few ppm has been performed on HCI in the XUV region, and XUV comb technology has not been applied to HCI. The aim of this work is to develop an XUV comb to enable measuring XUV transitions in HCI with an unprecedented precision. Since copies of the original frequency comb are generated simultaneously at all odd multiples up to a certain cut-off energy, the XUV comb covers a very broad spectrum. Any HCI transitions within this spectrum can in principle be driven, provided the excited state has a suitable lifetime. This will open up a new, unexplored region of high-accuracy frequency determinations in the XUV, which could lead to hints of new physics. Furthermore, this development paves the way for a novel generation of even more accurate atomic clocks operating at higher frequencies.

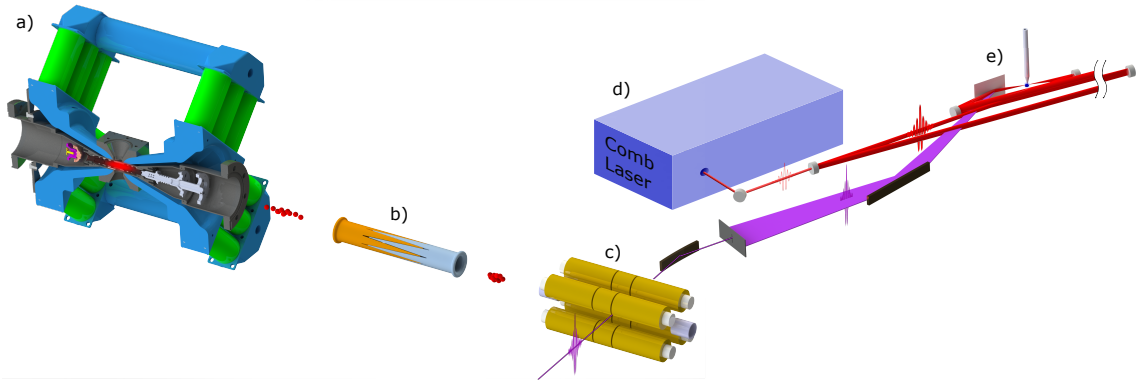

Figure 1.4: Schematic overview of the experiment. a) HCI production in a compact EBIT. b) deceleration of the HCI bunches. c) the HCI are retrapped in a linear Paul trap, where they are sympathetically cooled by a crystal of Be^+ ions. d) a FC produces 200 fs pulses at a rate of 100 MHz. e) the FC pulses are amplified inside a passive enhancement cavity. XUV radiation, produced in the cavity focus, is coupled out via a grating mirror and the desired wavelength, selected by a vertical slit, is send to the cold HCI in the Paul trap.

1.6 Experimental implementation

To enable the first XUV spectroscopy of HCI, a second generation of the earlier mentioned cryogenic Paul trap experiment is being constructed at the MPIK: CryPTEx II. A schematic overview of the experimental setup is shown in Figure 1.4. HCI are produced in a novel, compact EBIT (a), which operates at room-temperature and with permanent magnets rather than superconducting magnets, that are used in conventional EBITS, in order to reduce construction, maintenance and operation costs [87]. By pulsing a high voltage on one of the drift tubes, a bunch of HCI can be extracted from the EBIT. An electrostatic bender (not shown) selects the desired charge state by their q/m ratio. These ions are then decelerated by a pair of pulsed serrated electrodes (b). The serrated design produces a linearly increasing potential, which is quickly pulsed to zero when the ions are in the interlaced region. In this way, the longitudinal kinetic energy spread of the ion bunches is reduced. The ion bunch is then guided towards a linear Paul trap (c), where they are trapped by two switchable mirror electrodes on the trap axis. The ion bunch starts to oscillate between these two electrodes. Each time the bunch passes by the center of the trap, it interacts with a Coulomb crystal of hundreds of laser-cooled Be^+ ions, reducing the kinetic energy of the HCI. Eventually the HCI crystallize and become trapped inside the Be^+ crystal. The number of Be^+ ions can now be reduced such that one HCI is sympathetically cooled by a single Be^+ ion. The HCI can then be illuminated by XUV light to resonantly drive XUV transitions, and the HCI state can be read out via QLS.

In order to perform high-accuray frequency determinations in the HCI using an XUV

comb, the combs line spacing needs to be much larger than the linewidth of the transition. Otherwise, it would become very hard to determine the tooth number that is resonant while the repetition rate is scanned. Once the resonant tooth number has been determined, the absolute transition frequency is immediately known via the comb repetition rate and offset frequency. In our case, the comb laser (d) is operating at a repetition rate of 100 MHz with a central wavelength of 1039 nm and a 14 nm bandwidth. At such a high repetition rate, it is much harder to reach the peak powers required for HHG $> 10^{13}\,\mathrm{W/cm^2}$, as compared to kHz laser systems. Therefore, several amplification steps are necessary. The pulses from the oscillator are enhanced by several fiber amplifiers and subsequently compressed to an average power of 80 W with a 200 fs pulse duration. The pulses are then send into a passive enhancement cavity (e), situated in a large vacuum chamber. In this cavity, the incident pulses are resonantly overlapped and strongly focused on a gas target. High-order harmonics are produced in the cavity focus and propagate collinearly with the NIR beam. In order to separate the XUV radiation from the resonant cavity beam, a grating mirror is used, resulting in a spatially dispersed harmonic spectrum. The desired wavelength is then selected by a vertical slit, and the XUV light can be focused on the trapped HCI in the Paul trap by a few grazing incidence optics.

One of the main challenges of using a frequency comb for direct spectroscopy of a single atomic transition is that the laser power is divided over many ($\sim 10^5$) comb lines, of which only one contributes to driving the transition. Although there are alternative ways to use many modes of the comb spectrum, such as employing a two-photon excitation scheme [89], Fourier-transform spectroscopy [90] or Ramsey-comb spectroscopy [91], these methods come with their own challenges such as complicated alignment issues. To estimate what level of XUV power is required to obtain a reasonable excitation probability, calculations were performed by C. Lyu and Z. Harman [88]. The results are shown in Figure 1.5 for the $^3P_1 \rightarrow {}^1S_0$ transition in Ar^{6+} at 88 nm (14.1 eV) with a lifetime of 1.3 μs. For the calculations, the XUV comb was assumed to consist of 200 fs pulses at a repetition rate of 100 MHz, focused to an area of 10 $\mu\mathrm{m}^2$. The linewidth of the comb tooth was taken to be 100 kHz, which is on the same order of magnitude as the 122 kHz natural linewidth of the transition. For a 4 mW comb, the Rabi-frequency is 720 kHz, such that Rabi oscillations can be observed, as is visible in Figure 1.5f). The chaotic behavior due to the limited coherence time of 1.6 μs, visible in orange, is averaged out when using a large set of different noise samples, visible in blue. With 40 μW of power per harmonic, an average fractional population inversion of 0.14 can be reached, corresponding to a fluorescent photon rate of 17 kHz. If the power is increased to 4 mW, the average excited state population increases to 0.49, resulting in a fluorescent rate of 59 kHz. These calculations thus show that several tens of μW of power per harmonic is sufficient to observe resonant excitations in HCI, such that ultra-precise frequency determinations can be performed.

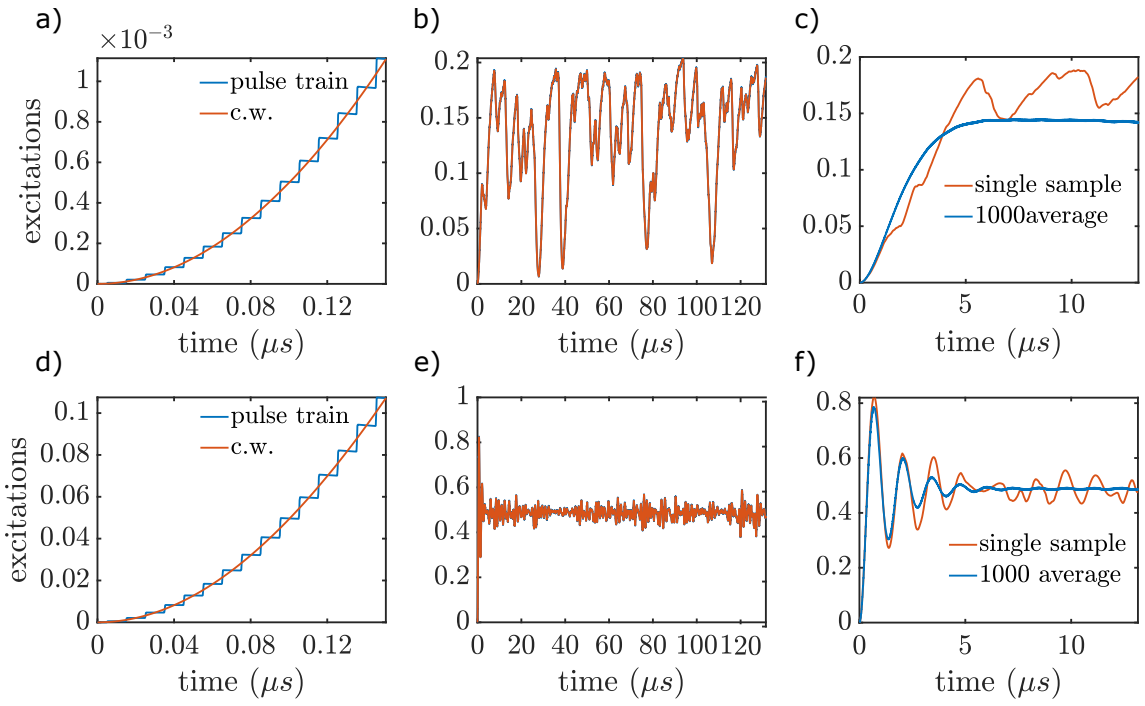

Figure 1.5: Excitation dynamics for the $^3P_1 \rightarrow {}^1S_0$ transition in Ar^{6+} at 88 nm (14.1 eV), interacting with 200 fs pulses, separated by 10 ns, from an XUV comb with a linewidth of 100 kHz and 40 μW per harmonic for a), b) and c), and 4 mW per harmonic for d), e) and f). The number of excitation is normalized such that full population inversion equals to one. The step-wise excitations visible in a) and d) originate from the pulsed nature of the radiation (blue solid line) and become smooth when continuous-wave (CW) light with the same average power is considered instead (orange solid line). In c) and f), the orange lines represent the dynamics of the first 10 μs in a) and d), respectively, while the blue lines show the behavior averaged over a 1000 samples. Clear Rabi-oscillations appear for the 4 mW comb. Figure from C. Lyu [88].

1.7 Thesis outline

The main objective of this thesis is the development of an XUV comb for HCI spectroscopy for tests of fundamental physics. The theoretical background and principles of HHG and enhancement cavities are treated in Chapter 2. The experimental setup, which was built from scratch in the scope of this thesis, is introduced in Chapter 3. First, the laser system is introduced, followed by the design and realization of the enhancement cavity. Subsequently, the vacuum system accommodating the cavity and the differential pumping system for removal of HHG target gas are described. In Chapter 4, experimental results of the first multi-photon ionization measurements at a rate of 100 MHz are presented. Xenon atoms were ionized in the focus of the enhancement cavity and images of the photo-electron distribution are analyzed. In Chapter 5, the results of intra-cavity HHG are discussed, where different gas mixtures were used to boost the output power of the XUV radiation. Finally, a summary and outlook are provided in Chapter 6.

Chapter 2

Theoretical background

In this chapter we cover the theoretical aspects that are relevant for producing an XUV frequency comb. We start with a brief treatment of ultra-short pulses that is key to understanding the principles of a frequency comb. Next, a theoretical description of HHG in the single-pulse regime is provided. Subsequently, harmonic generation with a phase-stabilized pulse train, resulting in an XUV comb, is discussed. We will then treat the basics of optical resonators and how they can be used to amplify laser radiation. Finally, we will consider the enhancement of femtosecond pulses, that is required for XUV comb generation, in such a cavity.

2.1 Ultrashort laser pulses

In this section, some of the basis properties of ultrashort laser pulses are introduced, following the treatment of J.-C Diels and W. Rudolph [92]. Subsequently, we describe the characteristics of a coherent pulse train. Finally, the frequency comb, already introduced in Section 1.2, is discussed in more detail.

2.1.1 Pulse propagation

The behavior of electromagnetic fields is described by Maxwell's equations for electrodynamics. Rewriting these equations in the absence of charges and currents in vacuum leads to the wave equation,

$$\partial_z^2 E(z,t) - \frac{1}{c^2}\partial_t^2 E(z,t) = 0, \tag{2.1}$$

here considered in one dimension. The plane wave solution represents a traveling wave propagating in z-direction at the speed of light $c = 1/\sqrt{\frac{\epsilon_0}{\mu_0}} = 299792458\,\mathrm{m/s}$, with ϵ_0 being the vacuum permittivity and μ_0 the vacuum permeability. The electric field component of this wave is given by

$$E(z,t) = E_0 e^{i(\omega_c t - kz)}. \tag{2.2}$$

The wave is oscillating at the carrier frequency ω_c and characterized by the wave number $k = \omega_c/c$. The oscillation amplitude is given by E_0. In the case of a pulse of light, the field consists of many waves oscillating at different frequencies ω. The pulse can then be represented by integrating over all frequency components,

$$E_t(z,t) = \frac{1}{2\pi}\int_{-\infty}^{\infty} A\left(\omega-\omega_{\mathrm{c}}\right) e^{i\omega t} e^{-ikz} d\omega, \tag{2.3}$$

where the amplitude factor $A(\omega-\omega_c)$ describes the amplitude of the different frequency components in the wave-packet. To find the frequency distribution of the pulse, a Fourier transformation can be applied. Equation (2.3) is already in an appropriate form such that the Fourier transform is simply given by

$$E_\omega(z,\omega) = \mathscr{F}\left\{E_t(z,t)\right\} = \int_{-\infty}^{\infty} E_t(z,t) e^{-i\omega t} dt = A\left(\omega-\omega_{\mathrm{c}}\right) e^{-ikz}. \tag{2.4}$$

In order to simplify the theoretical description of pulse propagation and interaction, $A\left(\omega-\omega_c\right)$ can be separated into the carrier frequency ω_c and an envelope function such that $A\left(\omega-\omega_c\right) = A(\omega)e^{-i\omega_c t}$ [93]. The wave number k can also be expanded around ω_c, such that $k = k_c + \delta k$, and Equation (2.3) becomes

$$\begin{aligned} E_t(z,t) &= e^{i(\omega_c t - k_c z)} \int_{-\infty}^{\infty} A(\omega) e^{i\omega t} e^{-i\delta k z} d\omega \\ &= A(z,t) e^{i(\omega_c t - k_c z)}. \end{aligned} \tag{2.5}$$

Hence, the wave-packet can be expressed as a fast oscillating carrier wave and an envelope function that determines the shape of the pulse in time and frequency domain. This separation is justified as long as the spectral bandwidth of the pulse is small compared to the carrier frequency. Or, equivalently, when the pulse envelope and phase vary by a small amount within one optical cycle, the slowly varying envelope approximation holds [92]. The pulse envelopes in the time and frequency domain are relation via the the Fourier transform:

$$A_t(z,t) = \int_{-\infty}^{\infty} A_\omega(z,\omega) e^{-i\omega t} d\omega. \tag{2.6}$$

Now let us observe the temporal evolution of the pulse amplitude at a specific position $z = 0$ in space,

$$\begin{aligned} E_t(0,t) &= A_t(0,t) e^{i\omega_c t} \\ E_\omega(0,\omega) &= A_\omega\left(0, \omega-\omega_{\mathrm{c}}\right). \end{aligned} \tag{2.7}$$

The amplitude distribution factors $A_t(0,t)$ and $A_\omega\left(0,\omega-\omega_{\mathrm{c}}\right)$ describe the pulse envelope in both the time and frequency domain, linked via the Fourier transform. Several possible shapes of the envelope function are sech^2, Lorentzian or Gaussian, the latter of which is

most widely used. The Gaussian temporal and spectral dependence yield

$$\begin{aligned} A_t(t) &= E_0 e^{-\frac{2\ln 2 t^2}{\tau^2}} \\ A_\omega(\omega-\omega_c) &= E_0\tau\sqrt{\frac{\pi}{2\ln 2}} e^{-\frac{\tau^2(\omega-\omega_c)^2}{8\ln 2}}. \end{aligned} \tag{2.8}$$

In the time domain, pulses are characterized by specifying a pulse duration τ which equals the full-width half-maximum (FWHM) of the intensity profile $I(t) = |E(t)|^2$. The spectral width Δf is given by the FWHM of the spectral intensity. Since τ and Δf are related via the Fourier transform, a minimal time-bandwidth product can be defined as

$$2\pi\tau\Delta f \geq 2\pi \cdot 0.441, \tag{2.9}$$

where the factor 0.441 is specific for Gaussian pulses and depends on the shape of the pulse. For bandwidth-limited pulses, which have the shortest possible duration for a given spectral bandwidth, the equality holds. If there is a frequency variation (chirp) across the pulse, the duration of the pulse will be larger than that of a bandwidth-limited pulse.

2.1.2 Train of pulses

Now we will discuss the behavior of the spectral distribution in case of multiple pulses instead of a single one. Consider a pulse train of N pulses, delayed by the repetition time T_{rep}. The electric field of the pulse train can then be expressed as [94]

$$E_{\mathrm{pt},t}(t) = \sum_n^{N-1} A_t(t - nT_{\mathrm{rep}}) e^{i(\omega_c t - n\omega_c T_{\mathrm{rep}} + n\Delta\phi_{\mathrm{CE}})}, \tag{2.10}$$

where $\Delta\phi_{\mathrm{CE}}$ is the carrier-to-envelope phase. If $\Delta\phi_{\mathrm{CE}}$ is zero, the envelope maximum overlaps with a maximum of the underlying electric field oscillating at the carrier frequency for every pulse. A non-zero carrier-to-envelop phase (CEP) is defined as the phase difference between the electric field maximum and the envelope maximum, as shown in Figure 2.2, where the pulse-to-pulse phase 'slips' by an amount equal to $\Delta\phi_{\mathrm{CE}}$. The electric field in the frequency domain is given by the Fourier transform of Equation (2.10)

$$\begin{aligned} E_{\mathrm{pt},\omega}(\omega) &= \sum_n^{N-1} e^{i(n(\Delta\phi_{\mathrm{CE}} - \omega_c T_{\mathrm{rep}}))} \int A_t(t - nT_{\mathrm{rep}}) e^{-i[(\omega-\omega_c)t]} \mathrm{d}t \\ &= A_\omega(\omega - \omega_c) \sum_n^{N-1} e^{i(n\Delta\phi_{\mathrm{CE}} - n\omega \mathrm{T}_{\mathrm{rep}})}. \end{aligned} \tag{2.11}$$

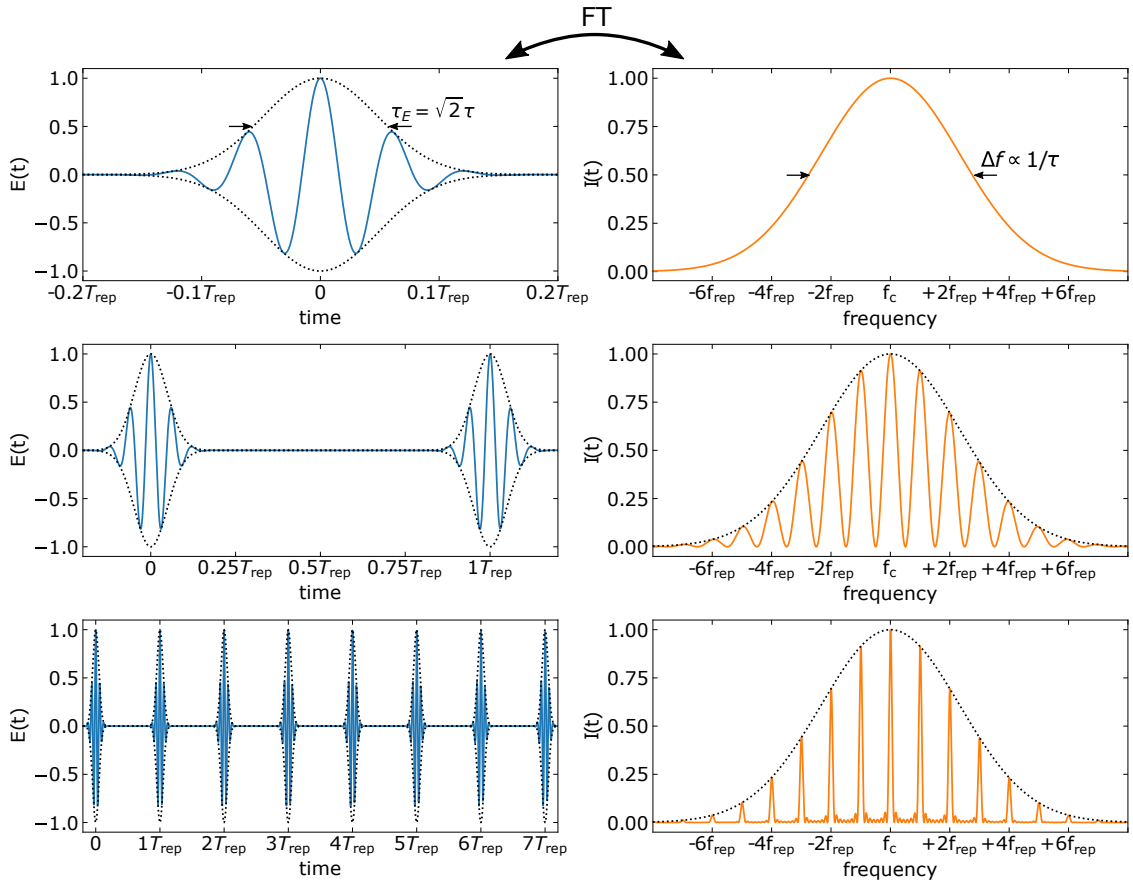

Figure 2.1: Pulse shape in both the time and frequency domain, which are linked via the Fourier transform. The oscillating electric field $E(t)$ under the pulse envelope $A(t)$ is shown in blue, the corresponding spectral intensity in orange. The pulse length of the electric field τ_E is related to the pulse duration τ via a factor $\sqrt{2}$. For more than one pulse, the intensity distribution is modulated by the pulse repetition rate f_{rep}, resulting in a series of equidistant sharp peaks when the number of pulses increases.

Here the relations $A(\omega) = \int A(t)e^{-i\omega t}dt$ and $\int f(x-a)e^{-ibx}dx = e^{-iba}\int f(x)e^{-ibx}dx$ were used to simplify the expression. With the identity $\sum_{n=0}^{N-1} x^n = \frac{1-x^N}{1-x}$, the electric field of the pulse train can be expressed as

$$E_{\mathrm{pt},\omega}(\omega) = A_\omega(\omega-\omega_c)\frac{1-e^{-iN(\omega T_{\mathrm{rep}}+\Delta\phi_{\mathrm{CE}})}}{1-e^{-i(\omega T_{\mathrm{rep}}+\Delta\phi_{\mathrm{CE}})}}. \tag{2.12}$$

Using $|1-e^{-ix}|^2 = (1-\cos(x))^2 + (-\sin(x))^2$ and the trigonometric identities $\sin^2(x) + \cos^2(x) = 1$ and $\cos(2x) = 1 - 2\sin^2(x)$, the laser intensity then yields

$$I_{\mathrm{pt},\omega}(\omega) = |E_{\mathrm{pt},\omega}(\omega)|^2 = I_0(\omega)\frac{\sin^2\left(N\left(\omega T_{\mathrm{rep}}+\Delta\phi_{\mathrm{CE}}\right)/2\right)}{\sin^2\left(\left(\omega T_{\mathrm{rep}}+\Delta\phi_{\mathrm{CE}}\right)/2\right)}. \tag{2.13}$$

The intensity spectrum of a train of pulses is thus that of a single pulse modified by a periodic function. This results in equidistant modes with their maximum intensity separated by $f_{\mathrm{rep}} = 1/T_{\mathrm{rep}}$. The electric field and intensity spectrum in the time and frequency domain, respectively, of pulse trains consisting of two and eight pulses are shown in Figure 2.1. For two pulses, a cosine modulation appears in the intensity spectrum, while for many pulses the modes become much narrower. To derive an expression for the electric field in the case of an infinite number of pulses, we can use the Poisson sum formula

$$\sum_{k=-\infty}^{\infty}\frac{1}{p}F\left(\frac{k}{p}\right)\mathrm{e}^{2\pi\mathrm{i}kx/p} = \sum_{m=-\infty}^{\infty} f(x-mp), \tag{2.14}$$

with $F(y)$ being the Fourier transform of $f(x)$. Using the fact that the Fourier transform of $\delta(t)$ is constant, we can rewrite Equation (2.11) as

$$E_{\mathrm{pt},\omega}(\omega) = A_\omega\left(\omega-\omega_c\right)\sum_{n=0}^{\infty}\delta\left(\omega T_{\mathrm{rep}}+\Delta\phi_{\mathrm{CE}}-n2\pi\right). \tag{2.15}$$

Thus, in the limit of $N \to \infty$, the electric field becomes a series of infinitely sharp frequency lines under the envelope. This pattern can be recognized as a comb of well-defined frequencies resulting from an infinite train of pulses with a fixed phase relation, hence the name frequency comb.

2.1.3 The frequency comb

In this subsection, we discuss the general principles of FCs, while a detailed description of the experimental realization is provided in Section 3.1.1. The intensity distribution of the pulse train in Equation (2.15) is only nonzero when the pulse-to-pulse phase $\omega T_{\mathrm{rep}} + \Delta\phi_{\mathrm{CE}}$ is an integer multiple of 2π. Using the definition of ϕ_{CE} as the pulse-to-pulse phase slip from Equation (2.10), we can define T_{CEO} as the time it takes, until ϕ_{CE} has changed by

an amount of 2π. The repetition rate f_{rep} and the carrier-envelope offset frequency f_{CEO} then become

$$\begin{aligned} f_{\mathrm{rep}} &= \frac{1}{T_{\mathrm{rep}}} \\ f_{\mathrm{CEO}} &= \frac{\Delta\phi_{\mathrm{CE}}}{2\pi T_{\mathrm{rep}}}, \end{aligned} \tag{2.16}$$

fully describing the regular pattern of frequency modes. This leads to the famous definition of the FC spectrum [21]

$$f_{\mathrm{n}} = f_{\mathrm{CEO}} + n f_{\mathrm{rep}}. \tag{2.17}$$

The comb thus consists of equidistant discrete *teeth* (modes) that are separated by f_{rep} and have an offset from zero of f_{CEO}. It is the combination of only these two frequencies that determine the absolute position of all frequency modes in the spectrum. The mode locations are thus independent of other properties of the pulse train, such as the temporal pulse shape or frequency chirp. Since these frequencies both lie in the RF domain, they can be easily counted and stabilized electronically.

The comb spectrum is illustrated in Figure 2.2. In practice, the number of modes in the comb spectrum is on the order of 10^5 and the width of the comb teeth is determined by the stability of f_{rep} and f_{CEO}. While the repetition rate can be easily detected by a fast photodiode and subsequently fed back to the oscillator via locking electronics, access to the offset frequency of the comb is more complicated. In the work that formed the basis for the development of the frequency comb, a self-referencing method to extract f_{CEO} was developed in the late 1990s [19, 20]. The technique compares two different parts of the comb spectrum. An octave-spanning spectrum is generated by spectral broadening in a non-linear fiber, giving rise to comb lines at twice the original frequency: $f_{2n} = 2nf_{\mathrm{rep}} + f_{CEO}$. Frequency doubling the original comb ($2f_n$) and mixing it with the broadened spectrum (f_{2n}) leads to a beat-signal from which the offset frequency can be detected: $2f_n - f_{2n} = f_{CEO}$.

With the comb fully defined, parts of the comb spectrum can be used to generate a beat signal with a CW laser to determine its absolute frequency. This can be done by measuring several beatnotes at different repetition rates, yielding a unique solution for the mode number n. Alternatively, if the wavelength of the CW laser is known with an uncertainty less than f_{rep}, for instance by using a wavemeter, a single beat signal suffices to determine the absolute CW frequency. By stabilizing the beat signal, the CW laser can be phase-locked to the comb, or vice-versa. Recent experiments have shown that in this way it is possible to transfer the stability of one CW laser to another via the frequency with an uncertainty that is independent of the phase noise of the comb [95]. Over the past few decades, frequency combs have proven to be indispensable tools for atomic clocks and frequency standards. They are widely used to transfer the stability of

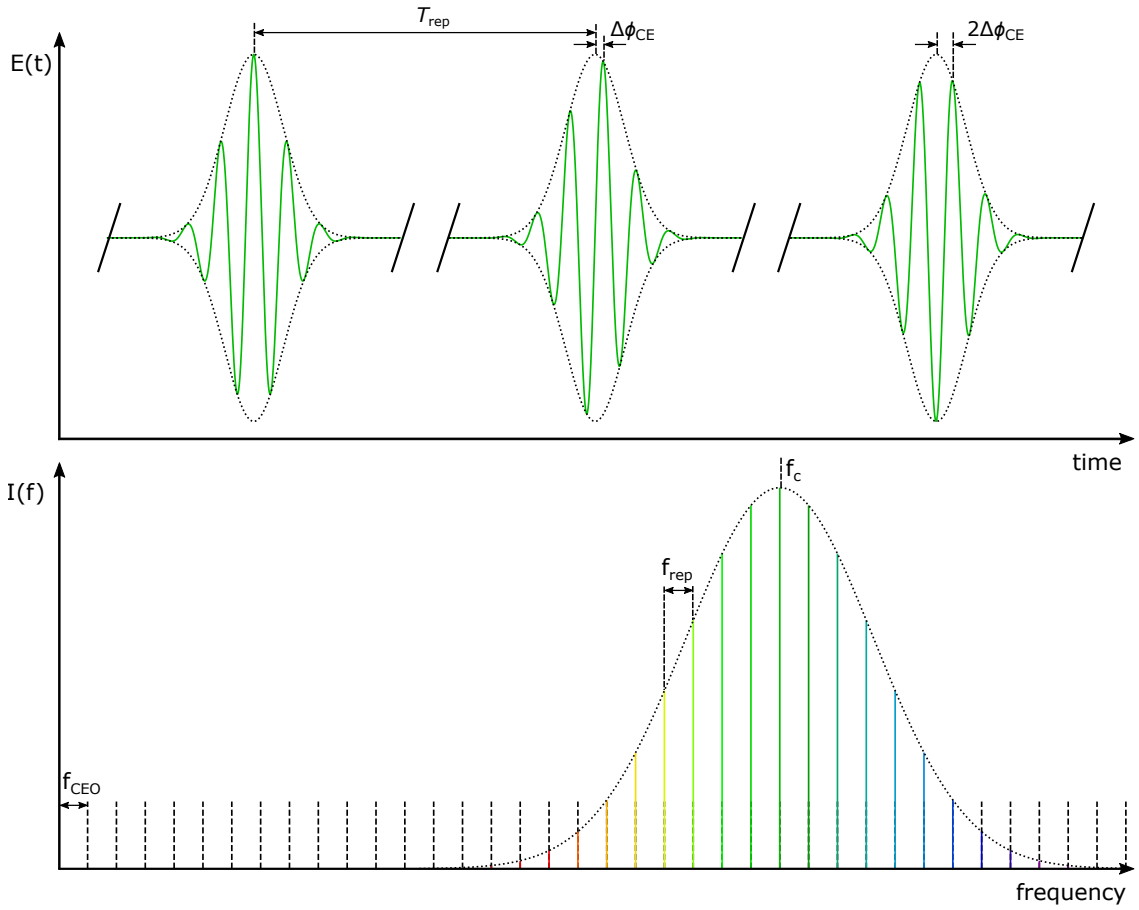

Figure 2.2: Schematic representation of a frequency comb in time and frequency domain. The comb modes, centered around the carrier frequency are separated by f_{rep} and the carrier envelope phase $\Delta\phi_{\mathrm{CE}}$ gives rise to a frequency offset from zero, f_{CEO}.

an extremely narrow line width laser, referenced to an ultra-stable cavity, to the clock laser interrogating the electronic transition. In this way, the absolute frequency of very narrow transitions in atoms and ions can be determined with extremely high precision [37, 62, 96, 97]. Nowadays, frequency combs are commercially available and have become a standard piece of equipment in many frequency spectroscopy labs.

2.2 HHG

The production of high harmonic radiation from an intense laser field was discovered in 1987 by focusing picosecond laser pulses into a gas jet [73, 74]. To fully understand the underlying physical process, a non-perturbative quantum mechanical model is required. However, a semi-classical description known as the three-step model (TSM) can provide an intuitive picture and even predict some important phenomena of the process [98, 99]. We therefore start this section with a discussion of the TSM, before we turn to the quantum mechanical description of HHG. Finally, the macroscopic HHG response and the principles of phase-matching will be covered.

2.2.1 The three-step model

The TSM is illustrated in Figure 2.3. A pulsed laser beam produces an electric field with a magnitude comparable to the Coulomb potential of an atom present in the laser focus. The electric field therefore modifies the Coulomb potential such that an outer electron can tunnel out (1.). The free electron is then accelerated by the steep electric field gradient of the oscillating laser field. Half a laser cycle later, when the electric field has changed sign, the electron can be driven back towards the parent ion (2.). It can then recombine with the parent ion and thereby emit a high-energy photon, releasing the excess energy the electron gained by the driving laser field (3.). This process can happen twice per laser cycle at specific ionization times, thereby generating a train of even shorter pulses with a much higher energy than the driving field. In a dense gas jet, the propagating laser field generates many XUV photons, which, as we will see in short, results in a collimated beam of odd integer multiples of the fundamental light.

2.2.2 Ionization by a laser field

In the first step of the TSM, the laser field perturbs the Coulomb potential of the atom. Depending on the intensity of the laser, several different regimes can be identified. The time-averaged energy of an electron executing a harmonic motion in an oscillating laser

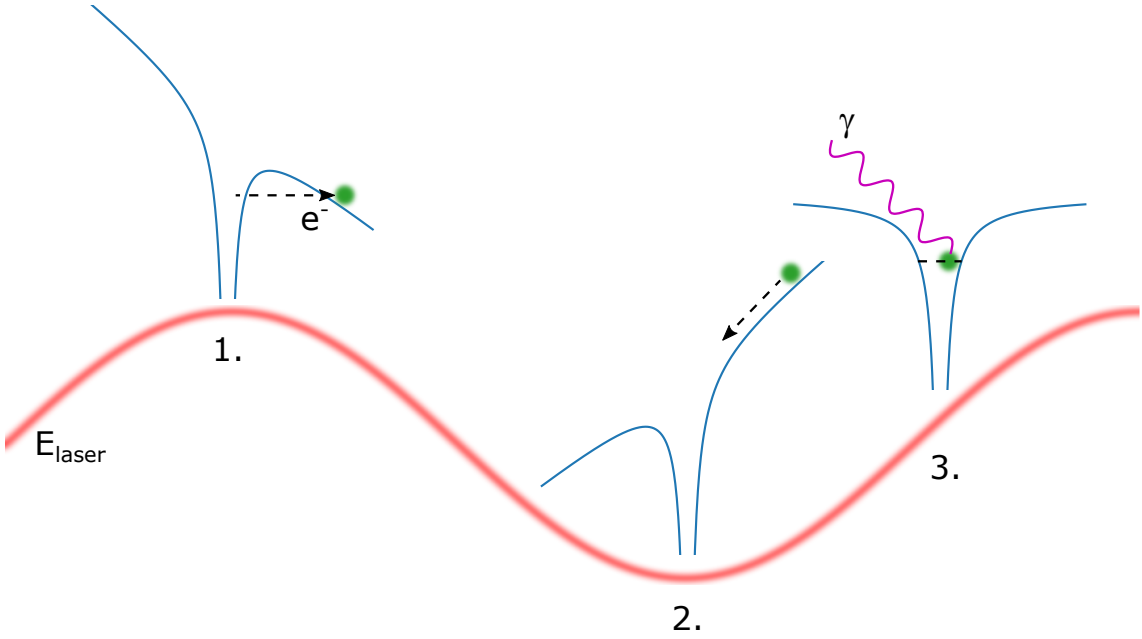

Figure 2.3: Schematic overview of the TSM. During the first step, the Coulomb potential of the atom is modified by the laser field so that the electron can tunnel out. Second, the electron is accelerated by the oscillating laser field. Finally, the electron can recombine with the parent ion under emission of a high-energy photon.

field is known as *ponderomotive energy* of the field and is given by

$$U_{\text{pond}} = \frac{e^2 E_0^2}{4 m_e \omega_c^2} = \frac{e^2 I_{\text{peak}}}{2 c \epsilon_0 m_e \omega_c^2}, \tag{2.18}$$

where I_{peak} is the peak intensity of the field. Consequently, the well-known Keldysh parameter can be defined as [100]

$$\gamma = \sqrt{\frac{U_{\text{ion}}}{2 U_{\text{pond}}}}, \tag{2.19}$$

with U_{ion} being the ionization potential of the atom. The Keldysh parameter is thus proportional to the laser frequency and inversely proportional to the laser intensity. For $\gamma \gg 1$, the ponderomotive energy is low compared to the ionization potential and multi-photon ionization (MPI) is dominant. In this process, many photons are absorbed for each photon that is emitted. The ionization rate depends strongly on the photon number N required for ionization and therefore scales with the laser intensity as I^N. This is discussed in more detail in Chapter 4, where the ionization of xenon is studied in the MPI regime. When $\gamma \sim 1$, the electric field is strong enough so that tunnel ionization becomes the dominant process. This is the regime in which HHG experiments are typically performed,

Element	U_{ion} (eV)
He	24.59
Ne	21.56
Ar	15.76
Kr	14.00
Xe	12.13

Table 2.1: Ionization energies of the most common gases used for HHG.

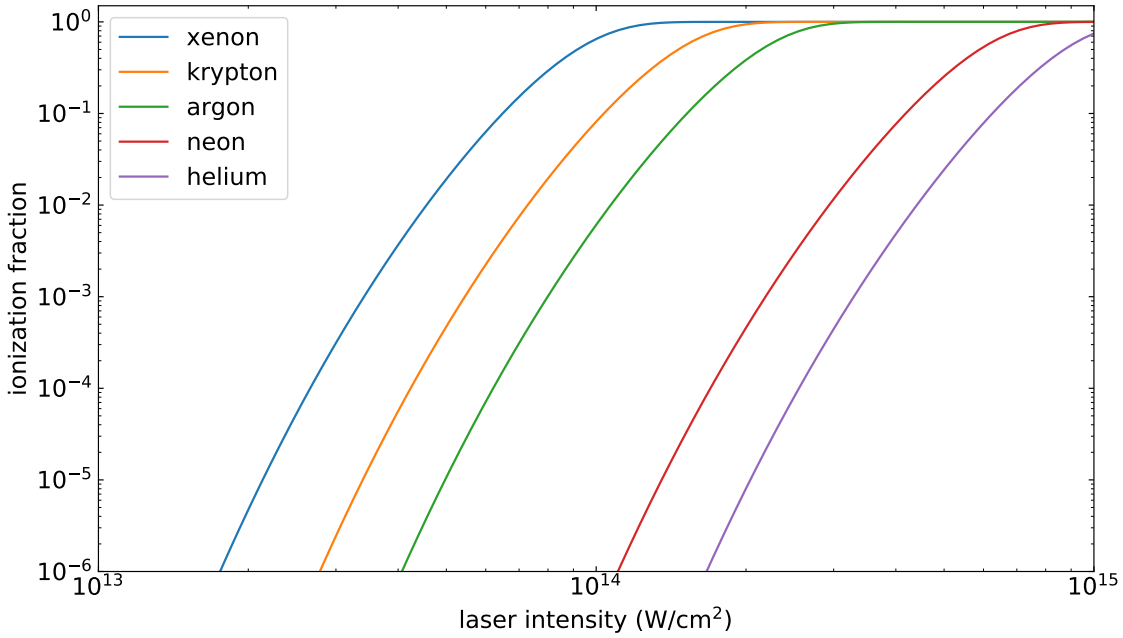

Figure 2.4: Ionization fraction as a function of the laser intensity for 200 fs pulses with a central wavelength of 1039 nm. The ionization rates were calculated according to modified ADK theory [101], using code from C. Benko [102].

as described in Chapter 5. With $\gamma \ll 1$, the electric field becomes so strong that it reduces the ionization barrier and the electron can easily leave the atom, a regime that is known as over-the-barrier, or barrier-suppression, ionization.

In order to calculate the ionization rate under the influence of an intense laser field, a theoretical method was developed by Perelomov, Popov and Terent'ev, which is now known as PPT theory [103]. A simplified formulation of this formalism was developed by Ammosov, Delone and Krainov, which is referred to as ADK theory [104]. Although this theory is easier to implement than PPT theory, it overestimates the ionization rates in the barrier-suppression regime. To improve the accuracy of ADK theory, Tong and Lin came up with a modified version that is based on an empirical formula, which is valid for both the tunnel ionization and the barrier-suppression regime [101]. The ionization fraction η

resulting from a laser field is given by

$$\eta = 1 - \exp\left(-\int_{-\infty}^{\infty} \omega_{\mathrm{ADK}}(t)\mathrm{dt}\right), \tag{2.20}$$

where $\omega_{\mathrm{ADK}}(t)$ is the instantaneous ionization rate calculated from modified ADK theory that is integrated over the laser pulse duration. The modified ADK rate is given by

$$\begin{aligned}\omega_{\mathrm{ADK}} =& \frac{C_l^2}{2^{|m|}|m|!}\frac{(2l+1)(l+|m|)!}{2(l-|m|)!}\frac{1}{\kappa^{2Z_c/\kappa-1}}\left(\frac{2\kappa^3}{F}\right)^{2Z_{c/\kappa-|m|-1}} \\ &\times \mathrm{e}^{-2\kappa^3/3F}(F)\mathrm{e}^{-\alpha\left(Z_c^2/U_{\mathrm{ion}}\right)\left(F/\kappa^3\right)}.\end{aligned} \tag{2.21}$$

In this equation, C_l represents the amplitude of the electron wavefunction in the tunneling region, l and m are the orbital angular momentum and magnetic quantum numbers of the valence electron(s) of the atom, $\kappa = \sqrt{2U_{\mathrm{ion}}}$, Z_c is the asymptotic charge seen by the electron, F is the laser field strength and α is an empirical fitting parameter for the barrier-suppression region. In Table 2.1, the ionization potentials of the most common gases used for HHG are shown. Using these values, the ionization fraction is plotted as a function of laser intensity in Figure 2.9, for 200 fs laser pulses centered around 1039 nm. Clearly, the ionization rate varies strongly for the different atomic species. It also becomes clear, that in order to ionize a significant fraction, laser intensities above $10^{13}\,\mathrm{W/cm^2}$ are needed. As we will see in Section 2.2.7, the ionization fraction of the gas is an important parameter for the macroscopic yield of HHG.

2.2.3 Semi-classical approach

After ionization, the motion of the electron can be well described by classical mechanics. The Coulomb force from the parent ion is sufficiently small during most of the electron trajectory so that the electron kinematics can be treated as a free charged particle moving in the presence of an oscillating electric laser field $E = E_0\cos(\omega t)$. We assume that the electron starts its trajectory with zero velocity at the ionization time t_i and define $\phi_i = \omega t_i$ as the corresponding phase of the driving field at this instant [105]. The velocity and position of the electron are then given by

$$\begin{aligned}x(\phi) &= \frac{eE_0}{m_e\omega_c^2}\left(\cos\phi_i - \cos\phi + (\phi-\phi_i)\sin\phi_i\right), \\ v(\phi) &= \frac{eE_0}{m_e\omega_c}\left(\sin\phi - \sin\phi_i\right),\end{aligned} \tag{2.22}$$

where the time evolution is expressed in terms of the laser phase $\phi = \omega t$. Several possible trajectories are shown in Figure 2.5 for different values of ϕ_i. It becomes clear that for values of ϕ_i between 0 and $\pi/2$, the electron trajectory leads back to the ion such that

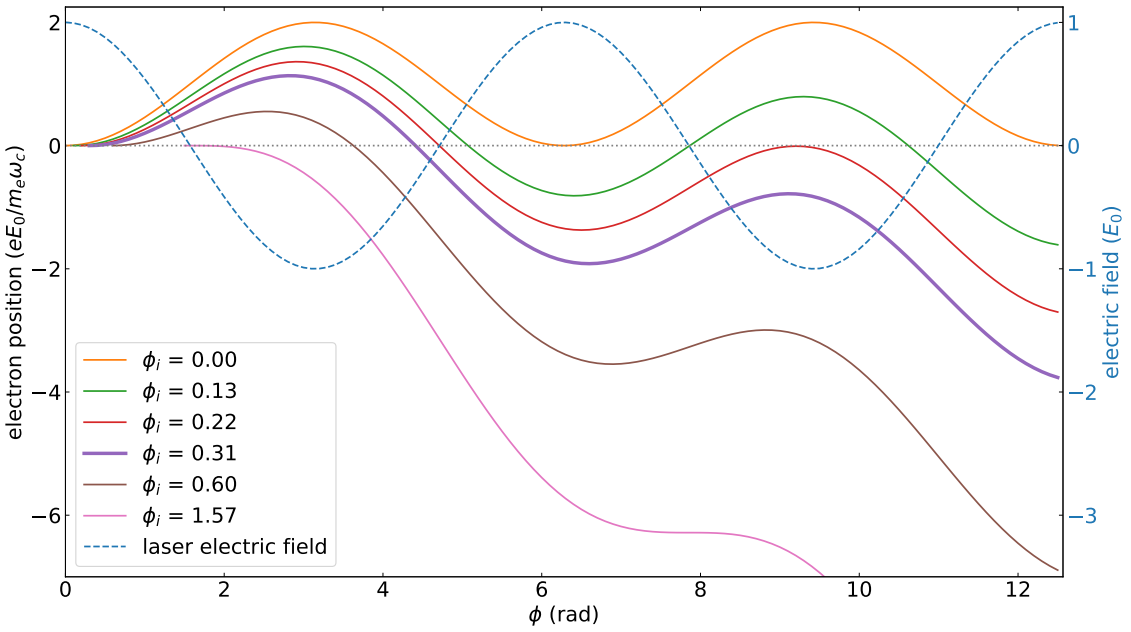

Figure 2.5: Position of the electron over time. A few possible electron trajectories are shown with indicated ionization phase ϕ_i. For ϕ_i=0.31 the electron has maximum kinetic energy when it returns to the parent ion.

recollision can take place. For $\phi_i < 0.22$ recombination could happen even after more than one laser cycle, while for $\phi_i > \pi/2$, the electron is driven away from the parent ion.

Upon recollision, the energy of the electron can be released as a high-energy photon. The kinetic energy of the electron follows from Equation (2.22) and (2.18)

$$E_{\text{kin}} = 2U_{\text{pond}} \left(\sin(\phi) - \sin(\phi_i)\right)^2 . \tag{2.23}$$

Solving for $x(\phi) = 0$ gives the phase of recombination, from which E_{kin} can be calculated. The result is shown in Figure 2.6, where the kinetic energy of the electron at the moment of recombination with the parent ion is shown in orange as a function of the ionization phase ϕ_i. The same distribution is also plotted against the recombination phase ϕ_r. The electron gains a maximum excess kinetic energy of $3.17U_{\text{pond}}$ for $\phi_i = 0.31$, corresponding to $\phi_r = 4.4$. Therefore the maximum energy of the emitted photon, the HHG *cutoff* energy, is given by

$$E_{\text{max}} = U_{\text{ion}} + 3.17U_{\text{pond}}. \tag{2.24}$$

Since the laser field is still close to its maximum value at the ionization time for which this largest energy is reached, harmonic generation is efficient even near the cutoff energy.

Electrons with $\phi_i < 0.31$, thus emitted before the kinetic energy peak, follow a trajectory that leads to recombination at $\phi_r > 4.4$ and therefore follow a *long* trajectory. Electrons

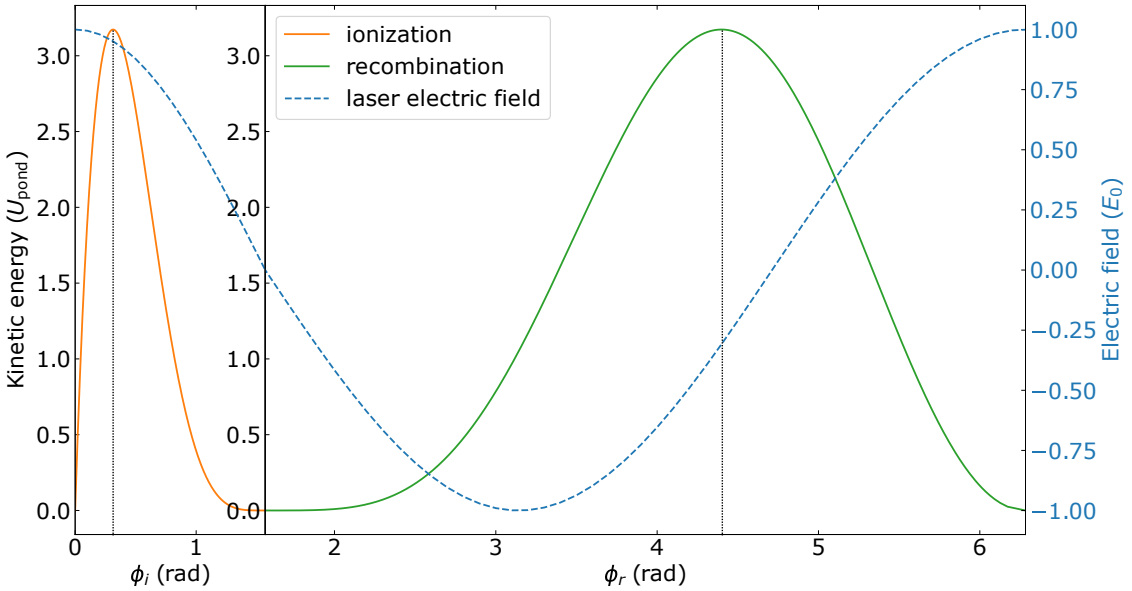

Figure 2.6: Kinetic energy of the electron at the moment of recombination, normalized to the ponderomotive energy. The maximum kinetic energy of $3.17U_{\text{pond}}$ occurs for an ionization phase of ϕ_i=0.31 and a recombination phase of ϕ_i=4.4, indicated by the dotted lines.

emitted at $\phi_i > 0.31$ recombine at $\phi_r < 4.4$ and follow *short* trajectories. Each ϕ_i leads to a specific ϕ_r as a solution of Equation (2.22) and so do $\phi_i + m\pi$ and $\phi_r + m\pi$. The long and short trajectories can thus take place every half-cycle of the laser field, with an alternating phase. This leads to harmonic generation with an alternating field direction twice per laser cycle. In frequency domain, this means that the harmonic field contains only odd multiples of ω_c. This is shown in Figure 2.7, where the electric field composed of odd harmonic orders $9 - 21$ is shown in orange. Indeed the phase changes every half cycle of the laser electric field as shown in blue. The intensity of the HHG field, which is emitted as a train of pulses separated by half a laser cycle, from a single laser pulse is shown in green.

2.2.4 Quantum theory of HHG

The preceding classical discussion of the TSM provides an intuitive understanding of the process and agrees well with experimental findings. It reproduces some of the basic features resulting from an analytical quantum mechanical description of HHG, known as the *Lewenstein model* [105, 106]. A brief summary of this model is provided here in atomic units.

The interaction between an atom and a driving laser field, linearly polarized in the x direction, can be described by the time-dependent Schrödinger equation in the length

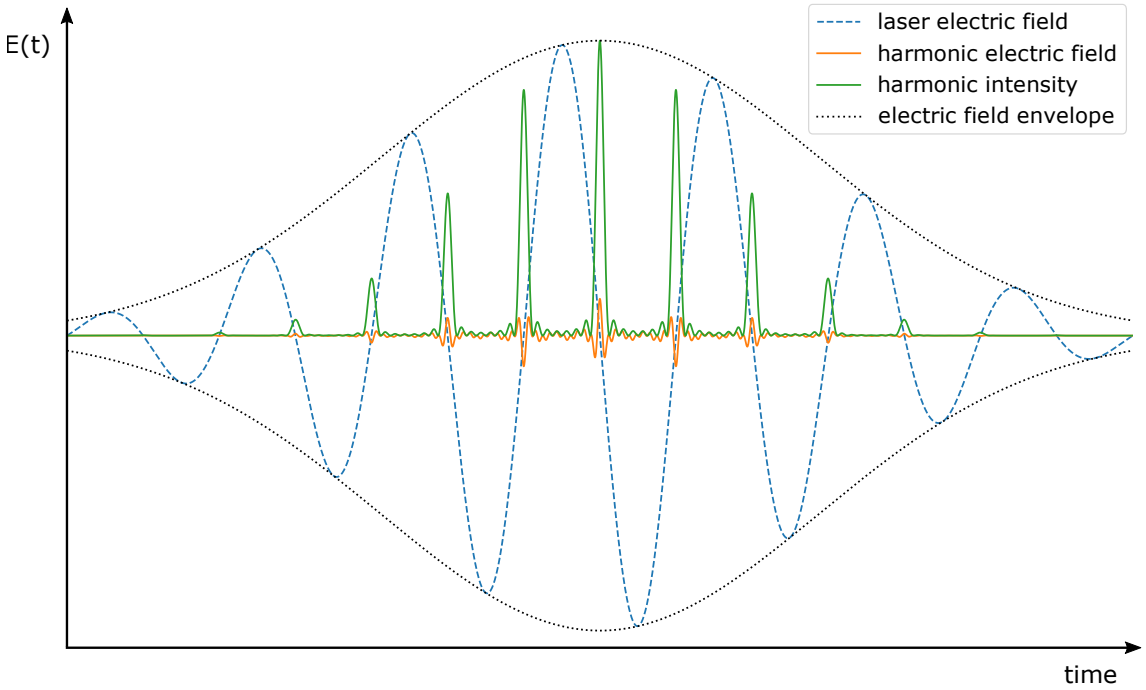

Figure 2.7: Illustration of HHG by the electric field of a single IR pulse. Harmonic bursts are emitted each half laser cycle, with alternating electric field directions due to the changing direction of the driving field. The intensity envelope of the HHG field, which here consists of harmonic orders 7 up to 21, is shown in green.

gauge

$$i\frac{\partial\psi(\mathbf{x},t)}{\partial t} = \left[-\frac{1}{2}\nabla^2 + V(\mathbf{x}) + E_0\cos(\omega t)x\right]\psi(\mathbf{x},t), \tag{2.25}$$

where $V(\mathbf{x})$ is the atomic potential. Now the following three assumptions, which are widely used within the *strong field approximation* (SFA), are made:

- Excited electronic states of the atom do not play a role in the process of tunnel ionization due to the high laser intensities.
- The effect of the atomic potential on the freed electron driven by the strong laser field is negligible.
- Depletion of the ground state population can be neglected.

Using these approximations, an expression for the time-dependent dipole moment $x(t) = \langle\psi(\mathbf{x},t)|x|\psi(\mathbf{x},t)\rangle$ can be obtained

$$x\left(t\right) = i\int_{-\infty}^{t} dt' \int d^3\mathbf{p} E\cos\left(\omega t'\right) d\left(\mathbf{p} - \mathbf{A}\left(t'\right)\right) d^*(\mathbf{p} - \mathbf{A}(t)) e^{-iS(\mathbf{p},t,t')} + \text{c.c.}. \tag{2.26}$$

Here $d(\mathbf{v}) = \langle\mathbf{v}|x|0\rangle$ is the dipole transition matrix element from the ground state $|0\rangle$ to the continuum state $|\mathbf{v}\rangle$, parallel to the electric field polarization axis. The canonical momentum $\mathbf{p}$ is defined as $\mathbf{p} = \mathbf{v} + \mathbf{A}(t)$, with the vector potential of the laser field $\mathbf{A}(t) = \int \mathbf{E}(t)dt = (-\frac{E_0}{\omega}\sin(\omega t), 0, 0)$. The quasi-classical action $S(\mathbf{p},t,t')$ is defined as

$$S\left(\mathbf{p},t,t'\right) = \int_{t'}^{t} dt'' \left(\frac{\left[\mathbf{p} - \mathbf{A}\left(t''\right)\right]^2}{2} + I_p\right). \tag{2.27}$$

Equation (2.26) has a physical meaning related to the three-step model. The first part of the integral, $E\cos\left(\omega t'\right) d\left(\mathbf{p} - \mathbf{A}\left(t'\right)\right)$ can be interpreted as the probability amplitude of the electron excitation to the continuum at time t'. The free electron wave function propagates until time t while acquiring a phase factor of $e^{-iS(\mathbf{p},t,t')}$. The quasi-classical action S thus describes the movement of the driven electron with momentum $\mathbf{p}$. At time t, the electron recombines with the parent ion with a transition amplitude equal to the term $d^*(\mathbf{p} - \mathbf{A}(t))$.

In the quasi-classical limit, the action defined in Equation (2.27) represents the sum over all relevant electron paths, the long and short trajectories. For each trajectory, an intensity-dependent dipole phase is acquired in the continuum, which can be defined as [107]

$$\phi_j(q,I) = q\omega_c t' - S\left(\mathbf{p},t,t'\right), \tag{2.28}$$

where q represents the harmonic order. The accumulated phase during the electron propagation in the laser field depends strongly on the laser intensity I and the trajectory j

considered. $\phi_j(q, I)$ therefore has a large influence on the spatial and spectral properties of the generated harmonics. Within a specific harmonic order, $\phi_j(q, I)$ is very sensitive to changes in the intensity for the long trajectories, whereas $\phi_j(q, I)$ is much less sensitive to intensity changes for the short trajectories. In both cases the dipole phase changes approximately linearly with the space- and time-dependent intensity $I(r, z, t)$:

$$\phi_j(q, I) \approx \alpha_{0,j}(q) - \alpha_j(q) I(r, z, t), \tag{2.29}$$

where $\alpha_{0,j}(q)$ and $\alpha_j(q)$ depend on both the harmonic order and the electron trajectory. The time variation of the intensity I induces a change in the instantaneous frequency, a chirp, to the harmonic field $\Delta\omega_j(t) = -\partial\phi_j(t)/\partial t$, which leads to spectral broadening and a decreased coherence time of the harmonic field. The radial variation of the intensity causes a wavefront curvature, which increases the divergence of the generated harmonics. Since $\alpha_{\text{long}}(q)$ is larger than $\alpha_{\text{short}}(q)$ by roughly a factor 25 for typical conditions [108], the long trajectories have both a shorter coherence time and a significantly larger divergence. For frequency metrology, the short trajectories are therefore preferred.

2.2.5 Macroscopic HHG response

So far, we discussed the emission of single photons by the interaction of an atom with a driving laser field. Now we consider how a superposition of many emitters in the medium leads to a coherent, directed beam of XUV light. The relative phases of the emitted photons from different atoms in the interaction region are dictated by the driving field and do therefore not change, except for possible perturbations due to for instance intensity fluctuations or variations in the laser spatial profile, as will discus in the next section. The HHG process itself is coherent, and the coherence properties of the emitted XUV radiation only depend on the driving laser characteristics.

The coherent light emission from a set of single emitters in a medium scales quadratically with the density, provided the relative phase stays constant everywhere in the emission volume [109]:

$$S_q = \rho^2 S_\phi. \tag{2.30}$$

Here, S_q is the yield of the q-th harmonic, ρ the gas density and S_ϕ a factor that accounts for phase-matching and re-absorption of the emitted radiation by the medium. For perfect phase-matching and without re-absorption, the equality $S_\phi = 1$ holds, while for all other cases S_ϕ takes a value between 0 and 1. In most practical cases, S_ϕ depends on the gas density and the quadratic scaling is not perfectly reproduced even for phase-matched generation.

For an efficient buildup of high harmonic radiation along the propagation direction

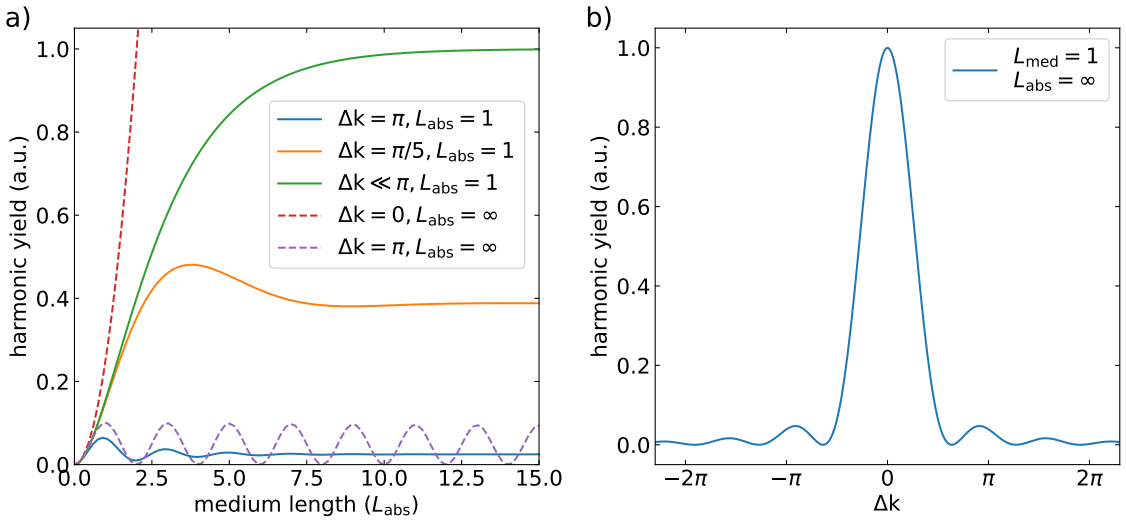

Figure 2.8: HHG yield for various phase matching conditions. a) harmonic signal as function of nonlinear medium length, for different values of Δk. When reabsorption by the medium is neglected ($L_{\mathrm{abs}} = \infty$), the signal either grows to infinity or oscillates with L_{med}, depending on the wave vector mismatch. b) yield as function of Δk for constant medium length.

within the nonlinear medium, phase matching of the laser-induced polarization and generated harmonic orders is required. In other words, the phase front of the generated field needs to match with the phase front of the laser field. The phase velocity of the qth harmonic is $v_q = \omega_q/k_q = q\omega_1/k_q$, while the phase velocity of the driving field is $v_1 = \omega_1/k_1$. We can therefore define

$$\Delta\mathbf{k}(q) = q\mathbf{k_1} - \mathbf{k_q}, \tag{2.31}$$

as the phase mismatch between the wave vector of the fundamental beam $\mathbf{k_1}$ and the q-th harmonic wave vector $\mathbf{k_q}$.

The generated XUV field results from a coherent sum over all atoms in the medium of length L_{med} and can be expressed as [110]

$$S_q \propto \left| \int_0^{L_{\mathrm{med}}} \mathrm{d}z d_q \exp\left[\mathrm{i} \left(\Delta\mathrm{k} + \frac{\mathrm{i}}{2L_{\mathrm{abs}}} \right) (L_{\mathrm{med}} - z) \right] \right|^2, \tag{2.32}$$

where d_q is the dipole amplitude for the qth harmonic. The effect of *reabsorption* of the generated XUV photons by the medium is represented by the absorption length $L_{\mathrm{abs}} = (\sigma\rho)^{-1}$, with σ being the ionization cross section for the harmonic radiation. Assuming d_q

and L_{abs} remain constant over the generation volume, Equation (2.32) becomes

$$S_q \propto |d_q|^2 \, e^{\frac{-L_{\mathrm{med}}}{2L_{\mathrm{abs}}}} \frac{\cosh\left(\frac{L_{\mathrm{med}}}{2L_{\mathrm{abs}}}\right) - \cos(\Delta \mathrm{k} L_{\mathrm{med}})}{\Delta \mathrm{k}^2 + (2L_{\mathrm{abs}})^{-2}} \overset{L_{\mathrm{abs}}\to\infty}{\propto} L_{\mathrm{med}}^2 \, \mathrm{sinc}^2\left(\frac{\Delta \mathrm{k} L_{\mathrm{med}}}{\pi}\right). \quad (2.33)$$

For $L_{\mathrm{abs}} = \infty$, phase matching in the absence of harmonic absorption is described by a sinc function, as shown in Figure 2.8. There, the quadratic growth of the harmonic signal with medium length is also shown. Depending on the value of Δk, the signal saturates due to reabsorption at a certain medium length. The coherence length of the emitted radiation can be defined as $L_{\mathrm{coh}} = \pi/\Delta \mathrm{k}$, which can be used to define a parameter space for which the harmonic yield for absorption-limited HHG is at least half of the maximum value. This is the case for $L_{\mathrm{med}} > 3L_{\mathrm{abs}}$ and $L_{\mathrm{coh}} > 5L_{\mathrm{abs}}$ [110]. Without absorption ($L_{\mathrm{abs}} = \infty$), the harmonic yield grows indefinitely in the case of perfect phase-matching. For non-phase-matched generation, the signal starts to oscillate with increasing medium length. So-called Maker fringes appear [111], which can also be observed experimentally [112].

2.2.6 Phase matching contributions

In a HHG geometry where a Gaussian driving laser beam is focused on a gas target in free space, four terms contribute to the phase mismatch between the harmonic and fundamental field [109]:

$$\Delta \mathbf{k} = \Delta \mathbf{k_g} + \Delta \mathbf{k_d} + \Delta \mathbf{k_n} + \Delta \mathbf{k_p}. \quad (2.34)$$

Here, $\Delta \mathbf{k_g}$ denotes the wave vector mismatch due to the Gouy phase and $\Delta \mathbf{k_d}$ the mismatch induced by the dipole phase, arising from the electron trajectory. $\Delta \mathbf{k_n}$ and $\Delta \mathbf{k_p}$ represent the wave vector mismatch due to the neutral gas dispersion and plasma dispersion, respectively. The different contributions and their origins are discussed below. For simplicity, only propagation along the laser direction z is considered.

The phase shift of a focused Gaussian laser beam in propagation direction z, compared to that of a plane wave with the same frequency, is known as the *Gouy* phase and is given by [113]

$$\phi_{\mathrm{Gouy}}(r, z) = -\tan\left(\frac{z}{z_R}\right) + \frac{k_1 r^2}{2R(z)}, \quad (2.35)$$

where $z_R = \pi w_0^2/\lambda_0$ is the Rayleigh range, w_0 the beam waist size at the laser focus, λ_0 the laser wavelength, r the radial coordinate and $R(z) = z + z_R^2/z$ the beam radius of curvature. The resulting phase mismatch between the fundamental and the qth harmonic

order due to the acquired Gouy phase at the optical axis ($r = 0$) is

$$\Delta \mathrm{k_g} = q\frac{\partial \phi_{\mathrm{Gouy}}(z)}{\partial z}|_{z\to 0} = -\frac{q}{z_R}. \tag{2.36}$$

The Gouy phase shift of the harmonic beam can be neglected due to its much smaller divergence. For small z, $\Delta \mathrm{k_g}$ is approximately constant and reaches a maximum at $z = 0$. By adjusting the position of the gas nozzle in relation to the laser focus, the size of the Gouy phase shift can therefore be tuned slightly.

The second component of the phase mismatch is induced by the dipole phase defined in Equation (2.28). Using the approximation in Equation (2.29), the wave vector mismatch yields

$$\Delta \mathrm{k_d} = -\alpha_j(q)\frac{\partial I(r,z)}{\partial z}, \tag{2.37}$$

where the proportionality constant $\alpha_j(q)$ is positive. Since the intensity varies with both z and r, the dipole wave vector mismatch can change substantially over spatial position within the nonlinear medium. However, within the laser focus $\Delta \mathrm{k_d}$ can be approximated to be zero [114].

The third contribution is the wave vector mismatch due to neutral gas dispersion of the generation medium and can be expressed as [115]

$$\Delta k_{\mathrm{n}} = q\frac{\omega_c}{c}P\left(1-\eta\right)\left(n_0 - n_q + n_2 I\right), \tag{2.38}$$

where P is the pressure in atmosphere and n_0, n_q are the refractive indices of the gas medium for the fundamental laser and the harmonic beam, respectively. n_2 is the intensity-dependent index of refraction, the value of which usually is small compared to the other wave vector mismatch contributions. The intensity dependent contribution to Δk_{n} can therefore be neglected. Values of n_q can be found in literature [116], while n_0 can be approximated well using the Sellmeier equations [117].

The last term in Equation (2.34), $\Delta \mathrm{k_p}$, incorporates plasma dispersion. The probability for a tunnel-ionized electron to recombine with its parent ion is relatively small, therefore many electrons are freed and a plasma is formed. Both the ions and the electrons cause dispersion, but the contribution from the ions is usually neglected due to their large mass and higher resonance frequencies. The change of the refractive index due to free electrons leads to a wave vector mismatch given by [118]

$$\Delta k_{\mathrm{p}} = q\frac{\omega_c}{c}(n_{0,\mathrm{el}} - n_{q,el}) \approx -q\frac{\omega_c}{2\pi c}p\eta N_a r_e, \tag{2.39}$$

where N_a is the atomic number density, and r_e the classical electron radius. The free-electron dispersion of the harmonic field can be neglected since the harmonic frequencies

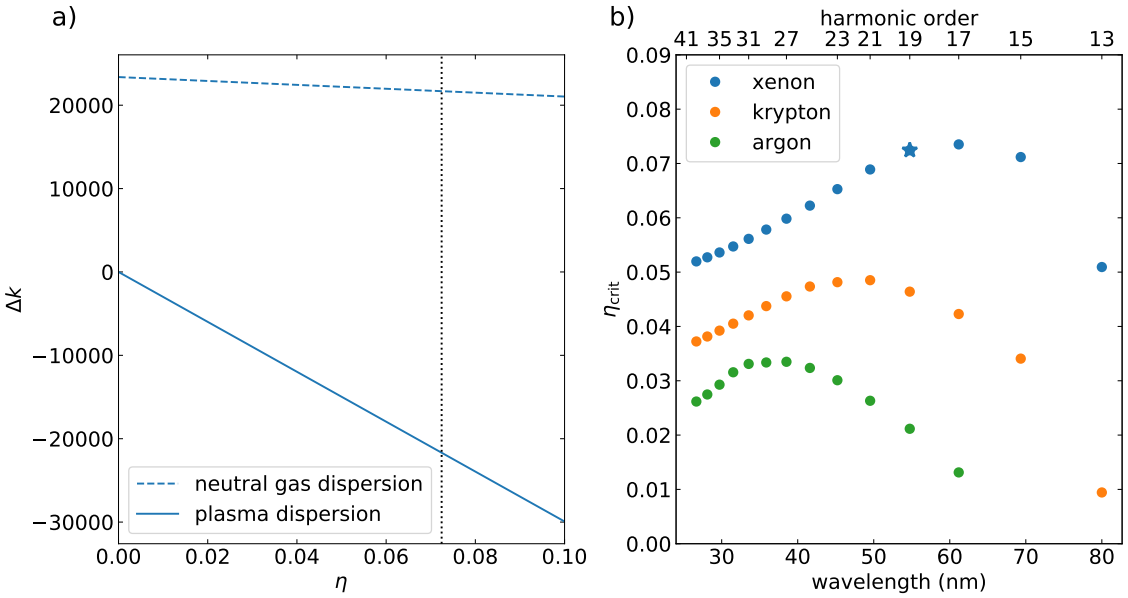

Figure 2.9: Phase matching of neutral gas dispersion and plasma dispersion due to free electron production. a) dispersion as function of ionization fraction for xenon gas with a pressure of 200 mbar in the interaction region using a driving laser at 1040 nm. The dotted line indicates the ionization fraction η_{crit} for which the neutral gas dispersion compensates the plasma dispersion. b) values of η_{crit} as function of wavelength for different gases. The critical ionization fraction drops for increasing ionization potential. The star marks the vertical dotted line shown in a).

are much higher than the plasma frequency.

2.2.7 Pressure-induced phase matching

Since the neutral gas dispersion contribution is positive while the plasma dispersion contributes negatively, it is possible to balance both contributions, as is shown in Figure 2.9a as a function of the ionization fraction η. Dispersion values are plotted for xenon gas, ionized by a 1040 nm driving laser at a pressure of 200 mbar. At the ionization fraction indicated by the vertical dotted line, the dispersion of both contributions is balanced. This defines the *critical* ionization fraction, given by [119]

$$\eta_{\text{crit}} = \left(\frac{\lambda_0^2 N_a r_e}{2\pi(n_0 - n_q)} + 1 \right)^{-1}. \tag{2.40}$$

Values for η_{crit} are usually on the order of a few percent and are shown in Figure 2.9 for xenon, argon and krypton and harmonic orders between 13 and 41. For gases with a lower ionization potential, the critical ionization fraction is larger due to larger refractive index differences. Furthermore, η_{crit} decreases for increasing driving wavelengths.

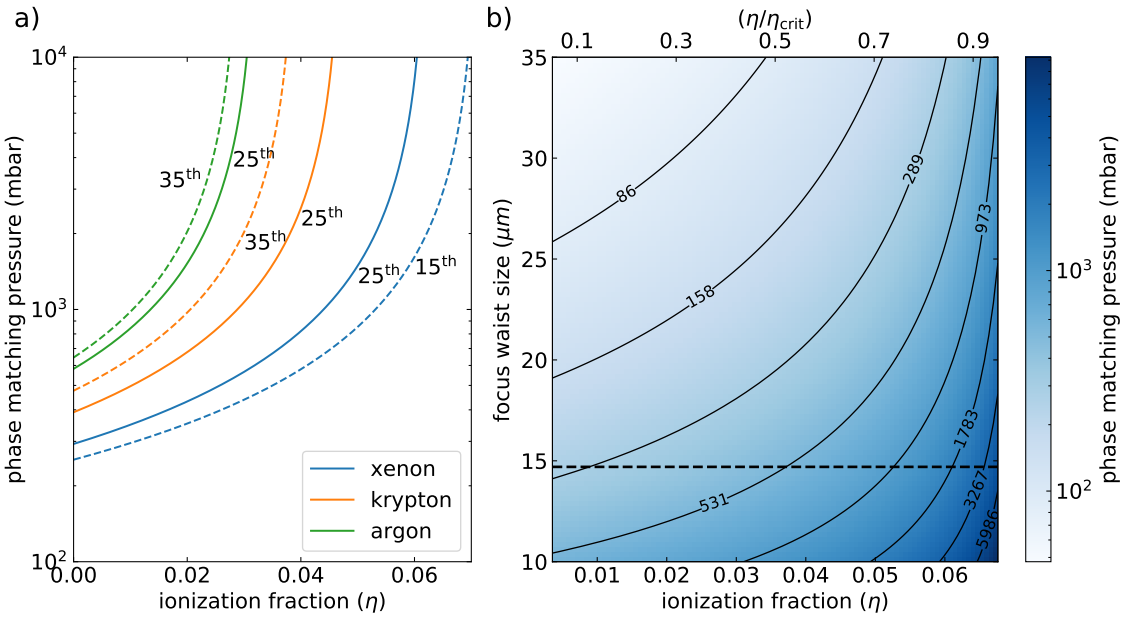

Figure 2.10: Pressure-induced phase matching conditions as a function of ionization fraction for a 1040 nm driving field. a) phase matching pressure for several gases and indicated harmonic orders, using a focus waist size of 14.7 μm. b) phase matching pressure color plot of xenon for harmonic 15, as function of ionization fraction and focus waist size. The horizontal dashed line indicates the waist size used in a). For such tight focusing, a relatively large pressure is needed to achieve phase matching for a significant ionization fraction.

Since the Gouy phase contributes negatively to the phase mismatch, ideal phase matching $\Delta \mathrm{k} = 0$ can only be achieved for ionization fractions $\eta < \eta_{\mathrm{crit}}$, assuming $\Delta \mathrm{k}_d \approx 0$. The gas density can be used as a parameter to adjust the dispersion contribution to compensate for the Gouy phase. By rewriting Equation (2.34) we obtain

$$P_{\mathrm{match}} \left[\frac{\partial \Delta k_{\mathrm{n}}}{\partial P} + \frac{\partial \Delta k_{\mathrm{p}}}{\partial P} \right] + \Delta k_{\mathrm{g}} = 0, \tag{2.41}$$

where the gas density was assumed to be linearly dependent on the pressure, i.e. assuming a constant temperature. The pressure for which phase-matching is achieved is now given by [120]

$$P_{\mathrm{match}} = P_0 \frac{\lambda_0^2}{2\pi^2 w_0^2 \Delta(n_0 - n_q)\left(1 - \frac{\eta}{\eta_{\mathrm{crit}}}\right)}, \tag{2.42}$$

where P_0 is the standard atmospheric pressure. Figure 2.10a shows P_{match} for a few gases and harmonics as function of ionization fraction. The pressure required for ideal phase matching increases with the ionization potential of the target gas. At low η, the phase matching pressure does not depend strongly on the ionized fraction, thus a large part of the harmonic spectrum can be phase-matched. As the ionization fraction increases, the phase matching pressure grows rapidly.

In Figure 2.10b, the dependence of p_{match} on the laser focus waist size w_0 and ionization fraction is shown for the 15th harmonic using xenon. For tighter focusing geometries, higher pressures are required for phase matching. The focus size used in this thesis is indicated by the horizontal dashed line. Since the pressure in the interaction region is $\sim 10\,\%$ of the nozzle backing pressure, it becomes clear that backing pressures of multiple bars are necessary to achieve phase-matching in xenon, even for small ionization fractions.

2.3 XUV frequency combs

In the previous section, we discussed the generation of XUV light by a single IR driving pulse. The HHG process causes photons to be emitted in bursts at odd multiples of the driving frequency, which results in a train of attosecond pulses collinear with the outgoing IR light. Within this pulse train produced by a single drive pulse, the different emitted harmonics have been shown to be phase-locked [121]. Also, the attosecond pulse train possesses a high degree of spatial coherence [122]. However, these properties do not automatically hold for series of attosecond pulse trains generated by multiple IR pulses.

The most widely used approach for HHG is to focus a high power laser onto a gas target. Typically, mJ pulse energies are used with wavelengths varying from 400 nm to the mid-IR in order to reach peak intensities in the $10^{14} - 10^{15}\,\mathrm{W/cm^2}$ region to generate harmonics with energies up to a few hundred eV. The requirement of high pulse energy usually leads

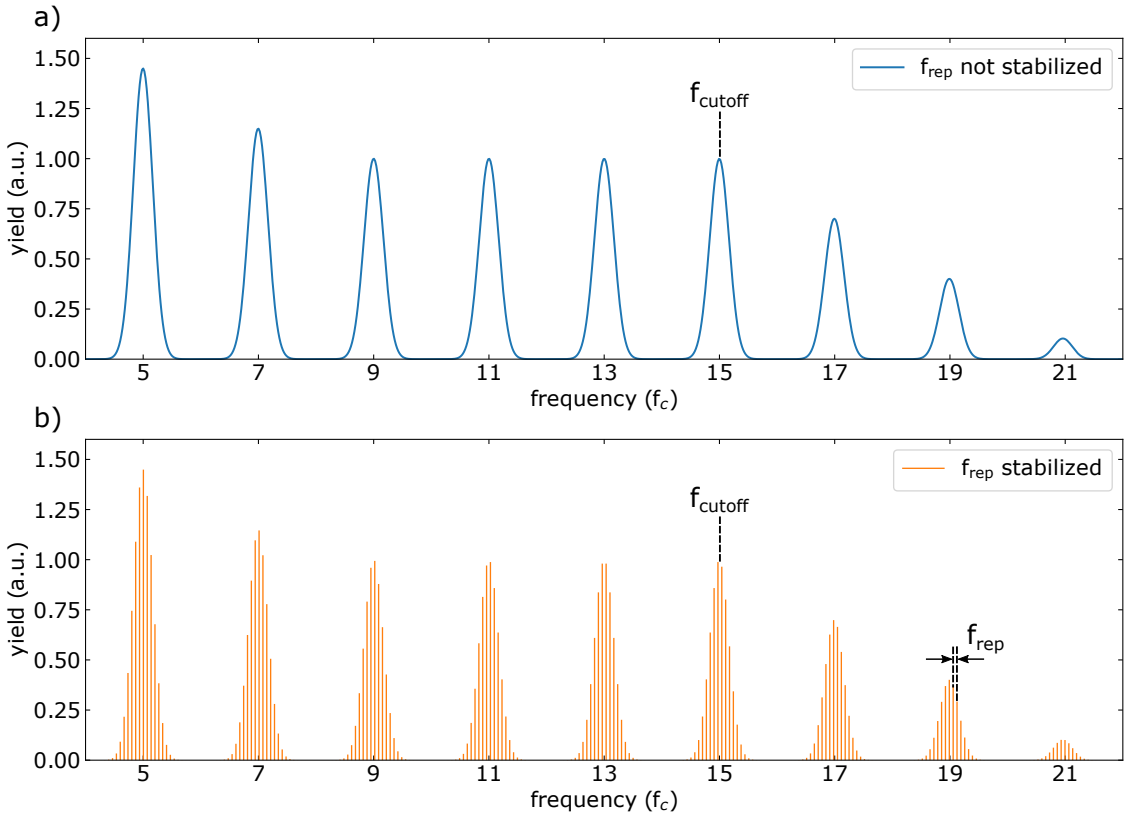

Figure 2.11: Harmonic spectrum of a driving pulse train. a) without a stable phase relation between consecutive IR pulses, each harmonic spans a broadband spectrum centered at odd multiples of the drive lasers central frequency f_c. In accordance with Equation (2.24), harmonics are generated up to a cutoff frequency $f_{cutoff} = E_{max}/h$. b) when f_{rep} and f_{CEO} are stabilized, a comb structure under the harmonic envelopes emerges. Each harmonic becomes a copy of the original comb, with equal repetition rate.

to a laser repetition rate of a few kHz, although high power systems at several hundred kHz exist [123, 124]. Even though CEP stabilization is very well possible [125], the repetition rate of such systems is almost never stabilized since the long time period between pulses makes stabilization very hard. Without f_{rep} stabilized, the harmonic spectrum looks like that shown in Figure 2.11a. Harmonics appear at odd multiples of the central driving frequency f_c, up to the cutoff frequency $f_{cutoff} = E_{max}/h$, defined in Equation (2.24). Each harmonic contains broadband radiation with its coherence properties determined by the IR pulse.

Now lets consider what happens when the driving laser repetition rate is indeed stabilized. The XUV bursts generated in a single IR pulse are produced in every subsequent pulse from the laser pulse train in the exact same way. The time at which the attosecond bursts appear is now fixed not only within a single IR pulse, but also between consecutive

drive pulses. The XUV radiation is generated at regularly spaced intervals, dictated by the temporal coherence of the driving laser. As described by Equation (2.13), the harmonic spectrum thus consists of an envelope determined by the shape of a single-pulse attoburst and an underlying structure governed by the properties of the pulse train. This is illustrated in Figure 2.11b, where the harmonic spectrum generated by a fundamental field with a stabilized repetition rate, for instance a frequency comb, is depicted. Each harmonic order q thus contains a copy of the original comb, centered around qf_c. Because the generated electric field oscillates q times as fast as the fundamental, the CEO frequency increases with the same factor. Since the repetition rate of the driving field governs the time structure of the generated harmonics, f_{rep} is the same for all harmonic orders. The resulting XUV comb can thus be described by a modified version of Equation (2.17):

$$f_{\mathrm{n,q}} = qf_{\mathrm{CEO}} + nf_{\mathrm{rep}}. \tag{2.43}$$

The preceding arguments only hold if the HHG process itself remains phase coherent over the duration of many IR pulses. Recently, it has been shown experimentally that this is indeed the case for coherence times as long as one second, corresponding to 154 million pulses [85].

The experimental realization of a stabilized pulse train for HHG is however more involved compared to the conventional systems mentioned earlier. Frequency combs typically run with $f_{\mathrm{rep}} \sim 100\,\mathrm{MHz}$ or larger, implying that the pulse energy is orders of magnitude below that of unstabilized high-power kHz systems. Since the HHG conversion efficiency strongly depends on the laser intensity, the frequency comb pulses need to be amplified in order for them to reach intensities feasible for HHG. Although the techniques of enhancing short pulses in fiber amplifiers rapidly advance, the standard solution for XUV combs has been the use of passive enhancement cavities. The HHG process then takes place in a cavity which recycles the infrared pulses, and therefore allows for operation at high peak intensities and high repetition rates.

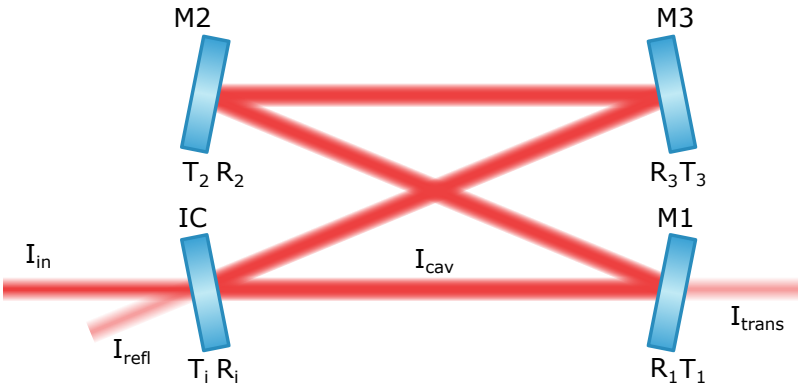

Figure 2.12: Schematic overview of an optical resonator in bow-tie configuration. The ingoing beam I_{in} enters through the back of the IC mirror. After reflection from the other cavity mirrors (M1, M2 and M3), the cavity beam overlaps with the incident beam at the reflective surface of the IC. The reflectivities and transmissions of the cavity mirrors are indicated by R_i and T_i.

2.4 Optical resonators

The principle of an optical cavity is very widely used in many different experimental fields. Of course, the laser itself contains a cavity, but its applications reach much further; from cavity ring-down spectroscopy used to trace rare gases for medical purposes to applying the strong electric field inside the cavity as a force to trap single molecules [126] to studying the interaction between a single cavity photon and a confined atom [127]. Most applications employ a cavity in combination with a CW laser, but for the scope of this work it is necessary to enhance a pulsed light source, which comes with some additional complications. This section will therefore first explore some basic properties of optical cavities. Subsequently, the enhancement of pulses in a femtosecond enhancement cavity is explored.

2.4.1 Energy relations

This subsection follows the treatment of optical cavities compiled by Nagourney [128]. We start by considering an optical cavity consisting of four mirrors in bow-tie configuration, as shown in Figure 2.12. The incident beam with intensity $I_{in} = |E_{in}|^2$ enters the cavity through the back of the input coupler (IC) mirror. The IC has a field reflectivity coefficient of $r_i = \sqrt{R_i}$ and a transmission coefficient of $t_i = \sqrt{T_i}$. R and T are the mirror reflectivity and mirror transmission, respectively. Energy conservation yields $r_i^2 + t_i^2 + l_i^2 = 1$, with l_i representing the field losses due to scattering or absorption. For IR mirrors coated with dielectric stacks, these losses are typically small and are therefore neglected in the rest of this section. After passing through the input coupler, the field reflects from the

other cavity mirrors M1, M2 and M3, which is summarized in a single cavity reflectivity coefficient $r_c = r_1 r_2 r_3$. The field inside the cavity in steady state can then be written as

$$E_c(\omega) = E_{in} t_i \left(1 + r_i r_c e^{i\phi(\omega)} + \left(r_i r_c e^{i\phi(\omega)}\right)^2 + \left(r_i r_c e^{i\phi(\omega)}\right)^3 + \dots\right), \tag{2.44}$$

where $\phi(\omega)$ denotes the total phase shift of the electric field after one cavity round-trip, due to, for instance, dispersion from mirror reflections or propagation through a gas. Here, a perfect overlap between the incident beam and the cavity mode is assumed, as mode matching effects are discussed in more detail later. Since the reflectivity coefficients in Equation (2.44) are smaller than one, the expression can be written as a converging geometric series

$$E_{\mathrm{c}} = \frac{E_{in} t_i}{1 - r_c r_i e^{i\phi}}. \tag{2.45}$$

In a similar way, an expression for the electric field that is reflected by input coupler mirror, as shown in Figure 2.12, can be derived:

$$\begin{aligned} E_{\mathrm{refl}} &= -E_{in} r_i + \frac{E_{in} t_i^2}{r_i}\left(r_i r_c e^{i\phi(\omega)} + \left(r_i r_c e^{i\phi(\omega)}\right)^2 + \dots\right) \\ &= E_{in}\frac{r_c t_i^2 e^{i\phi(\omega)} - r_i}{1 - r_i r_c t_i^2 e^{i\phi(\omega)}}. \end{aligned} \tag{2.46}$$

The square of the absolute value of Equation (2.45) yields the intra-cavity intensity

$$\begin{aligned} I_{\mathrm{cav}} &= \frac{I_{in} t_i^2}{1 + r_c^2 r_i^2 - 2 r_c r_i \cos\phi} \\ &= I_{in}\frac{t_i^2}{(1 - r_i r_c)^2 + 4 r_i r_c \sin^2(\phi(\omega)/2)} \\ &= \frac{t_i^2}{(1 - r_i r_c)^2}\frac{I_{in}}{1 + \frac{4 r_i r_c \sin^2(\phi(\omega)/2)}{(1 - r_i r_c)^2}}. \end{aligned} \tag{2.47}$$

The intra-cavity field thus reaches its maximum value when $\phi(\omega) = 0 + p2\pi$ for any integer p. At this value, the cavity is said to be at *resonance*. The total phase shift can be expressed as

$$\phi(\omega) = kL + \phi_d(\omega) = \frac{\omega}{c} L + \phi_d(\omega), \tag{2.48}$$

where L is the cavity path length and ϕ_d is the phase shift due to dispersion in the cavity. Omitting dispersion for the moment, we obtain

$$\frac{\omega}{c} L = p2\pi, \tag{2.49}$$

which defines the spacing between the cavity resonances, known as the *free spectral range* (FSR) of the cavity. It is given by

$$\Delta\omega_{\mathrm{FSR}} = \frac{2\pi c}{L}. \tag{2.50}$$

In order to find the width of the intensity peaks, we observe from Equation (2.47) that half the maximum intensity occurs at a phase $\phi_{1/2}$ for which

$$(1 - r_1 r_c)^2 = 4 r_i r_c \sin^2 \phi_{1/2}/2 \tag{2.51}$$

holds. For $\phi_{1/2}$, in case of a low-loss cavity, the solution is given by

$$\phi_{1/2} \overset{\phi_{1/2} \ll 1}{\approx} \frac{1 - r_1 r_c}{\sqrt{r_i r_c}}. \tag{2.52}$$

The FWHM of the resonance peak of the circulating field $\Delta\omega_{1/2}$ is a measure for the resonance peak width. It is given by

$$\Delta\omega_{1/2} = 2\phi_{1/2}\frac{L}{c} = \frac{2c(1 - r_i r_c)}{L\sqrt{r_i r_c}}, \tag{2.53}$$

and known as the *line width* of the cavity. Now, we can define the *finesse* ($\mathcal{F}$) of the cavity as the ratio of the FSR and the line width

$$\mathcal{F} = \frac{\Delta\omega_{\mathrm{FSR}}}{\Delta\omega_{1/2}} = \frac{\pi\sqrt{r_i r_c}}{1 - r_i r_c}. \tag{2.54}$$

If we define the losses inside the cavity $\mathcal{L}_{\mathrm{tot}}$ by an overall round-trip attenuation factor (1-$\mathcal{L}_{\mathrm{tot}}$), an effective cavity field reflection of

$$|r|^2 = e^{-(1-\mathcal{L}_{\mathrm{tot}})} \tag{2.55}$$

is obtained [129]. Plugging this into Equation (2.54) yields a simplified expression for the finesse

$$\mathcal{F} = \frac{\pi \exp\left(-(1 - \mathcal{L}_{\mathrm{tot}})/4\right)}{1 - \exp\left(-(1 - \mathcal{L}_{\mathrm{tot}})/2\right)} \overset{\mathcal{L}_{\mathrm{tot}} \ll 1}{\approx} \frac{2\pi}{\mathcal{L}_{\mathrm{tot}}}. \tag{2.56}$$

The same result can be derived directly from Equation (2.54) by assuming $Ti, Tc \ll 1$:

$$\begin{aligned}\mathcal{F} &= \sqrt{\frac{\pi^2\sqrt{R_i R_c}}{\left(1-\sqrt{(1-T_i)(1-T_c)}\right)^2}} \\ &\approx \sqrt{\frac{\pi^2}{\left(1-\sqrt{1-T_i-T_c}\right)^2}} \\ &\approx \sqrt{\frac{\pi^2}{\left(\frac{1}{2}(T_i+T_c)\right)^2}} \\ &= \frac{2\pi}{\mathcal{L}_{\text{tot}}},\end{aligned} \tag{2.57}$$

where the total losses are the sum of the losses from the input coupler and other cavity mirrors $\mathcal{L}_{\text{tot}} = \mathcal{L}_i + \mathcal{L}_c$. The finesse provides a measure for the quality factor of the cavity. A high finesse is reached by using high reflective, low-loss mirrors, minimizing the losses in the resonator and resulting in narrow peaks in the cavity transmission spectrum, the cavity resonances. On resonance, the intensity of the light field inside the cavity is larger than that of the driving field. Since this effect is the most important reason to utilize a cavity in this work, it is useful to characterize the enhancement factor β of the cavity at resonance ($\phi(\omega) = 0$) as the ratio between the intra-cavity intensity and the incident intensity. From Equation (2.47) we obtain

$$\beta = \frac{I_{\text{cav}}}{I_{in}} = \frac{t_i^2}{(1-r_i r_c)^2} \approx \frac{T_i}{\left(\frac{1}{2}(T_i+T_c)\right)^2} = T_i\frac{\mathcal{F}^2}{\pi^2}, \tag{2.58}$$

where similar approximations and manipulations as in Equation (2.57) were used. This result is valid for a ring cavity and differs from a two-mirror, linear Fabry-Perot cavity by a factor of 4 due to constructive interference of the overlapping forward- and backward traveling beam paths inside the cavity. In a similar way, the reflected intensity at resonance can be expressed as

$$I_{\text{refl,res}} = I_{in}\frac{(r_i-r_c)^2}{(1-r_i r_c)^2} \approx I_{in}\frac{4(T_c-T_i)^2}{(T_i+T_c)^2} = I_{in}\left(\frac{F}{2\pi}(T_c-T_i)\right)^2. \tag{2.59}$$

It becomes clear that the reflected power approaches zero when the transmission of the input coupler matches the losses in the rest of the cavity. If this is the case, the cavity is *impedance matched*. For $\mathcal{L}_i > \mathcal{L}_c$ the cavity is overcoupled, while for $\mathcal{L}_i < \mathcal{L}_c$ it is undercoupled. For a femtosecond enhancement cavity, it is desirable to have a low finesse, since a high finesse increases the amount of spectral filtering, which results in a lower average power and an increase of the pulse length inside the cavity [130]. We thus want

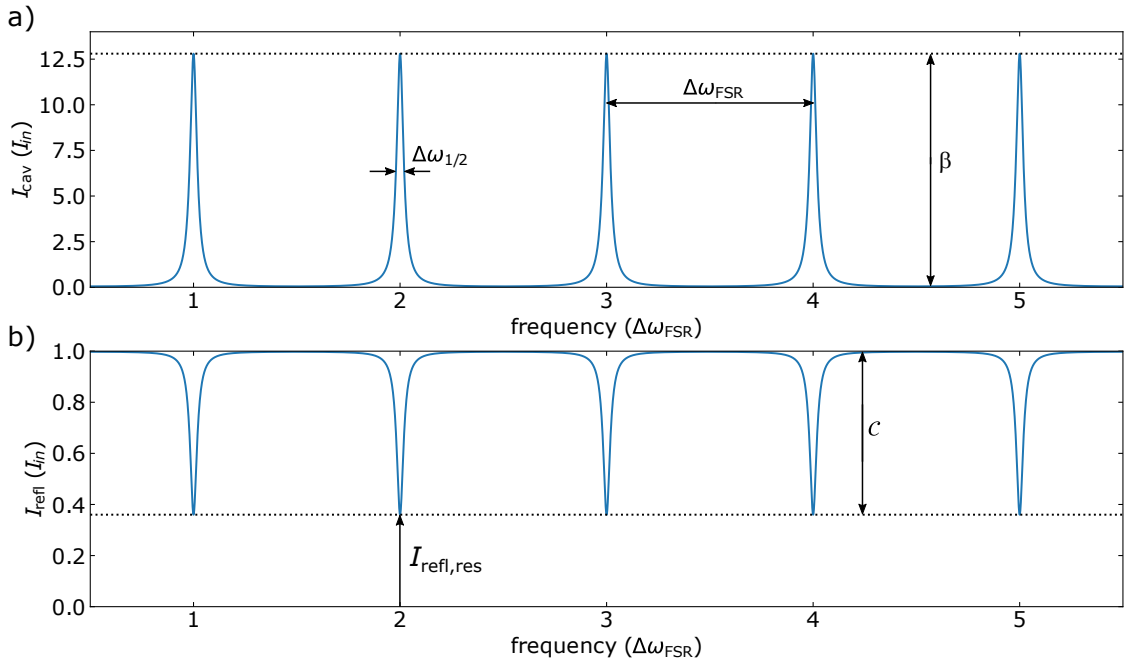

Figure 2.13: Cavity resonances as a function of the laser frequency for $T_i = 0.2, T_c = 0.05$, $\epsilon = 1$ and I_in=1. a) the intra-cavity intensity shows sharp resonances with cavity line width $\Delta\omega_{1/2}$, separated by the FSR. The circulating intensity is β times larger than the incident field. b) the reflected intensity dips when the cavity is resonant. The signal at resonance is given by $I_{\text{refl,res}}$ from Equation (2.59), while the depth ratio of the dips is characterized by the cavity contrast $\mathcal{C}$ from Equation (2.62).

to keep the finesse low, while maximizing the enhancement. For an impedance matched cavity ($T_i = T_c$), β equals $\frac{\mathcal{F}}{\pi}$, while for an overcoupled cavity the enhancement is given by $\beta = \frac{2\mathcal{F}}{\pi}$. The maximum enhancement for a given finesse is thus reached in the overcoupled case, where the losses are dominated by the input coupler.

Using the above definitions and assumptions, the intra-cavity and reflected intensities can now be summarized as

$$\begin{aligned} I_{\text{cav}} &= \frac{\beta I_{in}}{1 + \left(\frac{2F}{\pi}\sin(\pi\omega/\Delta\omega_{\text{FSR}})\right)^2} \\ I_{\text{refl}} &= I_{in}\frac{\left(\frac{\mathcal{F}}{2\pi}\left(T_c - T_i\right)\right)^2 + \left(\frac{2F}{\pi}\sin(\pi\omega/\Delta\omega_{\text{FSR}})\right)^2}{1 + \left(\frac{2F}{\pi}\sin(\pi\omega/\Delta\omega_{\text{FSR}})\right)^2}. \end{aligned} \tag{2.60}$$

Both intensities are shown as function of laser frequency ω in Figure 2.13. When the frequency equals an integer number times $\Delta\omega_{\text{FSR}}$, the circulating field possesses a sharp resonance, with its width determined by the cavity line width $\Delta\omega_{1/2}$ and the height by the enhancement factor β. The reflected intensity shows dips at the position of the cavity

resonances, indicating that light is coupled into the resonator. The depth of these dips depends on both the impedance matching and the spatial mode matching of the cavity, as discussed in the next section. Far from resonance, practically all incident light is reflected.

2.4.2 Spatial mode matching

So far we assumed that at resonance, all power from the incident beam was coupled into the resonator. In practice, only a part of the incident light beam profile spatially overlaps with the cavity mode and can be fed into the resonator. This effect can be taken into account by multiplying the circulating intensity from Equation (2.60) with the mode matching factor ϵ [131]. The reflected intensity at resonance is modified to become

$$I_{\text{refl,total}} = \epsilon I_{\text{refl}} + (1-\epsilon) I_{in}, \tag{2.61}$$

such that a *cavity contrast* $\mathcal{C}$ can be defined as the ratio between the decrease of the reflected intensity and the off-resonance intensity:

$$\mathcal{C} = \frac{I_{in} - I_{\text{refl,total}}}{I_{in}} = \epsilon - \epsilon \left((T_c - T_i) \frac{\mathcal{F}}{2\pi} \right)^2. \tag{2.62}$$

This ratio can easily be measured experimentally by placing a photodiode in the reflected beam. Similarly, the enhancement factor β can be determined by observing the amount of light that is leaking through one of the cavity mirrors, since this signal is directly proportional to the intra-cavity intensity. By removing the input coupler, calibration can be performed between the circulating power and the measured transmitted signal.

Now since both $\mathcal{C}$ and β depend on the mode matching factor ϵ, determination of this factor can be achieved by a direct measurement of the cavity finesse $\mathcal{F}$. When the cavity is at resonance, photons are stored inside the resonator for some time τ_c before leaking out through the mirrors or by scattering. Tuning the cavity at a resonance and then interrupting the seed laser thus yields an exponential decay of the circulating power over time given by

$$P(t) = P_0 e^{-t/\tau_c}, \tag{2.63}$$

where P_0 is the power at resonance, proportional to βI_{in}. Now by using Equation 2.55, we can write the losses per round-trip as

$$e^{-\alpha_L} = e^{-L/(\tau_c c)}, \tag{2.64}$$

which with Equation (2.56) then results in an expression for the finesse

$$\mathcal{F} = 2\pi\tau_c \frac{c}{L}. \tag{2.65}$$

Via such a *cavity ring-down* measurement, the finesse can thus be determined independently of the mode matching factor ϵ. Instead of rapidly turning off the laser, it is also possible to sweep its frequency across a cavity resonance at a rate much faster than the cavity lifetime. In this case, the light leaking out of the cavity, after the laser frequency has passed over the resonance, interferes with the off-resonant laser light reflecting from the input coupler [132]. A heterodyne beat is formed between the fixed-frequency cavity leakage and the chirped incident light due to the frequency scan, which can be fitted by a damped, chirped cosine wave to yield the decay time and thus provide an independent measure for the cavity finesse. The experimentally measured contrast or buildup can then be used to compute the mode matching factor ϵ.

2.4.3 Gaussian beam propagation

So far we have considered the longitudinal resonance properties of a ring cavity. In order to study the behavior of the resonators transverse mode profile, the formalism of *Gaussian beam propagation* and *ABCD matrices* is used [133], which will be briefly discussed in this section. We start by defining the electromagnetic wave propagating in the z direction as

$$E(x, y, z) = u(x, y, z)e^{-ik}, \tag{2.66}$$

where $u(x, y, z)$ is the complex scalar wave amplitude describing the transverse beam profile. By substituting into the wave equation (Equation (2.1)) and assuming that the z dependence of u is varying slowly compared to the transverse components, we arrive at the paraxial wave equation

$$\nabla_t^2 u(x, y, z) - 2ik\frac{\partial u(x, y, z)}{\partial z} = 0, \tag{2.67}$$

where the transverse Laplace operator is defined as $\nabla_t^2 = \partial/\partial x + \partial/\partial y$. The *paraxial* approximation is valid for waves traveling at angles $\theta \leq 30°$ from the optical axis. One of the analytical solutions of Equation (2.67) is the lowest order Gaussian spherical wave in free space, which is given by

$$u(x, y, z) = \frac{1}{\sqrt{1 + (z/z_R)^2}} \exp\left(-\frac{r^2}{\omega(z)^2} - ik\left(z + \frac{r^2}{2R(z)}\right) + i\tan^{-1}\left(\frac{z}{z_R}\right)\right) \tag{2.68}$$

as a function of the transverse radial coordinate $r^2 = x^2 + y^2$. The beam waist at position z is given by

$$w(z) = w_0\sqrt{1 + \left(\frac{z}{z_R}\right)^2}. \tag{2.69}$$

The wavefront curvature radius $R(z)$ can be expressed as

$$R(z) = z\left(1 + \left(\frac{z_R}{z}\right)^2\right), \tag{2.70}$$

which reaches infinity at $z = 0$, implying a planar wavefront at the focus. Although Equation (2.68) provides a full description of the properties of the Gaussian beam for any x, y and z, it is often easier to propagate the beam by using the complex q parameter defined by

$$\frac{1}{q(z)} = \frac{1}{R(z)} - i\frac{\lambda}{\pi w(z)^2}. \tag{2.71}$$

Equation (2.68) can now be rewritten as

$$u(x, y, z) = \frac{q_0}{w_0 q(z)} \exp\left(-ikz - ik\frac{r^2}{2q(z)}\right), \tag{2.72}$$

where q_0 is the beam parameter at the focus, defined as $q_0 = iz_r$. It is now very easy to propagate the q parameter to distance z from the focus in free space:

$$q(z) = q_0 + z. \tag{2.73}$$

The following beam parameters in free space can be extracted from the q parameter:

$$\begin{aligned} \text{Distance to waist} &= -\operatorname{Re}(q(z)) \\ w_0 &= \sqrt{\frac{\lambda}{\pi} Im(q(z))}. \end{aligned} \tag{2.74}$$

To propagate the beam parameters through more complicated optical elements such as lenses and curved mirrors, the ABCD matrix formalism can be used [133]. Let M_{tot} be a ray transfer matrix of the optical system of interest

$$M_{\text{tot}} = \begin{pmatrix} A & B \\ C & D. \end{pmatrix} \tag{2.75}$$

The q parameter at the exit then evolves from the incident beam q_1 according to

$$q_2 = \frac{Aq_1 + B}{Cq_1 + D}. \tag{2.76}$$

For each optical element in the system, a transfer matrix can be formulated. The total transfer matrix is then found by matrix multiplication of all elements:

$$M_{\text{tot}} = M_n M_{n-1} ... M_2 M_1. \tag{2.77}$$

The ray matrices for the optical elements used in our system are shown in Table 2.2. The ray matrix for a curved optical element depends on the incidence angle, and thus it is relevant in which plane this angle is located. The plane containing both the optical axis of the incoming and outgoing ray is the *tangential* plane. The plane orthogonal to that, containing only the ingoing ray, is known as the *sagittal* plane. In all cases, $R > 0$ for a converging lens.

Optical element	ABCD matrix
Free Space, refractive index n_0	$\begin{pmatrix} 1 & z/n_0 \\ 0 & 1 \end{pmatrix}$
Thin lens, normal incidence	$\begin{pmatrix} 1 & 0 \\ -1/f & 1 \end{pmatrix}$
Curved mirror, tangential plane	$\begin{pmatrix} 1 & 0 \\ -2/(R\cos(\theta)) & 1 \end{pmatrix}$
Curved mirror, sagittal plane	$\begin{pmatrix} 1 & 0 \\ -2\cos(\theta)/R & 1 \end{pmatrix}$
Curved interface, tangential plane $n_1 \sin(\theta_1) = n_2 \sin(\theta_2)$ $\Delta n_e = (n_2 \cos(\theta_2) - n_1 \cos(\theta_1))/(\cos(\theta_1)\cos(\theta_2))$	$\begin{pmatrix} \frac{\cos(\theta_2)}{\cos(\theta_1)} & 0 \\ \Delta n_e/R & \frac{\cos(\theta_1)}{\cos(\theta_2)} \end{pmatrix}$
Curved interface, sagittal plane $n_1 \sin(\theta_1) = n_2 \sin(\theta_2)$ $\Delta n_e = (n_2 \cos(\theta_2) - n_1 \cos(\theta_1))$	$\begin{pmatrix} 1 & 0 \\ \Delta n_e/R & 1 \end{pmatrix}$

Table 2.2: Ray matrices for optical elements used in this thesis. f is the focal length, positive for converging lenses, R is radius of curvature, positive for concave mirrors, θ_1 and θ_2 are the incidence and exit angle, n_1 and n_2 are the refractive indexes of the material before and after the interface, respectively.

2.4.4 Geometrical properties

The formalism described in the previous section can be used to find the transverse beam properties of the intra-cavity field [133]. We define q_1 as the incident beam on the input coupler. After a full round-trip through the cavity, the beam returns to the input coupler, where it now labeled as q_2. The ABCD matrix of all optical elements in the cavity M_{cav} can now be used to relate q_2 to q_1, as given in Equation (2.76). In the case of a ring cavity, the horizontal (tangential) plane needs to be treated differently than the vertical (sagittal) plane, due to nonzero incidence angles at the curved optics. Consequently, a separate ABCD matrix needs to be constructed for both planes, with horizontal and vertical beam properties being calculated separately. For stable cavity operation, we require that the

incident beam overlaps with the resonator beam after one full round-trip

$$q_1 = q_2 = \frac{Aq_1 + B}{Cq_1 + D}. \tag{2.78}$$

By solving for $1/q_1$, we obtain

$$\frac{1}{q_1} = \frac{D - A}{2B} \pm \frac{1}{2B}\sqrt{(A - D)^2 + 4BC}. \tag{2.79}$$

By comparing this expression with the definition of the q parameter in Equation (2.71), it can be seen that the first term in Equation (2.79) must be linked to the real part of $1/q$ since the elements of M_{cav} are real. The second term must then be purely imaginary, so that we can extract

$$\begin{aligned} R &= \tfrac{2B}{D-A} \\ \omega &= \sqrt{\tfrac{2\lambda|B|}{\pi\sqrt{4-(A+D)^2}}}. \end{aligned} \tag{2.80}$$

These values are only valid at the reference point chosen to set the equality in Equation (2.78). The curvature radius and waist size at other positions in the cavity can now be obtained by propagating q_1 through M_{cav} or by simply using Equations (2.70) and (2.69) for propagation in free space. In order to obtain a real value for the beam waist in Equation (2.79), A and D are constraint by

$$|A + D| \leq 2. \tag{2.81}$$

In all other cases, the cavity waist becomes imaginary, a non-physical situation which in practice means that it is not possible to overlap the beam in subsequent cavity round-trips. Equation (2.81) is therefore known as the *stability criterion* and defines a stability region of values for A and D for which stable cavity operation is possible.

2.5 Femtosecond enhancement cavity

In the previous sections, we discussed the enhancement of CW light in an optical cavity. When pulsed light needs to be amplified, the situation becomes slightly more complicated. In this section, the enhancement of femtosecond pulses in a resonator is discussed [82].

In order for a single-mode CW laser to be on resonance with the cavity, its frequency needs to match an integer multiple of the FSR. For pulsed light, all frequency modes need to be resonant with the cavity simultaneously. Although principally selective parts of broadband radiation could be enhanced, in practice passive enhancement can only be achieved when the frequency lines are evenly spaced, i.e. for driving lasers with pulse-to-pulse coherence. From Equation (2.17) we know that the FC modes are spaced by f_{rep},

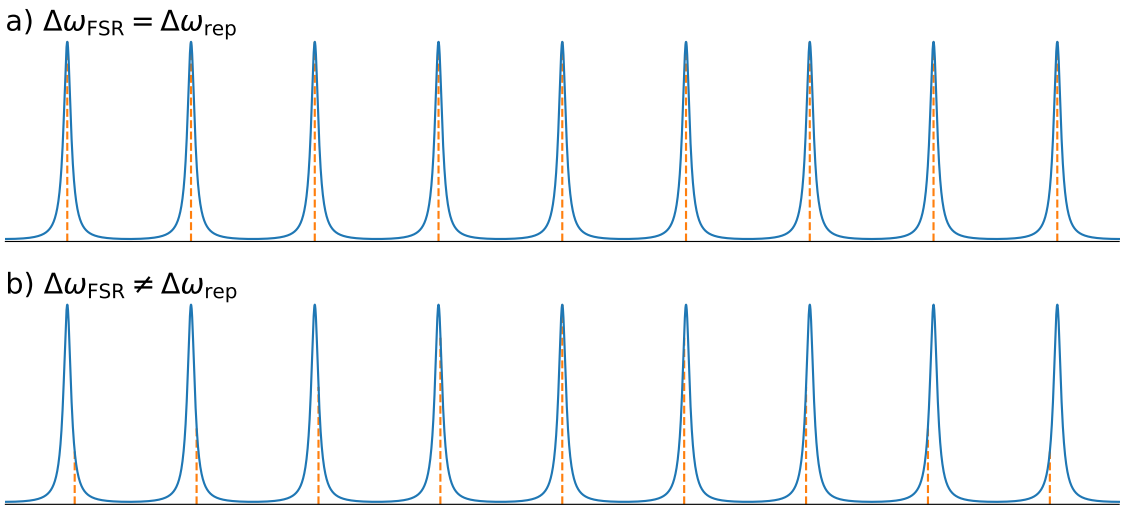

Figure 2.14: Overlap of frequency comb modes (orange, dashed lines) with the resonances of an enhancement cavity (blue, solid lined). a) When the cavities FSR matches the lasers repetition rate, each comb mode can be amplified. b) When there is a mismatch between ω_{rep} and $\Delta\omega_{FSR}$, only part of the comb modes is enhanced. In reality, the number of comb modes ($\sim 10^5$) is much larger than illustrated here, and a tiny mismatch is enough to modify the resonant spectrum.

so if this spacing matches $\Delta\omega_{FSR}$ of the cavity, the enhancement of all $\sim 10^5$ comb modes is possible, as shown in Figure 2.14a. However, when there is a mismatch between both frequencies only a part of the comb spectrum can be effectively enhanced, as illustrated in Figure 2.14b.

This leads to the most essential difference between an optical cavity for CW light and a femtosecond enhancement cavity (fsEC): dispersion of the different circulating wavelengths. Where for a CW cavity the mirrors reflect only one wavelength with a high efficiency, in an fsEC the cavity mirrors need to reflect the whole bandwidth of the incident pulses efficiently as well as introduce minimum phase differences between different parts of the circulating spectrum. In the ideal case, where there is no high-order dispersion, all cavity modes are evenly spaced by the FSR and all comb lines can be resonant at the same time. In practice, no ideal mirrors exist and some dispersion is introduced upon reflection from the mirror surface, resulting in a shift of the cavity's resonance frequency. Since now the cavity resonances are no longer evenly spaced, not all comb modes fit simultaneously in the cavity, reducing the enhancement of parts of the spectrum.

The total phase shift for one cavity round-trip was defined in Equation (2.48) as the sum of the propagation phase $\omega L/c$ and the dispersive phase ϕ_d. This term can be expanded

in a Taylor series around the central comb frequency ω_c:

$$\begin{aligned}\phi_d(\omega) &= \phi(\omega_c) + \phi'(\omega_c)(\omega-\omega_c) + \frac{1}{2}\phi''(\omega_c)(\omega-\omega_c)^2 + \frac{1}{6}\phi'''(\omega_c)(\omega-\omega_c)^3 + \dots \\ &= \phi_0 + \phi_1(\omega-\omega_c) + \phi_2(\omega-\omega_c)^2 + \phi_3(\omega-\omega_c)^3 + \dots\end{aligned} \tag{2.82}$$

The first term, ϕ_0, adds a constant shift to the electric field under the pulse envelope, but does not change its position. The second term, ϕ_1, is known as the group delay and causes a time delay of the pulse envelope, usually also affecting the offset phase. ϕ_2 named group delay dispersion (GDD) is responsible for symmetrically broadening the pulse in time. Third order dispersion (TOD), ϕ_3, and higher order terms cause the pulse to broaden in more complex ways.

Now consider what happens when a pulse is circulating inside a cavity where the mirrors add some dispersion each round-trip $\Delta\phi_{cav}(\omega)$. When ϕ_0 is the only non-zero dispersion term, a constant phase is added to the electric field under the envelope each round-trip. In order to avoid destructive interference at the IC with the incident pulses after a certain number of round-trips, the offset phase of the comb needs to be adjusted to ensure the electric field of the incoming pulses is shifted by the same amount. Equivalently, in frequency space, ϕ_0 shifts all cavity resonances by an equal amount, and f_{CEO} of the comb needs to be adjusted to change its modes by that same amount. With only ϕ_1 present, the pulse envelope is delayed during each round-trip, effectively changing the optical path length of the cavity. This effect can be compensated by changing the time interval between the arriving pulses by adjusting f_{rep} of the comb or by changing the cavity length.

In order to derive an expression for the resonance condition for a dispersive cavity as a function of the cavity length and laser frequency, we start by setting the total cavity phase shift from Equation (2.48) equal to an integer (p) multiple of 2π [135]:

$$2\pi p = \frac{\omega L}{c} + \phi_d(\omega) \tag{2.83}$$

For a FC, the angular repetition frequency $\omega_{\text{rep}} = 2\pi f_{\text{rep}}$, angular offset frequency $\omega_{\text{CEO}} = 2\pi f_{\text{CEO}}$ and angular mode frequency ω are related by an integer n such that we can rewrite Equation (2.17) to obtain

$$n = \frac{\omega - \omega_{\text{CEO}}}{\omega_{\text{rep}}}. \tag{2.84}$$

The mode numbers of the FC (n) and enhancement cavity (p) can now be related via

$$\begin{aligned}p &= n + m \\ &= \frac{\omega - \omega_{\text{CEO}}}{\omega_{\text{rep}}} + m,\end{aligned} \tag{2.85}$$

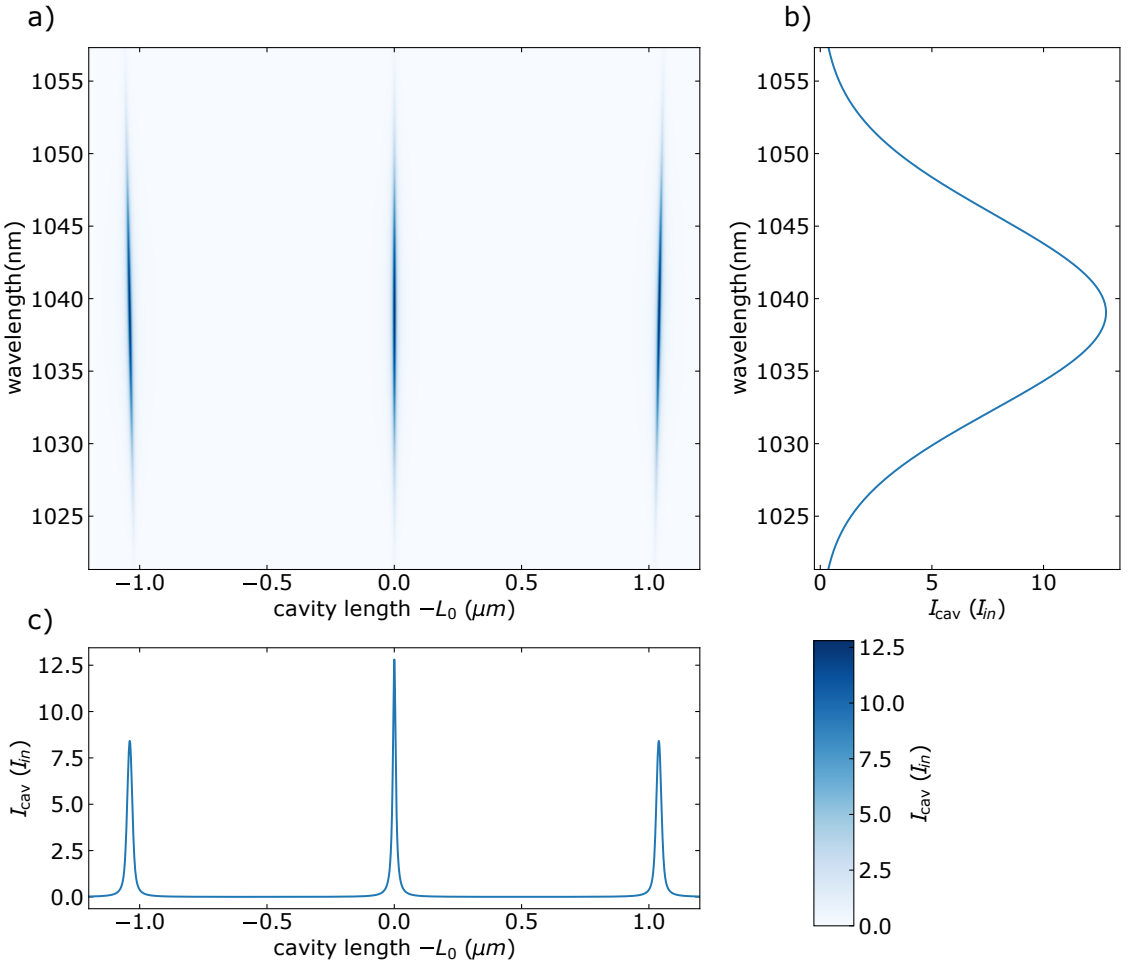

Figure 2.15: Simulation of a cavity ($\mathcal{F} = 25$) without dispersion, fed with 100 fs pulses at 100 MHz, with a 15 nm bandwidth centered around 1039 nm. a) resonance map of the three central fringes. At $L = L_0$, the comb modes align vertically and are all enhanced equally. Since the cavity FSR depends on wavelength, the neighboring fringes are tilted. b) intracavity spectrum at L_0, which is equal to the driving laser spectrum. c) Total enhancement as a function of the cavity length. Since the side fringes are tilted, the enhancement peak broadens and is lower compared to the central fringe. Graphical representation inspired by T. J. Hammond & A. K. Mills et al. [82, 134].

where m is an integer labeling the resonance fringe. Substitution in Equation (2.83) and solving for the cavity length L results in

$$L(\omega) = \frac{2\pi c}{\omega_{\text{rep}}} - \frac{2\pi c}{\omega}\left[\frac{\omega_{\text{CEO}}}{\omega_{\text{rep}}} - m\right] - c\frac{\phi_d(\omega)}{\omega}. \tag{2.86}$$

This relation describes at which cavity length L the FC mode frequencies ω are resonant. In the simplest case, without dispersion and $\omega_0 = 0$, the cavity length is independent of the laser frequency when $m = 0$. This means that the whole spectrum of the comb is amplified, as illustrated in Figure 2.15. The *resonance map* shows the enhancement factor as a function of the cavity length and laser wavelength [82, 134]. The length 0 indicates $L = L_0 = 2\pi c/\omega_{\text{rep}}$. The incident radiation is a 100 fs transform-limited pulse train centered at 1039 nm, the input coupler and the cavity transmission are the same as in Figure 2.13 ($T_i = 0.2$, $T_c = 0.05$). For $m = \pm 1$, the resonant spectra are slightly tilted, since the cavity FSR is frequency dependent. Therefore, only at L_0, all laser modes are resonant at the same cavity length and maximum enhancement is achieved while the neighboring modes show a reduced enhancement for any given cavity length. For higher values of m, the tilt increases and the enhancement is further reduced.

Now consider the more general case, where the constant and linear dispersive phase terms from Equation (2.82) are present, such that $\phi_d(\omega) = \phi_0 + \phi_1(\omega - \omega_c)$. Equation (2.86) then becomes

$$L(\omega) = \frac{2\pi c}{\omega_{\text{rep}}} - c\phi_1 - \frac{2\pi c}{\omega}\left(\frac{\omega_{\text{CEO}}}{\omega_{\text{rep}}} - m\right) - c\frac{\phi_0}{\omega} + \frac{c\omega_c\phi_1}{\omega}, \tag{2.87}$$

containing some frequency-dependent terms and some independent of ω. By setting the frequency-dependent part equal to zero and solving for ω_0, an explicit expression for the optimal choice of the comb's offset frequency can be obtained

$$\omega_{\text{CEO}} = \frac{(\omega_c\phi_1 - \phi_0)}{2\pi}\omega_{\text{rep}} + m. \tag{2.88}$$

By solving the frequency-independent part of Equation (2.87), ω_{rep} can be deduced:

$$\omega_{\text{rep}} = \frac{2\pi c}{L + \phi_1 c}. \tag{2.89}$$

Thus, for these choices of ω_{rep} and ω_0, the phase shift and group delay in the resonator can be matched. Equations (2.88) and (2.89) show that a constant phase offset of the cavity can be mitigated by a suitable choice of ω_0, demonstrating an equivalence between the two. The effect of such a constant phase is shown in Figure 2.16, where $f_{\text{CEO}} = 65$ MHz. The resonance fringes are shifted in position and slightly tilted, also affecting

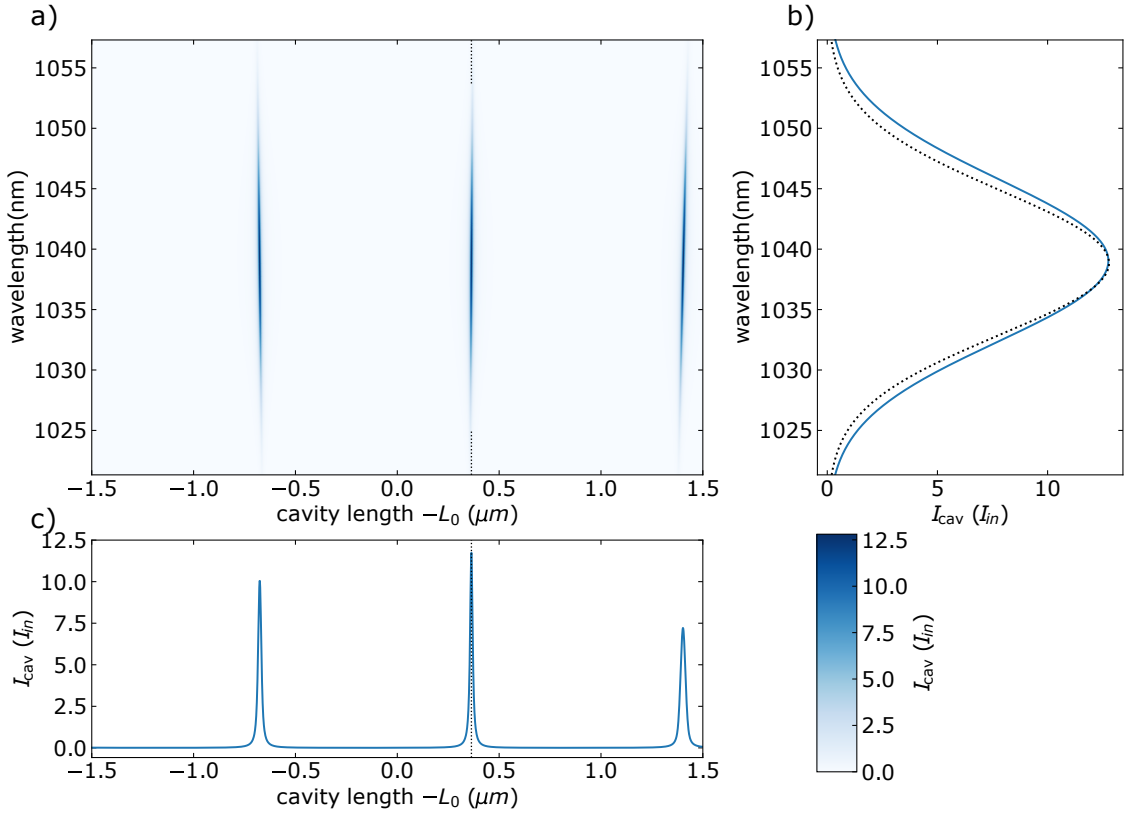

Figure 2.16: Resonance map similar to Figure 2.15, but with $f_{\mathrm{CEO}} = 65\,\mathrm{MHz}$. The fringes in a) are shifted and rotated, such that the central fringe is no longer exactly vertical. This results in slight spectral narrowing shown in b), where the dotted black line indicates the cavity spectrum at the position of the dotted lines in a) and b), and the solid blue line represents the incident spectrum. The enhancement β of the central fringe in c) has dropped from 12.8 to 11.7. Graphical representation inspired by T. J. Hammond & A. K. Mills et al. [82, 134]

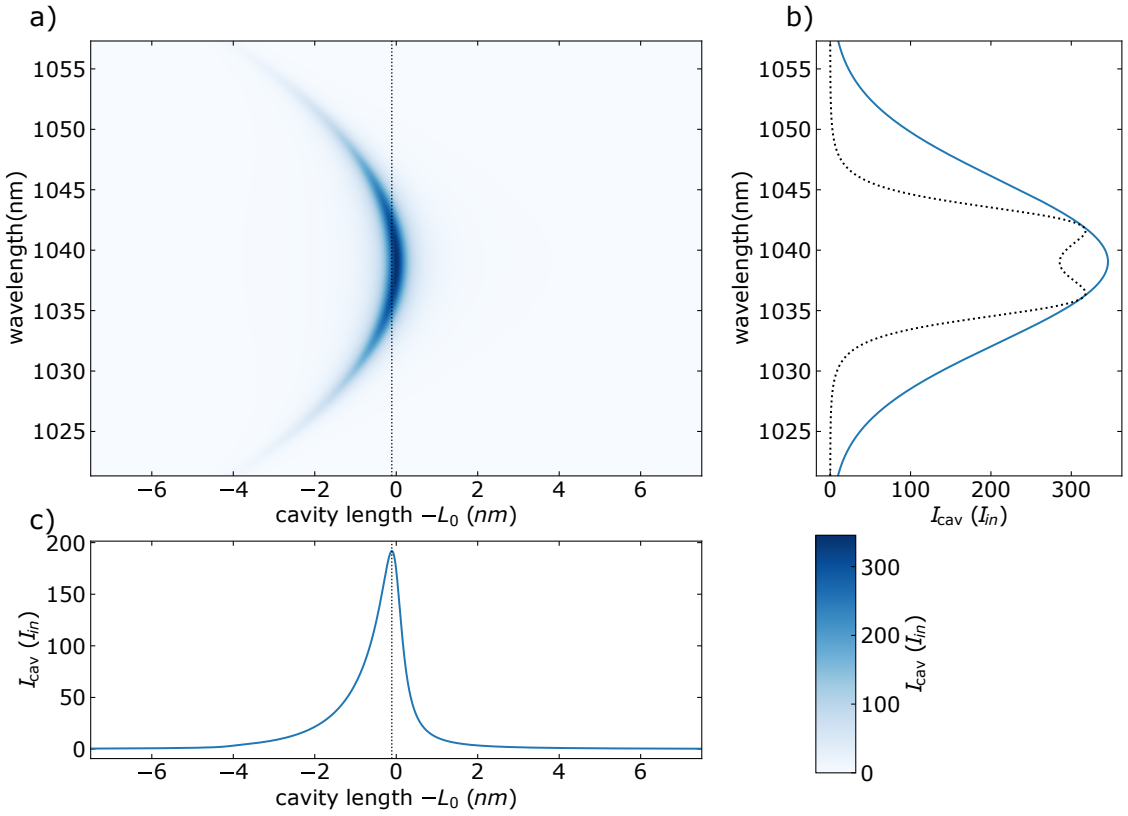

Figure 2.17: Resonance map for a cavity with $T_i = 0.007$, $T_c = 0.002$ and a round-trip GDD of $25\,\mathrm{fs}^2$. a) second-order dispersion causes a quadratic curvature of the resonance fringe. This causes significant spectral narrowing in b) (dotted line), compared to the input spectrum (solid line). c) the maximum attainable enhancement drops from 345 for a dispersive-less cavity to 192 and the broadened resonance peak becomes asymmetric. Graphical representation inspired by T. J. Hammond & A. K. Mills et al. [82, 134]

their enhancement. Since the central fringe is no longer independent of frequency, the resonant spectrum at the cavity length corresponding to the maximum enhancement is slightly narrowed.

With higher order dispersion terms present, the resonance fringes become nonlinear, and the cavity bandwidth decreases even further. This is shown for the case of a nonzero GDD in Figure 2.17. Here, realistic cavity parameters, $T_i = 0.007$ and $\mathcal{F} = 700$, were used with $\phi_2 = 25\,\mathrm{fs}^2$. The quadratic dispersion relation results in a parabola-shaped fringe and an asymmetric line shape. The resonant cavity spectrum is significantly narrower than the incident spectrum at any cavity length.

These example simulations show that GDD and higher orders of dispersion cannot be easily compensated by adjusting some experimental parameters. Therefore, it is very important that all intra-cavity elements only add a minimal amount of higher order dis-

persion to the circulating pulse in order to avoid spectral narrowing and pulse-broadening inside the cavity.

Chapter 3

Experimental setup

In this chapter, the experimental setup of the XUV comb is described. The apparatus is shown in Figure 3.1, with references to the relevant sections. First, an overview of the laser system is provided, followed by a detailed description of the most important part of the setup: the femtosecond enhancement cavity. Subsequently, the vacuum system hosting the resonator is reported. Finally, the design and realization of the differential pumping system for removal of the target gas in the cavity focus is presented.

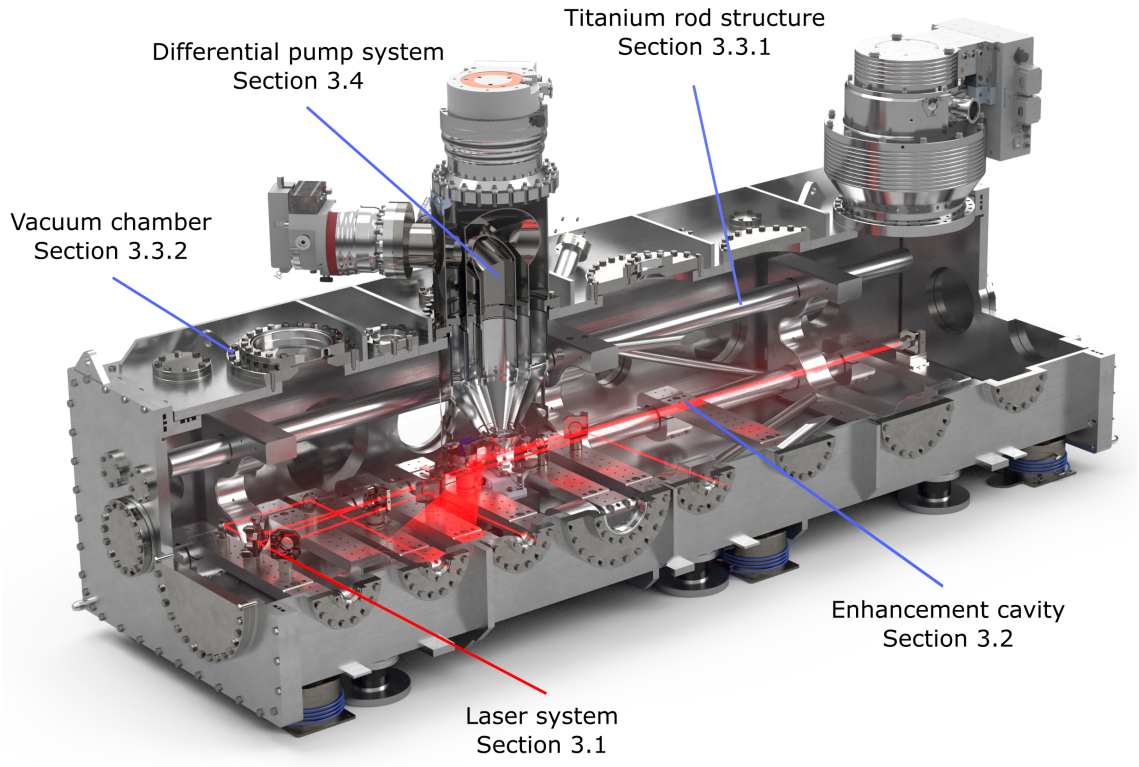

Figure 3.1: Overview of the experimental setup and its different parts.

3.1 Laser system

The first XUV combs were operated using mode-locked Ti:sapph lasers [23, 24], as it is also the standard workhorse for single-pass HHG systems. Typically, Ti:sapph lasers have an output power of up to a few Watts, which then requires a high finesse cavity ($F > 1000$) to amplify the pulses to the kW-level necessary for HHG. The generation of harmonics inside such a high finesse cavity has turned out to be difficult due to plasma instabilities and it is therefore more convenient to lower the cavity finesse and start off with a higher laser power [82]. Rapid evolution of laser technology over the past few decades has enabled the use of high power fiber-based laser systems, offering the advantage of both a better power scalability and robust alignment over time. For these reasons, Yb:fiber lasers are now typically used to feed fsEC for the generation of XUV light. We have also adapted such a laser system, which will be described in this section. First the commercial oscillator is introduced, followed by the home-build optical pulse characterization setup. Finally, a description of the home-built amplifier and compressor is provided.

3.1.1 Oscillator

In our setup, we use a commercial frequency comb (Menlo Systems, FC1000-250) with a 14 nm FWHM spectral bandwidth centered around 1039 nm. An overview of the oscillator and subsequent components of the purchased system is shown in Figure 3.2. The oscillator largely consists of Yb-doped fiber apart from a short free space part, where offset and repetition rate frequency can be modified. The repetition rate of 100 MHz can be changed up to 1% by moving the end mirror of the cavity with a motorized stage. Fast feedback can be applied to a piezo element to which the mirror is attached. The offset frequency can be adjusted by moving a second stage changing the amount of dispersion inside the oscillator. Fast feedback to the offset frequency can also be applied by acting on the oscillator pump power.

An overview of the electronics for stabilizing the comb parameters is shown in Figure 3.3. The repetition rate of the comb is detected by a fast photodiode, and can be stabilized to a 20 MHz signal provided by a direct digital synthesizer (DDS), which has a frequency resolution of 10 μHz. The 10^{th} harmonic of the detected signal at 1 GHz is mixed with a 980 MHz signal from a phase locked oscillator (PLO), a low-noise fixed frequency synthesizer. The resulting 20 MHz beat-note is compared with the DDS signal in an analog phase detector. A subsequent proportional-integral-derivative (PID) controller then provides feedback to the repetition rate by acting on the intra-cavity piezo. For the scope of this thesis, the DDS and PLO were referenced to a 10 MHz local oscillator, which in turn is referenced by GPS-data from atomic clocks. In this way, the repetition rate can be stabilized to a fractional uncertainty of 10^{-12} within 1 second, currently limited by the

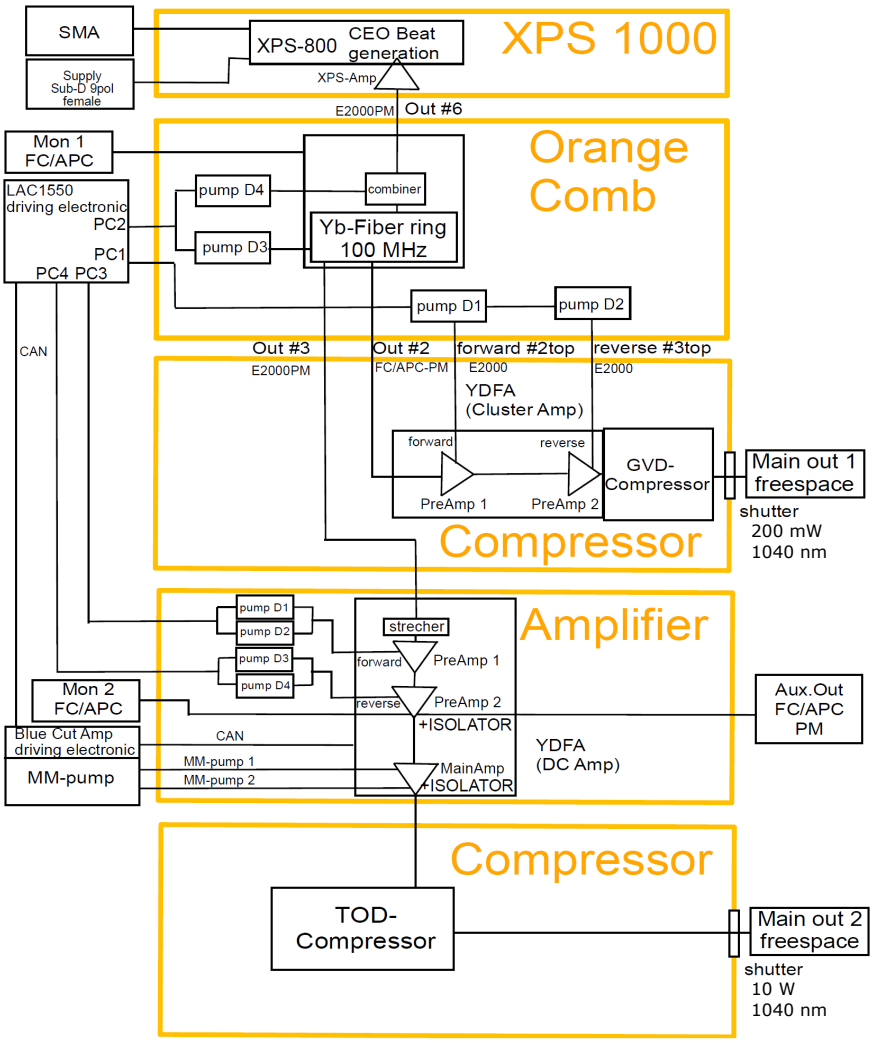

Figure 3.2: Overview of the commercial system with oscillator and subsequent amplifiers and compressors, provided by the manufacturer. The 'main out 1' output can be used for beating the comb with a CW laser for phase-locking. The high power output 'main out 2' is used to feed the home-built amplifier and enhancement cavity.

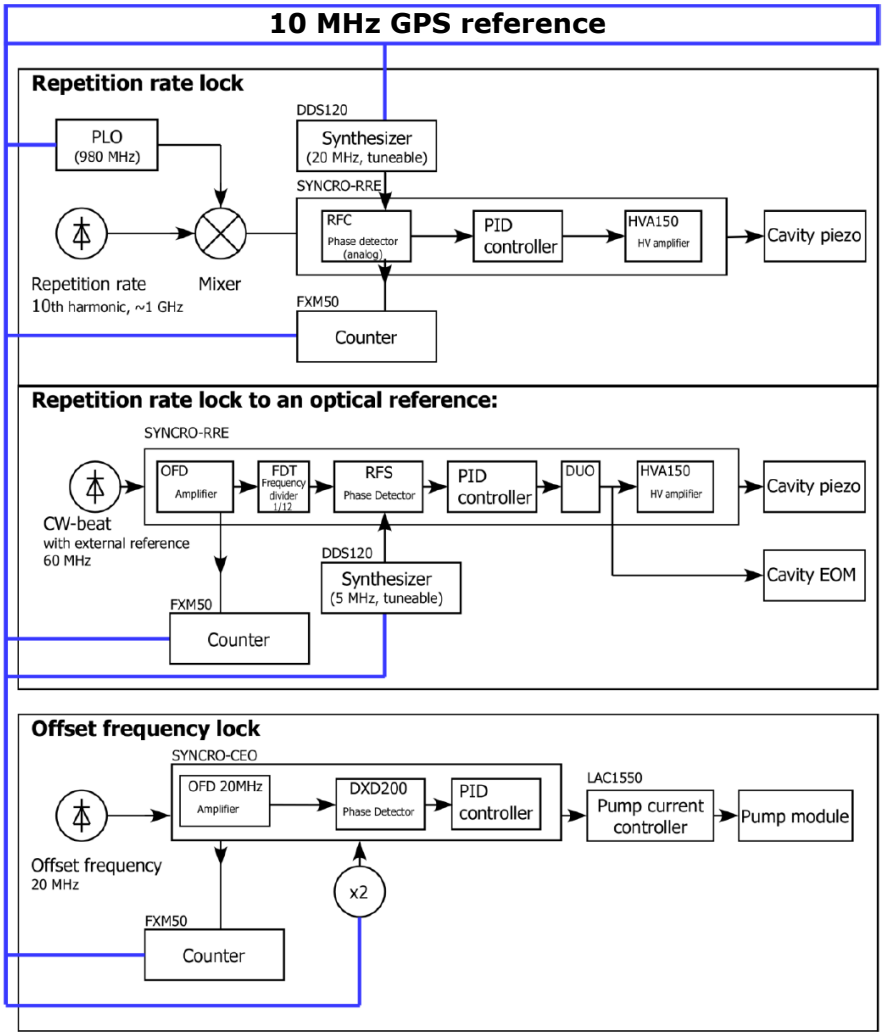

Figure 3.3: Overview of locking electronics of the laser system, provided by the manufacturer. Blue solid lines represent the 10 MHz reference signal. For the scope of this thesis, the repetition rate and offset frequency are stabilized to a GPS reference. For future experiments it is also possible to increase the stability by locking to an optical reference.

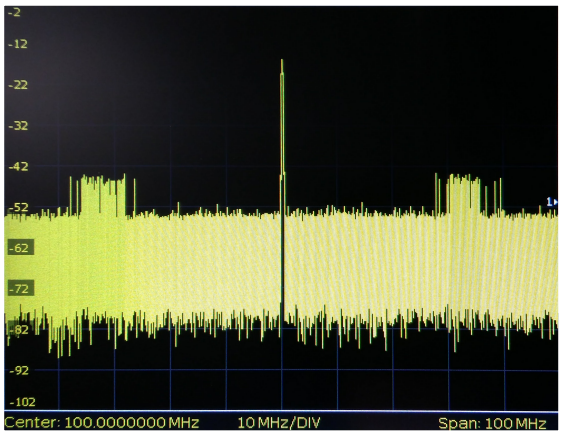

Figure 3.4: Beat-note of the comb with a 441 nm spectroscopy laser, sweep time 1 s. The central peak originates from the 100 MHz repetition rate, both symmetric signals on the sides are beat-notes with the laser.

frequency reference. The repetition rate stability can be further increased by locking it to an optical reference, which is planned for the future. The necessary locking electronics is already available and also shown in Figure 3.3.

The offset frequency of the comb is detected in the XPS-800 unit using a f-2f self-referencing scheme [19, 20], described in Section 2.1.3. The offset frequency beat signal is filtered and amplified before it is compared to the DDS 20 MHz frequency with a phase detector and fed into a PID controller, which provides feedback by adjusting the oscillator pump power. Although the offset frequency can be observed on a spectrum analyzer for any value, the band-pass filter in the OFD module prevents counting and locking the offset frequency for frequencies outside a 7 MHz bandwidth centered at 21.4 MHz. In practice, this is not limiting us since the free-running offset frequency of the comb is stable enough to run the cavity without locking f_{CEO}, as described in Section 3.2.3.

Part of the light from the oscillator is send to two subsequent fiber amplifiers and a compressor stage, before it exits as a free space beam of >200 mW. The output is subsequently broadened by a nonlinear fiber, and can be used to generate beat-notes with other optical lasers for locking them to the comb, or vice-versa, or determining their absolute frequency. This was, for example, applied to check the stability of the 441 nm laser used for the first optical excitation of a HCI in a Penning trap [136]. In Figure 3.4, the beat-note of this laser with the comb is shown on a spectrum analyzer. In the middle, the 100 MHz repetition signal is visible, surrounded by two symmetric beat-note signals of the 441 nm light. The width of the detected signal is a measure for the line-width of the 441 nm laser, in this case several MHz over a time-interval of 1 s. The line-width of the comb itself is ∼300 kHz.

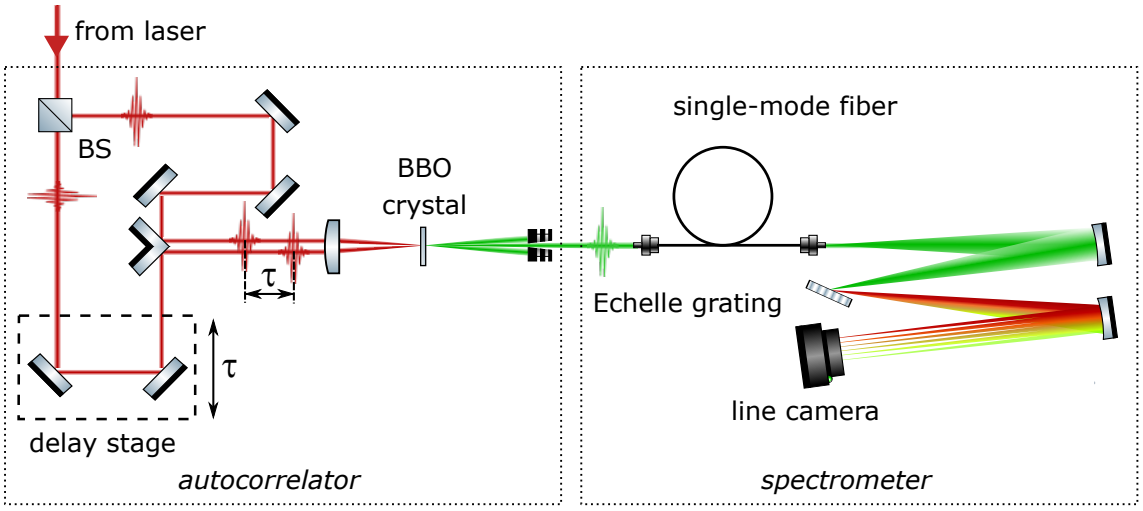

Figure 3.5: Autocorrelator and spectrometer setup, together forming a FROG for pulse characterization. A beamsplitter (BS) splits the pulse in two copies, one of which is delayed in time by a variable amount τ. Both pulses are focused in a BBO crystal and the emerging SHG signal is send to the spectrometer through a fiber. An Echelle grating and a sensitive line camera ensure a high spectral resolution. The wavelength range is adjustable by rotating the grating.

Finally, light is coupled out from the oscillator towards the high power output. It is first stretched by 60 m of fiber (XP980-PM, Nufern) to 24 ps before it is amplified by two pre-amplifiers. Subsequently, the fiber-coupled main amplifier further intensifies the pulses to an average power of $\sim$ 15 W. A free-space TOD grating prism (GRISM) compressor shortens the pulses to a minimum of 170 fs before exiting the system. This 12 W compressed output was used for MPI experiments in the fsEC, described in Chapter 4. For intra-cavity HHG, further amplification of the pulses is necessary, so the TOD compressor is bypassed and uncompressed pulses from the main amplifier are used for further amplification.

Because of its fiber-based operating principle, the pointing stability of the laser is excellent. Over timescales of months, the pointing of the beam does not change significantly, and the incoupling into the amplifier fiber or fsEC is never lost. Some minor alignment optimization is necessary at most. Furthermore, the system is turn-key and does not need any daily optimization or alignment.

3.1.2 Pulse characterization: FROG

For characterization of the amplified and compressed pulses we have built an optical gating setup together with a spectrometer. For measuring the duration of a femtosecond pulse, electronic devices are too slow. The pulses are therefore gated and compared to

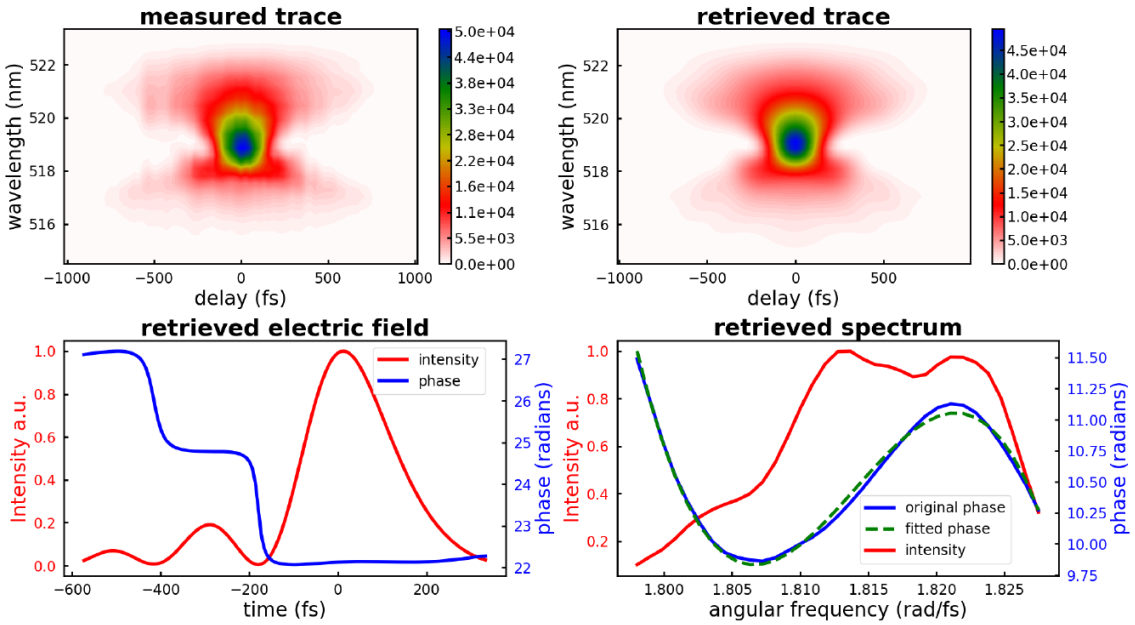

Figure 3.6: FROG-trace recorded after the grating compressor, at 69 W average power. A pulse length of 222 fs is measured. Figure from A. Ackermann [138].

each other, overlapping two copies of the same pulse in a non-linear medium and varying the time delay between both pulses [137]. We have implemented this technique, known as autocorrelation, by focusing two copies of the same pulse in a 100 μm beta-barium borate (BBO) crystal. For small delays, the pulses overlap inside the crystal and a SHG signal at 532 nm appears between the two beams behind the crystal, as shown in Figure 3.5. Measuring the intensity of the SHG beam with a photodiode as function of time delay results in an auto-correlation signal. By assuming a certain pulse-shape, the pulse duration can be inferred. However, the pulse-shape itself cannot be measured using auto-correlation, neither can information about the phase be obtained, and it therefore does not provide a complete characterization of the pulse.

By extending the autocorrelator with a spectrometer, a more comprehensive characterization of the pulses can be achieved. In frequency-resolved optical gating (FROG), the full frequency-doubled pulse spectrum is recorded for every time-delay step [139]. The fiber-coupled spectrometer in our setup uses an Echelle-grating (79 grooves/mm, 75° blaze angle) and a line camera (LC100, Thorlabs), resulting in an excellent resolution of 0.01 nm/pixel at 532 nm. In this way, a 2-D spectrum is obtained where the intensity is represented by a color scale as function of both wavelength and time-delay. This SHG-FROG-trace contains all information about the phase and duration of the pulse, but in a very non-intuitive manner and it can therefore not be easily extracted from the obtained data [140]. A phase-retrieval-based algorithm can be used to reconstruct the original pulse

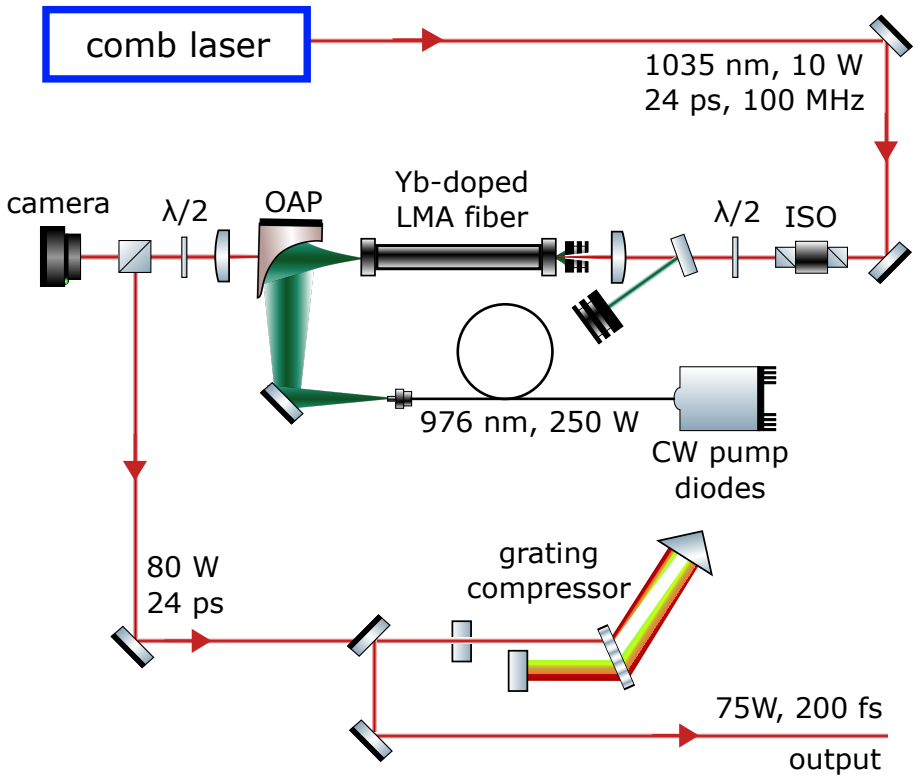

Figure 3.7: Overview of the home-built part of the laser system. Long pulses from the commercial comb are first amplified by a rod-type amplifier and then compressed by a grating compressor. ISO: optical isolator, $\lambda/2$: half-wave plate, OAP: off-axis parabolic mirror.

information by an iterative procedure. Different algorithms have been developed over time [141, 142]. We chose to use the freely available FROG software [141]. In Figure 3.6, an example of a FROG-trace is shown [138].

3.1.3 Amplifier and Compressor

To further amplify the 12 W pulses from the comb, a home-built chirped pulse amplification (CPA) system was developed, consisting of a rod-type fiber amplifier and a grating compressor. Compared to CW laser amplification, enhancing fs pulses presents more challenges. First, the high peak powers of ultrafast lasers can damage the amplification fibers, requiring stretching of the fs pulses to picoseconds or nanoseconds. Furthermore, the material of the long amplification fiber add a large amount of dispersion to the pulses, thereby stretching the pulses in time. Finally, non-linear phase shifts due to self-phase modulation (SPM) in the amplifier fiber can distort the pulse shape at high peak intensities in the fiber. Generally, two different approaches can be taken to tackle theses problems; either utilizing the SPM as a spectral broadening mechanism in the amplifier fiber itself, which

enables the out-coming pulse to be even shorter than the seed pulse [143, 144]. Or alternatively, stretching the pulse and using large mode area (LMA) fibers to try to minimize nonlinear phase shifts, i.e. operating the amplifier in the linear regime [145–147]. For frequency combs, the latter is more desirable, since operation in the non-linear regime strongly amplifies any spectral or amplitude noise present in the seed pulses [148]. In the linear regime, the amplified pulse coherence properties are mainly determined by the oscillator itself, and are not so sensitive to amplitude noise on the pump diodes.

Since a stretcher is already present in the comb laser providing sufficient long pulses, we decided to use these directly for amplification. The built-in TOD compressor is not suitable for high power of the amplified pulses, so have constructed our own compressor to shorten the amplified pulses to $\leq 200\,\mathrm{fs}$. An overview of the amplifier and compressor system is shown in Figure 3.7.

To protect the laser from any amplified back-reflections, a Farady isolator (PAVOS-Ultra-05-I-1015-1065, Soliton), capable of isolating up to 100 W average power, is installed right after the laser output port. The amplifier fiber is a 80 cm long Yb-doped photonic crystal fiber rod (aeroGAIN-ROD-MODULE-2.0 PM85, NKT photonics) with a $3300\,\mu\mathrm{m}^2$ mode field area, mounted in a rigid aluminum body with integrated water cooling. The fiber is pumped by a fiber-coupled 250 W CW diode (D4F2S22-976.3-250C-IS58.1, DILAS Diodenlaser GmbH) at 976 nm, which is coupled in the back of the fiber cladding with an off-axis parabolic gold-coated mirror (MPD229H-M03, Thorlabs). The mirror has a $\varnothing 3\,\mathrm{mm}$ central hole to couple out the seed pulses, which together with the coating induces losses of only 8% to the pump light due to the large beam diameter of 19 mm. At such high pump powers, these losses are significant and the mirror mount is water-cooled to transport away the generated heat. At the front of the fiber, the divergent pump beam is absorbed by a water-cooled beam dump with a central hole for letting through the seed pulse. After the collimating lens, the remaining pump light is separated from the seed beam by a dichroic mirror (Layertec).

The transmission of the seed pulses through the fiber without pump light is about 80%. When turning on the pump diodes the seed is amplified up to 93 W, as shown in Figure 3.8. The plot shows linear amplification directly after the fiber. A Gaussian mode profile appears both at low and high power. The pump wavelength is stabilized and fixed with an internal volume Bragg grating, although it could be slightly tuned by controlling the temperature of the pump diodes via setting the chiller temperature. Since the absorption feature in Yb at 975 nm is rather narrow [149], tuning could increase the pumping efficiency. In practice, this turns out not to be necessary and linear amplification is observed without changing the diode temperature.

One major concern with the amplifier fiber is fatal damage that can occur when the seed pulses are interrupted, for instance due to a loss of mode-lock or something blocking

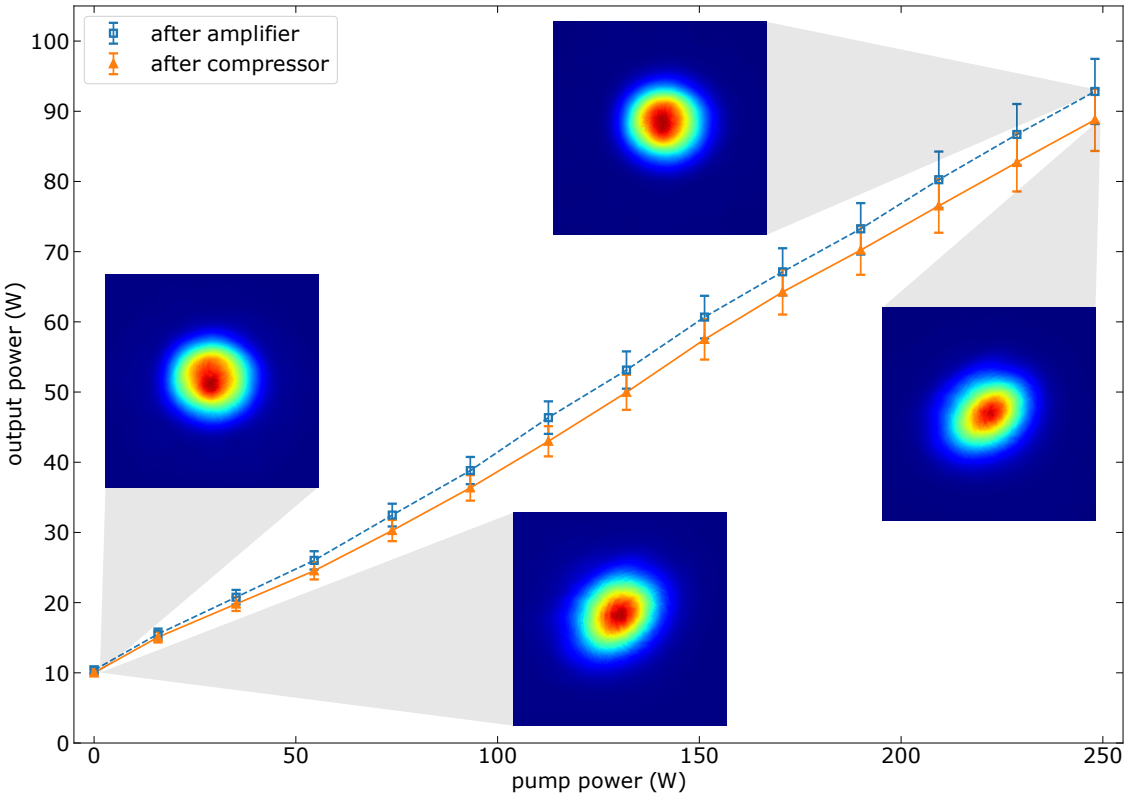

Figure 3.8: Performance of the main amplifier. Optical output power of the amplified pulses directly after the amplifier and after the compressor is measured as a function of amplifier diode pumping power at 975 nm. The insets show far-field beam profiles without amplification and with maximum amplification.

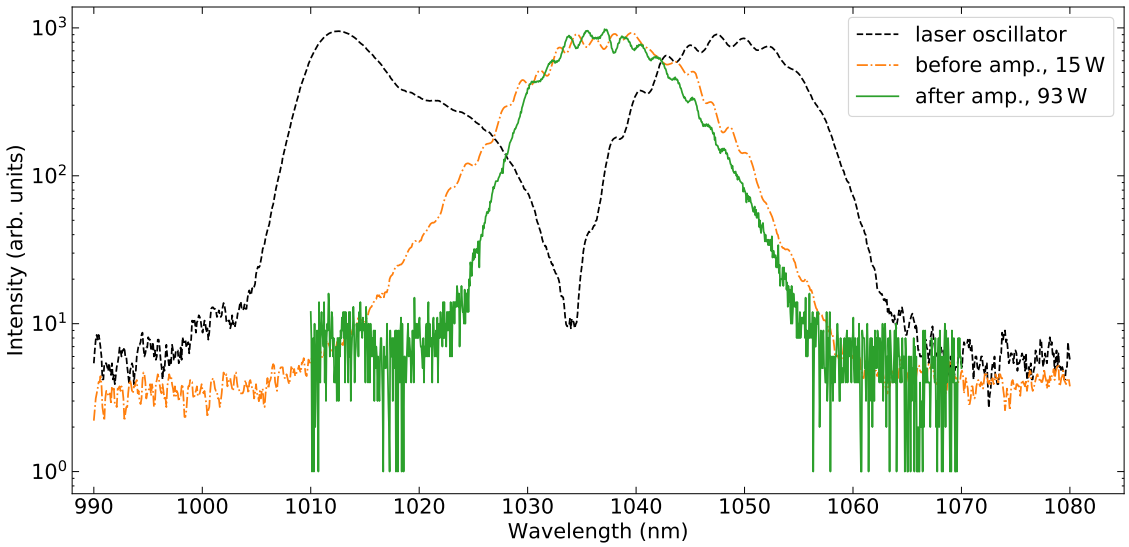

Figure 3.9: Pulse spectra at different positions in the laser system. The broad spectrum from the oscillator is significantly narrowed by the amplifiers in the commercial system. The main amplifier reduces the bandwidth only slightly.

the beam. With no seed available, pump energy is stored in the fiber until complete population inversion is reached. Now, when any seed pulse arrives the stored energy is converted in such a strong pulse, that it can destroy the fiber. In order to avoid this kind of damage, after the seed has disappeared the pump diodes must be switched off on the same timescale as the storage time in Yb of roughly 1 ms. Therefore, we have implemented a fast analog interlock circuit, monitoring the seed pulses with a fast photodiode. As soon as the measured value drops below a set threshold, the output of the current drive unit supplying the pump diodes is interrupted within 1.5 ms. A slower interlock operated by an Arduino microcontroller prevents switching on the pump current when not enough seed light is present. As a safety precaution, we operate the pump diodes with a minimum seed of 2 W, which is the estimated saturation power of the fiber, although other groups have used much lower seeding powers without observing damage [145].

A grating compressor is employed to shorten the amplified pulses. A 1000 lines/mm transmission grating (1158_28x18_6.35_H, Gitterwerk GmbH) is inserted between two reflective retro-reflectors and traversed four times. The diffraction efficiency into the first order is specified to be $> 98.5\%$, resulting in a total compressor transmission efficiency of 95%. The performance of the compressor is shown in Figure 3.8. Although not perfectly Gaussian, the beam profile after the compressor is of a very good quality. No thermal lensing is observed even at maximum output power. The compressed pulse length amounts to 220 fs. With a GRISM-compressor slightly shorter pulse lengths are possible, however the transmission is then also decreased [138]. In Figure 3.9, the spectrum of the system

is shown at different positions. The first amplifiers after the oscillator cause significant gain-narrowing, but the rest of the CPA setup does not alter the spectrum significantly.

3.2 Enhancement cavity

The majority of HHG experiments are carried out by focusing an amplified pulsed laser onto a gas target [150, 151]. Using an ultrafast laser with $\sim 1\,\mathrm{mJ}$ of power and short pulse durations $\sim 10\,\mathrm{fs}$, peak intensities $\sim 10^{14}\,\mathrm{W/cm^2}$ can be reached, which is sufficient for HHG. Such high pulse energies are typically reached by systems with a repetition rate of a few kHz [151]. To generate an XUV frequency comb, similar pulse energies are required at a much higher repetition rate. This means that the average power has to be much higher: a 0.1 mJ pulse train at a rate of 100 MHz will have an average power of $0.1\,\mathrm{mJ} \times 100\,\mathrm{MHz} = 10\,\mathrm{kW}$. As of now, such high average powers have not been realized yet with actively pumped amplifiers. It is however possible to reach such values inside an optical resonator, therefore passively enhancing the pulse train. In this section, the enhancement cavity for our 100 MHz laser pulses is described. First, the general design goals and criteria are determined. Then, a generic cavity geometry is discussed, followed by a specific design fulfilling our criteria. Finally, several important aspects of the cavity implementation, performance and operation are treated.

3.2.1 Design considerations

Previous experiments using intra-cavity HHG have shown a few important issues that strongly influence the performance and durability of XUV light generation. This knowledge is incorporated in the design of our system to optimize its operation.

Perhaps the most important parameter of the enhancement cavity is the focus waist size, which determines the volume of the focal spot. In this region, the interaction of target gas atoms with the intra-cavity beam will generate ultraviolet light. In principle, with a larger focal volume comes a larger number of target gas interactions, and therefore a higher HHG output if the phase-matching conditions can be kept the same. However, a larger focus decreases the IR intensity, dramatically reducing the efficiency of the HHG process due to its nonlinear nature. Typical waist sizes used in other XUV comb experiments vary between 5 and 25 μm [23, 24, 78, 83, 86, 152–154], a larger waist requiring either a higher cavity finesse or a very high power of the input beam in order to reach intensities necessary for HHG. Due to disturbing effects of the target gas plasma on the cavity mode [155], it is desirable to keep the cavity finesse low to reduce the sensitivity to such effects. Therefore, more recent experiments operate mostly with a finesse $\ll 1000$ [156–158] and a high input power $\gg 10\,\mathrm{W}$. However, in order to then reach a sufficiently high peak intensity for HHG, it is necessary to focus the laser strongly. Furthermore, to reduce the amount of persisting plasma in the focus, a small focus size is advantageous since ions leave the interaction region within a shorter time [159]. Thus, for optimal HHG conditions using a low finesse cavity and a limited amount of incident laser power, we need to keep the focus waist size

as small as possible.

The length L_0 of the enhancement cavity for which consecutive pulses overlap, given by Equation (2.86), is determined by f_{rep} of the comb, and is in our case 3 m. To achieve tight focusing however, curved mirrors have to be placed close to the focus. Therefore a linear cavity is ruled out and a bow-tie configuration is commonly used, with one short arm for focusing ($\sim$ 25 cm) and one long arm to match the cavity length to 3 m. This long arm could be folded multiple times, in order to decrease the overall size of the cavity. However, with each mirror that is added to the cavity comes a small amount of loss and dispersion for the intra-cavity beam. Moreover, since mirror degradation has shown to be a serious problem for intra-cavity HHG [80], having more mirrors means more effort to clean and eventually replace them. Hence we prefer to keep the number of optics in the cavity as low as possible, and thus choose a simple bow-tie geometry with one short and one long arm, which is also the easiest to align.

The XUV output coupling method is a critical part of the cavity. The various established methods, described in Appendix A, all have their advantages and disadvantages. Since the goal of our experiment is to perform frequency-resolved spectroscopy, we just need a single comb tooth to interact with the ion. Therefore, we need to spatially separate the high harmonics to select just a very small wavelength portion and send it to the ion. Using the Yost-style grating mirror as an output coupler [160] has the big advantage that it can couple out the high harmonics from the cavity, and spatially separate them at the same time. When using any of the other out-couplers, the harmonics are coupled out collinearly and still need to be spatially separated with a grating later-on. These two steps each introduce losses, while with the grating mirror both steps are combined and the losses are just determined by the grating design. The grating can be optimized for maximum diffraction efficiency of certain wavelengths, as will be described in Section 3.2.6. Since the experiment is designed for studying a large variety of highly charged ions, many different transitions could be probed at various wavelengths. Therefore we aim at using a large range of wavelengths between 40 and 150 nm. In this wide region, the grating is much more efficient than the hole-in-mirror output coupler. Furthermore, most out-coupling methods have the disadvantage that the cavity beam needs to travel through some material. Besides inducing losses, dispersion and heating, this limits the intra-cavity power due to the damage threshold of the material. The grating mirror only interacts with the cavity beam at the surface, therefore losses and dispersion can be minimized by choosing a suitable coating. Finally, in a recent implementation of the Yost grating, XUV generation over an extended time period has been shown to be possible and not severely limited by degradation of the grating [154]. Therefore we choose the grating mirror as out-coupling method.

During operation of the cavity, a target gas is introduced at the focus. Recent exper-

iments have shown that using a target gas mixture with several bars backing pressure improves the HHG yield significantly [80]. To allow for a high back pressure of the target gas, a differential pump system around the nozzle is planned. This structure requires that there is sufficient space in all directions around the focus, avoiding the optics or laser beams. It turns out to be challenging to design a cavity geometry having this feature together with a tight focus and a small incidence on the cavity mirrors, since the reflected beam from the focusing mirror will travel close to the focus. The minimal size of a differential pump system with multiple stages is limited by manufacturing and assembly issues, as will be discussed in more detail in Section 3.4. As a realistic and workable size, we set the free space around the focus to be a sphere with a minimum diameter of 20 mm.

In order to maximize the laser intensity in the focus and generate a symmetric XUV beam, a round focus shape is required, meaning a similar horizontal and vertical waist size. Also, phase-matching conditions are easier to be full-filled in a symmetric focus. One disadvantage that comes with the use of a bow-tie cavity geometry is an asymmetry of the focus size in the tangential and sagittal plane, known as *astigmatism*. The asymmetry arises from the non-normal incidence on the curved mirrors in the horizontal plane, whereas in the vertical plane the incidence is exactly normal. To avoid astigmatism, a different cavity geometry could be used, such as a symmetric Fabry-Perot or a more sophisticated non-planar bow-tie cavity. The former is not practical for HHG since tight focusing and inserting a grating mirror are not possible for a 3 m long Fabry-Perot cavity. The latter has been shown to be feasible for intra-cavity HHG [161], but requires a rather complicated cavity setup with many mirrors, therefore suffering from additional mirror dispersion and losses. In a planar bow-tie configuration, astigmatism could also be avoided by using a set of cylindrical cavity mirrors [162] or parabolic focusing mirrors [163]. Although the latter would provide an elegant solution to the astigmatism problem, the manufacturing of parabolic mirrors is costly and alignment of the cavity becomes significantly more difficult, since now also the rotation of the focusing mirror becomes an alignment parameter. In our cavity design, we have therefore chosen to use a single cylindrical mirror as input coupler. Rotating the input coupler is less of a problem since there is enough space for a larger mirror mount allowing rotational alignment. In this way we can stick to the minimum of five mirrors forming the resonator, and the piezo-controlled mirror for length stabilization can be kept small and planar. The asymmetry induced by the cylindrical mirror is enough to fully compensate the focus astigmatism while still fulfilling all other geometric requirements.

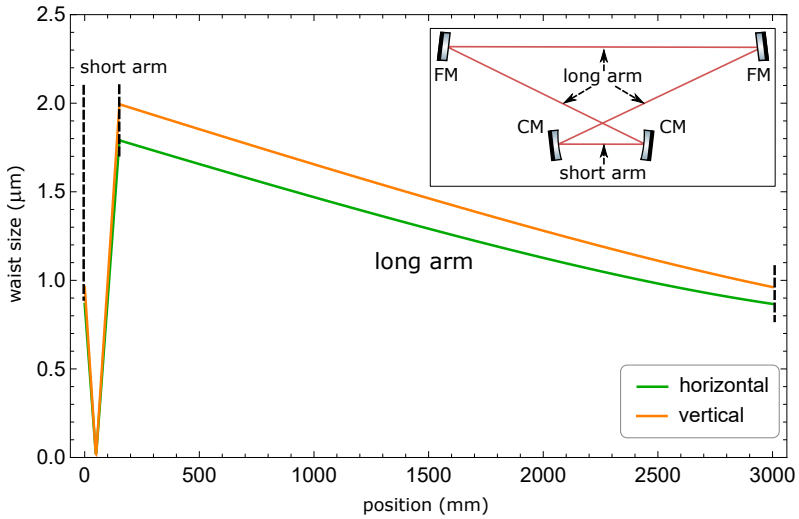

Figure 3.10: Waist size of the beam throughout the example cavity design illustrated in Figure 3.12. Curved mirrors (CM) are located at 0 mm and 151.5 mm, the two flat mirrors (FM) are placed at some location in the long arm according to the total cavity length. The inset shows the bow-tie cavity geometry.

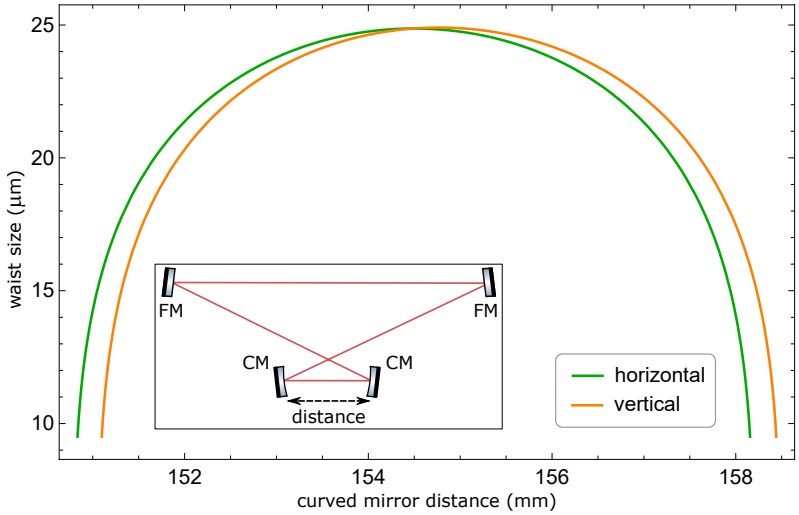

Figure 3.11: Focus waist size for the example cavity design shown in Figure 3.12. In the region where the horizontal and vertical curves overlap, stable cavity operation is possible. A small waist can be achieved by moving towards the edge of the stability region, however the amount of astigmatism is increased there. The inset shows the bow-tie cavity geometry.

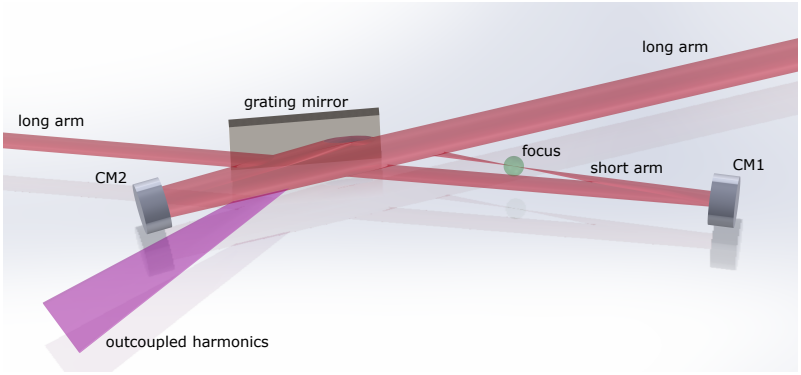

Figure 3.12: Focus region of a cavity geometry with small incidence angles on the focusing mirrors. Red beams represent the circulating field, focused by two curved mirrors (CM). The XUV-light (violet) is coupled out by the grating mirror. Available free space around the focus for differential pumping is represented by a green sphere with radius of 2.5 mm.

3.2.2 Geometry

Using the ABCD-matrix formalism, the propagation of Gaussian beams through the cavity can be calculated, as described in Section 2.4.3. Due to the asymmetry between the two planes induced by the bow-tie geometry and cylindrical mirror, this has to be done separately for the horizontal and the vertical plane. An example of a standard bow-tie geometry is plotted in Figure 3.10, where two focusing mirrors with radius of curvature (ROC) = 100 mm and ROC = 200 mm are placed at position 0 mm and 151.5 mm, respectively. Two other flat mirrors can be placed as convenient in the long arm such that the second round-trip overlaps with first one on the first curved mirror after exactly 3 m. The difference in horizontal and vertical beam profile arises from the small incidence angle on the curved mirrors, which is in this example case 1.3° and 2.75°. The focus size is mainly determined by the ROC of the focusing mirrors and their separation distance, thereby controlling the beam size inside the cavity. In Figure 3.11, the focus waist size is plotted as function of the curved mirror distance. The overlap between the horizontal and vertical curves is the region where stable cavity operation is possible. It becomes clear that in order to obtain a tight focus, the curved mirror distant has to be moved to the edge of the stability region, where the focus waist size drops. By doing so, the amount of astigmatism is increased, induced by the non-zero incidence horizontal angle on the focusing mirrors.

In Figure 3.12, a possible cavity geometry is shown with the afore-mentioned parameters. The design includes the diffraction grating, which is placed right behind the focus to couple out the generated XUV light shown in violet. The flat grating does not change the IR beam divergence, but it does occupy some space such that one of the curved mirrors has to be placed further away from the focus. Therefore, the curved mirrors have a different

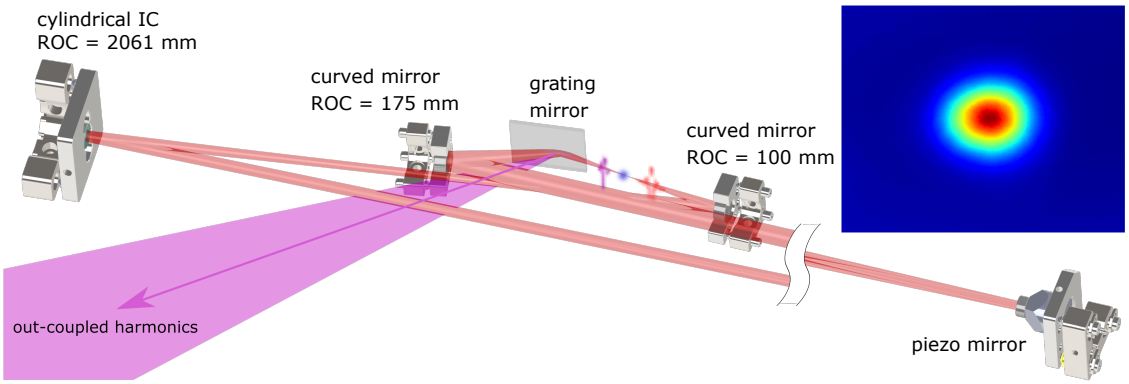

Figure 3.13: Overview of the final cavity design with large incidence angles on the focusing mirrors, allowing for 10 mm of free space around the focus in all directions. The depicted size of the cavity beam (red) is $2.15 \cdot w$, where the intensity has dropped to 0.01% of the total intensity. The direction of out-coupled harmonics is indicated in violet. The inset shows a beam profile of the Gaussian cavity mode, recorded after the ROC=100 mm curved mirror.

ROC. A geometry like in Figure 3.12 has been proven to work for intra-cavity HHG [86]. However, in this design the reflected beam runs very close to the focus, leaving only 2.5 mm of space for a differential pump system. Moreover, there is some amount of astigmatism at the focus.

To obtain enough free space around the focus but at the same time keeping a small focus waist, the incidence angle on the focusing mirror need to be increased. This is usually accompanied by a larger astigmatism, but when using a specific set of bigger incidence angles it is possible to still obtain a tight focus in both planes, which is used in the final design of our cavity shown in Figure 3.13. The resulting beam size is shown in Figure 3.14, where we use curved mirrors with ROC = 100 mm and ROC = 175 mm. A flat mirror mounted on a lead zirconate titanate (PZT) piezo element is placed in the long arm and the IC is located at 2623 mm. The focus waist size is shown in Figure 3.15, where now the horizontal and vertical stability region only have a small overlap due to incidence angles of 11° and 8° on the curved mirrors with ROC = 175 mm and ROC = 100 mm, respectively. This implies that the alignment of the cavity is more challenging, but once aligned in the center of the stability region a tight and round focus is achieved.

To verify that the focus waist size of the implemented cavity corresponds to the calculations, the horizontal and vertical size of the laser beam transmitted through the curved mirror before the cavity focus was recorded on a CCD camera (Thorlabs DCC1240M), as shown in the overview in Figure 3.19. By back-propagating the beam properties through the beam-path between the cavity and camera using the ABCD-matrix formalism, dis-

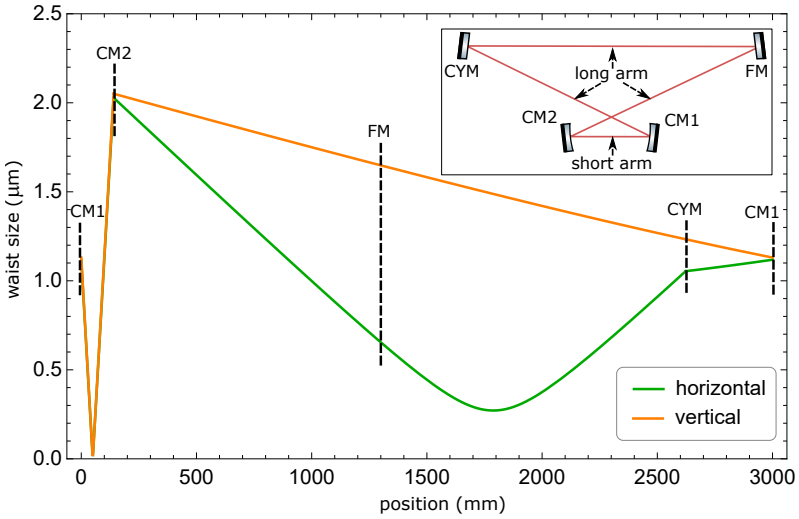

Figure 3.14: Waist size throughout the final cavity design. A cylindrical mirror (CYM) with a horizontal curvature of 2061 mm is used as input coupler to compensate for astigmatism at the focus, also inducing a loose focus in the long cavity arm. The position of the other curved mirrors (CM) and flat piezo mirror (FM) are indicated. The overall geometry is shown in the inset.

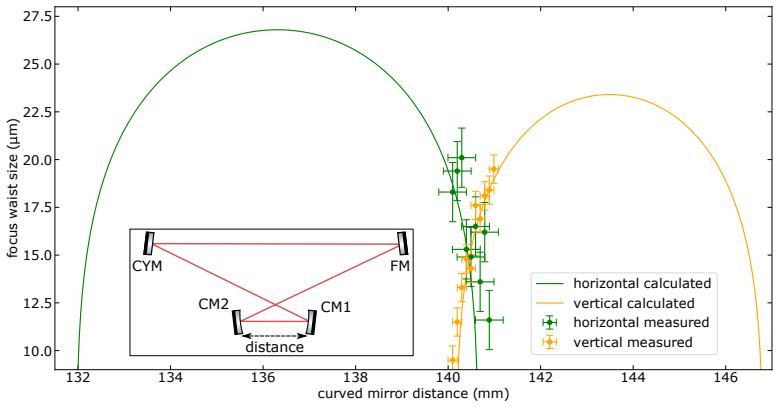

Figure 3.15: Focus waist size of the final cavity design. Due to the large incidence angles of 11° and 8° on the curved mirrors with ROC = 100 mm and ROC = 175 mm respectively, both stability regions are pulled apart, and only a small section of overlap remains for operating the cavity. In the center of that region, an astigmatism-free focus is achieved. Measurements confirm stable cavity operation with a waist of 14.7 μm in both planes.

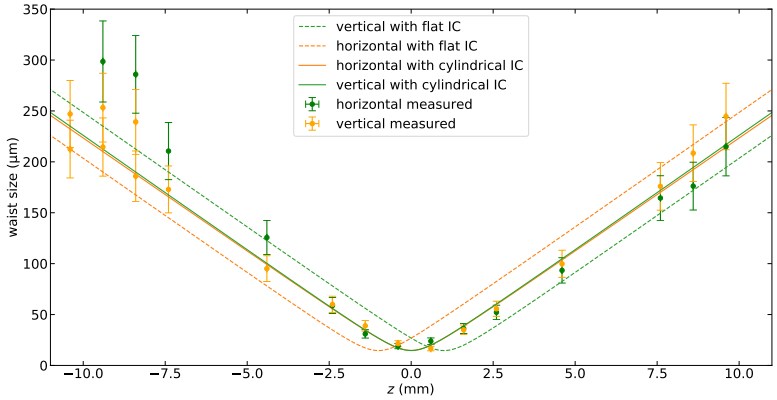

Figure 3.16: Horizontal and vertical waist size as function of longitudinal position near the cavity focus. Without compensation, the horizontal and vertical focuses are displaced by 2 mm. By utilizing a cylindrical IC, both foci can be overlapped again to produce a single, astigmatism-free focus. The effect of the cylindrical IC is confirmed by knife-edge measurements in both planes.

cussed in Section 2.4.3, the focus waist size can be determined from two images taken at two different positions in the beam [164]. By varying the distance between both curved mirrors with a translation stage, the stability region of the cavity can be probed, as shown in Figure 3.14. The vertical error bars arise from uncertainties in the position of optics in the beam path, horizontal errors from the uncertainty in measuring the curved mirror distance. Both errors are larger for the horizontal axis of the beam since the cavity needs to be re-aligned in this plane during the measurement because of the non-zero incidence angle on the curved mirrors. A good agreement between the measured and calculated waist is found, meaning that we can achieve a tight and round focus of 14.7 μm in the exact center of the stability region and stable operation there is possible.

Although now the horizontal and vertical focus waist sizes are the same, taking a closer look at the focus reveals that both are actually displaced in the longitudinal (z) direction, which becomes clear from the dashed lines in Figure 3.16. As mentioned before, this effect can be compensated by introducing a cylindrical mirror which changes the horizontal divergence of the cavity beam. For a cylindrical IC with a custom curvature of 2061 mm, the horizontal and vertical focus are brought together, as indicated by the solid line in Figure 3.16. The effect of the curved IC on the horizontal beam size in the cavity becomes clear in Figure 3.14. In the long arm of the cavity, a loose second focus emerges. This has the slight disadvantage of increasing the laser intensity on the mirrors there, but since the vertical beam size is still sufficiently large, this is not expected to be of concern.

In order to verify the effect of the cylindrical IC mirror, we performed a knife-edge measurement of the beam size in the focus region [165]. A razor blade mounted on an

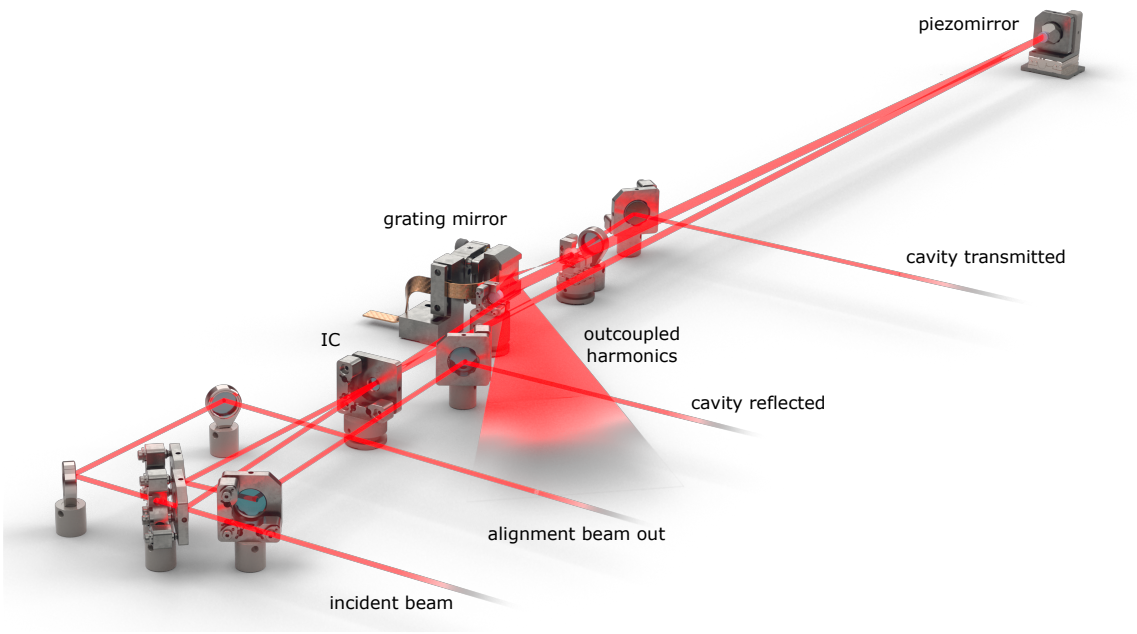

Figure 3.17: Overview of the resonators optical elements. The incident beam is sampled and send back for monitoring the alignment. Cavity reflected and transmitted signals are recorded for diagnostics.

XYZ-translation stage was moved in the cavity beam, while recording the transmitted intensity through one of the cavity mirrors on a photodiode. Fitting error functions to the intensity decay curves results in a measure for the beam waist. This was performed in both horizontal and vertical directions at various z positions in the beam, as shown in Figure 3.16. The large uncertainties arise from the interplay of edge-diffraction with the cavity mode [166]. The measurement points close to the focus are however precise enough to confirm that the vertical and horizontal cavity focuses overlap. The cylindrical IC has the expected effect and a single, round and tight focus with 14.7 μm waist size is obtained.

The final cavity geometry, shown in Figure 3.17, has large incidence angles which allow for 10 mm of free space around the focus in all directions. As a consequence, the long cavity arm comes very near to the curved mirrors, which need to be mounted in 'open' mirror mounts. The ROC = 100 mm mirror even needs to be placed slightly off-center in order not to block the cavity beam. An overview of the complete cavity is shown in Figure 3.13. By carefully placing the mirrors at the designed positions, a stable Gaussian cavity mode, shown in the inset, is obtained without the need for major adjustments in their position or angle.

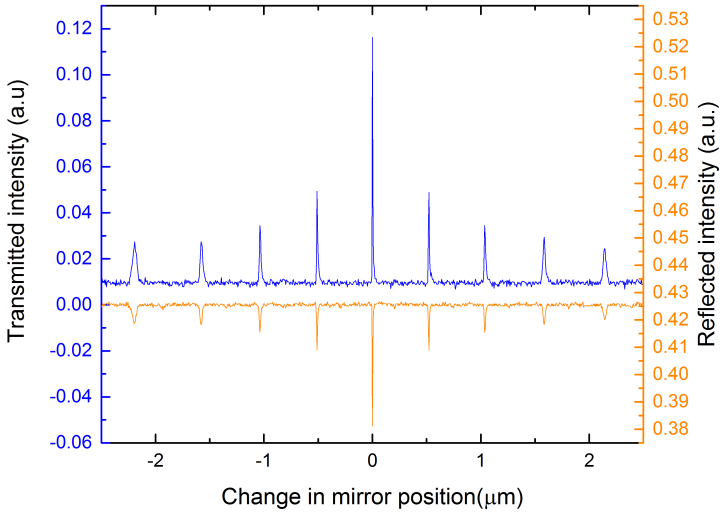

Figure 3.18: Transmitted and reflected intensity from the enhancement cavity during a scan of the cavity length. The central resonance corresponds to L_0=3 m, as described in Section 2.5, where maximum enhancement is achieved.

3.2.3 Length stabilization

As described in detail in Section 2.5, there is only one cavity length which fulfills the resonance condition for all comb wavelengths simultaneously. A recorded cavity scan with the strongest resonance fringes is shown in Figure 3.18. In order for the pulses to be enhanced, each incoming pulse envelope must overlap with the circulating pulse in the time domain. Furthermore, the optical carrier under the pulse envelope must also constructively interfere, implying that the frequency comb pulse-to-pulse phase shift equals the accumulated round-trip phase inside the cavity. In the frequency domain, the equivalent requirements are matching the repetition rate of the comb to the cavity length and adopting the carrier envelope offset frequency with that of the cavity. In practice this means that one needs to match and stabilize two degrees of freedom of the cavity in order to operate continuously at maximum enhancement: the repetition rate and offset frequency.

For the cavity length, similar methods as those that are used in stabilizing CW cavities can be employed such as the Pound-Drever-Hall (PDH) technique or the Hänsch-Couillaud (HC) method. The PDH method is based on modulating the lasers frequency and detecting the reflected light from the cavity with a fast photodiode [167]. This signal is mixed down using the modulation frequency and gives rise to an asymmetric error signal, which can be fed back to the cavity to keep it at resonance. The HC method does not require modulation

of the laser frequency. Instead it makes use of a polarization sensitive element inside the enhancement cavity [168]. The error signal is obtained by substracting the signal from two photodiodes looking at the two orthogonal polarization contributions in the reflected beam from the cavity. The HC method is widely used in frequency-doubling cavities, since there the usually Brewster-cut crystal automatically provides a means of filtering the polarization. In our setup we use te PDH method for length stabilization, although it would also be possible to employ the HC technique by utilizing the polarization-sensitivity of the grating mirror under grazing incidence.

Matching the offset frequency of the comb and cavity is achieved by manually adjusting the offset frequency until maximum enhancement is observed. In principle it is possible to also implement a feedback loop for this frequency by deriving PDH error signals from different parts of the spectrum and subtracting them [169]. However, the phase offset of Yb-doped systems is typically quite stable and minor manual adjustments are sufficient to keep f_{CEO} at the desired value. In practice, adjusting the offset frequency every 30 minutes or so is adequate for keeping the cavity on resonance.

A schematic overview of the stabilization setup is shown in Figure 3.19. We use a function generator to apply a 4 MHz modulation signal to an EOM inside the comb oscillator. Since different parts of the spectrum reflected from the cavity might have different offset phases when the cavity offset phase is not exactly matched to the comb, it is desirable to use only a small part of the spectrum for stabilization. Therefore, the cavity reflection is spectrally dispersed by a grating. Part of the spectrum is selected by a narrow slit and subsequently detected by a fast photodiode. A phase detector mixes the photodiode signal with the modulating RF and the output is low-pass filtered to remove the 4 MHz residual. By adjusting the phase of both modulation signals, a clean error signal, shown in Figure 3.21, is obtained, which is subsequently send to a PID controller (STEMLAB 125-10 Redpitaya). This cost-effective single-board computer has two analog inputs and outputs with a bandwidth of 50 MHz steered by an field-programmable gate array and is controlled via web-based applications. The standard PID controller application was further developed and characterized at the PTB, for optimal performance with optical cavities [170]. The 0-2 V output of the Redpitaya is pre-amplified to 8V and subsequently by another factor of 20 using an high voltage (HV) piezo amplifier (PD200 from Piezodrive Pty Ltd). The feedback signal is then fed onto a PZT element behind one of the cavity mirrors.

To avoid resonances between the moving mirror, a bullet-shaped mount was inserted between the mirror and the mirror mount [171], as shown in Figure 3.20. Owing to its high mass and hardness, tungsten carbide was chosen as the material for the bullet mount rather than copper. The ring-shaped PZT element (HPCh 150/12-6/2 from Piezomechanik GmbH) is glued between the half-inch mirror and the bullet mount with Torr Seal epoxy. The PZT has a stroke of 2 μm and can thus change the cavity path length up to 4 μm.

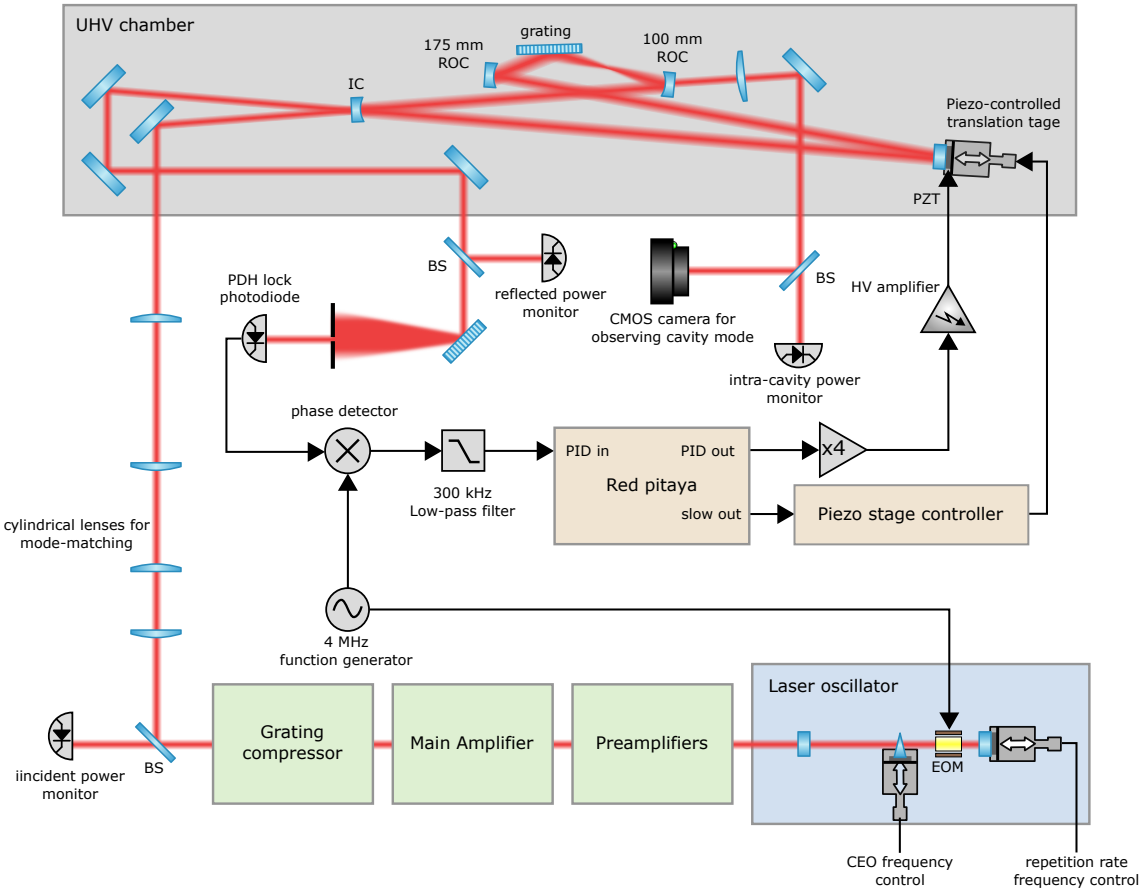

Figure 3.19: Schematic overview of the cavity locking electronics. Modulation is applied to an electro-optic modulator (EOM) inside the laser oscillator. The cavity is placed in an ultra-high vacuum chamber (UHV). Its reflection is spectrally dispersed and a small part is send onto a fast photodiode. The mixed signal is filtered and send to a PID controller. Fast feedback is applied to a piezo-elemet behind one of the cavity mirrors. Slow feedback is fed to a translation stage for compensating slow drifts.

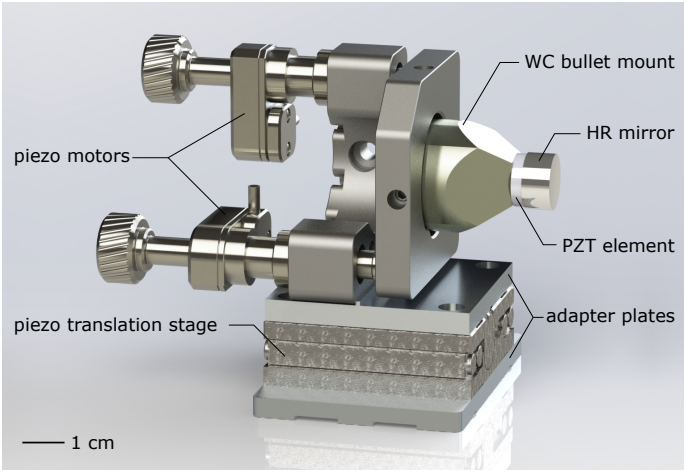

Figure 3.20: Mounting of the mirror for length stabilization of the cavity. The mirror is glued onto a ring-shaped PZT element, which is again glued on a Tungsten Carbide (WC), bullet-shaped mount, fixed inside a stainless steel 1" mirror mount. Two piezo motors can tip and tilt the mirror, thus allowing for alignment of the intra-cavity beam. This assembly is mounted on a piezo-controlled translation stage in order to enabling larger changes to the cavity length.

This is sufficient for locking the cavity at short timescales, but when locking over timescale longer than a few minutes, cavity length adjustments over a larger distance are necessary due to thermal effects changing the alignment and therefore the intra-cavity path length. Also, during set-up and initial alignment of the cavity, having a possibility to change the path length by several millimeters is indispensable since it is practically impossible to place the mirrors such that the cavity length is exactly 3 m. Therefore, the mirror mount is placed on a linear translation stage (Q-545.10U from Physik Instrumente GmbH) with a range of 13 mm and a minimal incremental step size of roughly 400 nm, originating from the slap-stick motion mechanism moving the stage. To prevent the cavity from unlocking when the necessary displacement becomes larger than the PZT range, the linear stage was incorporated in the feedback loop. The Redpitaya PID application was modified to send TTL pulses to the piezo stage controller and induce single steps following the PZT direction [172]. In this way, the continuous locking time of the cavity was improved from a few minutes to many hours.

3.2.4 Alignment

Since the cavity mode, due to its small stability region, is rather sensitive to misalignments of in-going as well as the intra-cavity beam, several alignment mechanisms were implemented in the setup to save time when aligning the cavity. An overview is shown in Figure 3.22. To adjust the distance between the two curved mirrors exactly in the middle

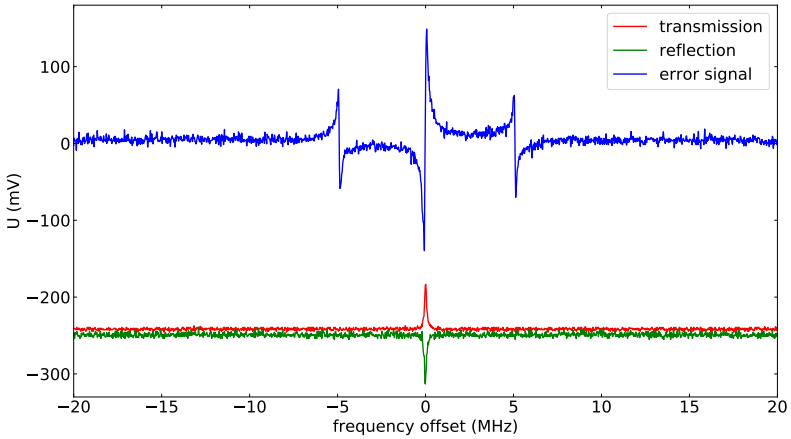

Figure 3.21: PDH error signal used for length stabilization of the cavity. Also shown are the cavity transmission and reflection, peaking exactly at the zero-crossing of the error signal.

of the stability region, the ROC = 100 mm mirror is mounted on a piezo stage with linear encoder (Q-521.24U from Physik Instrumente GmbH), which allows for a precision up to 1 nm. This stage was for instance used for varying the inter-curved-mirror distance in Figure 3.14.

In order to steer the intra-cavity beam while the chamber is evacuated, two of the resonator mirror holders are equipped with piezo motors using the slap-stick mechanism. These are the piezo mirror and input coupler, as the cavity mode has the largest sensitivity to small tilts of those mirrors forming the long arm. These four degrees of freedom can be manually tuned via a piezo controller and a remote controller, such that beam walk in horizontal and vertical direction can be performed. To overlap the in-going laser beam with the cavity mode, two steering mirrors just before the vacuum chamber are used. These adjustment possibilities are sufficient to retrieve optimal alignment on a daily basis and after small misalignments. However, in such a complex overall setup it occasionally happens that the cavity signal is completely lost due to a misalignment of one part somewhere in the beam line. To be able to retrieve the alignment with the cavity mode in such cases without having to open the vacuum chamber, we developed a beam pointing tracking system. Just before entering the cavity, a small part of the in-going beam is picked off and send to a close and far-field camera separated by a lens, uniquely determining the beam position and pointing. Two other cameras are looking at the cavity reflected beam in a similar manner. All four images are shown live in a python application, which can display, fit and store each beam position. In this way, an earlier alignment can be restored by manually adjusting the steering mirrors and IC before the vacuum chamber until the actual beam positions on the cameras overlap with the stored positions.

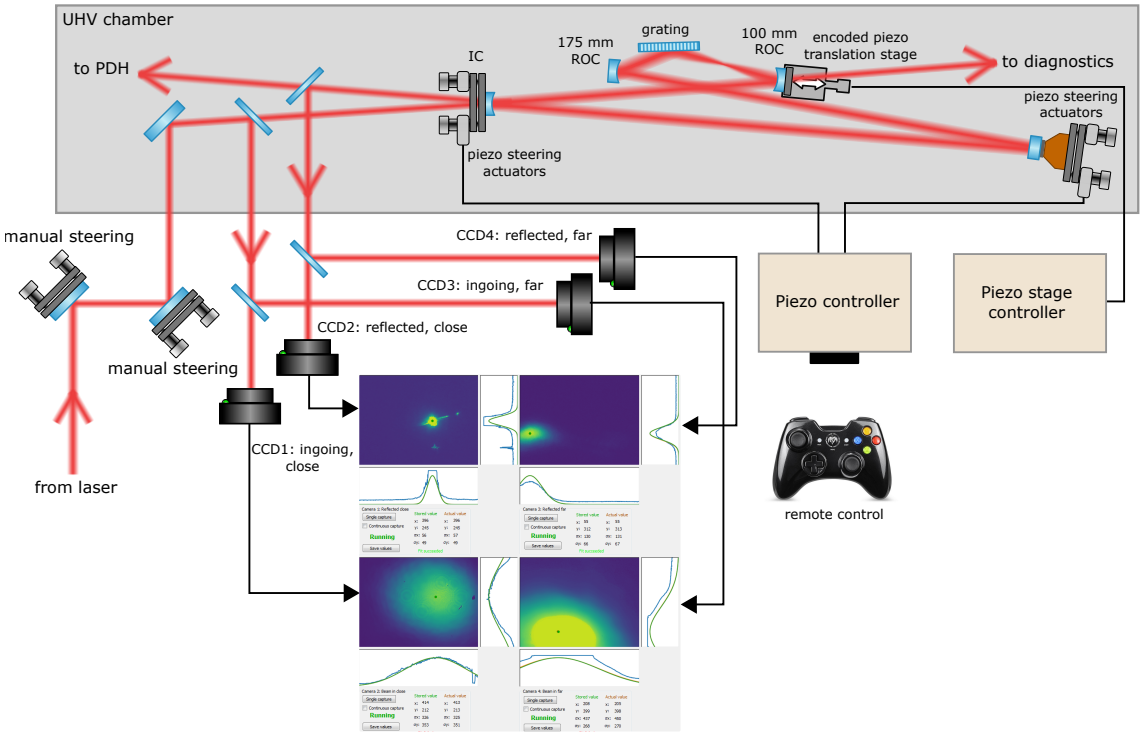

Figure 3.22: Overview of the various tools used for alignment of the cavity. Four cameras uniquely identify the beam position and pointing right before and after the cavity. This information is live displayed and stored, serving as a reference for daily operation. The cavity itself can by aligned using four remote-controlled piezo motors behind two of the mirrors.

3.2.5 Dispersion

As mentioned in Section 2.5, it is important to minimize dispersion from the cavity mirrors in order for all comb modes to be simultaneously enhanced. In order to calculate the effect of dispersion on the intra-cavity pulse, we recall the circulating complex electric field from Equation (2.45), which we now consider as a function of ω:

$$E_{\mathrm{circ}}(\omega) = \frac{\sqrt{1-R_iR_c}}{1-R_iR_c\exp(i\Delta\phi_{\mathrm{cav}}(\omega))}E_{in}(\omega). \tag{3.1}$$

The steady-state relative phase $\phi_{\mathrm{circ}}(\omega)$ of the circulating pulse and the cavity coupling efficiency $\beta_c(\omega)$ can then be determined by taking the argument and absolute value of E_{circ}, respectively [173]:

$$\begin{aligned}\phi_{\mathrm{circ}}(\omega) &= \arg\left(E_{\mathrm{circ}}(\omega)\right)\\ \beta_c(\omega) &= \left|\frac{1-R_iR_c}{1-R_iR_c\exp(i\Delta\phi_{\mathrm{cav}}(\omega))}\right|^2.\end{aligned} \tag{3.2}$$

The cavity coupling efficiency $\beta_c(\omega)$ is defined such that for ideal mirrors without dispersion $\beta_c(\omega) = 1$ at any frequency ω. The amount of dispersion inside the the cavity $\Delta\phi_{\mathrm{cav}}(\omega)$ can be obtained by integrating GDD curves which are usually supplied by the mirror manufacturer.

In our cavity we use Layertec mirrors coated with quarter-wave stacks of alternating SiO_2 and Ta_2O_5 layers. This type of coating generally ensures a low dispersion and high laser-induced damage thresholds (LIDT) with a reflectivity of R = 0.99996 and a GDD $< 0.5\,\mathrm{fs}^2$ over a bandwidth between 1020 and 1060 nm. For the IC mirror, three different coatings of R = 0.993, 0,987 and 0.980, each with a GDD $< 2\,\mathrm{fs}^2$, can be selected to adjust the buildup inside the cavity. The grating mirror is designed to have a very high reflectivity (R = 0.99999) at 75° incidence angle with a GDD $< 2\,\mathrm{fs}^2$, however these values might be slightly higher in practice due to the grating structure etched in the top layer. In Figure 3.23 the dispersion curves of the three different coatings provided by the manufacturer are shown, together with the resulting total intra-cavity GDD for a single round-trip. The black line shows the total cavity round-trip GDD by the data of the input coupler, grating mirror and three high reflective mirrors. Integrating this curve twice yields $\Delta\phi_{\mathrm{cav}}(\omega)$, which is shown in Figure 3.24a).

The circulating steady-state phase $\phi_{\mathrm{circ}}(\omega)$ is shown in Figure 3.24b), for three different input couplers. In Figure 3.24c, the power coupling efficiency $\beta_c(\omega)$ is displayed. Using a higher reflective IC increases the cavity finesse and decreases the bandwidth for which the enhancement is still high. Within the specified range of the mirrors (1020-1060 nm), they perform very well and almost no decrease in efficiency is observed.

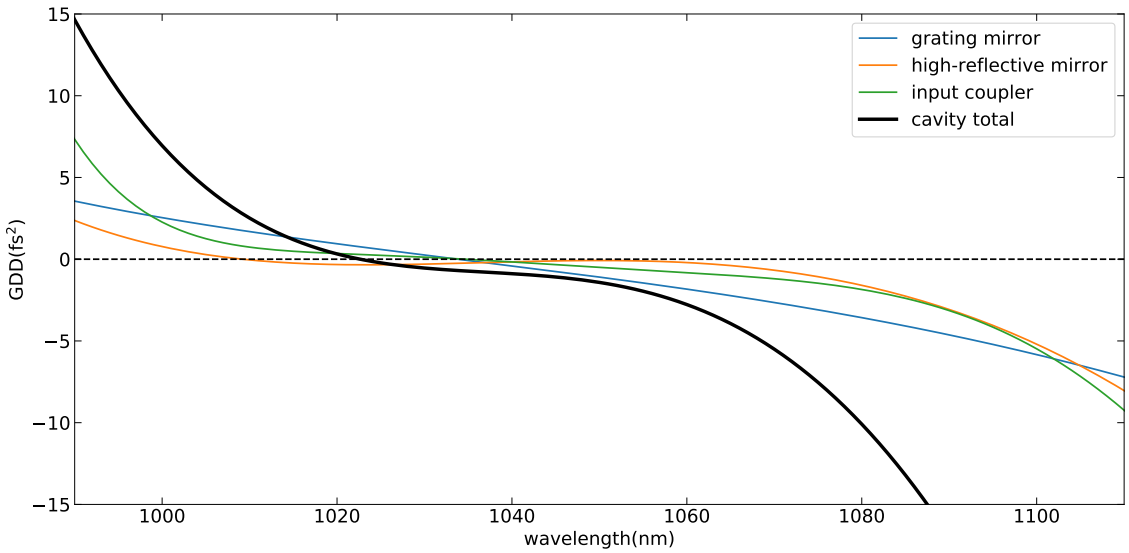

Figure 3.23: GDD of the various mirrors used inside the cavity as provided by Layertec. The input coupler data is taken for the R = 99.3% IC, both other IC coatings show a very similar behavior.

In Figure 3.25, the effects of cavity dispersion with a 99.3% IC on a 50 fs Gaussian unchirped incident pulse with a central wavelength of 1040 nm are shown. From Figure 3.25a), it becomes clear that the whole pulse spectrum is amplified in the cavity. Only a slight difference with the incident pulse arises in the high-wavelength tale of the spectral distribution. The time evolution of the circulating pulse is obtained by a Fourier transform of $E_{\mathrm{circ}}(\omega)$, yielding $E_{\mathrm{circ}}(t)$, which is shown in Figure 3.25. Slight pulse broadening is observed when comparing the incident and circulating pulse.

However, the amount of pulse broadening strongly depends on the incident pulse length since shorter pulses have a larger spectral bandwidth and their whole bandwidth needs to be supported by the cavity in order to efficiently enhance all comb modes. The relative broadening $\tau_{\mathrm{circ}}/\tau_{inc}$ can be found by comparing the width of the circulating pulses with the incident pulse width and is shown in Figure 3.26. Furthermore, the relative overall enhancement efficiency β_{total} for different pulse lengths can be calculated by integrating the coupling efficiency over the pulse spectrum:

$$\beta_{\mathrm{total}} = \int \beta_c(\omega) E_{\mathrm{inc}}(\omega) \mathrm{d}\omega. \tag{3.3}$$

The result is shown in Figure 3.26, again for three different input couplers. For pulses longer than 60 fs, no significant pulse broadening is observed, and the pulse is efficiently coupled into the cavity. For shorter pulses, broadening takes place and the enhancement efficiency drops. It should be noted here that for these simulations, a constant reflectivity

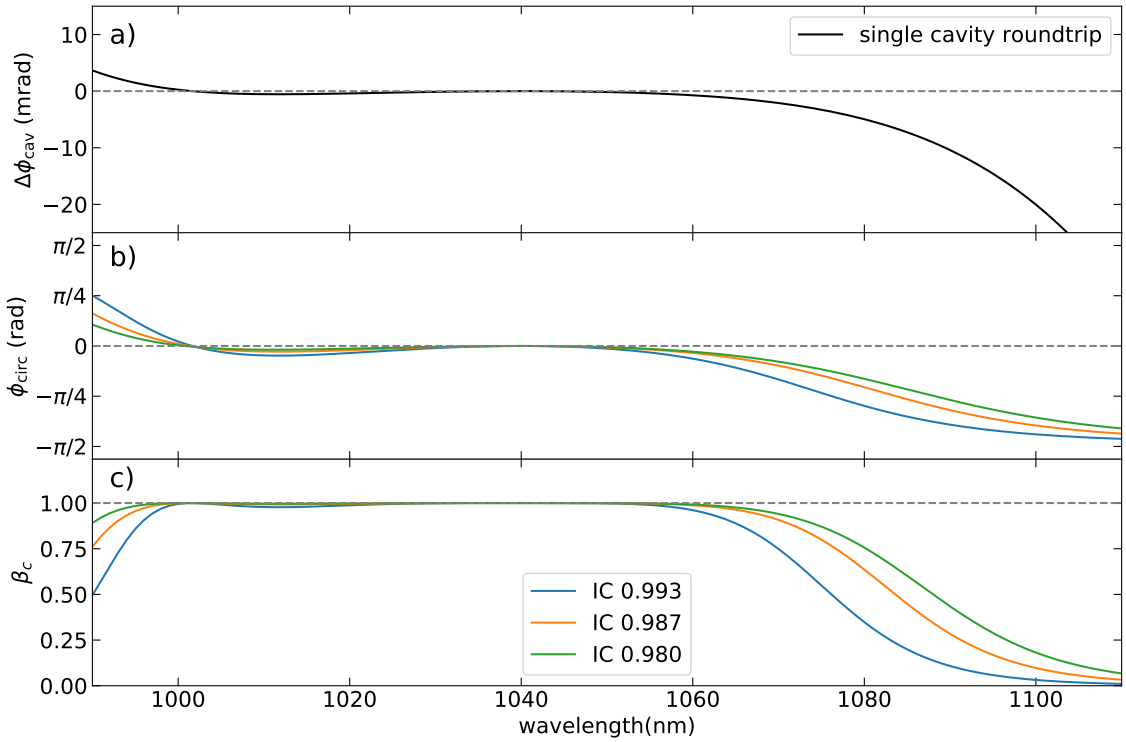

Figure 3.24: Effects of mirror dispersion on cavity phase and coupling efficiency. a) total phase shift as function of wavelength during a single cavity round-trip due to the cavity mirrors. b) steady-state phase shift of circulating pulse for different input couplers. c) enhancement efficiency $\beta_c(\omega)$ as function of wavelength, $\beta_c(\omega) = 1$ for ideal mirrors without dispersion.

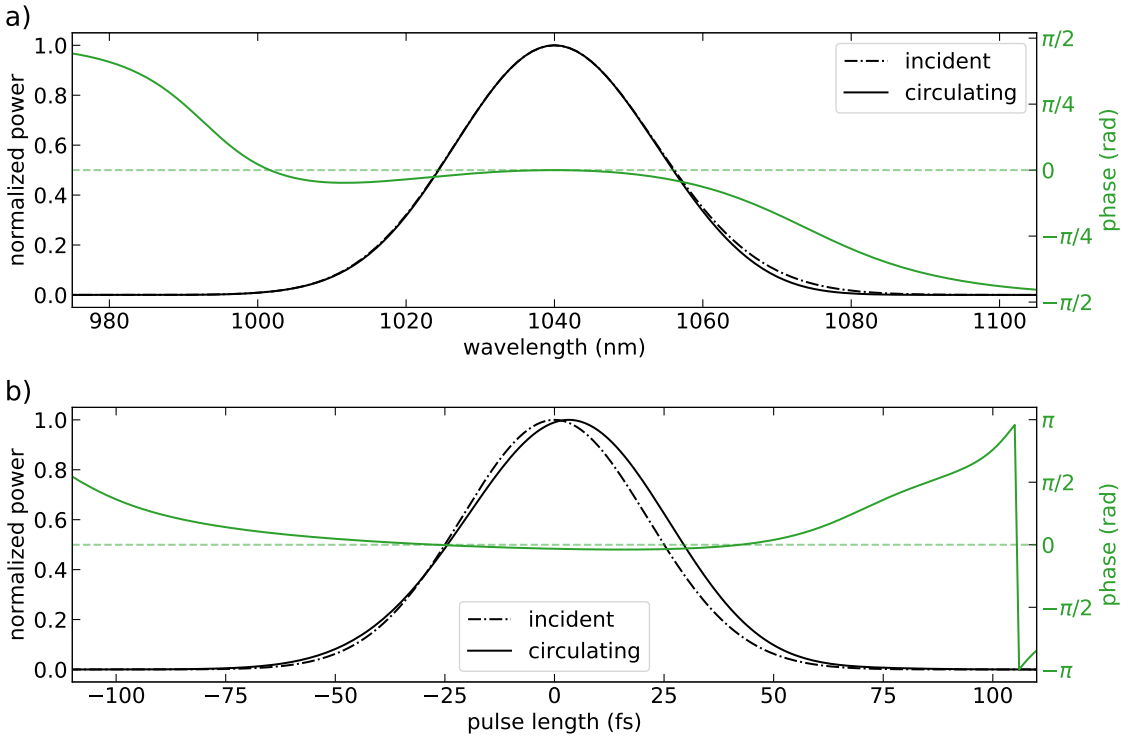

Figure 3.25: Pulse evolution in frequency (a) and time (b) domain for a 50 fs Gaussian pulse, using a R = 99.3% IC. The phase of the circulating pulse is shown in green. Incident pulse envelope (dash-dot) and circulating pulse (line) show almost no spectral and only slight pulse broadening.

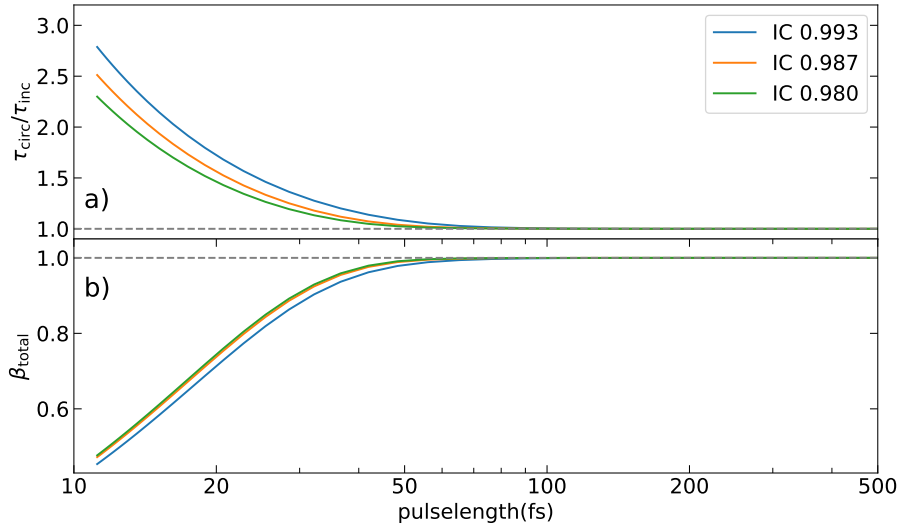

Figure 3.26: Pulse broadening (a) and total enhancement efficiency (b) when varying incident pulse length for different input coupler reflectivities. For pulse lengths below 60 fs, broadening takes place and the enhancement efficiency drops.

was assumed for all wavelengths. In reality the mirror reflectivity drops outside of the specified bandwidth, and the enhancement hence decreases there.

Enhancement cavities for pulses shorter than 60 fs have been demonstrated [174], recently even down to 19 fs [175]. For enhancing such short pulses, a very large mirror bandwidth together with low GDD is required. A high contrast in refractive index of the different layers in the multilayer coating results in a large bandwidth, therefore they use Nb_2O_5 with a refractive index of 2.20 for near-infrared in combination with SiO_2 (n = 1.44). The disadvantage of Nb_2O_5 is that it possesses a lower damage threshold and exhibits higher losses compared to Ta_2O_5, which has a slightly lower refractive index of 2.02. Choosing a coating design therefore involves a trade-off between high LIDT and low losses on the one hand and high bandwidth on the other hand. Since we prefer a robust setup and are not limited by bandwidth anyway, we choose for the former.

In order to measure the amount of dispersion present in the fsEC, several different techniques can be employed [82]. All of them make use of changes in the resonance condition to obtain information about the cavity dispersion. One method involves measuring the cavity length difference for two adjacent resonances. From these changes as function of the wavelength, relative to a reference wavelength, the amount of GDD is inferred [135]. During this measurement, f_{CEO} must be stable, but no locking of the cavity to the comb is required. However, the cavity reflection needs to be split into two spectrally resolved branches, which are both simultaneously monitored by a spectrometer and photodiode. Due to lack of space and limitations of our spectrometer, this method is not most suitable for our setup. In another technique, the cavity is locked using a narrow band of wavelengths within the resonant spectrum, while the comb repetition rate is changed [176]. Due to this difference between FSR and f_{rep}, a narrow feature emerges in the transmitted spectrum. The position of this feature as function of f_{rep} provides information about the cavity phase. In a third technique, the cavity is also locked at a certain wavelength, but now f_{CEO} of the comb is varied [177]. The transmitted spectrum is recorded for various offset frequencies and from this 2D map the intra-cavity GDD can be calculated. For this measurement, it is necessary to know the frequency offset difference for each measurement. Since an f-2f interferometer is attached to our oscillator we can easily measure this quantity and therefore adapt this method to determine the GDD of our cavity mirrors.

The cavity round-trip phase $\Delta\phi_{cav}(\omega)$ from Equation (3.1) can be defined to also include the combs carrier envelope offset phase $\phi_{CEO}^{\mathrm{comb}}$ explicitly [177]:

$$\Delta\phi\left(\omega, \phi_{CEO}^{\mathrm{comb}}\right) \equiv -\phi_{CEO}^{\mathrm{cav}} + \phi_{CEO}^{\mathrm{comb}} + T\omega + \psi(\omega), \tag{3.4}$$

with T representing the round-trip time and $\psi(\omega)$ all nonlinear phase terms. When locking the cavity at a certain optical frequency ω_{lock}, the round-trip phase $\Delta\phi\left(\omega, \phi_{CEO}^{\mathrm{comb}}\right)$ becomes

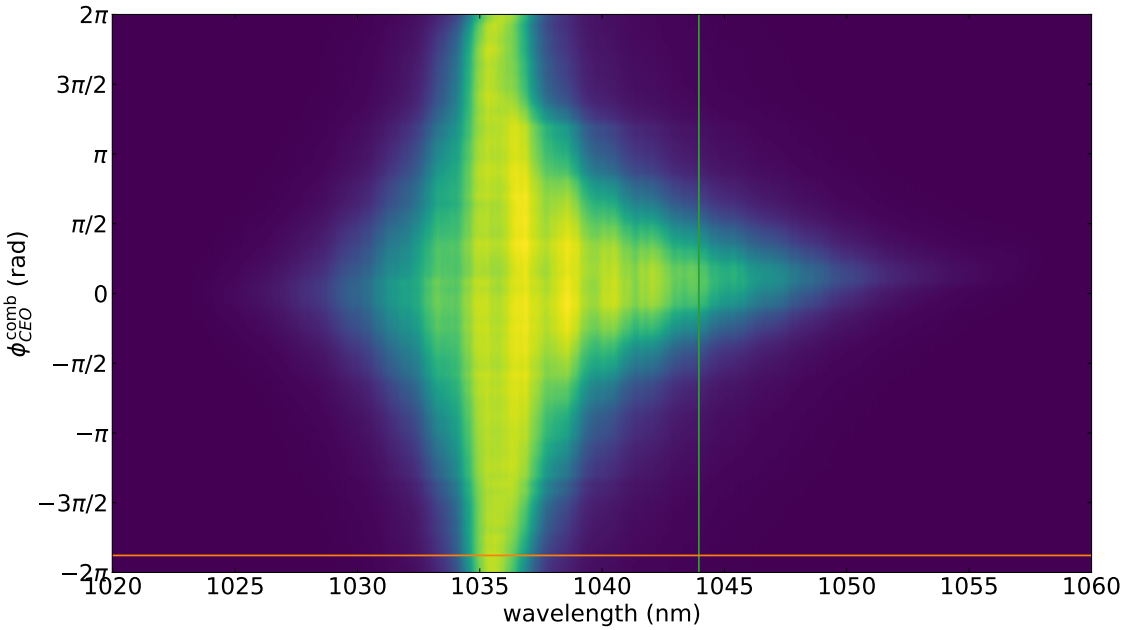

Figure 3.27: Color-coded cavity transmitted spectrum as function of comb offset frequency ϕ_{CEO}^{comb}. The cavity was locked at a wavelength of 1035.6 nm during the measurement, therefore this part of the spectrum is resonant with the cavity for any phase offset. Green and orange lines represent cuts through the 2D-distribution in Figure 3.28 a) and b), respectively.

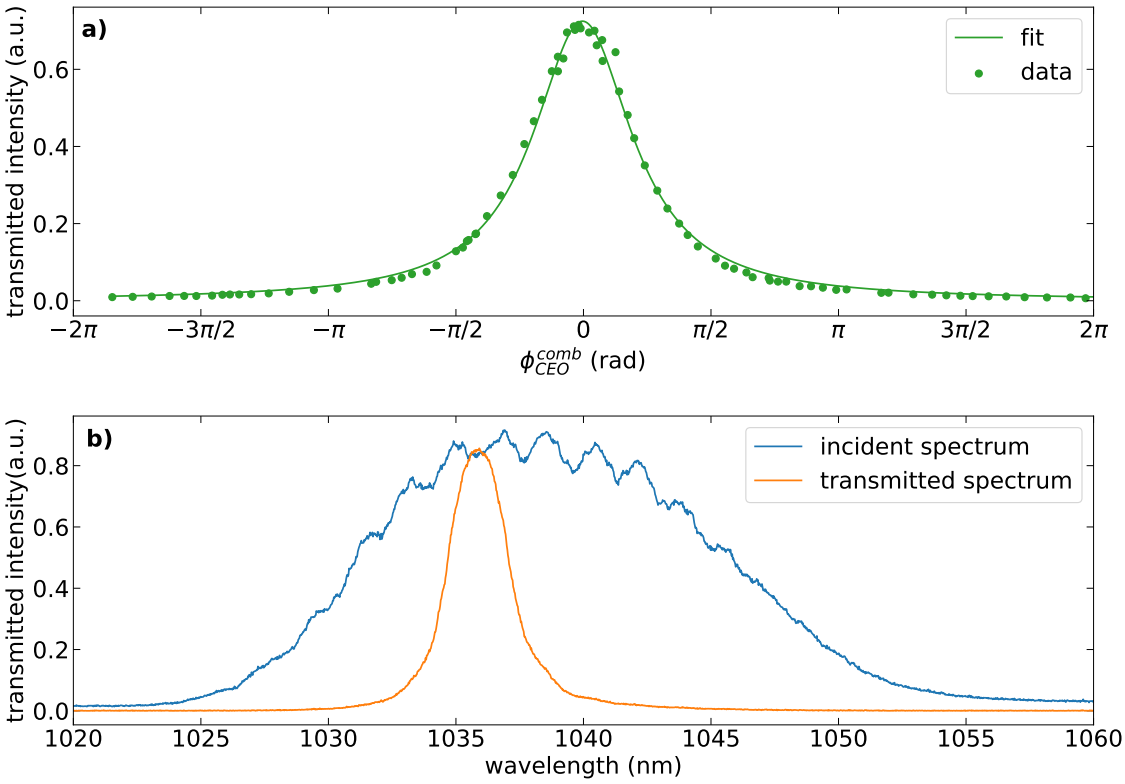

Figure 3.28: a) Transmitted cavity intensity as function of comb offset phase, at a wavelength of 1044 nm. The datapoints correspond to a slice at the position of the green line in Figure 3.27. A good agreement with the fitting model from Equation (3.7) is obtained. b) Comparison of the transmitted spectrum at a large phase offset of -5.9 rad with the incident spectrum. Only wavelengths close to the locking point at 1035.6 nm are resonant in the cavity.

equal to an integer (m) multiple of 2π. Therefore, T can be eliminated from Equation (3.4), resulting in

$$\begin{aligned}\Delta\phi\left(\omega,\phi_{CEO}^{\text{comb}}\right) &= \left(1-\frac{\omega}{\omega_{lock}}\right)\left(\phi_{CEO}^{\text{comb}}-\phi_{CEO}^{\text{cav}}\right)+\frac{\omega\left(2\pi m-\psi\left(\omega_{\text{lock}}\right)\right)}{\omega_{\text{lock}}}+\psi(\omega)\\ &= \left(1-\frac{\omega}{\omega_{\text{lock}}}\right)\left(\phi_{CEO}^{\text{comb}}-\phi_{CEO}^{\text{res}}(\omega)\right).\end{aligned} \tag{3.5}$$

All unknown terms are merged into a single parameter $\phi_{CEO}^{\text{res}}(\omega)$, which then yields the GDD by taking the second derivative

$$\frac{\partial^2\psi(\omega)}{\partial\omega^2}=\frac{\partial^2}{\partial\omega^2}\left(\frac{\omega}{\omega_{\text{lock}}}-1\right)\phi_{CEO}^{\text{res}}(\omega). \tag{3.6}$$

Now by recording the cavity transmission spectrum while changing the comb offset frequency, a 2D color map is obtained, shown in Figure 3.27. The observed intensity is proportional to the intra-cavity electric field from Equation (3.1)

$$I_{\text{trans}}\left(\omega,\phi_{CEO}^{\text{comb}}\right)=\left|E_{\text{circ}}\left(\omega,\phi_{CEO}^{\text{comb}}\right)\right|^2=\left|\frac{\sqrt{1-R_i(\omega)R_c(\omega)}E_{inc}(\omega)}{1-R_i(\omega)R_c(\omega)\exp(i\Delta\phi\left(\omega,\phi_{CEO}^{\text{comb}}\right))}\right|^2, \tag{3.7}$$

such that for each vertical slice through the 2D intensity distribution, a value of $\Delta\phi$ can be fitted for that specific wavelength, as is illustrated in Figure 3.28 a), which corresponds to the green line in Figure 3.27. The width of the visible peak is a measure for the round-trip losses $R_i(\omega)R_c$ caused by the mirrors. The data is fitted using Equation (3.7), with the losses $R_i(\omega)R_c$ and $\phi_{CEO}^{\text{res}}(\omega)$ as free parameters. The fit is performed for many different wavelengths and good agreement between the fitting model and the data is obtained for most fits. In Figure 3.28b), the incident spectrum is compared with a horizontal cut through the 2D intensity distribution at the position of the orange line in Figure 3.27. At such a large phase offset, the cavity is only resonant close to the locking wavelength of 1035.6 nm and a narrow transmitted spectrum is observed.

In Figure 3.29, the resulting measured GDD values are shown. Fast fluctuations in the calculated phase function are amplified when taking the numerical derivative in order to calculate the GDD, therefore a Gaussian filter is used to smoothen the data before differentiating. The resulting GDD is still much larger than the designed values, especially at the wings of the spectrum. This could be due to a reduced singal-to-noise ratio in the wings of the spectrum, as well as the overall rather narrow width of our comb spectrum of 15 nm making the measurement less accurate. Furthermore, the nonzero incidence angles of the cavity optics shift the GDD design curves to a different wavelength range, which then increases the total cavity GDD compared to normal incidence. Although the measured GDD appears to be larger than designed, from Figure 3.27 it becomes clear that there still

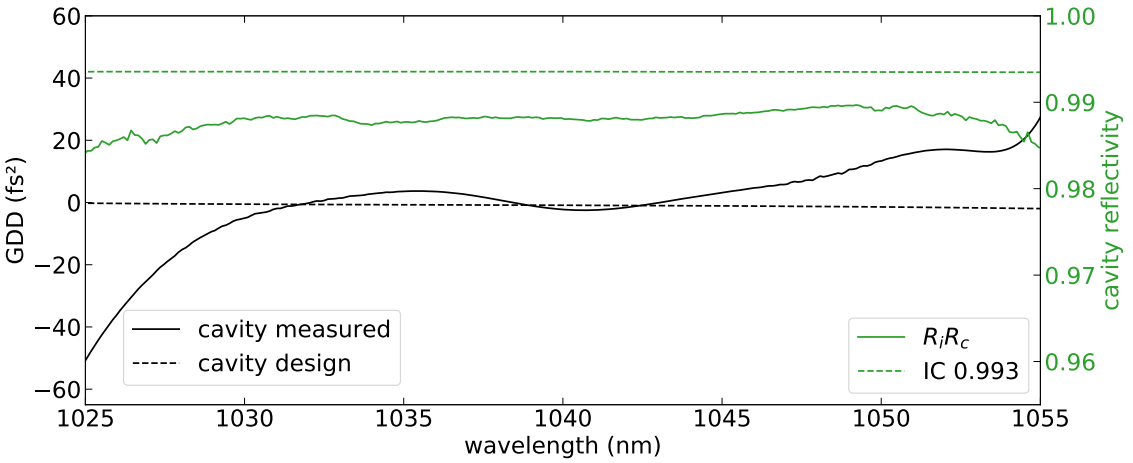

Figure 3.29: Measured cavity GDD and total cavity reflectivity R_iR_c as function of wavelength. The discrepancy between the measured and theoretical cavity reflectivity is most probably due to a damaged mirror coating on one of the cavity mirrors.

is one value of comb offset phase for which the whole spectrum is resonantly enhanced, so cavity dispersion is not limiting the buildup.

From the fitting model in Equation (3.7), the frequency-dependent total cavity reflectivity can be obtained as well, displayed in green in Figure 3.29, together with the theoretical reflectivity of the input coupler. As expected from our mirror design, the reflectivity is rather flat over the range of the incident spectrum, apart for some deviations in the wings. The difference between the measured curve and the input coupler reflectivity represent the additional losses inside the cavity, which in the case of this measurement can be attributed largely to one damaged mirror. The overall flat cavity loss spectrum proves that the mirror reflectivity bandwidth is good enough to enhance the whole comb spectrum inside the cavity.

3.2.6 XUV output coupler

The grating mirror is used to couple the high harmonics out of the cavity due to its ability to spatially separate the different harmonics and its high reflectivity for IR light [160]. This optic acts as a highly reflective mirror for the 1035 nm light, while short wavelengths are diffracted from the grating interface on the surface. The manufacturing of such an optic turns out to be complex, since no single company could produce both the multilayer mirror coating and etch the grating structure. Therefore, first the IR coating was deposited on special substrates suitable for etching by one company (Layertec). Then, the coated substrates were shipped to a second company for patterning the grating structure (Ibsen Photonics) by reactive ion etching. Since the etching process requires calibration of the

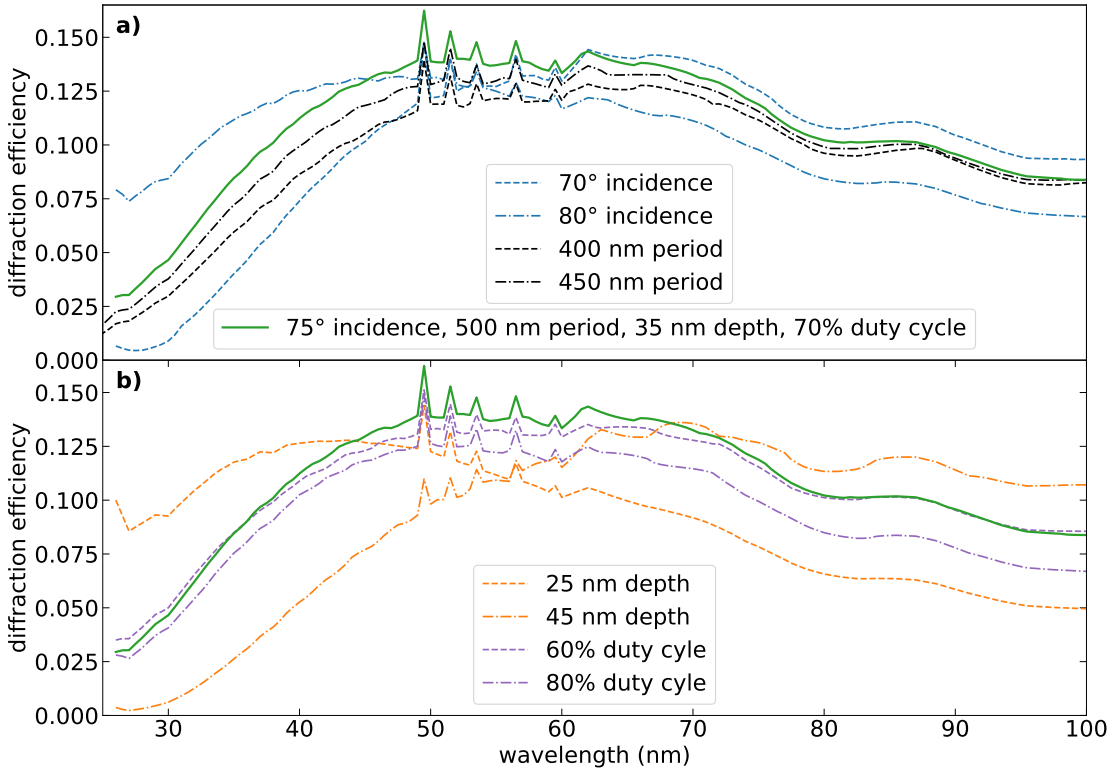

Figure 3.30: Theoretical diffraction efficiency of the grating as function of wavelength. The solid green line represents the efficiency for the final grating parameters, dashed and dash-dotted line show efficiency curves when changing the labeled parameter while keeping all other parameters equal.

machine parameters, thereby wasting the first few coated substrates, producing a few gratings is rather expensive, so the proper specifications need to be carefully determined.

Operation of the grating relies on Fresnel reflections from the vacuum-SiO_2 interface, which become substantial for large incidence angles. Software (PCGrate) was used to simulate the diffraction efficiency for each harmonic. The aim is to find an optimal set of parameters, including angle of incidence, grating period, grating depth and duty cycle, in order to maximize the diffraction efficiency in the minus first diffraction order for wavelengths between 40 nm and 80 nm.

First of all, the diffraction efficiency depends on the incidence angle, as is shown in Figure 3.30a) for three different incidence angles. A larger incidence angle principally results in a higher efficiencies due to increased Fresnel reflection at s polarization. However, at a certain point the efficiency starts to decrease again when an unblazed grating structure is used. This becomes clear from the curves, where the efficiency only increases for short wavelengths at a 80°. Also, the spot size of the IR light on the grating grows with larger

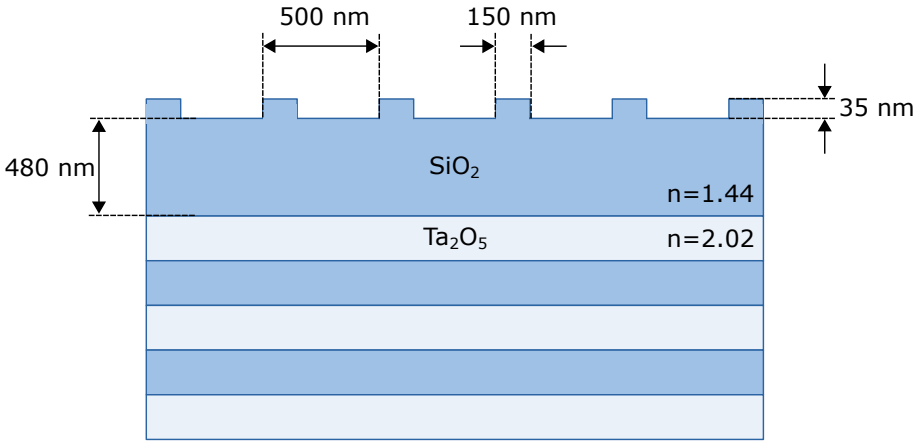

Figure 3.31: Schematic overview of the grating output coupler. The IR mirror consists of a quarter-wave dielectric stack with a thicker top layer. On the surface of the top layer, a grating structure is etched to diffract impinging XUV radiation.

incidence angles and the cavity design becomes very challenging accommodating a very large optic between the focus and the next curved mirror. In the first demonstration of the grating, it was optimized for a 70° angle [160], but by adjusting the cavity design we managed to fit the grating with a 75° incidence angle, for optimal enhancement between 40 and 100 nm.

Second, it becomes clear from Figure 3.30a) that the overall efficiency increases for longer grating periods. However, above 500 nm the IR light also slightly starts to diffract, inducing losses in the zero-order reflectivity. Therefore, the grating period is a trade-off between IR reflectivity and grating efficiency. We choose a period of 500 nm, where the diffraction losses of the infrared are still below 0.0001. Third, the depth of the grating strongly determines which range of wavelengths couple out most efficiently, as becomes clear from Figure 3.30b. A shallower grating favors shorter wavelengths. Finally, the duty cycle can be optimized, which in our case turns out be optimal at 70%, for a depth of 35 nm.

Under the influence of a sub-wavelength grating, radiation can couple to the next layer of the dielectric stack [178]. Since this layer has a higher refractive index than the neighboring layers, it can function as a waveguide, transporting power away from the incident IR light, therefore inducing losses to the cavity. This effect has been observed previously [130] and can be circumvented by doubling the thickness of the top SiO_2 layer. In our case, we set the top layer to be 480 nm thick and have observed no significant IR losses due to the grating.

The optimized parameters resulted in a grating design which is schematically shown in Figure 3.31. The grating is fixed in a special mount attached to a UHV compatible tip tilt mirror mount, and fixed by two teflon rods, as shown in Figure 3.32. In this

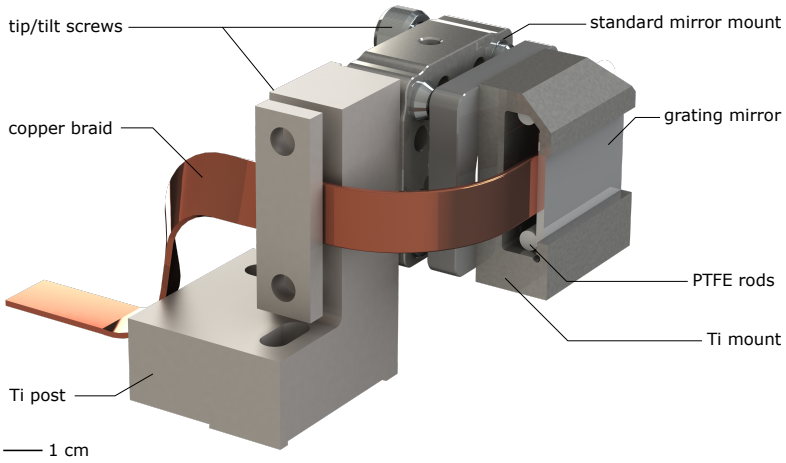

Figure 3.32: Mounting of the grating mirror. The grating is fixed in a titanium mount by small screws through the back of the mount, with PTFE rods to avoid contact between screws and the optic. This mount is fixed on a standard stainless steel mirror mount, such that the titanium mount can be adjusted in height. Heat generated at the grating mirror is conducted away by a copper braid glued to the backside of the optic.

way the grating can be replaced without changing its alignment, which proved to be very useful in practice since the narrow stability region of the cavity makes the position of each optic critical. The grating can also be translated vertically, such that a different spot is hit by the cavity beam, in case one spot becomes damaged or the grooves become filled with carbon molecules, as discussed in the next subsection. A solid custom titanium post holds the mirror in place and allows for maximum space next to and below the grating. Finally, the backside of the grating optic is attached to a $10\,\mathrm{mm}^2$ copper braid, in order to transport away any heat produced by the large circulating laser power impinging on the grating.

3.2.7 Mirror degradation

One of the major limitations of XUV generation inside an fsEC is degradation of the cavity mirrors and outcoupling optic. Under influence of XUV radiation, molecules containing a hydrocarbon chain are cracked and subsequently stick to the closest surface. These molecules will therefore build thin layers on all optics irradiated by XUV light, therefore degrading its optical properties [179]. Since these films are thin, the IR light resonant in the cavity is usually not so strongly affected. However, the grating structure of the output coupler can easily fill up with hydrocarbon molecules, thereby loosing its diffraction function, ultimately resulting in a strong decrease in outcoupled harmonic yield. These problems have been observed in other experiments using enhancement cavities [80, 154, 180], since a long time in the synchrotron community [181, 182] and also more recently in

Mass (a.u.)	Gas	Relative contribution	Background pressure (mbar)	Pressure @ ozone injection (mbar)
2	Hydrogen	100%	$5{\cdot}10^{-11}$	$1{\cdot}10^{-10}$
4	Helium	100%	$<1{\cdot}10^{-12}$	$<1{\cdot}10^{-10}$
14	Nitrogen	12%	$9{\cdot}10^{-12}$	$<1{\cdot}10^{-10}$
15	Hydrocarbon[1]		$2{\cdot}10^{-12}$	$5{\cdot}10^{-10}$
16	Oxygen	18%	$1{\cdot}10^{-10}$	$3.0{\cdot}10^{-6}$
18	Water	83%	$2{\cdot}10^{-9}$	$2{\cdot}10^{-9}$
28	Nitrogen	88%	$9{\cdot}10^{-11}$	$2{\cdot}10^{-9}$
32	Oxygen	82%	$1{\cdot}10^{-12}$	$4.4{\cdot}10^{-5}$
48	Ozone	15%	$<1{\cdot}10^{-12}$	$3{\cdot}10^{-8}$

Table 3.1: Partial pressures of various gases measured with a mass spectrometer. The relative contribution indicates ratio of the intensity of that mass peak to the integrated full ionization spectrum of the relevant gas molecule [185, 186]. [1]The relative contribution depends on the specific molecule.

nano-lithography [179, 183].

Several approaches to tackle this problem are possible. First, by using geometrical output coupling rather than an optic to separate the XUV from the IR light, degradation of the cavity mirrors can be largely avoided. A hole or a slit in the curved mirror directly after the focus can be used, as described in Appendix A. Due to larger divergence of low-order harmonics, there might however still be some degradation of the mirror in the vicinity of the hole or slit. This would then only influence the circulating light and not the XUV output coupling efficiency. Second, non-collinear HHG inside a cavity prevents the XUV radiation from hitting any cavity optic and is therefore probably the best way to avoid of mirror degradation. However, the operation of this out-coupling technique is technically challenging and has only recently been shown in a fsEC [156, 184].

Since we have chosen to use the grating mirror output coupler we have to minimize the amount of degradation on its surface. The most obvious means to do so is to prevent hydrocarbon molecules coming close to the optic at all. By cleaning every component before it is installed inside the vacuum chamber, and using UHV-compatible materials, we keep the amount of carbon molecules in the chamber as low as possible. This also involves wearing clean-room clothing to prevent contamination while the vacuum chamber is opened. In this way, we reach a nominal background pressure of $3{\cdot}10^{-8}$ mbar in the main vacuum chamber. A mass spectrometer (MKS Instruments) is used to monitor the amount of various gases present in our chamber. By measuring the abundance of different ionized molecule constituents, approximate partial pressures of molecular species can be inferred and are shown in Table 3.1. It becomes clear that the main pressure is mostly limited

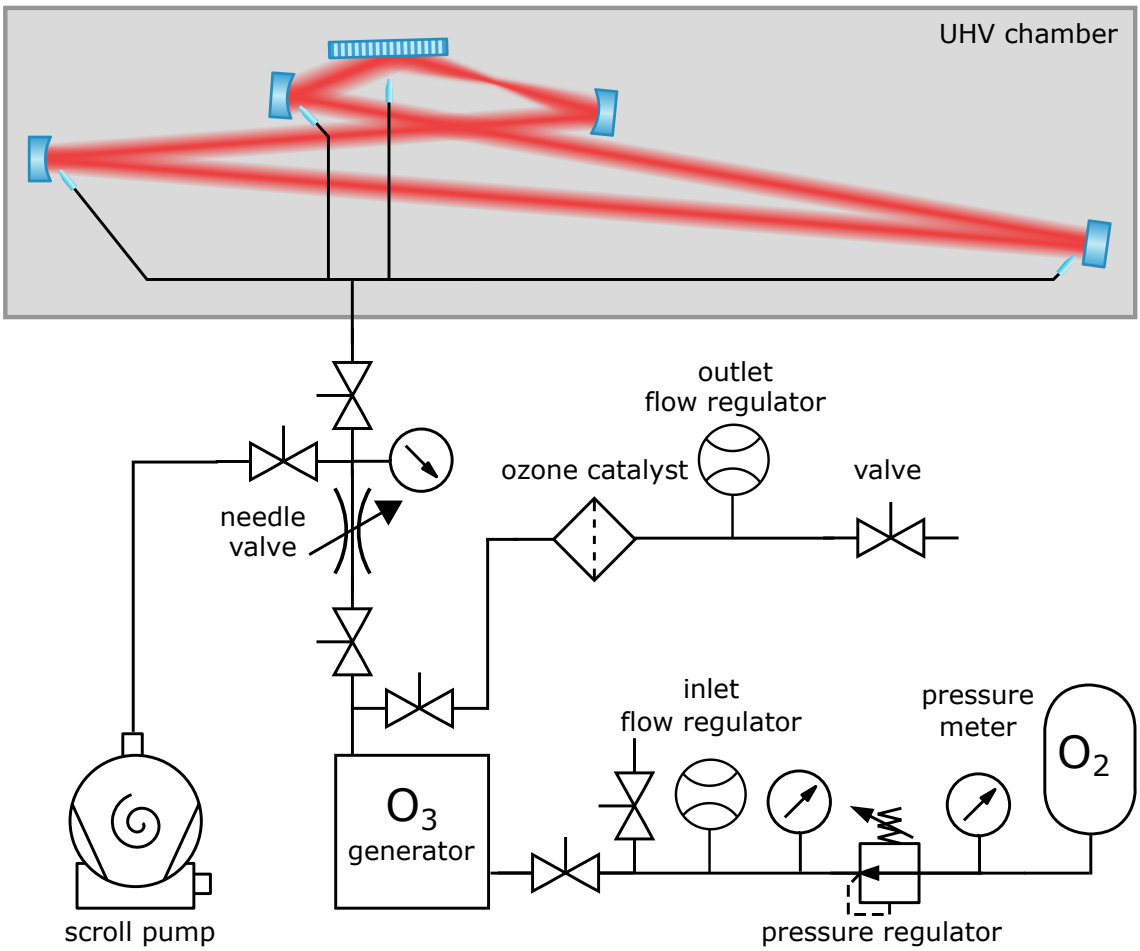

Figure 3.33: Schematic overview of the ozone injection system. The pressure from an oxygen bottle is reduced and a regulated flow is fed to the ozone generator. With a needle valve, the amount of O_3:O_2 mixture send to the nozzles in the vacuum chamber can be adjusted. Residual ozone is removed by a catalyst before the exhaust.

by water vapor, which is evaporating from the large surfaces of the vacuum chamber. The abundance of hydrocarbon molecules is at the 10^{-12} mbar level, and should therefore improve the lifetime of our mirrors significantly compared to systems operating in the high vacuum range.

Although avoiding hydrocarbon contamination will definitely help, there is no guarantee that after a long XUV exposure time, the grating will not get dirty eventually. We have therefore also installed an ozone injection system to be able to clean the grating and other cavity mirrors during operation. Using highly reactive ozone is a well-known trick to remove surface contaminants by oxidization [187], also employed in other XUV comb experiments [80, 82, 154, 157]. An overview of this setup is shown in Figure 3.33. High-purity oxygen from a bottle is fed to an ozone generator (Ozotech Poseidon 220) with

a pressure slightly ($\sim 200\,\mathrm{mbar}$) above atmosphere, specified to generate $\sim 2\%$ ozone at a flow rate of 0.5 l/min. The flow towards the cavity mirrors is regulated by a needle valve, while the remainder is filtered by an ozone-destroying catalyst (CARULITE 200) to prevent the toxic gas from escaping through the exhaust. Four nozzles with a $400\,\mu\mathrm{m}$ diameter are pointing towards the grating mirror and three consecutive cavity mirrors, supplying the most critical elements with a constant flow of the O_3:O_2 mixture. A scroll pump is connected to clear the tubing from residual gases prior to operation.

The amount of ozone present in the chamber during injection can be monitored with the mass spectrometer, as is shown in Table 3.1. Taking into account the relative contribution of the oxygen and ozone mass peaks leads to an ozone pressure of $2{\cdot}10^{-7}\,\mathrm{mbar}$ and $5{\cdot}10^{-5}\,\mathrm{mbar}$ for oxygen. This implies a mass ratio of $\sim 0.6\%$, which is slightly lower than what the generator is specified for, possibly due to the 5 m long tubing with a small diameter between the ozone generator and the nozzle outputs. Also, the mass spectrometer is located $\sim 0.5\,\mathrm{m}$ from the closest nozzle, so the local ozone concentration at the mirror surface might be higher than measured. Raising the oxygen pressure by opening the needle valve increases the ozone pressure further, but was limited here by the maximum operating pressure of the mass spectrometer ($10^{-4}\,\mathrm{mbar}$), whereas normally we operate at oxygen pressures around $10^{-3}\,\mathrm{mbar}$.

3.3 Vacuum system

For the simple reason that XUV radiation is strongly absorbed by air, a vacuum environment is obligatory for any HHG system. In the case of generating harmonics inside a cavity, the requirements of the vacuum system are more stringent compared to single-pass HHG. First of all, the dispersion and non-linear behavior of air are a problem for operating the cavity at high powers and turbulence causes additional distortions to the effective cavity path length. Moreover, as mentioned in Section 3.2.7, hydrocarbon molecules can contaminate the cavity optics under influence of both XUV and high power IR radiation. An UHV cavity environment reduces the abundance of such molecules by many orders of magnitude and therefore avoids mirror degradation problems. Furthermore, since the aim of this experiment is to deliver XUV radiation to HCI in a cryogenic Paul trap, the cavity vacuum chamber needs to be connected to the ion trapping chamber. To not spoil the vacuum at the ion location, with pressures in the range of 10^{-14} mbar, we need to start off with a UHV pressure and use differential pumping stages to bridge the remaining pressure difference. For certain wavelength ranges it is possible to use a thin window, for instance aluminum with a transmission between 20 eV and 73 eV, to separate both pressure regions, but since we want to be able to use any of the harmonics for spectroscopy, we prefer not to be limited by the transmission of such a window. Moreover, these windows are generally very thin for minimal XUV losses and therefore very fragile, meaning that the slightest pressure difference could cause a rupture. Using them as a wall between different regions of pressure is therefore far from ideal. For these reasons it is necessary to operate the whole fsEC inside an UHV environment.

Constructing such a large optical system completely inside a vacuum chamber requires a large chamber and a lot of planning and construction. The breadboard supporting the optical elements needs to be rigidly mounted on the optical table to avoid alignment instabilities, but at the same time needs to be decoupled from the vacuum chamber to avoid vibrations from the turbomolecular pumps on the optical elements. All alignment and positioning of optics inside the vacuum that need to be regularly changed have to be remote-controlled via vacuum-feedthroughs. Moreover, all parts installed in the chamber need to be UHV-compatible and cleaned. This sections starts with a description of the titanium rod structure, on which the optics in the vacuum are mounted. Subsequently, the large UHV chamber surrounding the rod structure is presented. Finally, the differential pump system for removing gas from the high-pressure region in the cavity focus is discussed.

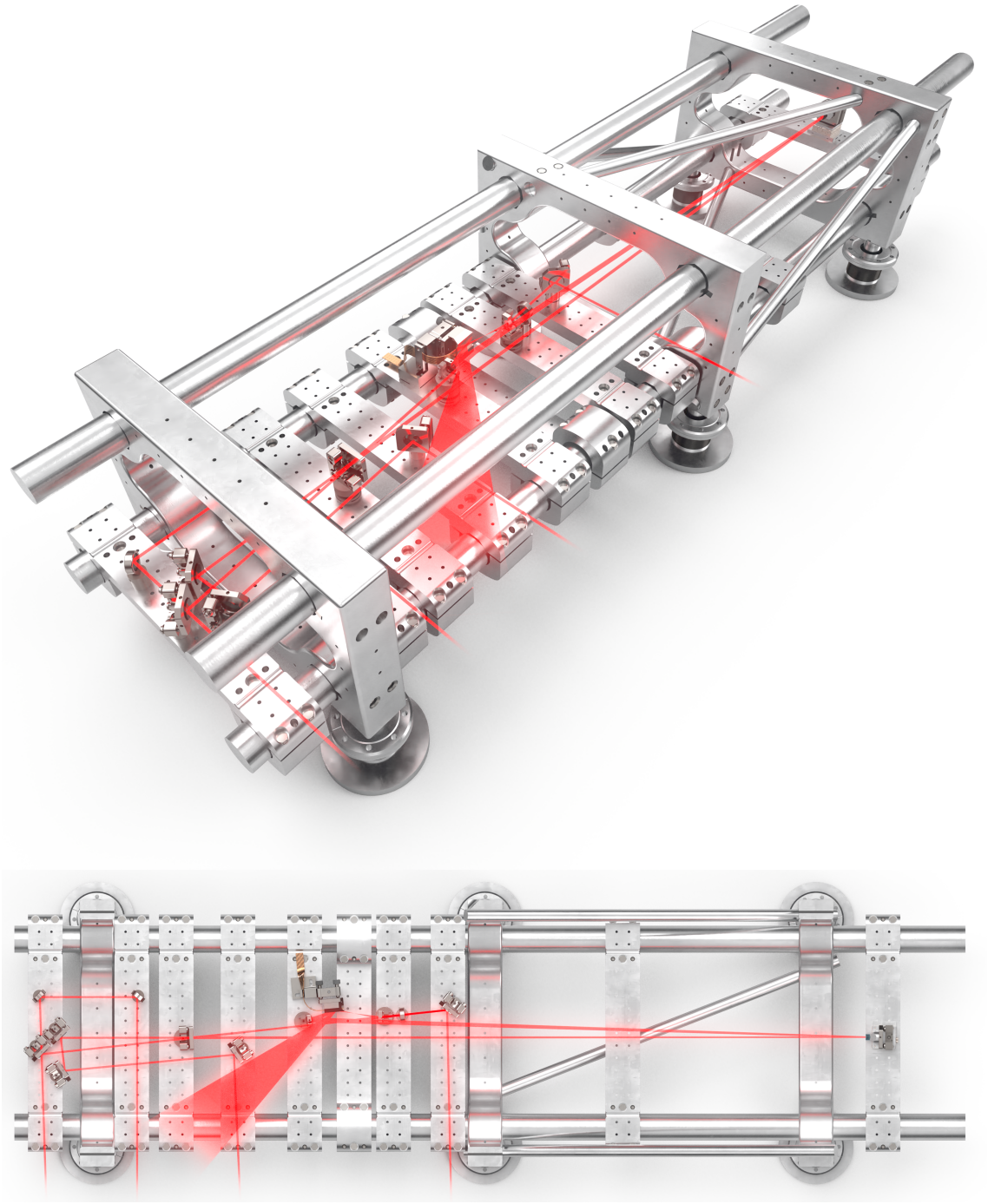

Figure 3.34: Overview of the titanium rod structure, 3D and top view. Three monolithic supports hold four massive rods, on which bridges can be mounted. Optical elements are fixed on these bridges functioning as optical tables that are removable and adjustable in position, but tightly attached to the rods. Diagonal slabs fix the rotational degree of freedom. The structure is supported by six feet, which are resting directly on the optical table.

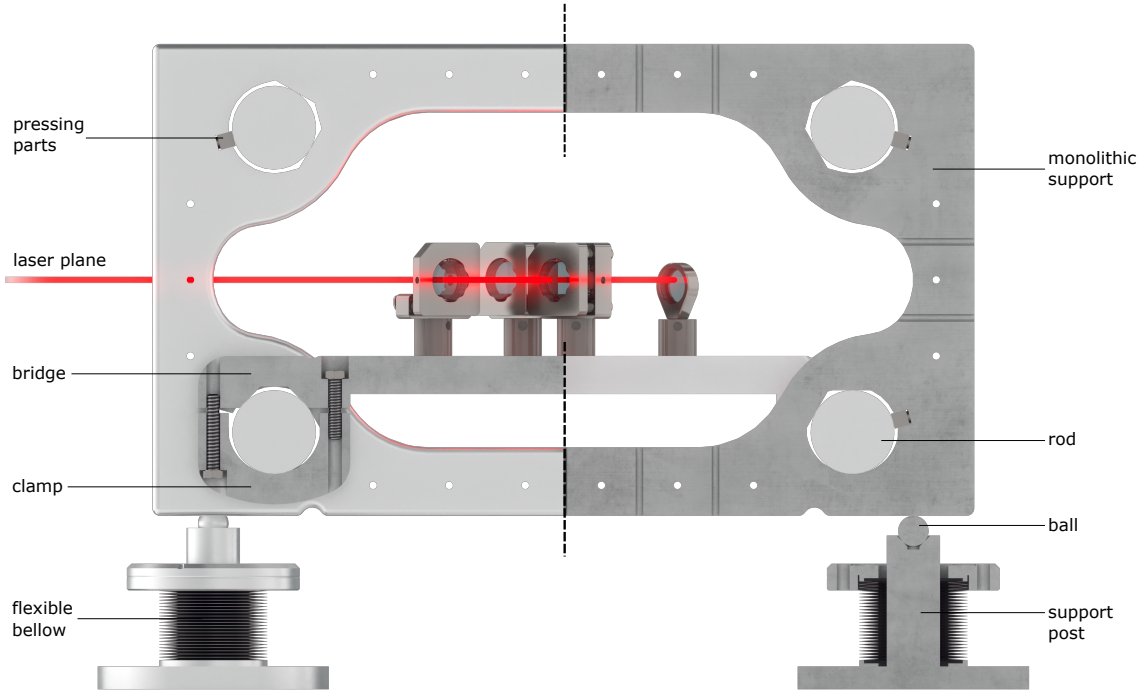

Figure 3.35: Front view of the rod structure. The monolithic supports are designed for maximum laser access at a height of 50 mm from the bridges, exactly between bottom and upper rods. Two clamps firmly press each bridge onto the supporting rods, which are fixed into the monolithic supports. The whole structure rests via steel balls on supporting posts, which are connected to the vacuum chamber by flexible bellows.

3.3.1 Titanium rod structure

Most optical setups use a large breadboard perforated with many threaded holes for fixating the position of all optical elements. When putting such a breadboard in vacuum, the large number of threaded holes impairs the vacuum pressure since air and contaminants hidden in these holes are pumped away only very slowly. For reaching the best pressures, it is desirable to design all parts in the vacuum as 'open' as possible, thus avoiding large surfaces and spaces not well connected to the rest of the chamber, to stimulate efficient pumping. The rod structure that we have designed therefore consists out of a number of smaller optical tables, which can be positioned at below the optic locations, leaving the space where no optics are required largely empty.

The long arm of the cavity has a length of almost 1.5 m, while the cavity path length should be stable to a fraction of the IR wavelength, meaning less $\ll 1\,\mu$m. The fractional stability of the cavity length thus needs to be on the order of $\sim 10^{-8}$, which is a very small number for such a macroscopic mechanical system. Of course the piezo-element follows small deviations of the cavity length in the μm regime by a feedback loop described in Section 3.2.3, but a mechanically stable mounting structure minimizes the need for such corrections and lowers the requirements for the feedback loop. To reach maximum intrinsic stability, the optical axis is placed close to the central axis of the mounting structure. In this way, vibrations and length variations of parts of the structure have a minimal influence on the optical path length. By introducing symmetry to the mounting structure, the cavity length becomes less sensitive to accelerations [188]. These principles are also used in the design of ultra-stable reference cavities for laser stabilization to a fraction of a Hz [189–191]. This type of cavities all have a Fabry-Perót geometry, different from the bow-tie design of our cavity, but the same idea still applies to the long arm of our fsEC. We have therefore chosen for a design with four massive rods ($\varnothing$ 55 mm) surrounding the optical axis of the cavity. The rods are held in place by three monolithic supports. Having these made from one piece of material allows for a maximum strength and precision in mounting the rods and avoids air-pockets between different parts pressed together. Diagonal slabs interconnecting two of the supports fixate the rotational degree of freedom of the structure. The inner part of the supports is mostly removed to provide maximum space for laser beams in the horizontal plane exactly between the bottom and top set of rods. An overview of the rod structure is shown in Figure 3.34.

The overall size of the rod structure was chosen such that, apart from the cavity described in this thesis, there is enough space to accommodate a second cavity, which can for instance be used for further MPI experiments, or for generating harmonics in a different energy range using a different coupling method. The dimensions of the accessible laser plane are 460 mm $\times$ 1925 mm, resulting in almost one square meter of space for

optical elements inside the vacuum, shown as front view in Figure 3.35. Rigid bridges can be attached to either the bottom or the top pair of rods, serving as optical tables on which the optics can be mounted, with a 50 mm beam height. These bridges can also be mounted upside down, increasing the distance to the optical axis to 125 mm. This is for instance necessary to make room for the translation stage of the differential pump system described in Section 3.4. The bridges can be installed at arbitrary positions and removed while the rod structure stays in position in the chamber. This allows for a large flexibility in installing optics, detectors, electrodes or other devices at any location in the chamber for dedicated experiments using either the IR or XUV light. Solid spheres are placed in a conical hole in the top of the supporting posts shown in Figure 3.35, on which the rod supports rest. One conical hole and one V-groove drilled in two of the supports uniquely define the horizontal position of the rod structure, the other four spheres serve just as vertical support.

The rod structure material determines its main properties, of which thermal expansion, strength, weight, vacuum compatibility and machining possibilities are the most relevant for this work. To minimize thermal drifts of the cavity length, it is desirable to use a material with a very low thermal expansion coefficient. The aforementioned ultra-stable reference cavities typically use ULE (ultra-low expansion glass, from Corning Incorporated) or recently also a single crystal of silicon [189]. These materials are however very hard to machine and handle and it is nearly impossible to fabricate the rod structure solely out of such material, let alone the costs. Using different materials for the rods and the rest of the structure would be possible, but adds a lot of complexity to the interfaces where two materials with different thermal expansion coefficients meet. Materials such as stainless steel or tungsten carbide come with a high stiffness (Youngs Modulus of 193 Gpa and ~ 500 Gpa, respectively), reducing the sensitivity of the cavity length to environmental vibrations [189]. However, they also have a very high density (8000 kg/m^3 and 15.000 kg/m^3, respectively), which would result in a very heavy rod structure, complicating handling and support requirements. Titanium (grade 5) has a significantly smaller thermal expansion coefficient (9 μm/K) than both 316 steel (16 μm/K) or aluminum (23 μm/K), while still possessing a high stiffness (modulus of 119 Gpa) and low density (4420 kg/m^3). Moreover, machining of titanium is not an issue and with computer numerical control (CNC) pocket milling and wire erosion, all parts of the structure can be produced with a very high precision. Finally, titanium exhibits a good UHV compatibility and is non-magnetic.

3.3.2 Vacuum chamber

To accommodate the titanium rod structure, a custom vacuum chamber tailored to the needs of the experiment was designed. Rather than a cylindrical shape, as is typical

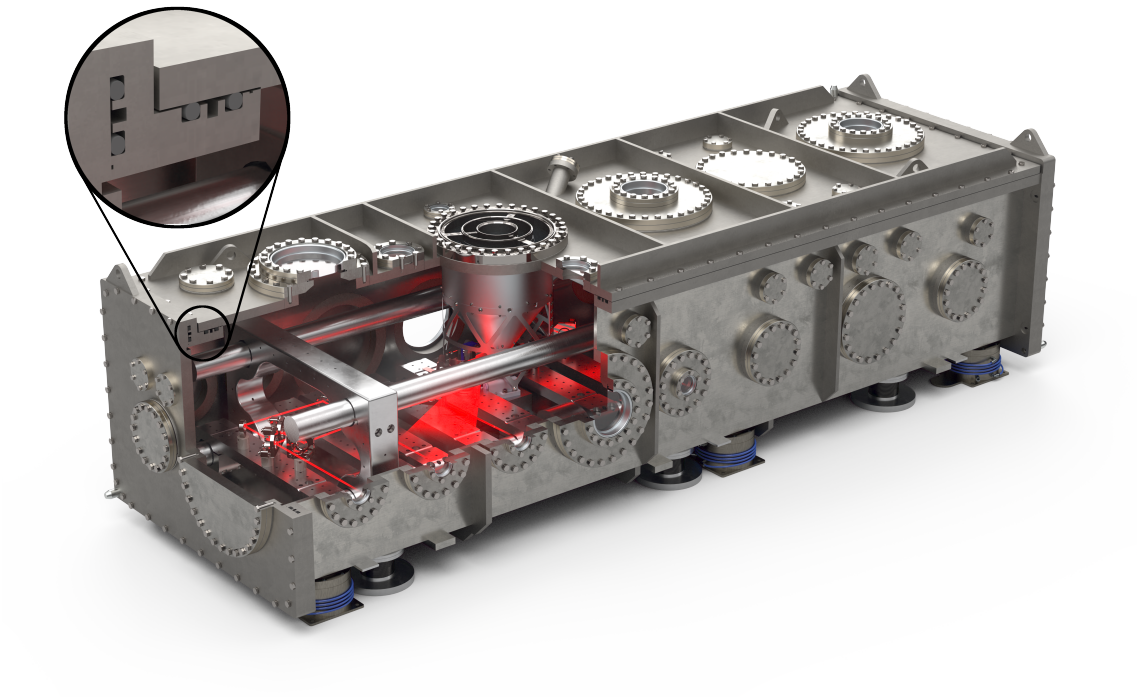

Figure 3.36: Overview of the vacuum chamber, consisting of a main body, a large top lid and two side lids. The lids are sealed with double FKM rings, between which a a third groove can be separately pumped. Alternatively, a small groove for sealing with indium is available. Optical access is provided by many flanges at laser height.

for vacuum systems to resist atmospheric pressure, the chamber is rectangular-shaped to exactly fit the rod structure, and waste minimum space on the optical table. This means the walls need to be either sufficiently thick or reinforced to prevent them from bending. A small amount of bowing is in principle not a an issue for metal flanges when no equipment is attached to the flanges, however it becomes dangerous when view-ports are attached since they might break due to bending forces during evacuation, causing catastrophic damage to the turbopumps. Therefore, the chamber is build of 10 mm stainless steel walls, reinforced with perpendicular slabs at regular distances. An overview of the vacuum chamber is shown in Figure 3.36.

The rod structure can be inserted and accessed in the vacuum chamber either through the top flange, covering the whole upper side of the chamber, or through the two side flanges on the long ends. This comes with the additional advantage that new flanges can be designed with a different pattern of holes for adaptation to future needs, without replacing the whole chamber. The flanges all have a thickness of 20 mm and the top one is additionally reinforced for supporting heavy equipment such as turbopumps.

Copper gaskets (ConFlat, CF) seal all standard flanges of the chamber to reach UHV pressures. For the three large flanges however, copper sealing would be expensive and complicated to handle. Therefore, these are sealed with FKM O-rings, which perform well up to a pressure of 10^{-8} mbar. To avoid the O-rings limiting our vacuum pressure, two of them are used for each flange. The space between both rings is can be pumped by a separate pump via many small canals through the vacuum chamber side of the flange. Standard quick release flange ("kleine Flansch", KF) parts are glued the vacuum chamber at the exit of each canal, interconnected with bellows and leading to a scroll-pump. This sealing method ensures a good final pressure while still being able to easily open and close the flanges. When frequent re-opening is no longer necessary or a better sealing is required, there is also the possibility to remove the O-rings and seal with indium in a tiny groove next to the O-ring grooves.

To provide optical access to the optics inside the chamber, a large number of CF flanges are positioned in the horizontal laser plane. For electrical feedthroughs controlling the experiment, many CF 40 flanges are added at a different height. The lid contains several large flanges for connecting turbomolecular pumps with a high pumping speed. Large flanges are also present exactly above, below and to the sides of the cavity focus to allow for the installation of the vertical differential pumping system and its alignment. Three more angled CF 40 flanges are also aligned exactly towards the focus region and can be used for observation or manipulation equipment.

One of the main challenges when setting up a cavity inside a vacuum chamber, are vibrations on the cavity mirrors originating from the turbopumps. In principle one could use a different type of pump without moving parts, for instance getter pumps or diffusion

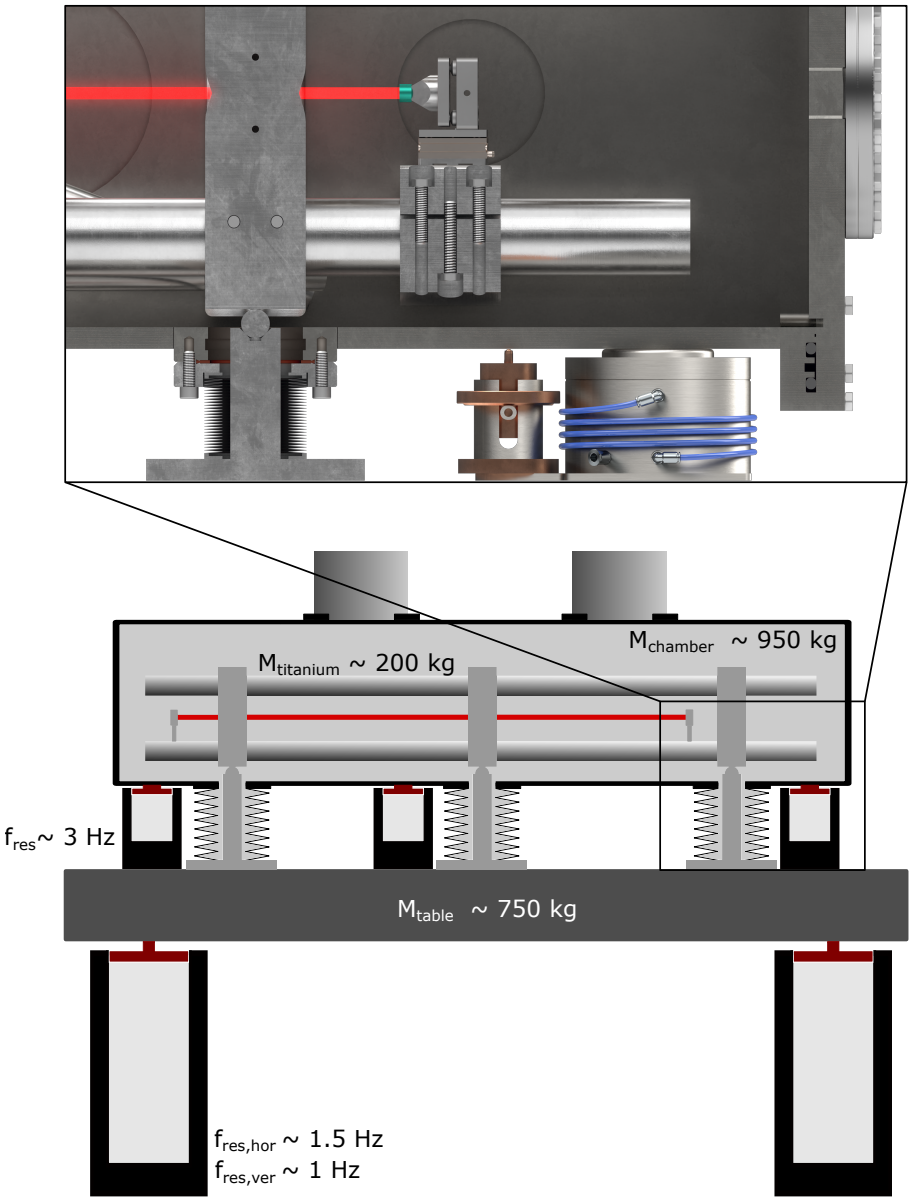

Figure 3.37: Schematic overview of the vacuum chamber and rod structure. The structure with the optics rests on solid feet which are directly attached to the optical table. The vacuum chamber is connected to the feet by means of flexible bellows, and is supported by pneumatic vibration isolators to damp vibrations originating from turbomolecular pumps on top of the chamber. The table itself is also isolated from vibrations by a set of isolators, which have a resonance frequency different from the feet of the vacuum chamber to avoid undesired couplings [192]. The inset shows a detailed view on one of the vibration isolators and its sensor.

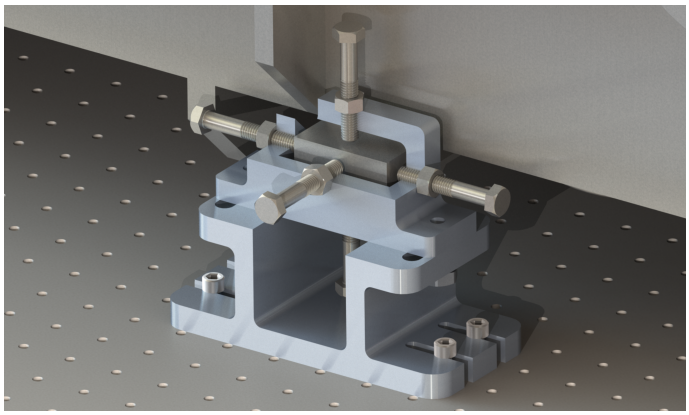

Figure 3.38: Assembly for limiting the vacuum chamber movement. A steel slab welded to the chamber sticks out and is surrounded by bolts. The movement margin of the vacuum chamber can be set for each direction by adjusting the bolts screwing depth through the aluminum assembly (cut for better visibility of the bolts) and fixating its position with the countering nut.

pumps. However, for the high gas load imposed by the HHG and ozone nozzles such pumps are not suitable and the use of turbopumps can not be avoided. To minimize disturbances of the cavity, the optical elements need to be mechanically decoupled from the turbopumps. One possibility is using bellows between the pumps and the vacuum chamber and support the pumps directly from the wall or floor. In the tight space of our lab, there is no room for such constructions, which is why we have implemented a decoupling between the vacuum chamber, with the pumps directly attached, and the optical table. As shown in Figure 3.37, the chamber is resting on air-lifted pistons (BIAIR 0,5-EDSTAHL/T-SO, Bilz Vibration Technology AG). The rod structure containing all optics is supported by its own solid feet, standing directly on the optical table. These feet and the vacuum chamber are connected by flexible bellows. In this way, the vacuum chamber is floating freely around the optical setup, additionally functioning as a low-pass filter due to its large mass (950 kg). The optical table is isolated from environmental vibrations by six large pistons (S-2000A-628, Newport Spectra-Physics GmbH). To avoid cross-talk between both sets of isolators, the resonance frequency of the smaller pistons (3 Hz) is chosen to be different from that of the large cylinders (1 Hz).

While the vacuum chamber is lifted by the pistons, it can in principle freely move in all directions. In practice the horizontal margins for movement are small and the pistons only allow a large room to move in vertical direction. The vacuum chamber can therefore be tilted, before the pistons restore the original position by changing their pressure accordingly. However, during this movement, which can be induced by a person accidentally touching the chamber or when new parts are added, the vacuum chamber could collide with delicate parts of the setup, such as the shields of the differential pump system, as

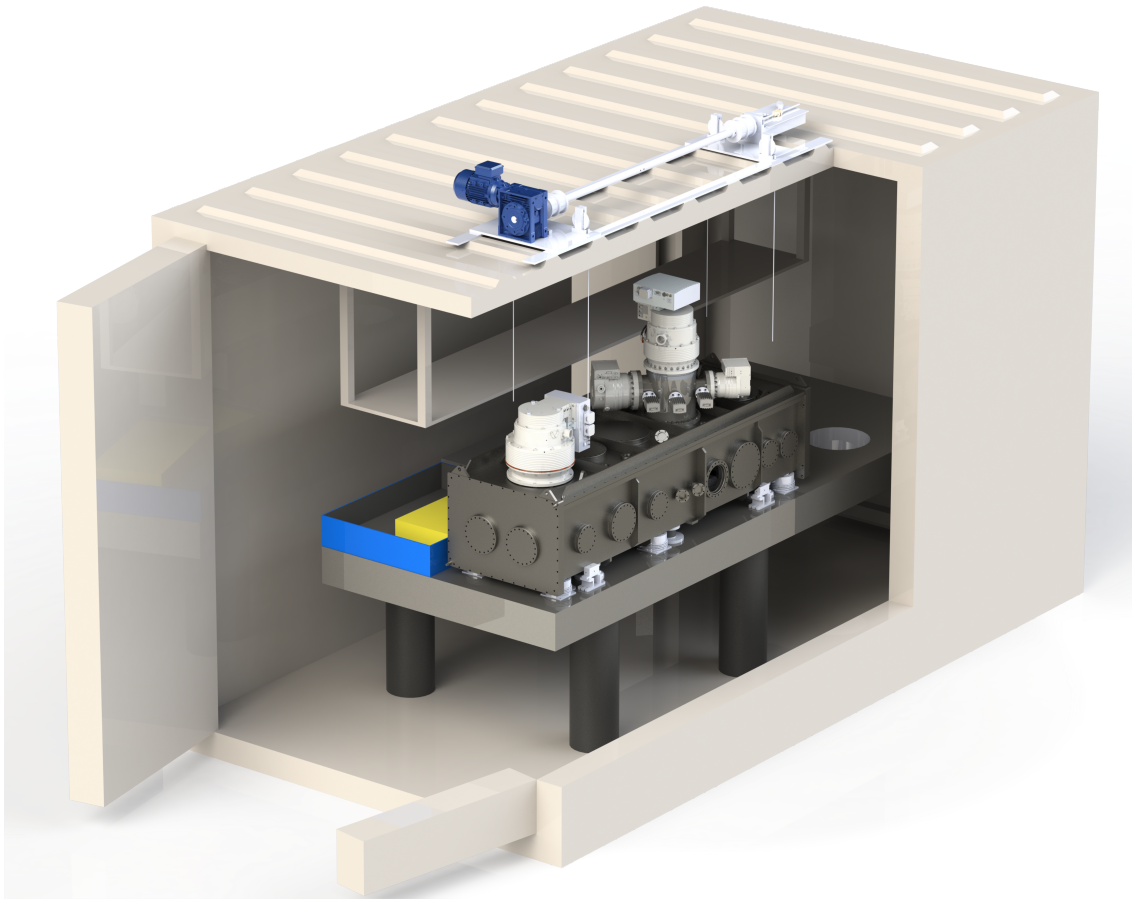

Figure 3.39: Overview of the container in which the experiment is build. Thermally and acoustically isolated walls establish a stable environment for the experiment. The frequency comb (blue), amplifier (not visible) and vacuum chamber(grey) are placed on one large optical table, leaving also space for a future Paul-trap with vertical cryogenic supply above the hole. A lifting construction is placed on the roof for lifting different parts of the heavy vacuum chamber setup.

explained in Section 3.4. To prevent this from happening the range of movement of the chamber needs to be restricted. This is achieved by inserting an assembly containing several bolts which function as end-stops of the chamber, as shown in Figure 3.38. Short slabs, welded to the vacuum chamber stick out sideways and are surrounded by the aluminum assembly, which is fixed on the laser table. Fine-threaded bolts are screwed through the hollow top part just far enough so that they leave a tiny bit of space for the slab to move freely in all directions. The movement margins for each direction can be adjusted with the appropriate bolt. Three of these assemblies arranged in a triangle close to the edges of the vacuum chamber then limit its movement in all directions.

3.3.3 Container

The experiment is set up in a custom-sized 15 feet container (CARU Containers GmbH), shown in Figure 3.39. The container, located in a large experimental hall, provides a noise-free and stable environment for the XUV comb. The walls, ceiling and floor are isolated with 10 cm of thermal isolation to keep the temperature inside stable. The temperature inside the container is regulated by an air-conditioning device, which can easily be improved further to 0.1 K stability [193]. A perforated metal layer on the inner walls of the container drastically reduces the acoustic noise. A home-built electrical lifting construction was placed on the roof of the container. Controlled from the inside, four cables through the ceiling can vertically lift different parts of the vacuum chamber in a controlled manner, such as the lids or the differential pump system. The container provides enough space to accommodate the Paul trap on the laser table in the future, with the cryogenic supply coming through the hole in the table. A horizontal beamline will supply ions from an EBIT outside the container.

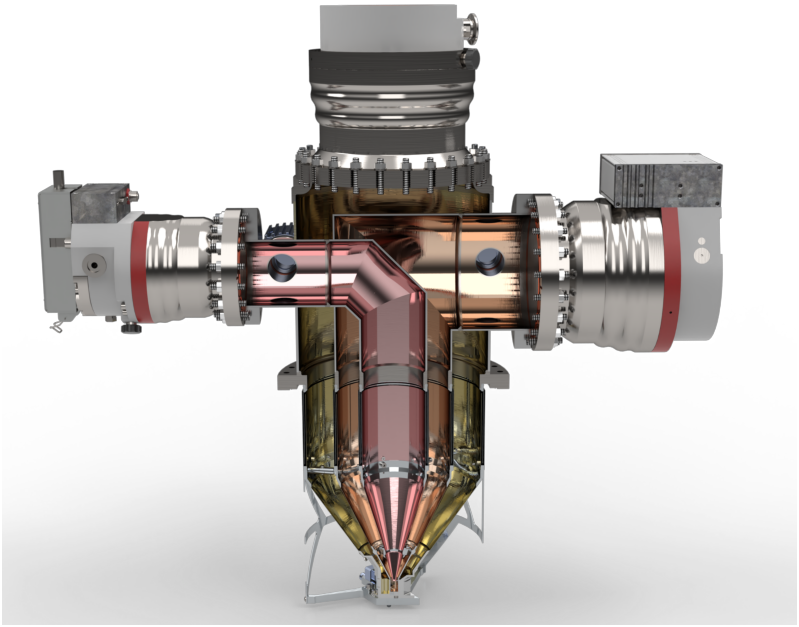

Figure 3.40: Overview of the differential pump system, vertically cut to show the nested shell structure. The first, second and third stage are pumped by 300, 500 and 1300 l/s turbopumps, respectively. The pump speed roughly matches the vacuum tubing conductance of each stage.

3.4 Differential pump system

The efficiency of the HHG process in the cavity focus strongly depends on the local gas density [109]. For maximum efficiency, a high gas density is required, especially when generating higher photon energies. To avoid multiple interactions of the target gas with consecutive pulses, also a high speed of the gas is needed. This can be achieved by mixing the heavy HHG target gas, usually xenon or krypton, with a much lighter gas such as Helium [80]. To keep the HHG gas density at the same value, the mixture density i.e. pressure needs to be increased by a factor equal to the mixing ratio. Even though the nozzle is placed very close to the laser focus, this still means a backing pressure of up to ~ 90 bar is required for a He:Xe mixing ratio of 9:1. At such high pressures, a large amount of gas is injected into the vacuum chamber, deteriorating the UHV environment in the chamber. To improve the chamber pressure during HHG operation, a gas-catching construction can be used, pumping away the target gas mixture with a separate pump [130] directly above the nozzle. In our setup, we have extended the principle of such a gas-catch system to a differential pumping system completely surrounding the focus and consisting of three separate stages.

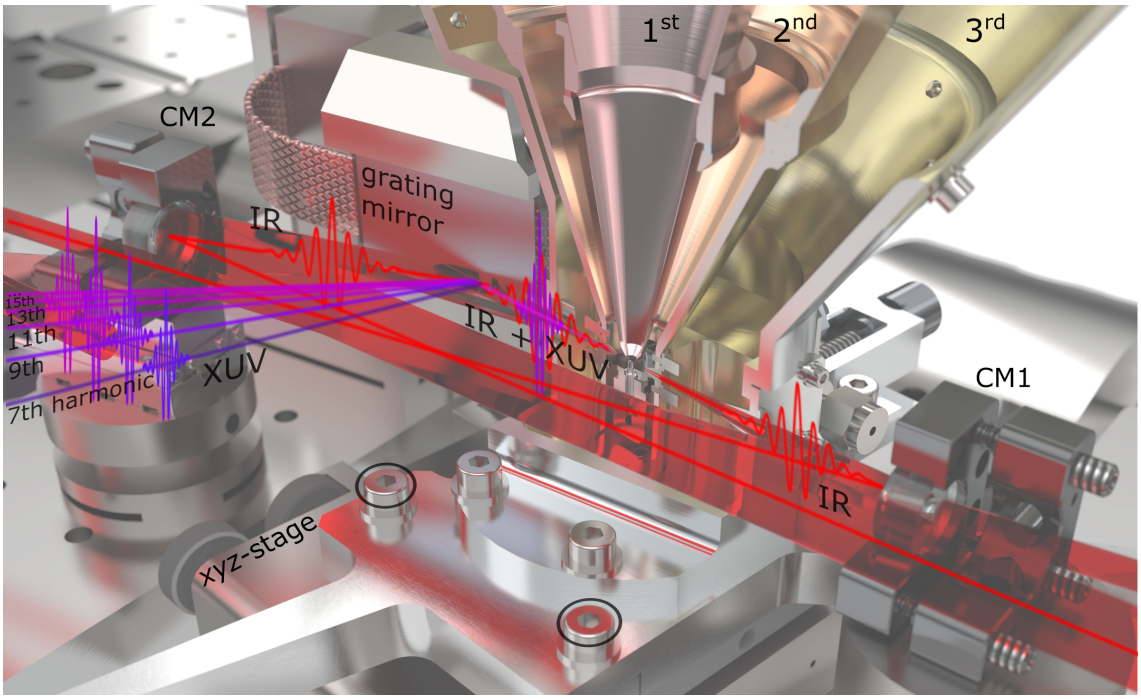

Figure 3.41: Sectioned pumping system inserted around the cavity focus. The three differential stages fill the tight space around the HHG interaction region, fitting between the curved cavity mirrors (CM1, CM2) and the grating mirror. The system is put in place vertically and subsequently fixed to the xyz-translation stage by four screws, two of which are visible and marked. Generated harmonics diffract off the grating mirror and leave the cavity under a different angle depending on their wavelength.

3.4.1 Design overview

As discussed in Section 3.2.1, the free space around the focus is strongly limited by other cavity beams, curved mirrors and the grating. Due to the designated cavity design, there is however 10 mm space between the focus and the next cavity beam. Therefore, the pump system is constructed in a conical shape, starting with a very small diameter close to the focus and increasing in size at larger vertical distance from the optics plane, where more space is available. An overview of the system is shown in Figure 3.40. The outer diameter of the third stage is limited by the CF 250 flange trough which the system is inserted in the vacuum chamber. Each stage is connected to a separate turbopump with 300 L, 500 L and 1300 L pumping speed for the first, second and third stage respectively. The diameter of the nested vertical tubes was adjusted for each stage such that the tubing conductance roughly equals the pumps suction power, for maximal pumping efficiency.

One of the challenges when constructing the three-stage pump system is decoupling the vibrations between the lower and upper part of the tubing. The lower part is mounted directly on the titanium rod structure such that it has a fixed position with respect to the laser focus. The upper part has to be attached to the vacuum chamber and turbopumps, and is therefore prone to vibrations. To avoid transferring vibrations from the upper part to the lower part, they need to be mechanically decoupled.

A solution using flexible bellows would drastically reduce the effective pumping speed, since three nested bellows would be required for the three stages. Due to their harmonica-shaped structure, they need a lot of space and practically no room would be left when nesting three of them inside each other. Furthermore, harmonica-shaped walls would greatly reduce the conduction of the tubing. We therefore planned a solution with flat walls for maximum conductance. For each stage, the lower part of the pumping system holds two parallel, vertical walls with a slightly different diameter, as in a U-shape. In between those two walls, there is a third vertical wall which is only attached to the upper part of the pumping system. In this way, there is a channel with a width of 2 mm and a length of twice 10 cm connecting the stages. The narrow cross-section of this channel ensures that particles can only flow between the stages at a very small rate, while the lower part of the pump system is now mechanically decoupled from the vacuum chamber. This also allows moving lower assembly for alignment with the laser focus.

3.4.2 Lower section

To achieve maximum gas density in the laser focus, the nozzle needs to be placed as close to the focus as possible. In practice this means a distance of roughly 100 μm, since for shorter separations the nozzle starts to distort the cavity mode. The high laser intensity and close vicinity to the focus could melt metals because of strong absorption, which is

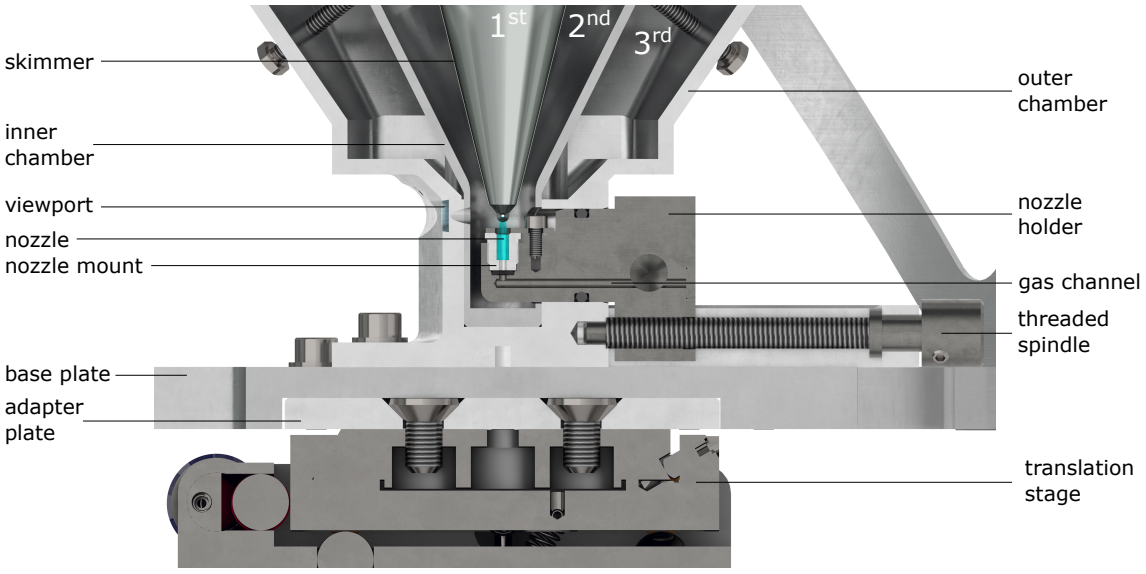

Figure 3.42: Cut along the nozzle gas supply line. The nozzle is glued in a an aluminum mount, which is screwed in a stainless steel holder. High pressure gas is supplied through a canal connected to the gas tubing. The whole steel nozzle holder can be horizontally retracted by a threaded spindle, such that the nozzle can be replaced without taking apart the rest of the pump system. A small glued window provides visual access for monitoring the nozzle-laser alignment, which can be adjusted by moving the XYZ-translation stage.

why glass nozzle materials are preferred. We use small quartz nozzles (Hilgenberg GmbH) with a length of 7 mm and an outer diameter of 2 mm, decreasing to 0.5 mm at the top. They are glued in a small aluminum nozzle mount using Torr Seal epoxy. The small mount is then screwed into a fine-threaded larger stainless steel nozzle holder, sealed by a tiny O-ring, as shown in Figure 3.42. A canal, drilled straight through the nozzle holder, supplies the high-pressure gas and is connected to 1/16" stainless steel tubing. The nozzle holder can be retracted horizontally as a separate unit with a threaded spindle, enabling exchanging the nozzle without disassembling any other part of the multi-layered shell structure surrounding the nozzle. Sealing between the high-pressure region close the nozzle and the main vacuum chamber is provided with an O-ring.

A vertical cut through the laser plane intersecting the differential pump is shown in Figure 3.43. Most of the gas exiting the nozzle under high pressure is propelled in forward (vertical) direction. Special nozzle shapes, such as Laval-type [194] or Campargue-type [195] can be employed to modify the dynamics of the emerging jet. For our purposes, the density very close the nozzle is the most important parameter and this is maximal for a simple orifice separating a high-pressure reservoir with the vacuum [196]. The emerging vertical jet can be captured by placing a skimmer with an orifice $\varnothing 2$ mm at a vertical distance of 0.5 mm from the nozzle [197]. This skimmer then forms the first, most inner,

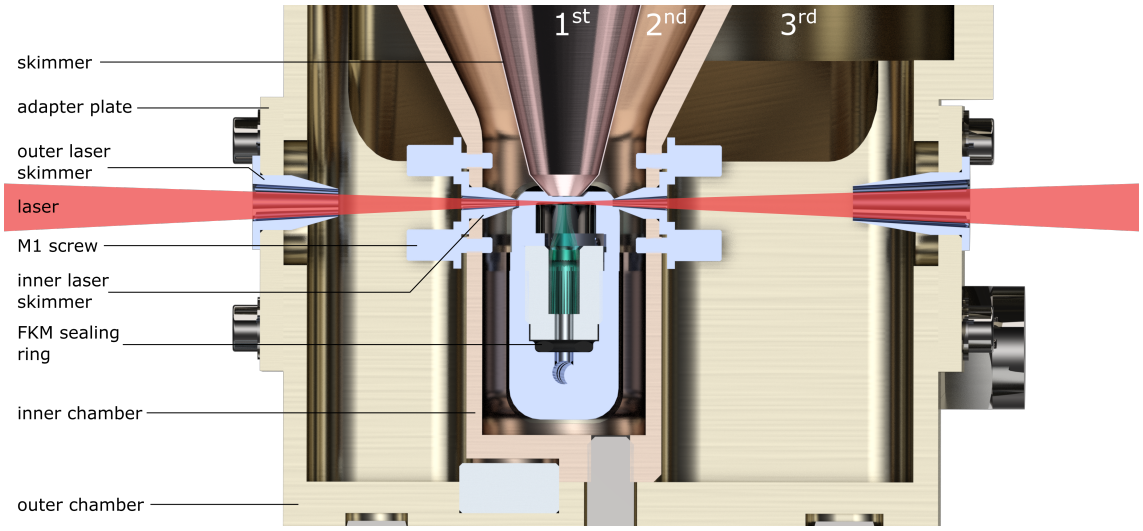

Figure 3.43: Cut view on the interaction region. The laser enters and exits the 3rd pumping stage through two large skimmers, glued to an adapter plate which is screwed onto the outer chamber. Two smaller skimmers for access to the 2nd stage are attached by small screws. The first stage is formed by a skimmer centered above the nozzle.

stage of the pump system. The second stage is formed by a thin-walled chamber surrounding the nozzle. The laser enters and exits this chamber through two holes, in which small skimmers can be inserted to further reduce the amount of gas escaping through the apertures. The third and outer stage consists of an asymmetric chamber, formed such that it optimally fills the available space between the curved mirror, grating mirror and other cavity beams. Also here two skimmers, with an orifice diameter adjusted to the size of the laser at that position, can be inserted to reduce the outward gas flux through the laser openings.

3.4.3 Nozzle alignment

To maneuver the nozzle precisely below the laser focus, the lower part of the pump system is mounted on a translation stage (Newport 8081-UHV). With five picomotors, this stage can move in all xyz directions, as well as tilt in θx and θy with a travel range of 3 mm. The stage is directly attached to the titanium rod structure, and can adjust the nozzle position below the focus in steps of ~ 30 nm, exploiting the mechanical decoupling of the lower part of the pump system. The main drawback of this stage is the maximum load of 13 N, originating from the springs and many degrees of freedom, which puts a stringent upper limit on the total mass of the lower part of the pump system.

To reduce the mass and maximize the pumping volume of each stage, the tube walls are made of 0.15 mm aluminum sheets. The conical walls are attached to the two small

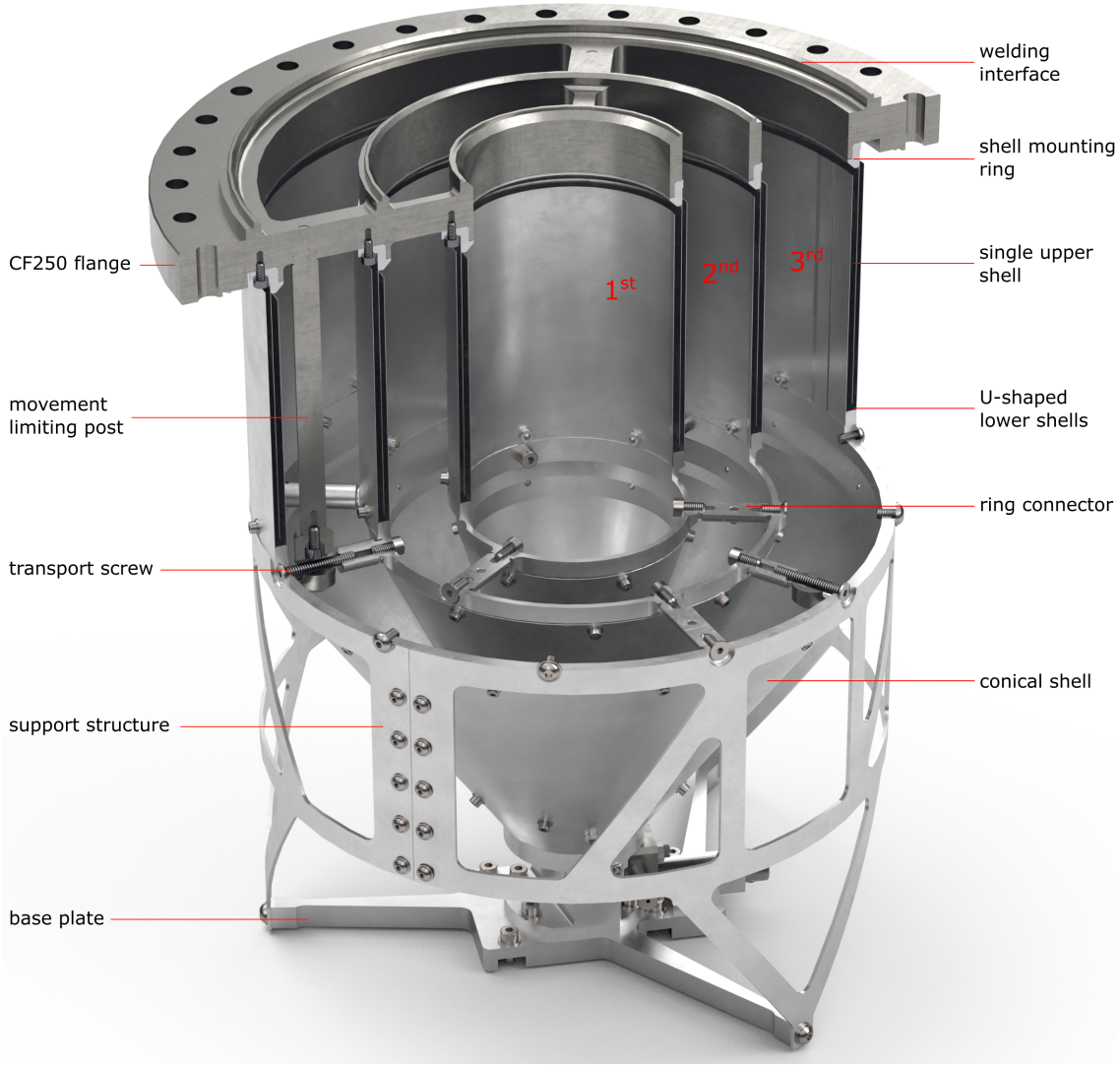

Figure 3.44: Sectioned view of the shells connecting the lower part (aluminum texture) to the upper part (steel texture) of the pump system. The shells of the lower part are party glued, party screwed on supporting rings, which are interconnected and supported by the base plate via a round structure. The double vertical lower shells form a U-shape, between which the upper shells attached to the CF 250 flange are placed. Movement between the upper and lower part is limited to 2 mm in every direction by removable screws intersecting the limit posts extending from the large flange.

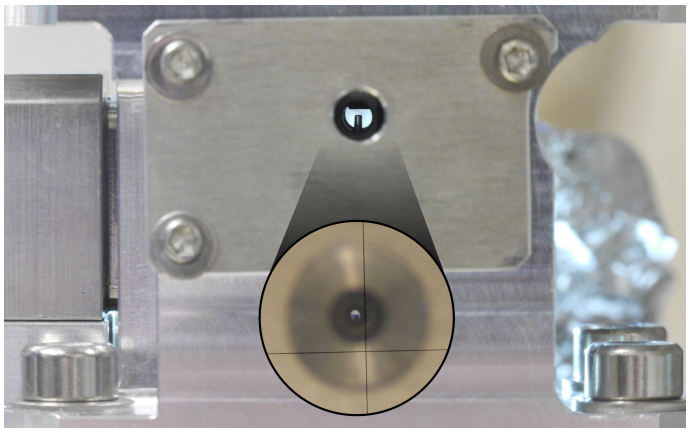

Figure 3.45: View of nozzle through laser holes in the differential pump system, without laser skimmers. Holes in the skimmer adapter plate (⌀ 3.5 mm) and inner chamber (⌀ 2 mm) are visible, aligned with the nozzle. Above the nozzle the skimmer forming the first pump stage can be seen. The inset shows the view with laser skimmers inserted through an alignment telescope, such that only a tiny hole of ⌀ 0.45 mm remains, which is partly blocked by the nozzle.

aluminum chambers surrounding the focus, which had to be CNC-milled due to their complex shape and therefore have slightly thicker walls. The top side of each conical sheet is screwed to an aluminum ring, also holding two vertical sheets. These three rings are interconnected by radial removable rods. To support and stabilize the weight of the rings and tubing, the outer ring is sustained by a perforated sheet, attached to the three horizontal extensions of the base plate, which rests on the translation stage and also holds both aluminum chambers. Most of the shells are connected by screws as opposed to gluing, to enable replacing individual parts when necessary.

The translation stage can move the lower part of the pump system as a whole to adjust nozzle-focus alignment. However, the relative alignment of the nozzle, laser skimmers and first stage skimmer can not be changed during operation. Therefore, these degrees of freedom have to be fixed during assembly of the pump system. First of all, the four laser skimmers need to be positioned exactly in a straight line. This axis is defined by the two inner laser skimmers, of which the position is not adjustable. The outer two skimmers are glued to a small plate, which is then screwed onto the outer chamber, as is visible in Figure 3.43. Via the margin of these screws, appropriate alignment of the laser skimmers can be achieved. Now the nozzle position needs to be adjusted to this laser axis defined by the laser skimmers. The height of the nozzle can be changed slightly by the screwing depth of the aluminum nozzle mount in the nozzle holder. Larger changes are realized by choosing an appropriate drilling depth in the nozzle mount before gluing the nozzle. The horizontal position of the nozzle can be adjusted by a retraction spindle, and accordingly

locked with a separate fine-threaded screw. In the remaining direction, along the laser axis, no changes in nozzle position are possible, but this is also not necessary since small deviations can be adjusted with the translation stage.

With the nozzle aligned to the laser axis, the skimmer orifice of the first pump stage needs to be centered above the nozzle. The top edge of the skimmer (Beam Dynamics, model 40.5 Ni) rests on the rim of a ring-shaped aluminum part attached to the chamber of the second stage. The diameter of this rim is slightly larger than the conical wall of the skimmer, leaving room for horizontal alignment of the skimmer orifice to the nozzle. The vertical distance to the nozzle can be set to exactly 0.5 mm by inserting an appropriate number of thin rings between the skimmer and the underlying rim. The skimmer position is then locked by a ring, holding the first stage conical sheet, which is pressed vertically onto the skimmer and fixed with screws. The three layers of nested sheets are put together in such a way, that the inner stage can be removed in order to re-align or replace the skimmer without the need for disassembling the outer two stages.

3.4.4 Upper section

The upper part of the pump system is attached to a modified CF 250 flange, with milled protrusions to provide maximum throughput for the three stages. For each stage, a vertical sheet located in between the double shells of the lower pump system is glued to an aluminum ring. These three rings are then screwed on the bottom side of the big flange. The tubing walls on top of the flange are thicker and welded to the flange to support the weight of the turbopumps. Also the inner tubing and the pump flanges are welded together to be leak-proof. Each stage has a separate small flange for monitoring the pressure.

The upper and lower part of the pump system are mechanically decoupled, but to protect the delicate sheets and make transport of the whole system easier, both parts can be connected. Three vertical rods, attached to the CF 250 flange inside the third stage tubing, reach down to the supporting ring of the lower part of the pump system, as shown in Figure 3.44. From the outside, a screw can be inserted, such that it perturbs the hole in the rod. The three rods are designed to provide a 2 mm margin in every direction, thus leaving 4 mm total freedom of movement between the upper and lower part of the pump system. The rods function as end-stops to the movement of the lower part of the pump system. In this way, deformations of the sheets caused by collisions are avoided during transport and alignment.

To put the pump system in its position in the vacuum chamber, it is inserted vertically through the flange centered above the laser focus. The horizontal extensions of the base plate are formed such that they do not collide with any of the cavity optic mounts while the pump system is lowered. The margins are however small, ~ 1 mm, therefore large guidance

rods on top of the vacuum chamber are used to let the system descend exactly vertical [198]. The careful lifting and lowering of the system, with its total weight including pumps exceeding 100 kg, was performed by the lifting construction described in Section 3.3.3. Once in the correct position, the base plate of the lower part is connected to the translation stage by inserting four screws.

3.4.5 Pressure measurements

In Figure 3.46, pressure measurements of the differential pump system are presented. Three full-range hot cathode/Pirani combined pressure gauges (FRG730CF35S, Agilent Technologies GmbH) are monitoring the pressure in each stage. The main chamber pressure is monitored with the same gauge placed at the lid. In a), the chamber pressure is measured before and after inserting the pump system for helium and krypton target gases. Without pump system, the backing pressure was limited to ~ 10 bar since at higher values the fore-vacuum pressure started to increase, reducing the main pump speed and increasing the chamber pressure drastically. When inserting the pump system, also larger fore-vacuum pumps (total pumping speed 110 m^3/h) were installed to back the turbopumps. Due to differential pumping, the pressure in the main chamber improves by an average factor of 100 for Kr and 93 for Helium using backing pressures between 0.5 and 10 bar.

In Figure 3.46b) the pressure in the different pumping stages is shown. Without the laser skimmers installed, the pressure decrease is roughly one order of magnitude for each stage. Inserting the skimmers primarily improves the pressure of the third stage and main chamber while pressure in the first two stages remains roughly equal. This indicates that the small skimmers significantly reduce the gas load on the third stage due to the much smaller aperture of $\varnothing$ 0.45 mm, compared to the $\varnothing$ 2 mm hole without skimmers present. The influence of the outer skimmers is much smaller, since the pressure in the main chamber decreases only by a factor of 1.7. The gas escaping the second stage through the tiny skimmer orifice is mostly directed towards the laser axis, and thus will exit also through the larger skimmers of the third stage. Therefore, the pressure in the main chamber does not improve as much as the pressure in the third stage. This result also shows that the leakage through the triple wall construction for mechanical decoupling is not limiting the main chamber pressure, since the improvement of pressure in the third stage does not translate to an equally big improvement in the main chamber. It can therefore be concluded that most gas is escaping through the laser holes, and the rest of the pump system is sufficiently leak-tight.

Due to the very small aperture in the inner laser skimmers, alignment of the pump system with the cavity beam is challenging. Since the inner skimmers only very moderately

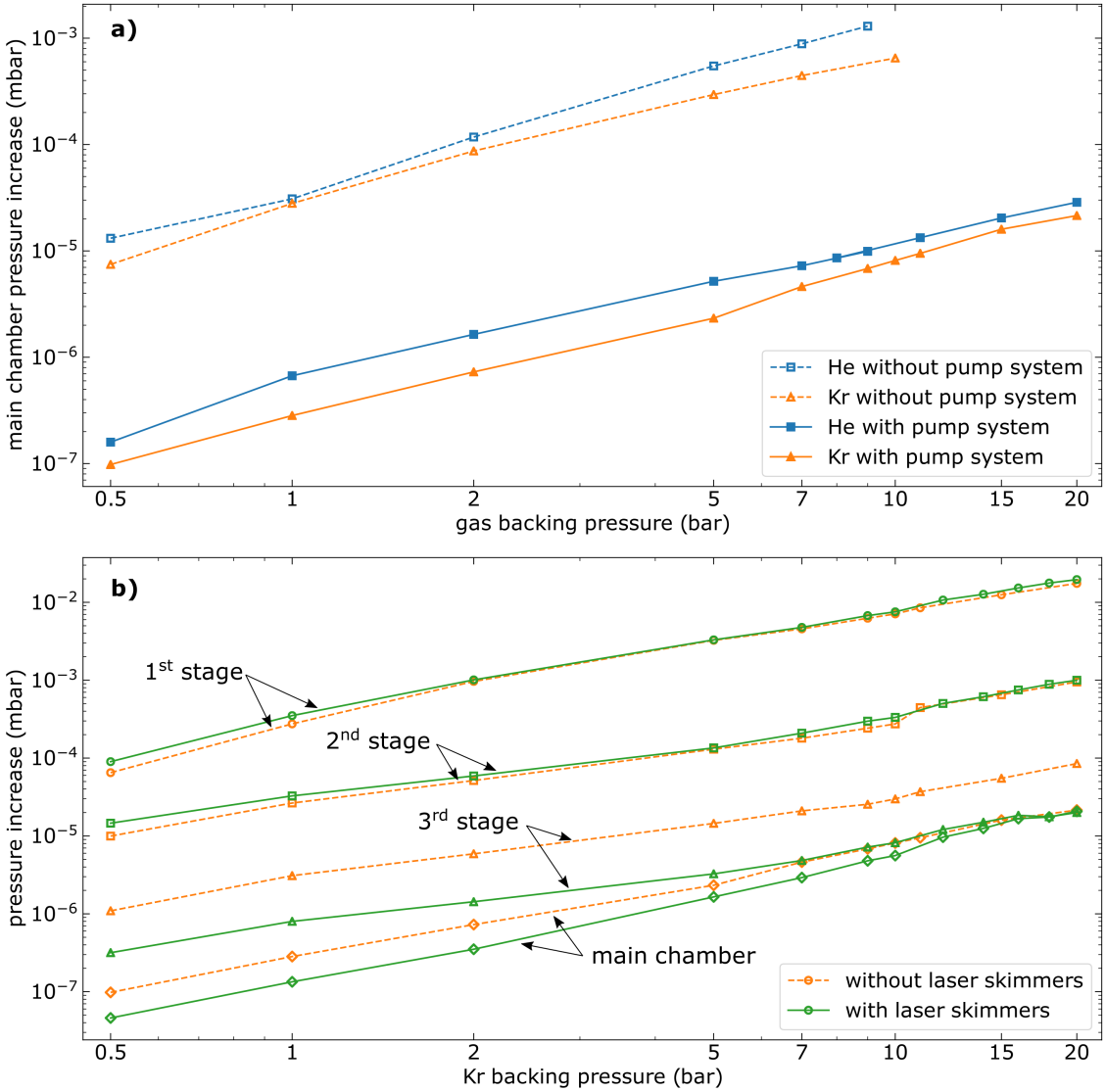

Figure 3.46: Vacuum pressure measurements with differential pump system. a) Influence of the pump system on the main chamber pressure as function of target gas backing pressure. A two order of magnitude improvement is achieved over a large pressure range for krypton as well as helium. b) Krypton pressure in the different stages of the pump system. The laser skimmers mostly affect the pressure in the 3rd stage and the main chamber.

improve the main vacuum but make the alignment a lot harder, the skimmers were removed for initial operation. This is possible without disassembling the pump system because of the aluminum plates at the outside of the third stage chamber. When these plates are removed, an $\varnothing$ 8 mm hole provides access to the M1 screws of the inner skimmer. With special tools, the screws and skimmers can be removed or placed back through these holes. Also the outer skimmers were removed by replacing the aluminum plates with equivalent ones without a glued skimmer. An IR-fluorescent powder was glued around the entrance hole on one of these plates, to assist in aligning the laser with the pump system.

Chapter 4

Intra-cavity velocity-map imaging of xenon at 100 MHz

As a first application of the newly developed experimental apparatus described in the previous chapter, we have studied multi-photon processes in xenon atoms using the VMI imaging technique. The results were published in a paper [199], that forms the basis of this chapter. First, we provide a brief introduction to the velocity-map imaging (VMI) technique and MPI processes. Then, the small modifications to the setup compared to the description in Chapter 3 are discussed. Subsequently, the obtained photoelectron distributions of xenon are presented and interpreted. The chapter is concluded by a comparison to other published MPI studies, underpinning the advantages and possibilities of our setup.

4.1 Introduction to VMI

Since the ion imaging technique was introduced in 1987 [200] by Chandler and Houston, it has become a widely used experimental tool for studying ionization dynamics in atoms and molecules. At first, the attainable energy resolution was limited by the finite extend of the interaction volume. This changed in 1997 with the invention of the velocity-map imaging technique [201]. Here, charged particles produced in the laser focus are accelerated towards a detector by electrostatic elements. The original 3D particle distribution is imaged onto a 2D plane, where the arrival position of the particle only depends on its initial velocity vector. The extraction field configuration ensures that the particles impact coordinates on the detector are independent of the location of the ionization event. As long as the initial distribution possesses cylindrical symmetry, which can in practice be achieved by setting a suitable laser polarization, it can be reconstructed from the 2D projected data by the inverse Abel transform [202]. This transformation requires that the axis of symmetry is parallel to the projection plane, as depicted in Figure 4.1. The forward Abel transform

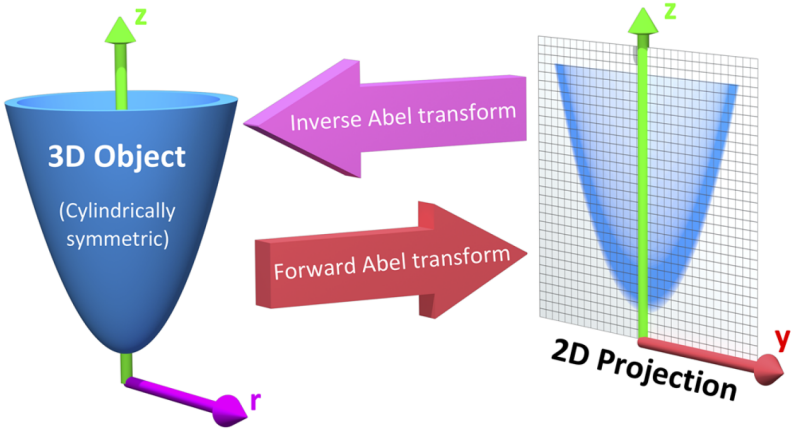

Figure 4.1: Graphical illustration of the Abel transforms. A cylindrically symmetric 3D object is mapped to its 2D projection via the forward Abel transform. The inverse transform maps the 2D projection to the 3D object. Figure from Hickstein et al. [203]

can be written analytically as

$$F(y,z) = 2\int_y^\infty \frac{f(r,z)r}{\sqrt{r^2-y^2}}dr, \tag{4.1}$$

where r and z are the coordinates of the 3D distribution, while y and z are those of the projection. $f(r,z)$ is the density of the 3D object, while $F(y,z)$ is the observed intensity in the 2D projection. The inverse Abel transform then yields

$$f(r,z) = -\frac{1}{\pi}\int_r^\infty \frac{dF(y,z)}{dy}\frac{1}{\sqrt{y^2-r^2}}dy. \tag{4.2}$$

While the inverse Abel transform can be analytically evaluated for some mathematical functions, experimental data requires numerical evaluation, which in practice gives rise to several issues. A simple numerical approach of Equation (4.2) involves loops over r, z and y, requiring a lot of computation time and needing a large number of sampling points to give accurate results. Moreover, at $y = r$ a singularity of the integrand arises. For these reasons, simple numerical integration of experimental data does not provide reliable results.

Several algorithms to resolve these issues have been developed over the past decades, such as the recursive method by Hansen and Law [204], the iterative correction procedure by Vrakking [205], the basis set expansion (BASEX) method by Dribinski et al. [206], and the maximum entropy reconstruction by Dick [207]. One of the most widely used methods is the BASEX, which expands the experimental image as a linear combination of analytical basis functions, for which the inverse Abel transform can be calculated exactly. This method is also used for the data analysis in this chapter.

4.2 Multi-photon ionization of xenon

Studies involving multi-photon ionization processes, in particular of the noble gases, have led to significant advances in the understanding of atomic ionization dynamics over the course of the last half century. Due to its low ionization potential of 12.13 eV, many studies were dedicated to xenon. In 1977, it was found that the photoionization yield is enhanced when the laser becomes resonant with one of the intermediate states [208]. A few years later, the absorption of additional photons after the ionization was observed, a process known as above-threshold ionization (ATI) [209]. The early work on xenon was mostly performed using low laser intensities and long pulses [210, 211]. For pulses longer than the time it takes the photoelectron to leave the interaction volume, the kinetic energies of the emitted photoelectrons are nearly independent of the laser intensity, as the ponderomotive energy of the freed electron is converted into kinetic energy as it leaves the laser field. However, when the laser pulse is sufficiently short, there is no time for the electron to accelerate. The observed electron energy spectrum then resembles the photoelectron energies and angular distribution at the moment of ionization [212]. In this short-pulse region, resonantly excited Rydberg states shift, due the additional ponderomotive energy induced by the high intensity laser field, by the same amount as the ionization threshold and excitation into the continuum can occur via these resonant states. In this way, sharp features appear in the electron energy spectra, which are known as *Freeman resonances*. The observed photoelectron energy and angular momentum distributions often reflect the characteristics of the dominant intermediate states [213].

The position of the ATI peaks is given by [214]

$$E_e = nhf - (U_{\text{ion}} + U_{\text{pond}})\,, \tag{4.3}$$

where n is the total number of absorbed photons. From the photoelectron angular distribution (PAD) of the ATI peaks, information can be obtained about the relevant ionization channels. Switching between different channels in noble gases has been observed by changing the laser wavelength [215] or the laser intensity [216, 217]. Since such investigations rely on the simultaneous absorption of many photons, they usually take place at laser intensities $> 5 \cdot 10^{12}\,\mathrm{W/cm^2}$, due to very low count rates per laser shot in lower intensity ranges. Since typically kHz laser systems are used [214, 218–228], data acquisition becomes very slow when the number of photoelectrons drops well below one per laser shot [229, 230].

Recent progress in laser technology has also enabled MPI studies at repetition rates of several hundred kHz [124, 150, 231–233], in one case even of 6 MHz [234], speeding up data collection. However, such increases require more amplification for keeping a high peak intensity. As described in Section 2.5, short pulses at a high repetition rate

can be amplified by a passive enhancement cavity if the laser repetition rate and carrier-envelope offset can be controlled. In this way, high intra-cavity peak powers can be reached that enable MPI of noble gases. Although these passive femtosecond cavities have been recently implemented for HHG experiments, they have never been adapted for studying MPI processes.

For the work in this chapter, we employ a fsEC for MPI imaging at a repetition rate of 100 MHz. A VMI setup is integrated around the tight cavity focus and enables collection of electron spectra in a fraction of a second, allowing live observation of spectral features. As an example application, we show Xe photoelectron images at intensities of $1 - 7 \times 10^{12}\,\mathrm{W/cm^2}$. With the perfect knowledge of the pulse-to-pulse phase differences inside the cavity, future pump-probe experiments could probe ionization time-delays [235], with better timing and phase accuracy. Since these phases are coherently imprinted on both the outgoing electrons and ions, 100 MHz-modulated matter waves could be produced. Furthermore, streaking techniques could be extended to lower recollision energies, where electron re-scattering is not fully understood [236]. Finally, the high rate and coherence will enable atomic and molecular precision experiments at much reduced intensities.

4.3 Modifications to the experimental setup

During these measurements, the fsEC amplified the seed pulses by a factor of 160 in s-polarization due to the grating mirror. To allow for p-polarization, namely parallel to the micro-channel plate (MCP) detector surface above the ionization region, half-wave plates are inserted before and after the cavity focus. Each of the zero-order, anti-reflection coated plates (B. Halle Nachfl. GmbH) induces $\sim 1\%$ losses due to reflection, reducing the power enhancement to ~ 50. Losses due to dispersion were marginal, and the wave plates caused no significant spectral narrowing of the intra-cavity spectrum, as shown in Figure 4.3b). The modulation arises due to a minor satellite pulse from the oscillator.

Xenon, forming a tenuous vertical jet, was injected through a nozzle with $50\,\mu$m diameter, mounted on a five-axis translation stage, described in Section 3.4.3. Instead of the differential pump system (Section 3.4), three ring-shaped electrodes ($\varnothing_{inner} = 7\,$mm, $\varnothing_{outer} = 20\,$mm, vertical separation 4.3 mm) are installed around the cavity focus. They shape the electric field of 730 V/cm that accelerates the photoelectrons towards the MCP. The electrodes are mounted on the same stage as the nozzle, and are axially aligned to it. The laser passes between the negatively biased lower (repeller) electrode, and the positively biased middle (extractor) electrode, intersecting the effusive gas jet. In the field-free region between the upper electrode and the front plate of the MCP (Photonis, $\varnothing_{inner} = 25\,$mm, Chevron configuration), which are both at ground potential, the photoelectrons radially expand according to their momentum. The MCP detector can measure

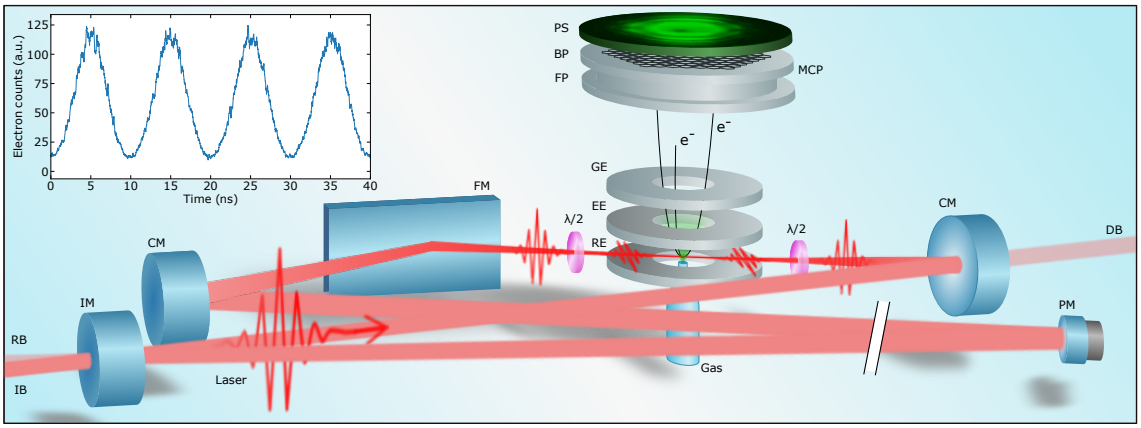

Figure 4.2: Schematic overview of the experimental setup. A 10 W frequency comb feeds at 100 MHz rate 172 fs-long 1039 nm pulses into a resonant bow-tie cavity, where they are enhanced in intensity and focused on an effusive gas target. There, multi-photon ionization generates photoelectrons that are detected on a MCP with its screen imaged by a camera. Waveplates are inserted in the cavity in order to rotate the polarization parallel to the imaging plane. IB: incoming beam, RB: reflected beam, IM: input coupler mirror, CM: curved mirror, DB: diagnostic beam, FM: flat mirror, PM: piezo mirror, $\lambda/2$: half-wave plate, RE: repeller electrode, EE: extractor electrode, GE: ground electrode, FP: front plate, BP: back plate, PS: phosphor screen. Inset: the arrival of the electrons at the detector strongly modulated by the arrival times of the individual laser pulses, which are separated by 10 ns.

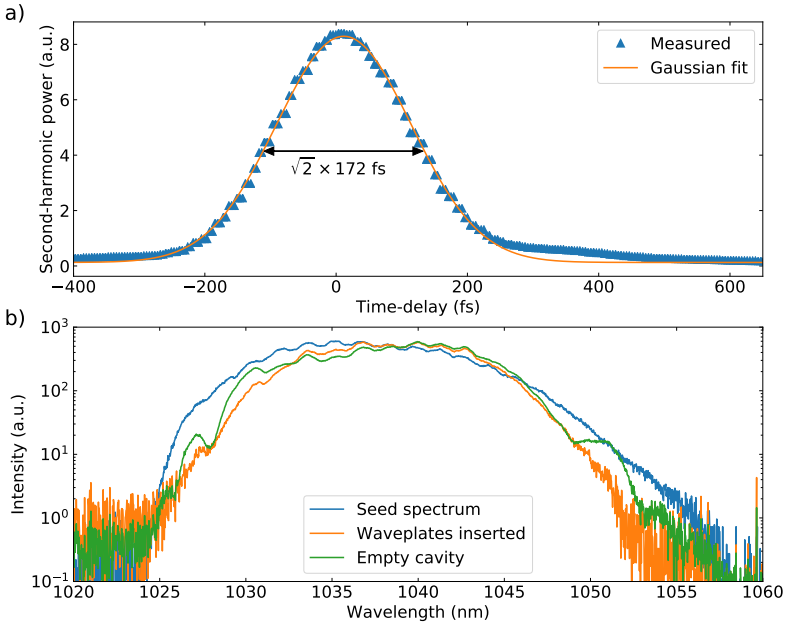

Figure 4.3: a) Autocorrelation measurement of the pulse length before entering the cavity, fitted assuming a Gaussian shape. b) Comparison of the seed spectrum (blue) and intra-cavity spectrum with (orange) and without (green) half-wave plates inserted showing no significant spectral narrowing due to dispersion of the plates. The modulation arises due to a minor prepulse from the oscillator.

the time-of-flight of single electrons by means of the electric pulse decoupled from its back plate with a capacitor, and also image the electron position by means of a phosphor screen and a camera (Thorlabs DCC1240M). The inset of Figure 4.2 shows the electron bunches arriving at 10 ns intervals, synchronized by the 100 MHz laser pulses. The temporal width of the bunches is limited by the resolution of the data-acquisition system.

A calibrated photodiode measured the transmitted light leaking through one of the cavity mirrors. This signal yields the intracavity average power, and, together with the pulse length, the peak intensity seen by the Xe atoms. The measured pulse length before the cavity is shown in Figure 4.3a) , and is estimated to be 180 fs inside the cavity due to the IC and group delay of the wave plate material. VMI measurements were carried out at vacuum pressures between $10^{-5} - 10^{-7}$ mbar, which at low intensities of $\sim 1 \times 10^{12}$ W/cm^2 result in electron count rates of a few kHz increasing to many MHz at higher intensities of $> 5 \times 10^{12}$ W/cm^2. Since in all cases we recorded less than one ionization event per laser pulse, space-charge effects due to electrons and ions are negligible. Data acquisition times of just a few seconds were sufficient for collecting adequate statistics.

4.4 Results & discussion

Figure 4.4 displays images of the phosphor screen. a) and b) show the electron distribution for polarizations orthogonal (s-polarization) and parallel (p-polarization) to the imaging plane, respectively. Using s-polarization, we see clear ATI rings reproducing the rotational symmetry of the emitted photoelectrons around the polarization axis. After turning the polarization parallel to the imaging plane, we become also sensitive to their angular momenta. To reduce the influence of external distortions in the electric field, causing the irregular shape of the ATI rings in b), circularization and symmetrization methods were applied to the data [237]. The result is shown in c), where the features are now fairly circular. Finally, the BASEX algorithm was used to obtain the electron distributions shown in d). The dark spot in the center of images b) and c), and bottom left of a) is due to damage on the phosphor screen.

4.4.1 Photoelectron kinetic energy distributions

In Figure 4.5, we show Abel-transformed images for various laser intensities and acquisition times. For a), we used an intensity of only $1.4 \times 10^{12}\,\mathrm{W/cm^2}$, below which the camera noise became larger than the signal. The peak intensity was calculated from the measured intra-cavity power, and can also be calibrated based on the ponderomotive shift of the photoelectrons. This is shown in Figure 4.6. In b), we plot the radially integrated peak position of the ATI rings for different laser intensities. One example of an electron energy spectrum, from which the peak positions are obtained, is shown in c). Each measurement is individually calibrated by setting the difference between ATI rings equal to the photon energy $E_{ph} = 1.20$ eV. The resulting ring positions (dots) can then be compared to the photoelectron energies based on the ponderomotive shift at a given laser intensity (dashed lines), calculated from Equation (4.3). Deviations can arise not only from image imperfections, but also from shifting and broadening due to states moving into resonance at certain laser intensities and focal volume averaging [238]. Overall, we achieve a fair agreement within 40% between the peak intensity measured *in situ* and the value inferred from the ponderomotive shift, showing a good control over the laser parameters in the cavity focus.

With increasing laser intensity, the number of ATI rings in Figure 4.5 increases since more photons are available for ionization. Within the ATI rings, a substructure is visible, providing information about the angular momentum of the outgoing photoelectrons. This can be used to determine whether the ionization process is non-resonant, or takes place via a resonant intermediate state. In Figure 4.6a)), the ponderomotive shifts of the relevant levels which can be reached by a certain number of photons from the $^1S_0\,5p^6$ ground state of Xe are depicted for intensities in the $10^{12}\,\mathrm{W/cm^2}$ region. Due to selection rules, only levels with odd parity can be reached by 10 photons, since the ground state is also parity-

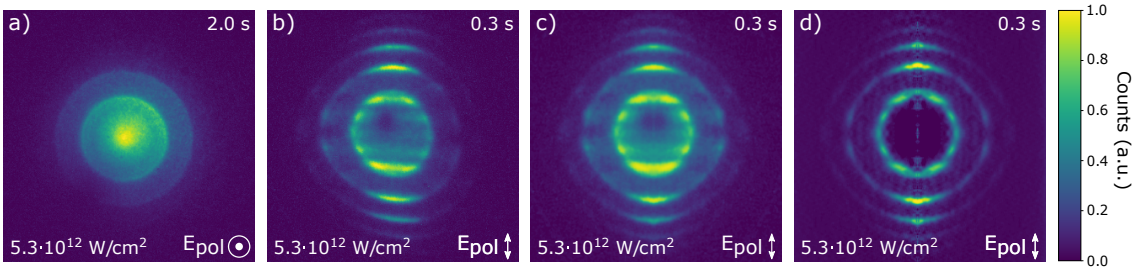

Figure 4.4: Images of photoelectron spectra from xenon, where the laser travels from left to right. a) and b) are raw images, with orthogonal laser polarization, as indicated in the lower right corner. c) processed image from b), using circulization and symmetrizing tools to compensate the influence of distortions in the electric and magnetic fields on the electron trajectories [237]. d) shows the inverse Abel-transformed image of c).

odd. Excitation from these states by one or more photons then results in the observed ATI rings. With each photon absorbed, the maximum attainable angular momentum increases by one. This is clearly visible in the Abel-transformed images, for instance in Figure 4.5f), where the first ring contains two nodal planes, the second ring shows three nodes and the third ring exhibits four faintly visible minimums. This increase in maximum angular momentum with ATI ring number is evident in all recorded images.

However, in the majority of the images, most of the signal is concentrated towards the direction of the laser polarization (vertical) in broad features, which hints towards non-resonant ionization [217]. For some images, for instance in Figure 4.5k), the first ring shows a minimum in the vertical direction. This originates from the damaged spot on the phosphor screen. Due to the symmetrization and the inverse Abel transformation, the dark spot translates into a local minimum in the first ring, as can be seen from Figure 4.4. From higher order rings, however, it is still evident that also for these images most of the electrons are vertically directed. In order to determine whether ionization also takes place via certain resonant states, we take a closer look at the PADs.

4.4.2 Photoelectron angular distributions

When comparing the angular signal distribution of the different images in Figure 4.5, it becomes clear that the pattern changes around an intensity of $4.5\times10^{12}\,\mathrm{W/cm^2}$. Below this intensity, the number of nodes in the first and second ring is two and three, respectively. This suggests that the electrons originate directly from a p-state, most likely $\mathrm{Xe}^+(^2P_{3/2})\,8p$, referring to Figure 4.6a). At higher intensities, for instance in Figure 4.5i), four and five nodes are visible in the first and second ring, respectively. The vertical node in the first ring is, as discussed previously, an artifact and therefore not considered here. This points towards two-photon ionization from the $\mathrm{Xe}^+(^2P_{3/2})\,4f$ state, which shifts into resonance

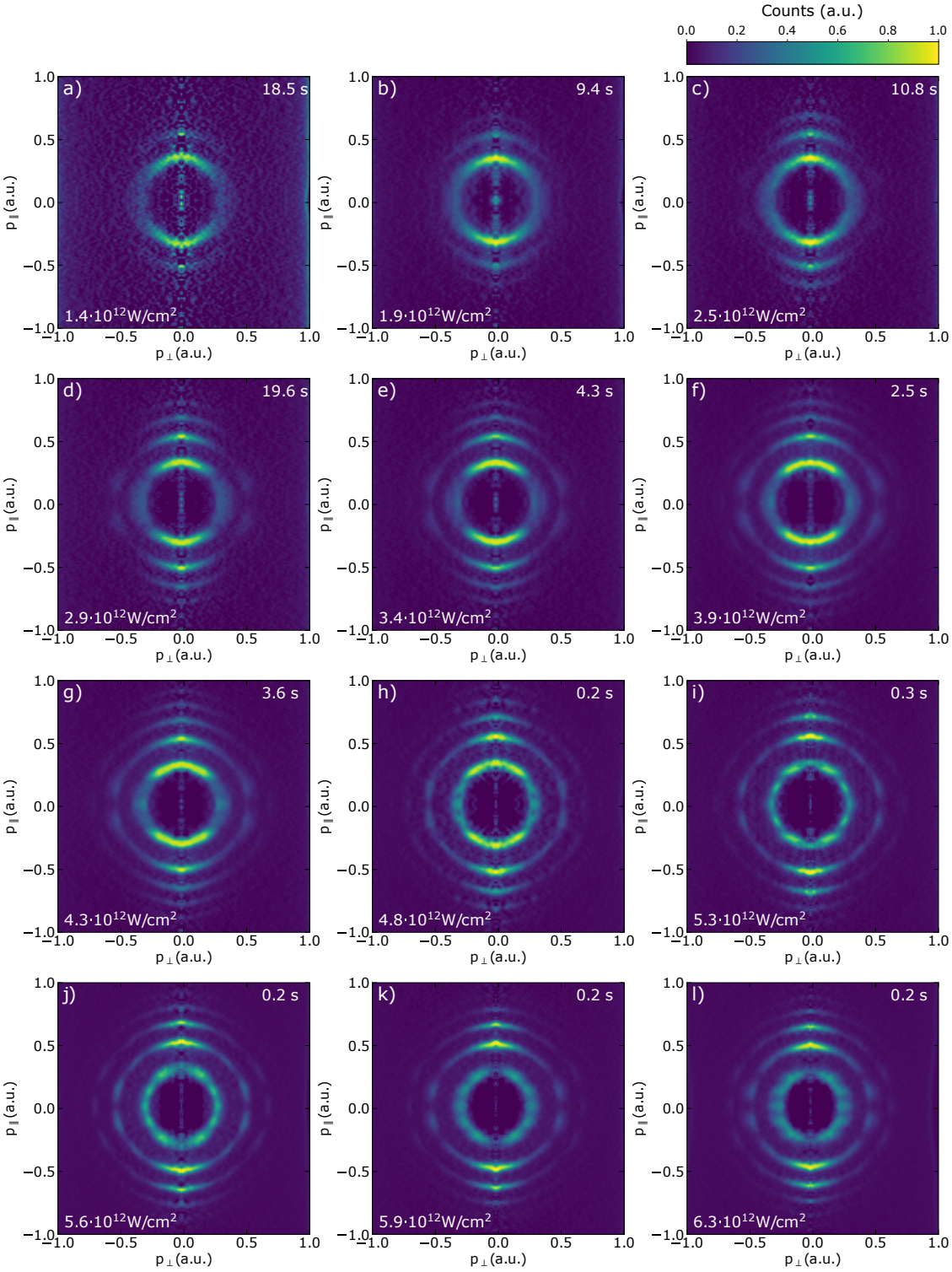

Figure 4.5: Abel transformed images of xenon for various laser intensities between 1 and $7 \times 10^{12}\,\mathrm{W/cm^2}$. The laser polarization is vertical, thus parallel to imaging plane, and camera exposure times are indicated. For the lowest laser intensities (images a)-c)), the xenon backing pressure was increased slightly to speed up the data collection.

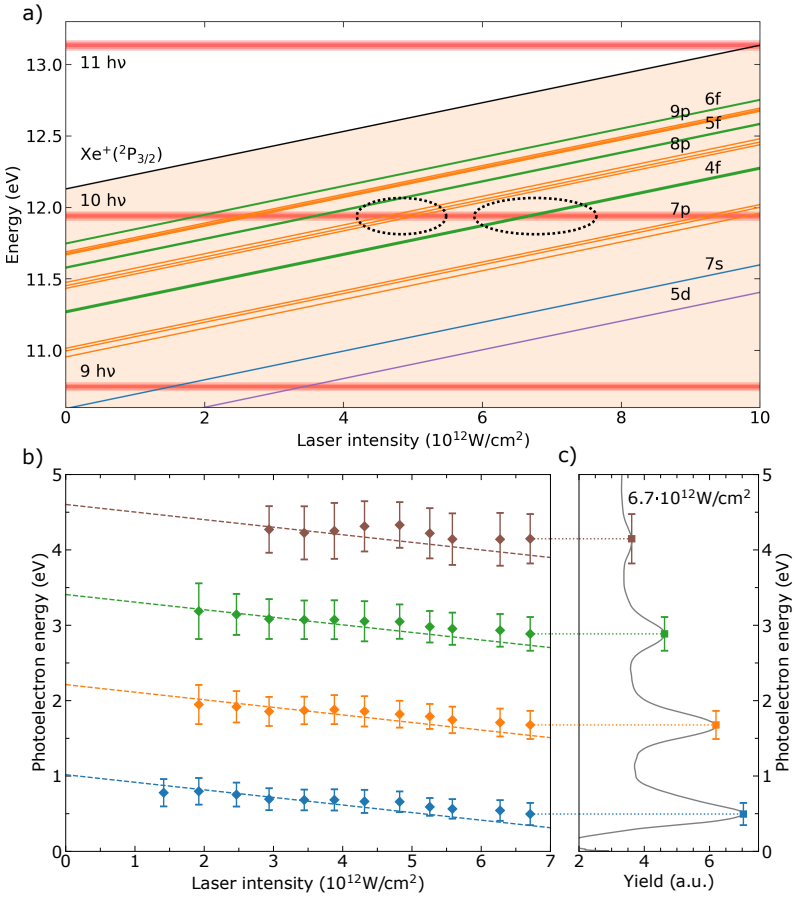

Figure 4.6: Ponderomotive shift of xenon levels. a) energy levels of the fine structure in $Xe^+(^2P_{3/2})$, shifted ponderomotively at the peak intensity of the laser field. Red lines indicate which levels are accessible by absorption of 9, 10 or 11 photons, with the line width representing the spectral width. The most likely observed resonant states are marked by dotted ellipses. b) positions of the ATI peak maxima for various intensities. Dashed lines indicate the expected position of non-resonant ATI peaks for the corresponding ponderomotive shifts. The error bars represent standard deviations of the fitted peak widths. c) radially integrated photoelectron spectrum at $6.7 \times 10^{12}\,\mathrm{W/cm^2}$.

Intensity (10^{12} W/cm^2)	β_2	β_4	β_6	β_8	β_{10}
2.9	-1.68 ± 0.01	1.60 ± 0.02	-0.77 ± 0.03	0.32 ± 0.02	-0.36 ± 0.02
3.4	-1.64 ± 0.01	1.63 ± 0.02	-0.83 ± 0.04	0.28 ± 0.02	-0.38 ± 0.02
3.9	-1.64 ± 0.01	1.63 ± 0.02	-0.78 ± 0.03	0.31 ± 0.02	-0.48 ± 0.02
4.3	-1.56 ± 0.01	1.61 ± 0.02	-0.99 ± 0.02	0.52 ± 0.03	-0.53 ± 0.03
4.8	-1.55 ± 0.02	1.64 ± 0.03	-1.19 ± 0.03	0.85 ± 0.04	-0.68 ± 0.04
5.3	-1.71 ± 0.02	1.82 ± 0.03	-1.32 ± 0.04	0.97 ± 0.05	-0.68 ± 0.06
5.6	-1.49 ± 0.02	1.74 ± 0.03	-1.34 ± 0.03	0.86 ± 0.03	-0.96 ± 0.05
6.3	-1.64 ± 0.02	1.75 ± 0.03	-1.12 ± 0.03	0.87 ± 0.03	-0.81 ± 0.04
6.7	-1.50 ± 0.01	1.52 ± 0.02	-1.07 ± 0.02	0.84 ± 0.02	-0.97 ± 0.03

Table 4.1: β parameters of the least-square fitted curves in Figure 4.7 according to Equation (4.4).

around $6{\times}10^{12}\,\mathrm{W/cm^2}$. Both of these states are indicated by the dotted lines in Figure 4.6a). The calculated intensity at which these states become resonant is however slightly higher than the observed peak intensity.

In order to corroborate the statement that resonant ionization occurs via the $8p$ and $4f$ states, depending on the laser intensity, we take a close look at the PAD of the second ATI ring. We chose this ring for further analysis since the first ring is altered by the dark spot and the signal of the third ring becomes too weak at lower laser intensities. The Abel-inverted signal is integrated over a radius interval of 0.4 eV in steps of 0.6°. To reveal the underlying contributions of the photoelectron partial waves of different angular momenta, the PAD can be expressed as a sum of Legendre polynomials P_l [215]

$$I(\theta) = \sum_{l=0}^{n} \beta_{2l} P_{2l} \cos(\theta), \tag{4.4}$$

where θ is the angle between the polarization axis and the emission and β_{2l} are the anisotropy parameters [239] for the different partial waves. In Figure 4.7, polar plots of the PADs are shown for intensities above $2.5 \times 10^{12}\,\mathrm{W/cm^2}$. The data was fitted according to Equation (4.4) using the least-squares method and the resulting β parameters are listed in Table 4.1. To prevent the center-line noise, induced by the Abel-inverse transform, close to the laser polarization axis from affecting the fitting result, angles close to the vertical ($< 6.4\,°$) were excluded from the fit. Although the circularization method has corrected radial malformations in the recorded images, distortions in the electric field could also cause slight changes in the angular direction. To account for this effect, a small offset of θ was added as an additional fitting parameter.

As becomes clear from Figure 4.7, the fits reproduce the number and size of the lobes

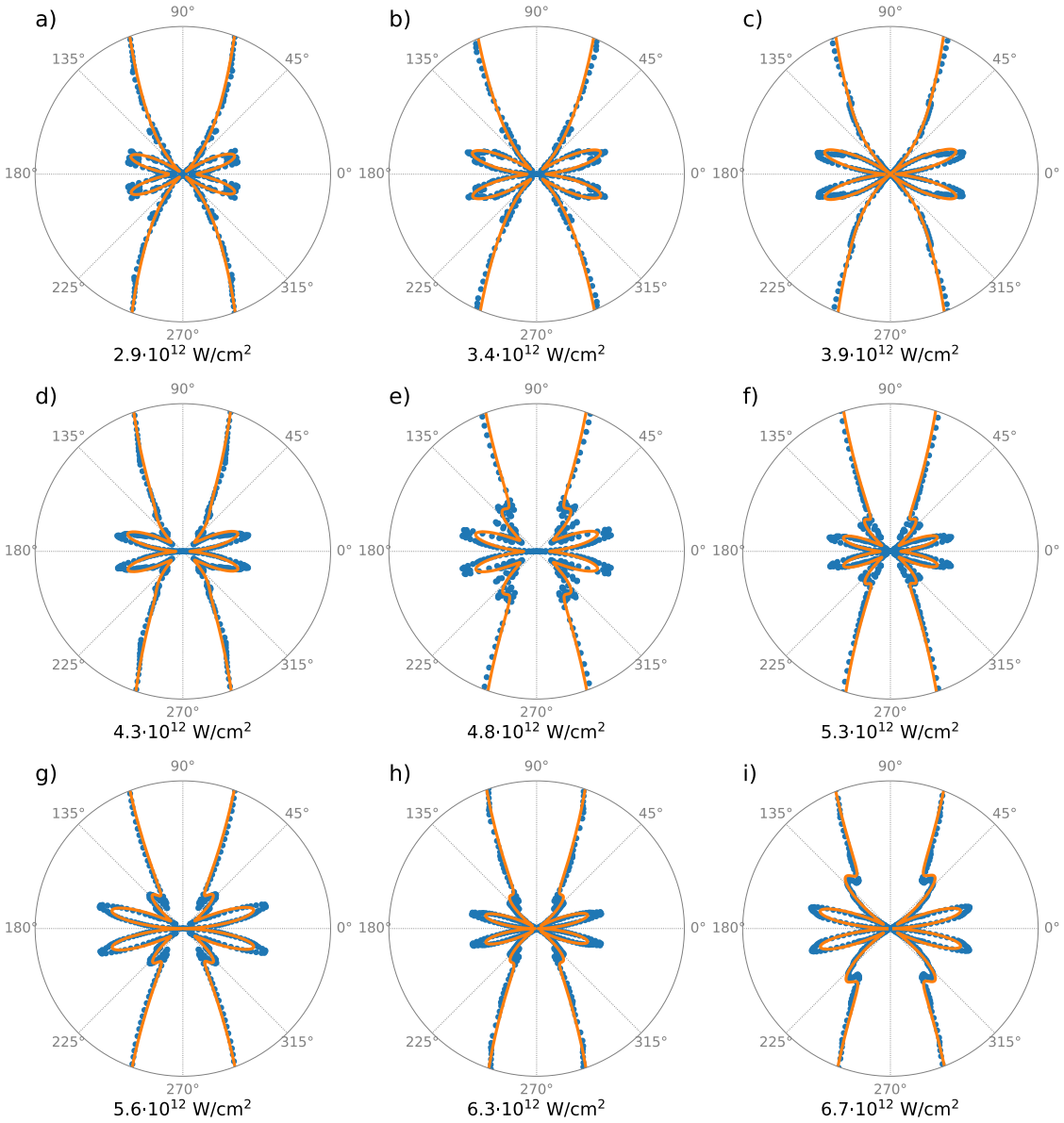

Figure 4.7: Polar plots of the PADs of the second ATI rings in Figure 4.5 at indicated laser intensities. To make the non-vertical signal features more clear, the maximal shown (normalized) intensity is set to 0.3. The data (blue circles) is fitted by a sum of even Legendre polynomals according to Equation (4.4) with the fitting coefficients shown in Table 4.1.

in the data well. From the polar plots it also becomes clear that above an intensity of $4.5{\times}10^{12}\,\mathrm{W/cm^2}$, an extra lobe becomes visible. This is reflected in the values of the β parameters in Table 4.1. Below $4{\times}10^{12}\,\mathrm{W/cm^2}$, the values of β_8 and β_{10} are roughly 0.3 and 0.4 respectively. Above $5.5{\times}10^{12}\,\mathrm{W/cm^2}$, their values increase to 0.9. This indicates that at higher intensities, the contributions from $l = 4$ and $l = 5$ partial waves increase. Subtracting two units of angular momentum for the second ATI ring, we arrive at an electronic state with $l = 3$. At lower intensities, the contributions are largely limited to β_2, β_4 and β_6, thus the maximum angular momentum is $l = 3$, hinting towards a p state. The non-zero values of β_8 and β_{10} at low intensities could be explained by a contribution from non-resonant ionization. The PAD fits thus support the earlier statement that resonant ionization from the $8p$ and $4f$ states is observed.

However, the absence of Freeman resonances in Figure 4.6c) suggests that the observed rings could also originate completely from non-resonant ionization. However, due to inhomogeneities in the extraction electric field, our energy resolution is limited to an estimated $\sim 100\,\mathrm{meV}$. This is not sufficient to resolve any sharp Freeman resonances and likely explains their absence in the observed photoelectron energy spectra.

To improve the measurement resolution, several modifications are possible. First of all, a better shielding of the field-free region is crucial for obtaining close to perfect circular features. For the current setup, possibilities for mounting the shielding were limited since the electrodes were installed on the same translation stage as the nozzle, while the MCP was mechanically decoupled from them and mounted directly on the titanium structure. A future design should include a complete electric and magnetic shielding of the region between the upper electrode and the MCP. Second, one of the current limitations is that the position of the ATI rings changes over timescales of several seconds to minutes, and their position is therefore not always reproducible by the voltages that are applied to the electrodes. This could be due to charge accumulation on some isolating parts close the photoelectron trajectories, most likely on the nozzle. Since the nozzle is fabricated from glass and positioned within a few mm or less of the laser focus, particles could accumulate at its surface and their charge could distort the electric field set by the electrodes. Third, the resolution could be further increased by using an MCP with a larger surface and lowering the voltages on the electrodes. Alternatively, an extra set of electrodes could be employed to be able to change the magnification of the electron imaging [240].

For the current experiments, the intensity range was limited by camera noise on the low side and laser power available on the high side. Using a cooled camera reduces the thermal noise and will therefore enable collecting spectra over longer acquisition times at lower intensities. The laser power available at the time of these measurements was limited to the 10 W from the commercial comb laser. By now, we can use the full 80 W from the amplifier, thus increasing the power by a factor of 8. By removing the grating mirror from

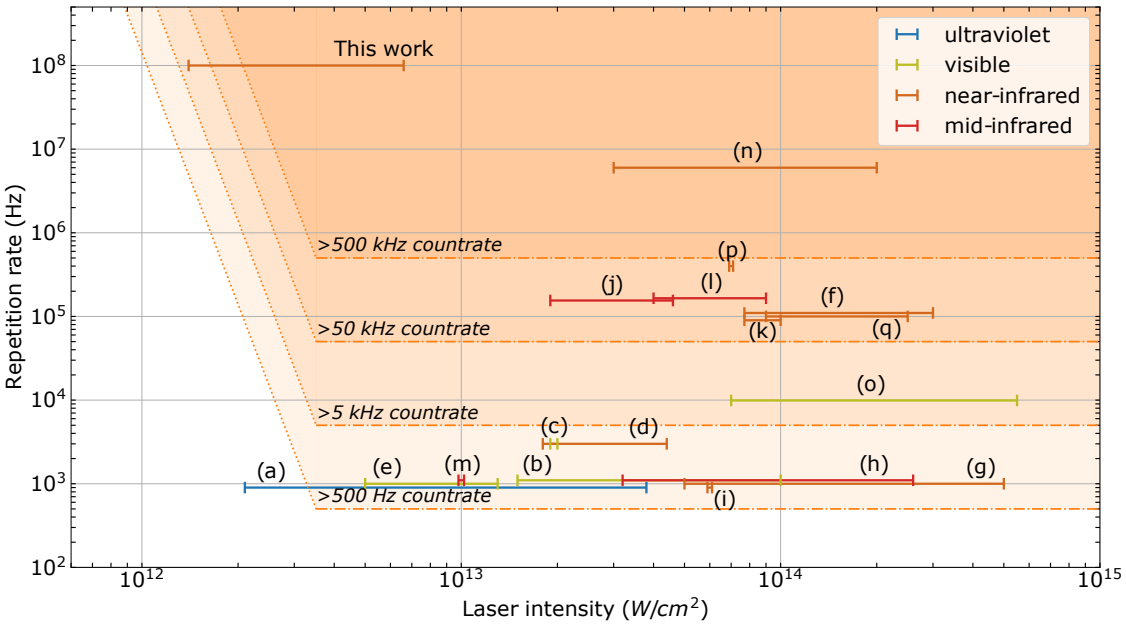

Figure 4.8: Comparison of selected published VMI experiments using ground-state noble gases in the short pulse regime. (a) Goto *et al.* [217], (b) Helm *et al.* [213], (c) Zherebtsov *et al.* [223], (d) Li *et al.* [225], (e) Kaminski *et al.* [215], (f) Salières *et al.* [229], (g) Hickstein *et al.* [241], (h) Blaga *et al.* [230], (i) Marceau *et al.* [227], (j) Baudisch *et al.* [233], (k) Paulus *et al.* [231], (l) Wolter *et al.* [150], (m) Bergues *et al.* [222], (n) Liu *et al.* [234], (o) Kübel *et al.* [228], (p) Furch *et al.* [124], (q) Eremina *et al.* [232]. Shaded regions indicate the achievable photoelectron count rate, either limited by a maximum yield of one electron per laser shot (dash-dotted lines) or the ionization rate scaling with I^n, here illustrated for an n=10-photon process (dotted lines). Clearly, this scaling strongly depends on the laser wavelength used.

the cavity and reducing the incidence angles on the mirrors, the cavity becomes insensitive to polarization and the intra-cavity wave plates are no longer necessary. This will increase the enhancement from 50 to $\gtrsim 300$. By using an input coupler with a higher reflectivity, larger amplifications up to several thousand could be achieved, ultimately limited by either plasma dispersion or damage thresholds of the mirrors.

4.4.3 Acquisition time benchmark

Putting these findings in the broader context of short pulse MPI studies on ground-state noble gases, we emphasize that so far, no experimental data has been reported at intensities below $5 \times 10^{12}\,\mathrm{W/cm^2}$ using near-infrared light. Since the ionization rate scales as I^n, with n being the number of required photons, it becomes clear that signal rates drop steeply at low intensities and the data acquisition time needed for good singal-to-noise ratios becomes very long. With a repetition rate of 100 MHz, we can acquire electron spectra

five orders of magnitude faster than conventional laser systems operating at kHz rates and therefore go to much lower intensities. This is illustrated in Figure 4.8, where we compare a selection of published MPI experiments using fs pulses on noble gases. At higher intensities, the electron count rate is also limited by the laser repetition rate, since space-charge effects limit the count rate to one ionization event per laser shot. Because the acquisition of a single, high-resolution spectrum can require the recording of up to a billion photoelectrons [229], our setup has the distinct advantage that such images can be recorded within reasonable time frames of seconds to several minutes. As demonstrated by this experiment, an enhancement cavity in combination with a frequency comb is a powerful tool for MPI studies, which can now be extended to include electrons with very low energies, close to the ionization threshold.

Chapter 5

High harmonic generation

In this chapter we present and discuss the generation of high harmonics inside the newly developed fsEC, which will also be published [242]. We start with a general characterization of the cavity, determining its enhancement and FSR. Subsequently, we present the outcoupled harmonic spectra for three different target gases. In order to improve the harmonic yield, the amount of steady-state plasma in the focus needs to be reduced, which we achieve by using He:Xe gas mixtures. Finally, we test the performance of the system by generating continuous XUV output for over five hours and compare the measured yield to other published experiments.

5.1 Cavity operation

In order to generate harmonics, the cavity needs to be operated at high circulating powers. As described in Section 2.4, the cavity enhancement is mainly determined by the transmission of the input coupler. To obtain maximum enhancement for a given finesse, the losses in the cavity should be dominated by the input coupler, and residual cavity losses should be minimized. In Table 5.1, the cavity parameters are shown for three different input couplers. The enhancement was measured by observing the transmitted cavity signal, while the contrast was determined from the cavity reflection. The finesse F and mode matching factor ϵ were then calculated using Equations (2.57) and (2.62), respectively. The cavity losses $\mathcal{L}_{\text{cav}}$ were assumed to be the same in all cases, and calculated to be 0.00130(2). It becomes clear that in all cases, the losses are indeed dominated by the input coupler. The mode matching factor ϵ varies slightly over the different measurements. Since the transverse and longitudinal cavity mode profile does not depend on the IC transmission, this difference is most likely due to imperfect alignment of the incident beam with the cavity mode. Swapping the input coupler for a different one changes its position and angle by a small amount, which is nevertheless sufficient to affect the cavity mode such that re-alignment is necessary. Also, the rotation of the cylindrical optic is freely adjustable and needs to be optimized, such that the curved axis is exactly vertical, by observing the

input coupler	enhancement β	contrast $\mathcal{C}$	finesse F	mode matching factor ϵ	cavity losses $\mathcal{L}_{\text{cav}}$
R_i=0.9935	320	0.42	805	0.75	0.0013
R_i=0.9872	176	0.23	446	0.69	0.0013
R_i=0.9804	122	0.15	301	0.64	0.0013

Table 5.1: Cavity parameters for three different input couplers. The cavity enhancement and contrast are measured measuring the transmitted and reflected power with an incident average power of 1 W. The finesse, mode matching factor and cavity losses are calculated using the relations in Section 2.4.

cavity mode. Therefore, it is almost impossible to exactly retrieve the previous mirror position after the IC has been exchanged. In practice, the overlap of the incident beam with the cavity mode is not exactly reproduced, which results in a different value of ϵ.

As described in Section 2.4.2, the cavity finesse can also be measured by sweeping the laser frequency over a cavity resonance at a rate much faster than the lifetime of the intracavity photons while measuring the exponential decay time of the light leaking through the cavity mirrors. Such a ring-down measurement is shown in Figure 5.1. The signal is fitted to a damped cosine wave with a second order chirp, to account for the interference between the light leaking out of the cavity and the off-resonant incident light reflected from the input coupler. The measured intensity decay time of 1.1 μs corresponds to a cavity finesse of 692(11). For this measurement, the input coupler transmission was $T_i = 0.0065$, indicating that the cavity losses are 0.002.

The increased amount of cavity losses, compared to the 0.0013 determined from the cavity enhancement in Table 5.1, is most likely due to a damaged coating on one of the curved mirrors. When this mirror was replaced, the enhancement increased significantly and inspection of the mirror showed some clearly damaged spots originating from insufficient cleaning of the substrate before the coating was applied. The same defect caused thermal drifts of the cavity alignment, probably due to excessive heating of the substrate, over the course of several minutes when operating at circulating powers above $\sim$ 100 W [172]. In Figure 5.2, images of both curved mirrors that are taken with a thermal camera (Infracam, FLIR) are shown. The indicated temperatures are uncalibrated and in reality higher since transmission through a ZnSe vacuum window effectively decreased the measured temperature. The images were taken before the damaged mirror was exchanged, whereas the comparison of the different input couplers (Table 5.1) was performed afterwards.

For the results in the rest of this chapter, the input coupler resulting in the largest enhancement, $R_i = 0.9935$, is used. In Figure 5.3, the circulating power as function of incident power is shown (blue datapoints). The average enhancement was fitted to be 316(8), reaching an average power of more than 25 kW at an input power of 75 W. Taking

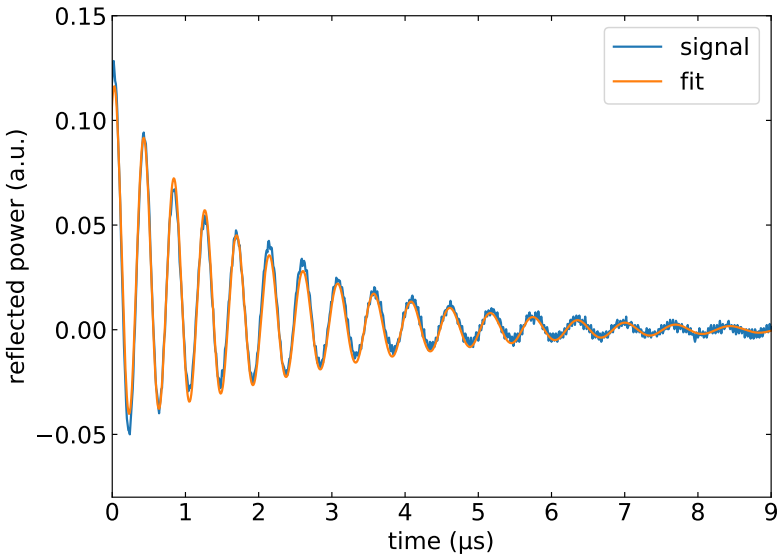

Figure 5.1: Ring-down measurement of the cavity with an input coupler transmission $T_i = 0.0065$. The cavity reflection is recorded with a fast phototiode and fitted with a damped cosine with second order chirp. The measured intensity decay time of 1.1 μs implies a finesse of 692(11).

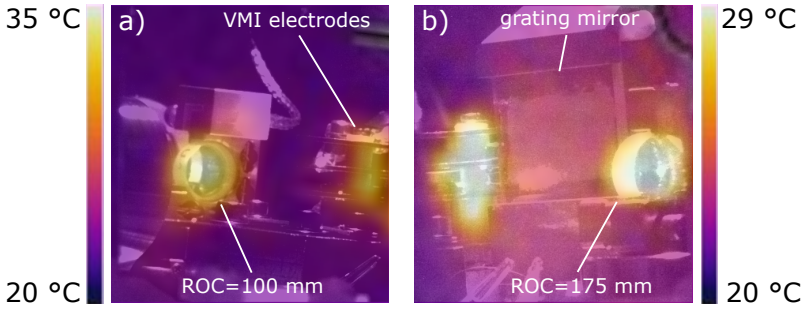

Figure 5.2: Heating of cavity mirrors at 700 W of circulating power. Picture of a) the ROC = 100 mm and b) ROC = 175 mm curved mirror, overlaid with a thermal camera image. On the right side of a) and left side of b), also the VMI electrodes are visible, as well as the grating mirror in the middle of b). The indicated temperatures are lower boundaries.

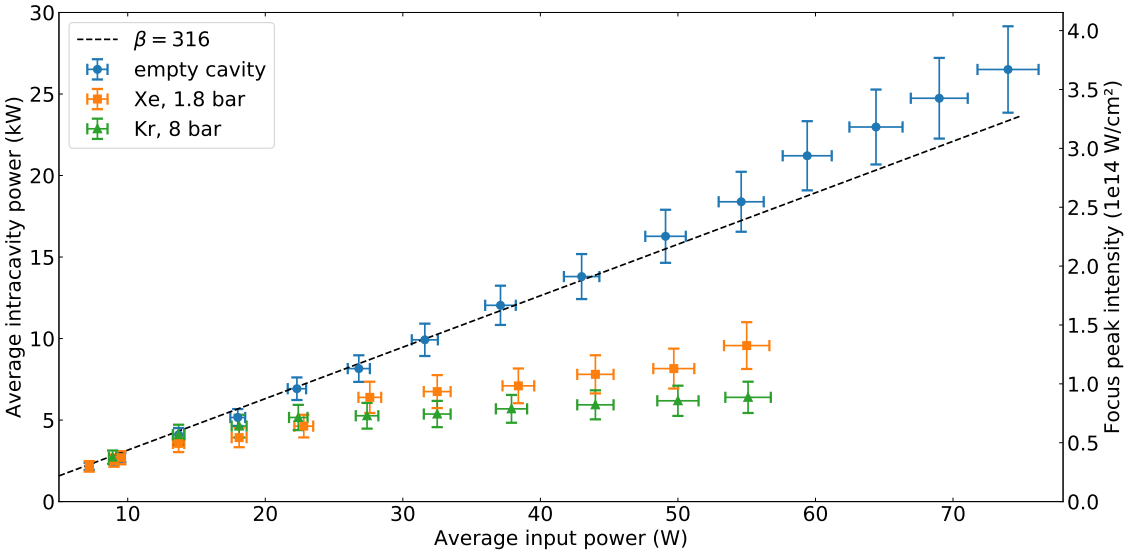

Figure 5.3: Intra-cavity power as function of incident power. With a $R_i = 0.9935$ input coupler, an average enhancement of $\beta = 316(8)$ is reached for an empty cavity. When target gas is introduced the circulating power 'clamps' due to the dispersion of the produced plasma, limiting the attainable peak intensity. Intensity clamping can be reduced by using shorter pulses [83].

into account the 200 fs pulse duration and the 679 μm^2 focal area, this translates to a focus peak power of 2.5 GW, which is equivalent to a peak intensity of 3.7×10^{14} W/cm^2. We can thus achieve sufficiently high peak intensities to drive the HHG process.

5.2 Detection of harmonics

In Figure 5.4, a schematic overview of the harmonic detection setup is shown. The spatially dispersed harmonics impinge on a plate that is coated with sodium salicylate. Under influence of XUV radiation, this scintillating material absorbs light below 350 nm and emits broad fluorescence around 420 nm [243]. Since the quantum efficiency of sodium salicylate is constant between 35 and 100 nm, the material is very suitable for comparing the yield of the different harmonic orders. The fluorescence is observed with an electron multiplying CCD camera (Luca R EMCCD, Andor), mounted above the vacuum chamber, via a large flat mirror under 45°. The intensity from the fluorescent screen is proportional to the number of photons arriving at the plate, thus to obtain the harmonic power, the amount of fluorescence needs to be multiplied with the photon energy.

To measure the absolute power of the individual harmonics, a GaAsP photodiode (G1127-04, Hamamatsu Photonics) is used. The sensitivity of this type of diode steeply drops above 680 nm and it therefore is insensitive to near-IR radiation. The photodiode is

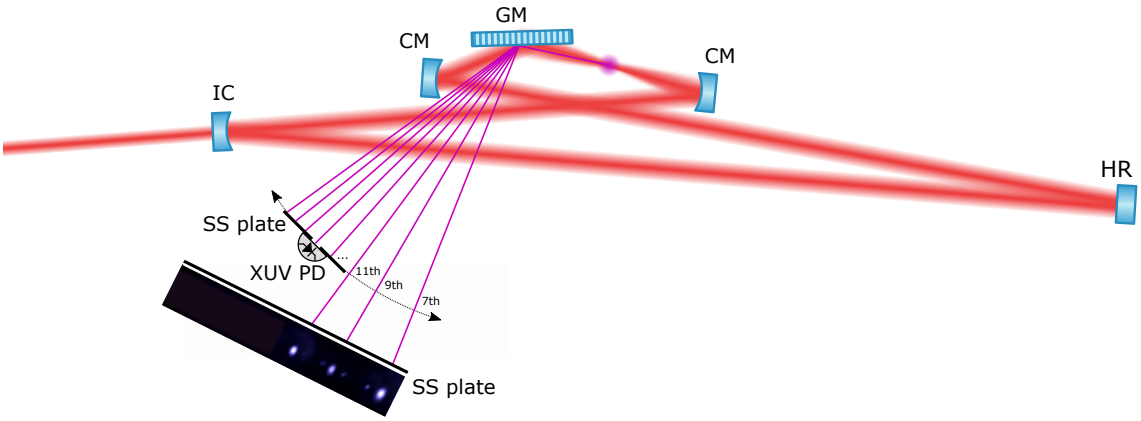

Figure 5.4: Schematic overview of the detection of harmonic radiation. The different orders are spatially dispersed by the grating mirror (GM) and send towards a glass plate coated with sodium salicylate (SS). The fluorescence of the plate is observed using a camera mounted above the vacuum chamber and via a flat mirror under 45°(not shown). An example image is shown, where the different harmonics can be identified by their position on the screen. For measuring the absolute power of the harmonic orders, a GaAsP photodiode (XUV PD) is used. It is mounted behind a second, smaller sodium salicylate screen with an aperture. The screen and photo diode can be moved such that different orders can be observed. IC, input coupler; CM, curved mirror; HR highly reflective flat mirror.

mounted behind a smaller, second plate coated with sodium salicylate, with a small hole in front of the diode. This plate can be moved in order to measure the power of different harmonics. Fluorescence from the small plate can be used to identify the harmonic order that is falling onto the photodiode. The resulting photodiode current is measured with an picoampere meter (Model 152, Keithly), and calibrated via a responsitivity curve measured by the PTB, which was cross-checked with a power measurement of the 235 nm photo-ionization laser for Be^+. The ampere meter adjusts the input impedance while measuring the current. For currents below 1 nA, it is 1 MΩ and for currents above that limit the resistance is decreased.

One of the main free parameters for the generation of harmonics is the nozzle position. Only when the nozzle is located right below the cavity focus, the gas density is high enough for HHG. In Figure 5.5a), a plasma plume of xenon ejected from the nozzle below the focus is shown. In this picture, the plume traverses through the VMI electrodes while the differential pump system was not yet in place. Once aligned, the plasma can thus be easily observed. However, with the pump system in place, its walls hinder the view such that it becomes hard to achieve a rough focus-nozzle alignment. Therefore, the vacuum chamber is flooded with 0.1 mbar of xenon. The cavity focus then becomes visible as a bright spot of plasma, as shown in Figure 5.5c). Through the small view-port in the wall

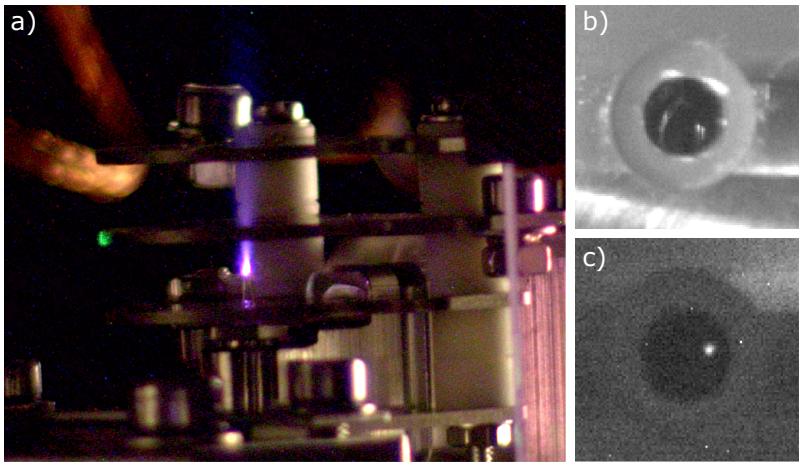

Figure 5.5: Plasma production in the cavity focus. a) a vertical plasma plume of xenon gas from is produced when the nozzle is aligned below the focus. The differential pump system is not inserted on the picture, instead the VMI electrodes are visible as horizontal dark stripes. b) with the pump system inserted, the nozzle can be observed through a small window slightly right of the image center. c) by flooding the chamber with xenon, the laser focus becomes visible as a bright dot of plasma and the nozzle can be positioned below it.

of the pump system, the nozzle position can be observed, as shown in Figure 5.5b), and then be moved towards the bright xenon plasma dot using the XYZ translation stage. In this way, a rough alignment in vertical and one horizontal direction is obtained. A finer alignment in all directions is achieved by optimizing the harmonic yield.

5.3 Generation of XUV radiation

In Figure 5.6 images of the fluorescence of generated harmonic orders are shown for three different target gases: argon, krypton and xenon. The orders are identified by their position on the screen. The small dots in between the uneven orders are due to second-order diffraction of higher-order harmonics. For instance, in the case of xenon, these dots appear at position 7.5, 8.5 and 9.5, and are thus induced by the 15th, 17th and 19th harmonic order. Since the 21st and higher orders are much weaker, no second order dots appear at position 10.5 and higher. The small, bright harmonic spots originate from the short trajectories with a small phase coefficient α_{short}, as discussed in Section 2.2.4. For some harmonic orders, a fainter, larger halo is visible, for example in case of the 13th and 15th harmonic in xenon, originating from the long trajectories with a much larger value of α_{long} [244]. Since we are only interested in the phase-coherent short trajectories for spectroscopy, we will focus on these from now on.

From Figure 5.6, it becomes clear that the number of generated harmonics varies with

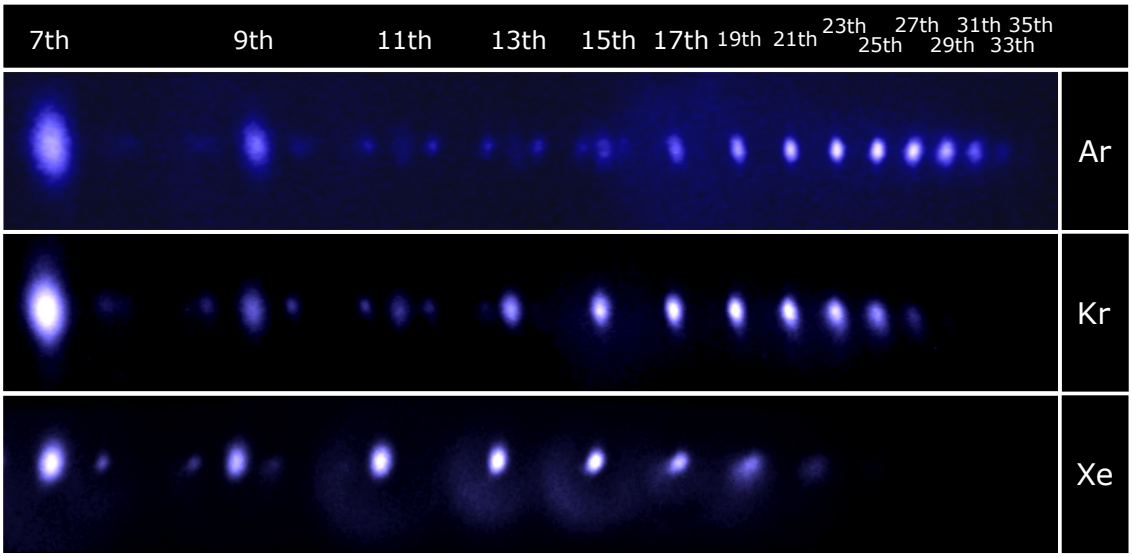

Figure 5.6: Fluorescence images of various harmonic orders for three different target gases on a screen coated with sodium salicylate. The faint dots located between the odd harmonic orders originate from second-order diffraction from the grating mirror. The intensities of the various orders for the same gas are to scale, the different images for different gases are not. The harmonic orders for xenon are slightly offset horizontally due to a different position of the fluorescence screen.

the gas species used. The cut-off energy depends on the the ionization potential of the atom (Equation (2.24)). Since the ionization energy increases from heavier to lighter noble gases, the cut-off energy and highest generated harmonic order increases in a similar fashion.

In Figure 5.7, the vertically integrated intensity of the fluorescent screen is shown for xenon gas at a pressure of 5 bar and 5.6 kW circulating laser power. The harmonic position is translated to a linear wavelength scale. In order to estimate the output power, each harmonic order is integrated over the gray area. The resulting total intensity is calibrated using the photodiode, as will be discussed in short. Below 100 nm, the fluorescence of the sodium salicylate is no longer constant and an additional correction is necessary for the 7th and 9th order [243]. Using xenon gas, we observe harmonics up to the 23th order.

In Figure 5.8, the harmonic spectrum obtained with a krypton target gas is shown. A larger backing pressure is needed for an optimal yield. At 8 bar, harmonics up to the 29th order are observed. In accordance with Figure 2.10, the phase-matching pressure for argon is higher than that of krypton and xenon.

The harmonic spectra shown in Figures 5.7 - 5.9 were obtained while operating the cavity in scan mode. That means, a sawtooth voltage was applied to the PZT, scanning the cavity length back and forth. In this way, the XUV exposure of the mirrors is decreased

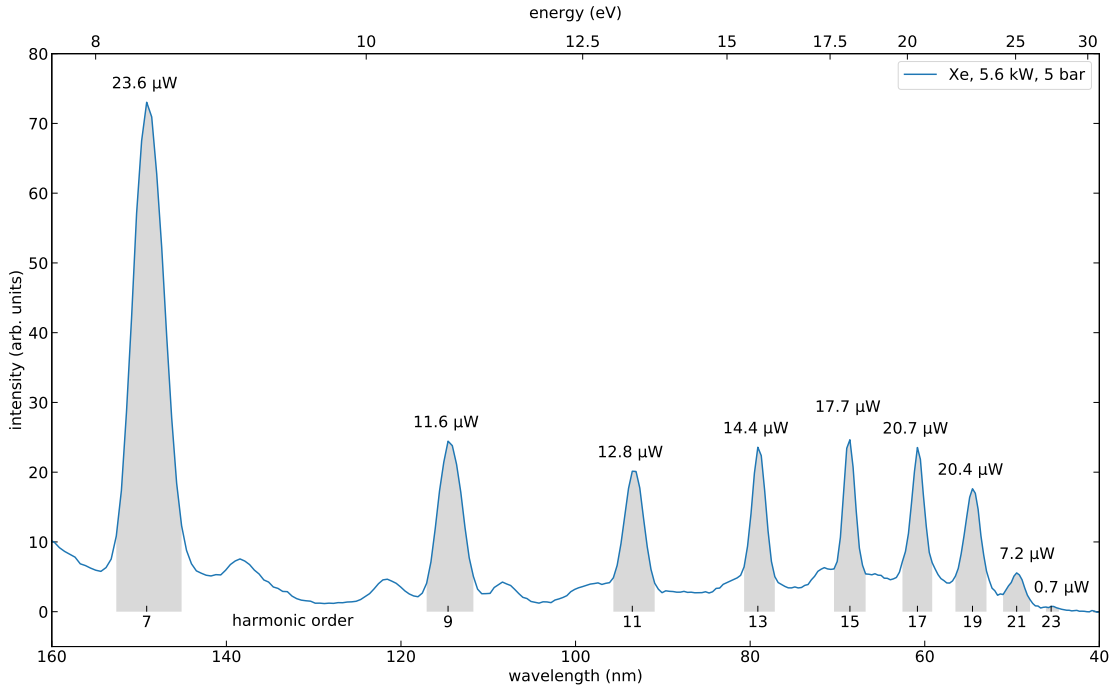

Figure 5.7: Vertically integrated fluorescence signal for xenon target gas with 5 bar backing pressure and 5.6 kW intra-cavity power. The indicated harmonic powers are obtained by integrating over the gray areas and calibrated using a GaAsP photodiode measuring the 15th harmonic.

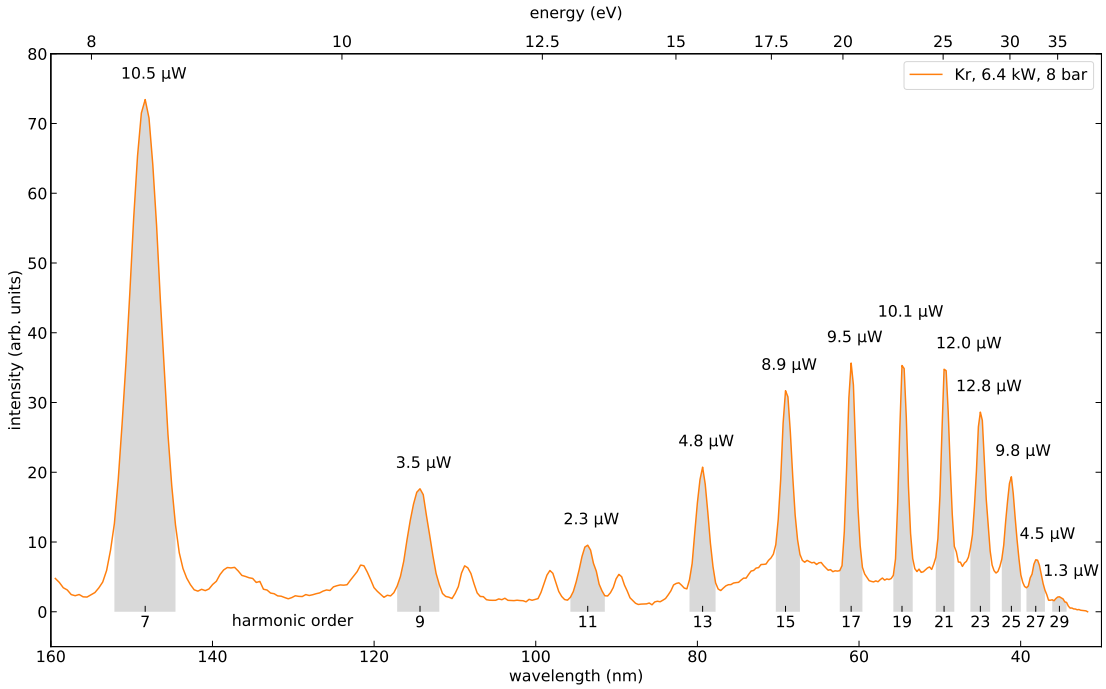

Figure 5.8: Integrated fluorescence spectrum for krypton gas with 8 bar backing pressure and 6.4 kW circulating power. The harmonic powers are calibrated using a photodiode observing the 15th harmonic.

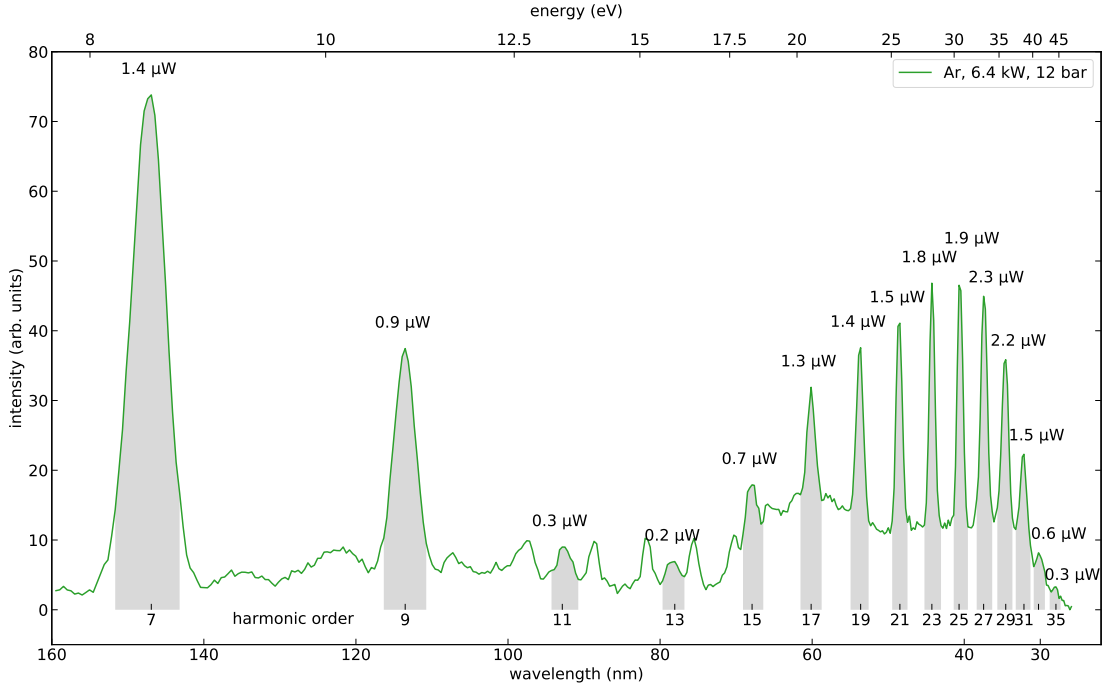

Figure 5.9: Integrated fluorescence spectrum for argon gas with 12 bar backing pressure and 6.4 kW. The harmonic powers are calibrated using a photodiode observing the 17th harmonic.

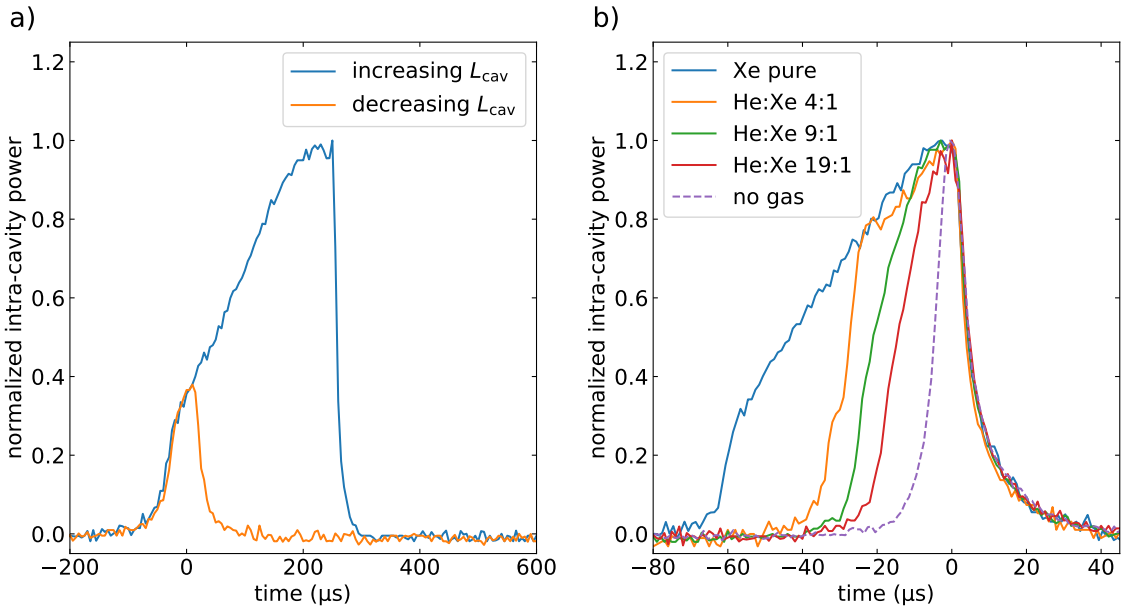

Figure 5.10: Cavity transmitted intensity while the scanning its length across the main resonance peak. a) comparison of scanning direction. When the cavity length is increased, the steady-state plasma phase shift causes a broadened lineshape, while for decreasing length, the resonance is narrower and smaller. b) This effect is decreased when using gas mixtures to increase the speed of the Xe atoms such that the amount of steady-state plasma is lowered.

by roughly two orders of magnitude compared to when the cavity would be locked, while still harmonics can be observed. In Figure 5.10a), the circulating power is shown during such a scan with 2.5 bar of xenon. A large asymmetry of the resonance lineshape arises between the forward and backward direction of the sweep. This effect can be attributed to the generation of plasma in the cavity focus, and is known as plasma-induced cavity bistability [79, 82, 155]. Over short timescales, comparable to the pulse length, nonlinear phase shifts limit the maximum peak intensity, while for longer timescales, involving many pulses, the steady-state plasma induces a phase shift that can significantly shift the fsEC resonance. From Equation 2.39, we know that plasma adds a negative phase-shift to the cavity dispersion, whereas neutral gas adds a positive shift (Equation (2.38)). Therefore, the plasma shifts the cavity resonance to higher frequencies. For the fixed laser frequency to stay at resonance, the cavity length must be increased to compensate the plasma phase shift. This is indeed what is observed from the blue line in 5.10a); an increasing cavity length can partially compensate the plasma phase shift and the cavity stays in resonance with the laser much longer than it would without plasma. For the opposite direction (orange solid line), the negative plasma phase further decreases the effective cavity length and causes the cavity to sweep over the resonance even faster. The resulting resonance is therefore narrower and smaller than it would be without the plasma present.

In order to calibrate the harmonic yield that is observed from the fluorescence screen, the powers of the 7th up to the 17th harmonics were measured by the photodiode, both in scan mode and with the cavity locked to resonance. When scanning, the harmonic power is extrapolated from the time the cavity spends on resonance. To remove the ambiguity between the two different lineshapes arising from the scan direction, an asymmetric scan was used, where the decrease in cavity length was swept 19 times faster than the increase. In this way, the resonance peak width and height during a decreasing cavity length are reduced further, and the HHG signal from this peak becomes negligible. To reduce the influence of vibrations on the resonance lineshape, the scan rate was increased to 500 Hz, with an amplitude of $\Delta L = 0.76\,\mu$m. The resulting measured powers are shown in Figure 5.11. For the harmonic orders 11 up to 17, there is a fair agreement between the scanned and locked values, however for harmonic 7 and 8, the fluorescence signal is much larger than the photodiode signal. This could be due to the larger divergence of these low-order harmonics. The harmonic beam could therefore be clipped by the finite size of the hole in front of the photodiode. Also, the fluorescence yield of the sodium salicylate is not completely clear above 100 nm [243]. Excluding the latter two harmonics, a rough calibration for the intensity observed from the screen can be obtained, with an estimated uncertainty of 20%. Deviations could be due to errors in the integration limits of the individual harmonics and to inhomogeneities in the thickness of the layer of sodium salicylate on the glass plate.

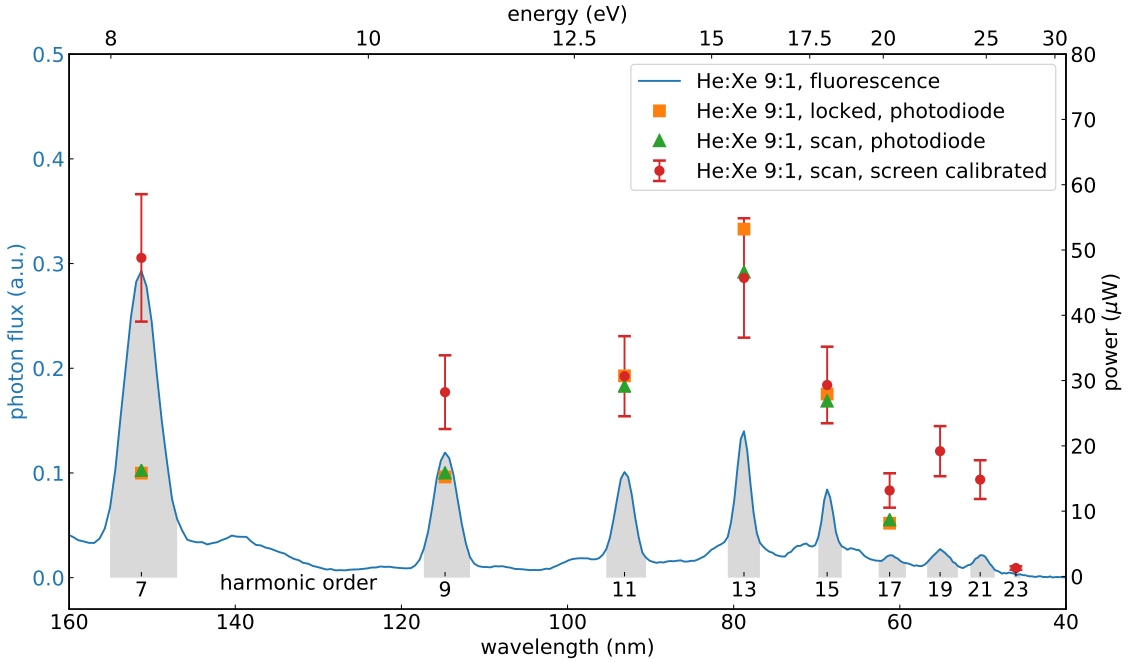

Figure 5.11: Power calibration of the harmonic spectrum for the He:Xe 9:1 mixture. The fluorescence of the screen is shown by the solid blue line. The harmonic powers measured with the photodiode in scanned and locked cavity operation are shown in orange and green, respectively. From the integrated photon flux of the fluorescent screen (grey areas), the harmonic powers are calculated (red circles, right axis). Deviations below 100 nm are likely due to larger divergence of the harmonics and non-constant fluorescence of the sodium salicylate.

In Figure 5.3, the behavior of the intra-cavity power is shown while 1.8 bar of xenon (orange) and 8 bar of krypton (green) are injected. Above roughly 5 kW for xenon and 7 kW for krypton, the circulating power does not increase further when then incident power is raised. This effect, known as intensity clamping, can be attributed to a dynamic frequency change over the duration of the pulse, caused by the increase of the ionization fraction during the laser pulse [83]. When the resulting phase change is larger than $\pi/\mathcal{F}$, the cavity enhancement is decreased. The circulating power thus clamps at a value where the phase shift roughly equals $\pi/\mathcal{F}$. To increase the attainable cavity power, the finesse could be lowered or the pulse length could be decreased. While reducing the finesse without increasing the incident power will result in a lower circulating power and is therefore not very promising, pulse compression has been shown to increase the circulating power [83]. Since we cannot further compress the pulses with the current setup, we turn our attention to reducing the amount of steady-state plasma, as will be discussed in the next section.

5.4 Reducing steady-state plasma

The accumulation of plasma over the timescale of many laser pulses, and the subsequent formation of a steady-state plasma, prevents matching of the phase velocities of the driving and harmonic fields. To further increase the XUV output power, the interaction time of the gas atoms with the laser field must be minimized [80]. We are thus interested in the time it takes a xenon ion to travel through the ion-generation volume, which we label τ_{ion}. The size of this volume strongly depends on the laser intensity and ionization fraction. It is therefore useful to define a second parameter, that only depends on other experimental parameters, τ_{beam}, as the transit time of a target gas atom through the focal volume of the laser beam. We will now briefly explain how both parameters can be calculated.

τ_{ion} is defined as the flight time of an ion through the FWHM of the ionization probability profile of a single pulse: $\tau_{\mathrm{ion}} = \eta_{\mathrm{FWHM}}/v_{\mathrm{gas}}$, where v_{gas} is the speed of the gas. As discussed in Section 2.2.2, the ionization fraction after interaction with a single laser pulse η_{pulse} can be estimated by

$$\eta_{\mathrm{pulse}}(r) = 1 - \exp\left(-\int_{-T_{\mathrm{rep}}/2}^{T_{\mathrm{rep}}/2} w\left(x,t\right) \mathrm{d}t\right), \tag{5.1}$$

where $w\left(x,t\right)$ is the ionization rate that can be calculated using ADK theory. This expression and the ADK rates were evaluated numerically using publicly available code repositories [102].

In a similar way, we set $\tau_{\mathrm{beam}} = \sigma_{\mathrm{FWHM}}/v_{\mathrm{gas}}$, with $\sigma_{\mathrm{FWHM}} = \sqrt{2\ln 2}w_0$ the FWHM of the laser intensity profile. The translational velocity of the gas perpendicular to the laser

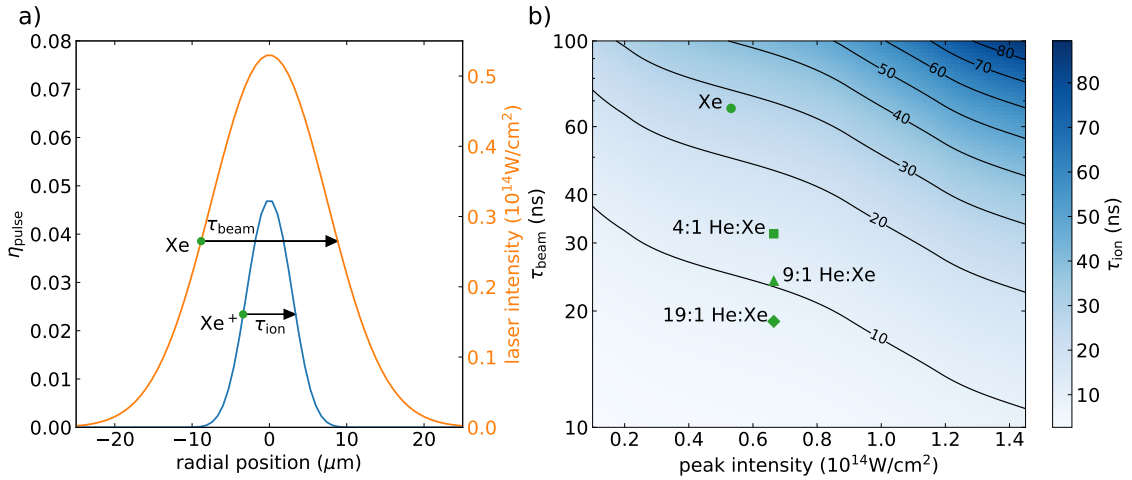

Figure 5.12: Plasma formation in the interaction region. a) radial profile of the driving laser intensity (orange) and ionization fraction η (blue) for 4 kW of circulating power. The FWHM of both profiles define τ_{beam} (τ_{ion}) as the time it takes an atom (ion) to leave the focal (generation) volume of the laser. b) color map of τ_{ion} as function of τ_{beam} and the laser intensity. Since the time between two laser pulses is 10 ns, steady-state plasma accumulates when the ions need longer than that to clear the generation volume. Using helium mixtures increases the speed of the atoms and ions, as indicated by the green markers that represent the experimental conditions for optimal yield of the 15th harmonic. Graphical representation inspired by G. Porat and C. Benko *et al.* [80, 132]

propagation direction is given by [80]

$$v_{\text{gas}} = \sqrt{5RT/M_{\text{avg}}}, \tag{5.2}$$

where R is the ideal gas constant, T the gas temperature and M_{avg} the average molar mass of the gas. In Figure 5.12a) the laser intensity and ionization probability profiles are shown. Their relation to the parameters τ_{beam} and τ_{ion} is also sketched. When the time between two laser pulses, in our case 10 ns, is smaller than τ_{ion}, the amount of plasma starts to accumulate over multiple pulses, resulting in a nonzero steady-state ionization fraction η_{steady}.

Phase-matching can thus only be achieved when the steady-state ionization fraction becomes smaller than the critical ionization, $\eta_{\text{steady}} \lesssim \eta_{\text{crit}}$ as discussed in Section 2.2.7. This means that $\tau_{\text{ion}} \lesssim T_{\text{rep}}$ must hold, such that the ion generation volume is cleared of any remaining ions between two consecutive pulses. In Figure 5.12b), the calculated values of τ_{ion} are plotted for the case of xenon in a colormap as a function of the laser peak intensity. On the left vertical axis, τ_{beam} is indicated, which is independent of laser intensity. The values of τ_{ion} and τ_{beam} for the generated harmonics shown in Figure 5.7 are indicated by the green dot labeled 'Xe'. Almost three pulses pass before the majority of the ions has left the generation volume.

In order to reach the phase-matching regime at a laser repetition rate of 100 MHz, we need to decrease τ_{ion} to below 10 ns, thus the speed of the gas has to be increased. Equation (5.2) indicates that, to boost the gas velocity, we can either increase the temperature or decrease the mass of the gas. Increasing the temperature would in practice mean heating the nozzle to several hundred degrees Celsius in order to make a significant difference. Since the already complicated design of the nozzle inside the differential pump system makes it very hard to implement heating to these temperatures, we have chosen to reduce the average mass of the gas. This can be done by mixing the generation gas, xenon, with a lighter carrier gas, for instance helium [80]. At room temperature, the gas speed of xenon is 306 m/s. Adding helium increases the average speed of the mixture to 1084 m/s for a 19:1 Xe:He mixing ratio. This is sufficient to reach the single-pulse regime, as becomes clear from Figure 5.12b). Due to its much higher ionization potential, helium does not contribute to the HHG process nor does it add additional plasma. The dispersion is comparable to xenon and the absorption can be neglected for harmonic orders below the 21st.

In Figure 5.13, we show the yield as a function of xenon backing pressure for harmonic orders up to the 21st. For pure xenon, most of the harmonics have their maximum yield at a backing pressure af 4 bar. The density in the interaction region is estimated to be 10% of the backing pressure for a gas nozzle diameter of 50 μm at a distance of 100 μm

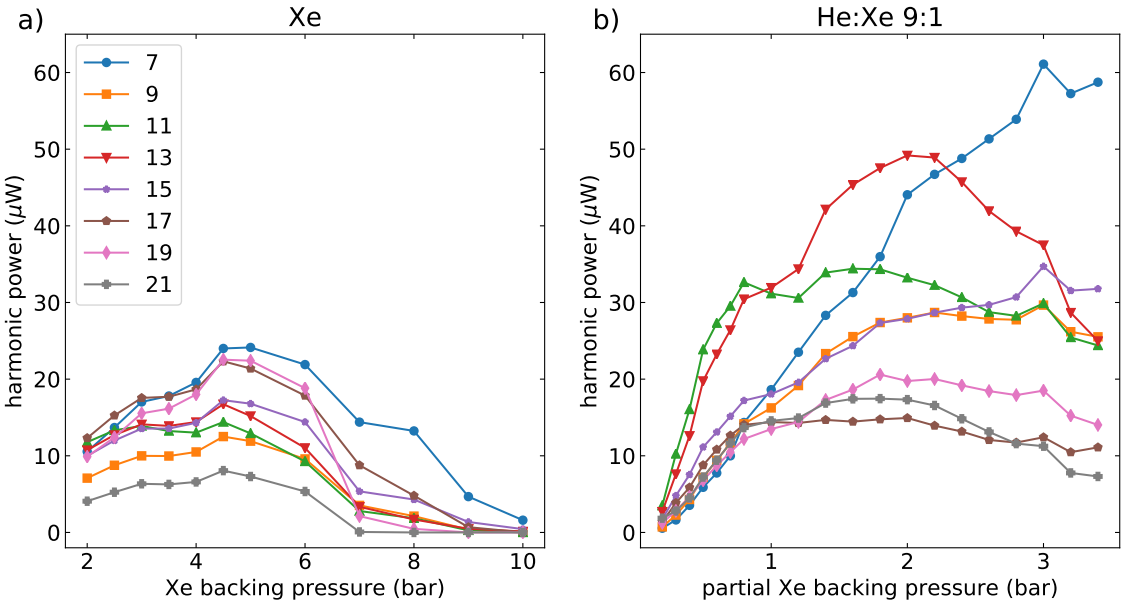

Figure 5.13: Power of various harmonics as a function of xenon backing pressure for pure xenon and a 9:1 He:Xe mixture, measured by integrating the fluorescence signal from the screen and using the calibration shown in Figure 5.11. The data was taken while sweeping the cavity length over a resonance. A clear improvement of the harmonic yield for the gas mixture is visible.

from the nozzle orifice [82]. A phase matching pressure of 400 mbar is in accordance with the calculated pressures in Figure 2.10. For the 9:1 He:Xe mixture, the yield of most harmonic orders is increased significantly. For the 17th and 19th harmonic there is a slight decrease. In order to compare the backing pressures, the partial xenon pressure is indicated, the total backing pressure thus being ten times higher. Due to limitations of the vacuum pumps, as mentioned in Section 3.4.5, the maximum partial xenon pressure was limited to 3.4 bar, although it seems as if higher pressures would increase the yield for some harmonics even further.

In Figure 5.10, the lineshape of the cavity resonance is shown for the different gas mixtures. For comparison purposes, the resonance heights were normalized. The cavity bistability effect is decreased with an increasing mixing ratio, clear evidence for the fact that the amount of steady-state plasma is lowered. The most prominent improvement is achieved when switching from pure xenon to a 20% Xe mixture. Using larger mixing ratios further reduces the resonance linewidth by smaller amounts. This can be understood from Figure 5.12b), where it can be seen that switching from pure xenon to a mixture with 20% xenon results in the largest decrease of τ_{ion} and τ_{beam}. Closer to the single-pulse regime, when both values approach 10 ns, the improvements become smaller.

To verify that the increase of harmonic yield is not solely caused by an increase of

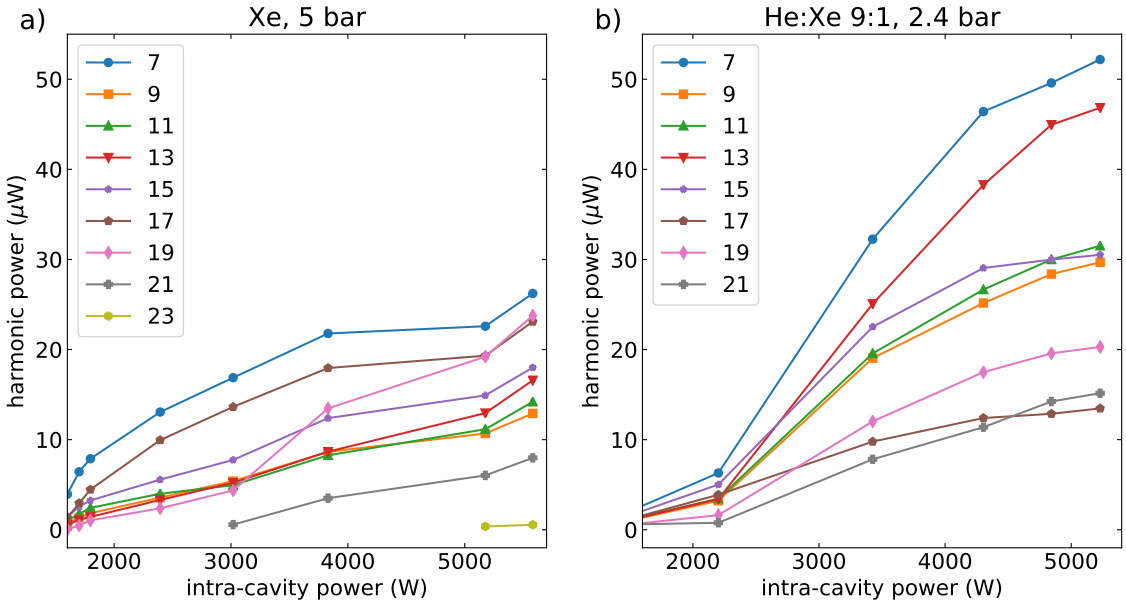

Figure 5.14: Harmonic power as a function of circulating cavity power for pure xenon (a) and a 9:1 He:Xe mixture (b), measured by integrating the fluorescence signal from the screen and using the calibration shown in Figure 5.11. The data was taken while sweeping the cavity length over a resonance.

intra-cavity power due to reduced non-linear plasma effects for the gas mixtures, we show the harmonic yield as a function circulating power in Figure 5.14. The fluctuations in the harmonic yield of individual harmonics with increasing laser intensity, for instance the 19th harmonic for pure xenon, can arise from the interference between contributions from the different electron trajectories in the generation process [244]. It is clear that for the 9:1 He:Xe gas mixture, the yield of most harmonics is higher for the same circulating power. For pure xenon, the harmonic yield saturates around 4 kW of circulating power, while for the mixture, no such saturation is observed. This could be due to the ionization fraction increasing above η_{crit} for high laser intensities and pure xenon, therefore deteriorating the phase matching conditions and reducing the harmonic yield. For the gas mixture, no saturation is observed. The lower amount of η_{steady}, causes the ionization fraction to stay below η_{crit} even for higher laser intensities, increasing the harmonic yield. Remarkably, the yield of the 17th and 19th harmonic is lower for the gas mixture than for pure xenon, as was also observed for the pressure scans.

In order to disentangle the effect of phase-matching from other intensity-dependent effects on the harmonic yield, we have determined the intensity-dependence of the single atom response [80, 245]. We observed the harmonic yield as a function of intra-cavity power for a very low backing pressure of 900 mbar. With such a low density, reabsorption of harmonics becomes negligible and the phase mismatch Δk from Equation (2.34) only

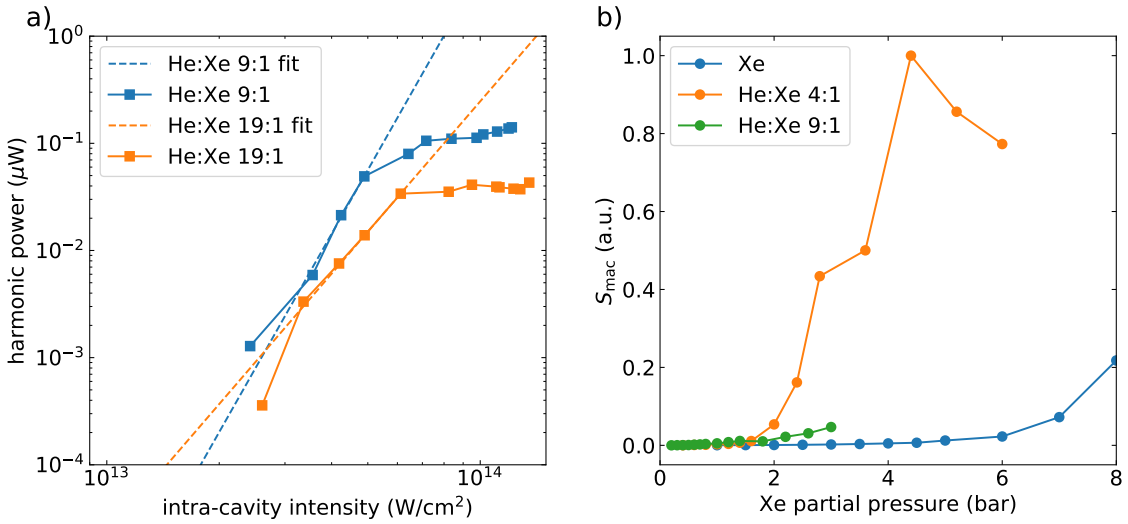

Figure 5.15: Single atom response of xenon, measured at a 900 mbar total backing pressure. At low circulating power, the harmonic yield scales as I^{N_q}, and the value for N_q is determined from the fits in a) to be 5.1 ± 0.4. The macroscopic response is then given by the yield divided by the single atom response, as shown in b). The peak for the 4:1 gas mixture indicates phase matching, while a global maximum is not observed for the 9:1 mixture. The latter is probably due to the limited pressure range originating from the vacuum pumps.

depends on ϕ_{Gouy}. Plasma-related effects on both the cavity performance and phase-matching are thus minimized. In Figure 5.15a), the 15th harmonic power is plotted for various laser intensities. For low laser intensities, $\eta \ll 1$ and the harmonic yield scales as the single atom response I^{N_q}. Here, N_q is a fitting parameter for harmonic order q, which is smaller than the value of q for high-order harmonics. From the low-intensity part of the scan, we determine $N_q = 5.1 \pm 0.4$ from measurements using the 9:1 and 19:1 He:Xe mixtures, which agrees with previous results [80, 245]. Now we can divide the harmonic power S_q by the scaling of the single atom response to obtain the macroscopic yield: $S_{\mathrm{mac}} = S_q / I^{N_q}$. The result is shown in Figure 5.15b) for the 15th harmonic, where the effects of a varying laser intensity no longer make any difference. A peak is observed for the 4:1 He:Xe mix around 4 bar, indicating that this is the pressure for which phase-matching takes place, as was discussed in Section 2.2.7. For pure xenon, no clear peak is observed, while for the 9:1 He:Xe mixture, the datapoints are limited to below 3 bar and more data at higher pressures is needed to determine whether a peak will appear. These findings indicate that the increased harmonic yield that is observed by using He:Xe gas mixtures is most likely due to improved phase-matching conditions.

In Figure 5.16, the power of the 15th harmonic is shown for various backing pressures of xenon and different gas mixtures. In a), where the cavity length was scanned, the

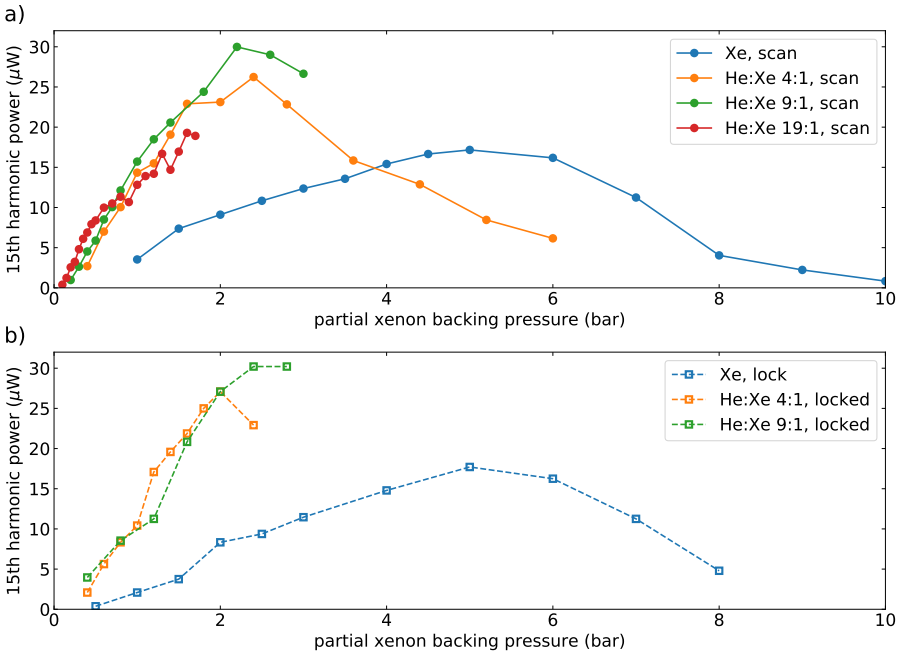

Figure 5.16: Power of 15th harmonic as function of (partial) backing pressure for different gas mixtures, while scanning the cavity length (a) and locking the cavity on resonance (b). The maximum backing pressure of the 9:1 and 19:1 He:Xe mixtures was limited by the fore-vacuum pumps.

gas mixture (He:Xe)	backing pressure (bar)	τ_{beam} (ns)	τ_{ion} (ns)	peak intensity (10^{14}W/cm^2)	15th harmonic power (μW)
Xe	5	67	30	0.71	17
4:1	2.4	32	12	0.47	26
9:1	2.2	24	11	0.71	30
19:1	1.6	19	9	0.74	19

Table 5.2: Experimentally optimized parameters that yield maximum 15th harmonic power for the different gas mixtures.

improved power output for the gas mixtures is clearly visible. The largest improvement is again caused by switching from pure xenon to a 4:1 He:Xe mixture. The 9:1 mixture results only in a modest increase, while for the 19:1 mixture the maximum pressure was limited to below the phase-matching pressure. This suggests that the 4:1 He:Xe mixture already brings the system close to the single-pulse regime, as is confirmed by Figure 5.12b). Increasing the mixing ration further is expected to improve the harmonic yield by smaller amounts [80]. A similar conclusion can be drawn from Table 5.2, where the experimental parameters for optimal 15th harmonic yield are summarized. The largest yield increase from pure xenon to the 4:1 He:Xe mixture is accompanied with the most significant decrease of τ_{beam} and τ_{ion}.

In Figure 5.16b), we show the harmonic yield while the cavity is locked. The measured powers are very similar to those in a), which were obtained while sweeping the cavity. This shows that the setup can be reliably operated while producing continuous XUV output, and no immediate degradation is noticeable. Since, ultimately, we are interested in uninterrupted HHG for spectroscopy, we will test the long-term stability of our setup in the next section.

5.5 Continuous operation

To demonstrate the long-term stability of our experimental apparatus and investigate possible mirror degradation issues, we have monitored the XUV output over the course of several hours while the cavity was locked to resonance. The results are shown in Figure 5.17, where in a) the power of the 15th harmonics is plotted using pure xenon at 5 bar backing pressure. At short timescales below 100 s, the harmonic power is stable to within 15 %, as is shown in the inset. Over the course of several minutes, the output shows drifts which are probably of thermal origin and are visible as oscillations in the long-term measurement. The two large drops in the signal are cases where the cavity lost its lock for a short moment, which can be caused, for instance, by the CEO frequency drifting too far or excess vibrations. The right inset shows the intra-cavity power for short timescales below 20 ms. The IR power is stable within 6%, except for negative spikes that are induced by vibrations from the vacuum pumps. In b), the powers of the 13th up to the 19th harmonic are recorded using the fluorescence screen. The oscillations of the 15th and 19th order are due to variations in the intra-cavity power, which are probably caused by alignment effects, as will be discussed in the next section. The oscillations are strongest for the 19th harmonic, since the yield of this order depends most strongly on the laser intensity in the range between 3 and 4 kW, as can be seen from Figure 5.13.

During this measurement, ozone was injected in the vacuum chamber to prevent degradation of the grating and cavity mirrors, as discussed in Section 3.2.7. The oxygen/ozone

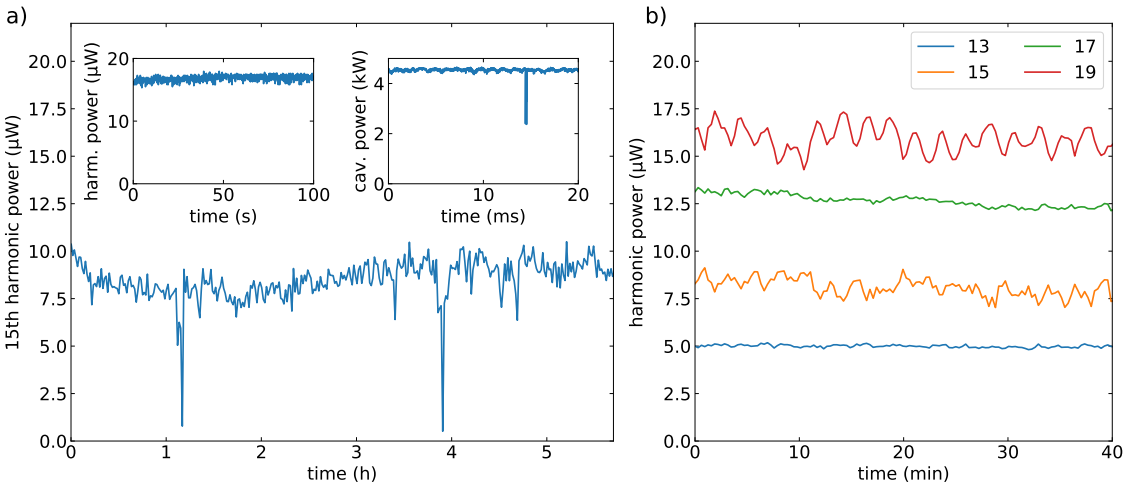

Figure 5.17: Continouos operation of the XUV comb. a) The 15th harmonic output using pure Xe gas was monitored with the XUV photodiode for over more than 5 hours. Long-term fluctuations are most likely due to thermal effects slightly changing the cavity alignment. The two lower spikes are due to the cavity loosing its lock. The left inset shows that the XUV power is very stable on the short term, with only slight thermal drifts. The IR circulating power is shown in the right inset. b) power of the 13th up to the 19th harmonic over a time period of 40 minutes, simultaneously measured using the fluorescence screen.

mixture increased the pressure in the main chamber to $1{\cdot}10^{-3}$ mbar. The cavity power slightly decrease over time, which can be attributed to thermal drifts that can be compensated by realignment, as will be discussed in the next section. Apart from these drifts, we have not observed any signs of degradation of the IR mirrors over the course of the measurements presented in this chapter. Also, we have not observed a decreased XUV outcoupling efficiency due to filling of the grooves of the grating mirror over more than five hours of continuous operation, as becomes clear from Figure 5.17.

5.6 Discussion

Although the pointing stability of the laser system is excellent, the cavity needs regular readjustments during operation at high power. Due to the narrow stability region, the cavity mode is rather sensitive to misalignments. When operating at low intra-cavity powers or in scan mode, this is not much of a problem since the alignment does not change over time. However, when the cavity is locked at kW power levels, the circulating power drops over time and adjustments are necessary to retrieve the initial value. It is clear that these drifts are caused by heating of some part of the cavity, but despite efforts to find the element that causes the largest change [172, 246], to date it is unclear

which mirror contributes most. The grating mirror is cooled via a copper braid, of which the installation did not result in any change in thermal stability. Since the transmission through the HR-coated mirrors is only a few ppm, it seems unlikely that absorption of the PZT element behind the flat mirror is the main problem. Most probably, the curved mirrors contribute to the cavity drifts since the long cavity arms pass close by their edges, as is visible in Figure 3.13. In order to reduce these thermal effects, a cooling system was designed which connects each mirror to a massive water cooled copper body in the vacuum chamber [246]. Furthermore, we are planning to implement machine learning algorithms to automatize the cavity alignment, such that manual intervention is no longer necessary.

One of the drawbacks of the differential pump system is the increased amount of vibrations on the cavity optics, resulting in enhanced relative intensity noise on the intra-cavity power in lock. Despite the use of low-vibration, magnetically levitated turbopumps and mechanical decoupling of the lower and upper parts of the construction, vibrations are likely transferred by some of the thin sheets touching each other while the translation stage below the lower part is moved in order to align the nozzle with the cavity focus. By design, this could be prevented by moving the vacuum chamber to a suitable position where there is no physical contact between the upper and lower sheets, using the adjustable end-stops shown in Figure 3.38. In practice the lever arm of the end-stops is large and optimization of the 3-D parameter space without visual feedback of the sheets turns out to be difficult. In order to provide better feedback and live monitoring of the vibration amplitudes, microphones attached at different locations on the vacuum chamber and laser table could be used. Another possibility would be to provide active feedback to the PZT element at the rotation frequency of the turbopumps, thereby canceling part of the vibrations and exonerating the PDH feedback loop.

As was discussed in Section 3.4.5, the differential pump system improves the main chamber pressure by two orders of magnitude and enables high nozzle backing pressures. However, currently the backing pressure is limited by the capacity of the pumps. Large backing pressures above 25 bar result in mbar pressures at the exit of the differential pump system, which are very harsh conditions for turbopumps. After exchanging the initial pump with one that is designed to work under such circumstances (Edwards STPH301C), we are now limited by the fore-vacuum pump capacity. In order to provide a complete comparison of the different gas mixing ratios, it is necessary to increase the pressure up to 100 bar, and we are therefore expanding the pump capacity as well as increasing the conductance of the vacuum tubing to allow for reaching such backing pressures.

The observed increased harmonic power due to the gas mixtures is substantial. However, it is not as large as what was recently achieved using a comparable apparatus, where generated powers of 2 mW and 0.9 mW were reported for the 11th and 17th harmonics, respectively [80]. With a calculated grating out-coupling efficiency of 10%, we estimate

the generated power for the 13th harmonic to be 0.5 mW. There are several possible causes for this difference. First of all, we could be limited by absorption of the harmonics. In the main chamber the pressure is kept below 10^{-4} mbar so absorption is negligible, but close to the nozzle, in the first stage of the differential pump system, the pressure could be higher. Since the pressure gauge is located in the upper part of the pump system, we do not have a good estimate for the pressure close to the nozzle and it might be well above 1 mbar, which is the regime where absorption can become significant. Because helium absorption is negligible and the partial xenon pressure is similar for the different gas mixtures, this would mean that the relative amount of absorption is independent of the gas mixture used. To find out whether this is the case, more accurate modeling of the harmonic yield could be employed and compare the observed yield with the calculated one. The ADK rates used in Figure 5.12 are known to be inaccurate for low intensities, and could be improved by using PPT theory [247]. Second, the harmonic yield scales quadratically with the number of emitters within the phase-matching region (Equation (2.30)). Since our focus waist is 75% of the reported value [80], our focal area is smaller by 60%. This gives the advantage of reaching higher intensities as well as reduced steady-state plasma effects, but in the ideal case of phase-matched HHG it poses the ultimate limit for the attainable yield. A third possibility is that the out-coupling efficiency of the grating is overestimated. This efficiency is very sensitive to the groove depth, as shown in Figure 3.30. Measuring the groove depth of our grating would improve the knowledge of the out-coupling efficiency.

With its low ionization potential, xenon renders the highest HHG yield of the non-radioactive noble gases. A practical drawback of xenon is the rather high cost. With the gas mixtures, in addition a large amount of helium is consumed, making long-term operation of the XUV comb expensive. To perform accurate frequency determinations, long operation times are however essential and therefore we plan to implement a gas-recycling system. By catching the exhaust gas from the vacuum pumps of the differential pumping system and re-compressing it to high pressures, we will be able to recycle the majority of the HHG gas and enable long-term, cost-efficient operation.

5.7 XUV power benchmark

In conclusion, we have successfully commissioned the first XUV comb at the MPIK. Output powers up to 49 μW were observed, corresponding to a generated power of 0.5 mW and a conversion efficiency of $9.6{\cdot}10^{-8}$, which is comparable to MHz-rate single-pass systems [250]. In Figure 5.18, an overview is provided of out-coupled powers of several high-repetition-rate systems reported in literature. Long-term continuous XUV generation was demonstrated with 8 μW of output power at 69 nm (17.9 eV) for over 5 h without signs of degradation. These results provide an encouraging framework towards direct frequency

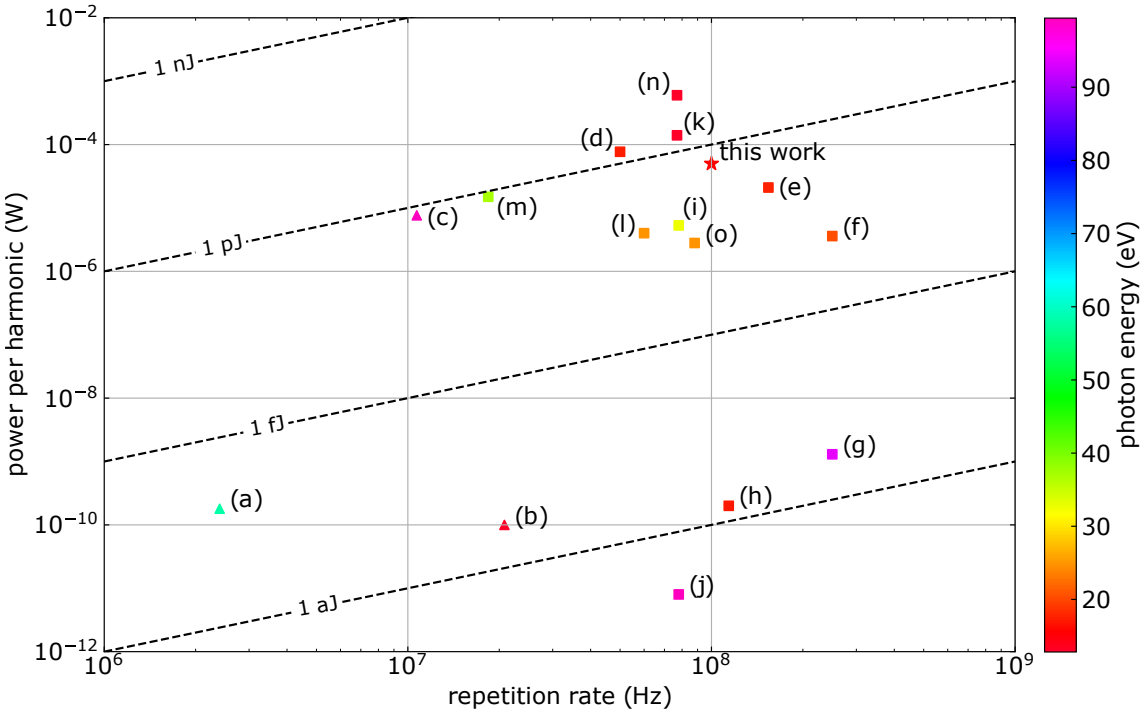

Figure 5.18: Overview of outcoupled XUV powers reported in literature above 10 eV with repetition rates higher than 1 MHz. (a) Emaury *et al.* [248], (b) Vernaleken *et al.* [249], (c) Hädrich *et al.* [250], (d) Lee *et al.* [78], (e) Cingöz *et al.* [86], (f) and (g) Carstens *et al.* [84], (h) Gohle *et al.* [24], (i) and (j) Pupeza *et al.* [83], (k) Porat *et al.* [80], (l) Mills *et al.* [154], (m) Saule *et al.* [251], (n) Zhang *et al.* [184], (o) Corder *et al.* [180]. Single pass configurations are indicated by triangular data points and enhancement cavity results by the squares. The photon energy is illustrated by the marker color.

harmonic order	lower bound (eV)	upper bound (eV)	lower bound (nm)	upper bound (nm)	gas mix (He:Xe)	power (μW)
7	8.34	8.38	147.98	148.74	9:1	59
9	10.72	10.77	115.13	115.65	9:2	28
11	13.11	13.16	94.22	94.60	9:3	34
13	15.49	15.55	79.74	80.03	9:4	49
15	17.88	17.94	69.11	69.35	9:5	32
17	20.26	20.33	60.99	61.19	Xe	22
19	22.65	22.72	54.57	54.74	Xe	22
21	25.03	25.11	49.38	49.53	9:1	17
23	27.42	27.50	45.09	45.22	Kr	13
25	29.81	29.89	41.48	41.60	Kr	10
27	32.19	32.28	38.41	38.51	Kr	4.5
29	34.58	34.67	35.77	35.86	Ar	2.2
31	36.97	37.06	33.46	33.54	Ar	1.5
33	39.35	39.44	31.43	31.51	Ar	0.6
35	41.74	41.83	29.64	29.71	Ar	0.3
35	41.74	41.83	29.64	29.71	Ar	0.3

Table 5.3: FWHM bandwidths of the harmonic orders of the XUV comb. The maximum observed output power available for spectroscopy is also indicated.

comb spectroscopy of highly charged ions in the XUV region. In order to facilitate the selection of suitable candidates transitions in HCI, we provide an overview of the output power and bandwidth estimate of the XUV comb for the different harmonic orders in Table 5.3.

Chapter 6

Conclusions and outlook

The motivation for the research presented in this thesis is to enable ultra-high precision spectroscopy of highly charged ions (HCI) for precision tests of fundamental physics. Since such measurements become more accurate when the measurement frequency is as high as possible, a frequency comb in the extreme ultraviolet (XUV) region was developed.

In order to produce XUV light, a new experimental apparatus was constructed at the Max-Planck-Institut für Kernphysik, described in Chapter 3. First of all, sufficient laser power needed to be generated to drive the nonlinear high harmonic generation (HHG) process. A frequency comb laser system was developed that delivers 200 fs pulses at an average power of up to 80 W at a repetition rate of 100 MHz. Further amplification was achieved by constructing an enhancement cavity, in which femtosecond pulses were resonantly amplified up to a factor of 300. Second, due to XUV radiation being absorbed in air, the enhancement cavity had to be placed in an ultra-high vacuum (UHV) chamber. A tailored design of the vacuum system minimized vibrations from the pumps on the cavity mirrors, while providing stable mounting of the optics in the vacuum and high pumping power. Third, to prevent the high pressure of the HHG gas required for phase-matching in the cavity focus from deteriorating the vacuum in the rest of the chamber, a differential pump system was constructed. Despite tight space constraints near the cavity focus, the three stages of the pump system are able to reduce the pressure in the main chamber by two orders of magnitude.

As a first application of our newly developed enhancement cavity, we performed multi-photon ionization measurements of xenon, as discussed in Chapter 4. Photoelectron spectra were recorded using the velocity-map imaging (VMI) technique, and from the angular distributions resonant Rydberg states could be identified. Over the course of the last few decades, multi-photon ionization (MPI) of xenon has been investigated by many experiments, which has led to a profound knowledge about ionization dynamics in strong laser fields. However, at low intensities close to the ionization threshold, several phenomena are not fully understood, for instance the appearance of asymmetry features in subcycle attosecond streaking [236] and electron anticorrelations in double ionization [234]. Since

the MPI signal rate is steeply dependent on the laser intensity, data-acquisition times become unfeasibly long when the intensity is lowered and kHz laser systems are used. In our system running at 100 MHz, we can acquire photoelectron spectra orders of magnitude faster than conventional lasers, and therefore study MPI at much lower intensities. At stronger fields, the high repetition rate also results in high count rates compared to low-rate systems, since space charge effects force one to limit the electron yield to one per shot at most.

My results demonstrate the feasibility of using an enhancement cavity for ionization studies. Currently, a new cavity, which will be polarization-insensitive, is being constructed in our group. Together with an improved electrode design, integrated nozzle and sufficient shielding, we will be able to reach a higher energy resolution than now. These improvements will also allow for longer data-acquisition times and thus enable going to even lower intensities. Besides, the three-dimensional shape of the photoelectron wave packets could be obtained by tomographic reconstruction from electron spectra taken at different polarization angles [252]. Moreover, in order to probe specific electronic resonances, the laser spectrum could be narrowed using the dispersion properties of the femtosecond enhancement cavity (fsEC), as described in Section 2.5. By using an atomic beam instead of a nozzle in order to reduce Doppler shifts, metastable states could be resonantly populated by multi-photon processes. In this case, many of the frequency comb lines contribute to the excitation, and the metastable states, for instance in the case of helium, can be easily detected by a micro-channel plate [253]. Finally, using two counter-propagating pulses that are both resonant in the cavity will enable pump-probe experiments that could measure ionization time delays [235], with better timing and phase accuracy than currently possible. Since the phases are coherently imprinted on both the outgoing electrons and ions, 100 MHz-modulated matter waves could be produced.

In Chapter 5, the results on the generation of high-order harmonics are discussed. XUV radiation was produced using three different target gases; xenon, krypton and argon. With xenon, harmonics ranging from the 7th up to the 23rd order were observed at intra-cavity powers between 5 and 6 kW. Owing to its higher ionization potential, harmonic orders up to the 29th were observed using krypton. Consequently, with argon we reached the highest harmonic orders, up to the 35th, corresponding to an energy (wavelength) of 42 eV (30 nm). Due to its relatively low ionization potential, the observed harmonic yield was the highest for xenon, with which an average power of 18 μW was detected in the 15th harmonic. To improve the phase matching conditions and raise the harmonic power output, He:Xe gas mixtures were used to boost the speed of the target gas [254]. This reduced the amount of steady-state plasma in the resonator focus, and therefore lowered the effect of the plasma-induced cavity bistability, as is clearly visible from the cavity transmission signal while scanning over the main resonance. With a He:Xe 9:1 mixing

ratio, the yield of the 15th harmonic improved to 32 μW. The highest observed XUV power was 49 μW for the 13th harmonic. Larger gas mixing ratios could likely increase the yield of some harmonic orders even further, but the capacity of the vacuum pumps prevented using sufficiently high partial backing pressures. Finally, continuous operation of the system was demonstrated for a time period of over five hours. During this time, roughly 8 μW was produced at the 15th harmonic and no signs of mirror degradation affecting operation were observed.

This amount of XUV radiation is sufficient to drive transitions in HCI with kHz excitation rates, as was described in Section 1.6. Furthermore, it should be noted that the indicated harmonic powers are directly available for spectroscopy, without the need for further spectral filtering since the outcoupled harmonics are already spatially dispersed by the grating output coupler. Moreover, there is no need for blocking large amounts of parasitic infrared radiation, which is customary for single-pass HHG experiments and induces additional XUV losses. Finally, the demonstrated stable, continuous XUV output over long timescales is crucial for future high-precision frequency determinations.

In Table 6.1, we summarize the performance of the newly built XUV comb and provide some estimates for driving transitions in HCI. $\sim 50\,\mu$W of power in the 13th harmonic is equivalent to a flux of 2×10^{13} photons per second. When focused to a diffraction-limited area of $3.2\,\mu\text{m}^2$ with $f/20$, this results in a spectral brilliance of 7.8×10^{17} photons/(s$\times$mrad$^2\times$mm$^2\times$0.1% bandwidth), which is on the same order of magnitude as a modern synchrotron [255]. Assuming a 100 kHz linewidth of the comb teeth and a similar natural lifetime of the HCI transition, we can expect a fluorescence rate of 21 kHz, which is sufficient for direct detection. However, both the coherence time of the laser and the excited state lifetime are much shorter than the time it takes to build up a significant population fraction, such that Rabi oscillations will not be visible. This changes when the comb is stabilized to a 1 Hz linewidth [256], such that equally narrow, forbidden transitions could be probed. Although now the fluorescence rate is limited to 0.5 Hz by the spontaneous emission rate, Rabi flops with a 54 ms π-time could be observed using quantum logic spectroscopy [59].

Recently, the first cold Be^+ ions were observed in the superconducting cryogenic Paul trap experiment (CryPTEx) II, as is shown in Figure 6.1. Crystals as well as individual ions can be cooled to temperatures ≤ 25 mK and stored for over 12 hours. Simultaneously, an electron beam ion trap (EBIT) delivers highly-charged ions which are slowed, bunched and subsequently transferred to the Paul trap. The next steps will include sympathetic cooling and co-trapping of the HCI with the Be^+ ions and the installation of a Raman laser system for sideband cooling of the ions to the motional ground state. This part of the experiment is currently located in a separate laboratory, and in order to provide XUV light to the ions, the EBIT, the Paul trap, the beamline connecting the two and the

harmonic order	13	
power per harmonic (μW)	50	
flux per harmonic (photons/s)	2.0×10^{13}	
flux per comb tooth (photons/s)	2.9×10^{8}	
average intensity per tooth (W/cm^2)	2.2×10^{-2}	
focal area[1] (μm^2)	3.2	
average brilliance[2] (photons/(s$\times$mrad$^2\times$mm$^2\times$0.1% BW)	7.8×10^{17}	
comb linewidth (Hz)	1×10^{5}	1
spectral photon density (photons/Hz$_{\mathrm{BW}}$/s)	2.2×10^{2}	2.2×10^{7}
excited state lifetime (s)	1.6×10^{-6}	0.16
saturation intensity (W/cm^2)	2.6×10^{-2}	2.6×10^{-7}
fluorescence rate[3] (Hz)	2.1×10^{4}	0.5
Rabi flopping time[4] (ms)	0.17	54

Table 6.1: Estimated XUV yield parameters, starting with a 100 MHz, 200 fs pulse train with a bandwidth of 14 nm centered at 1039 nm. Two different cases are examined, one with a laser linewidth of 100 kHz and a similar natural linewidth of a HCI transition, and one where the laser is stabilized to a 1 Hz linewidth and is used to drive a 1 Hz forbidden transition. [1]The XUV focal area was estimated from the divergence of the harmonic beam [83] and a $f = 150$ focusing optic at a distance of 1 m from the generation volume, neglecting the spatial chirp due to the angular dispersion of the grating. [2]The average brilliance was estimated at the XUV focus and assuming a constant intensity distribution over the harmonic bandwidth (BW). [3]In case of the 0.16 s excited state lifetime, the fluorescence rate was limited by the spontaneous emission rate. [4]The indicated time is an estimate for the duration of a π-pulse that takes all population into the upper state: $t_\pi = \pi/\Omega$, with Ω the Rabi frequency.

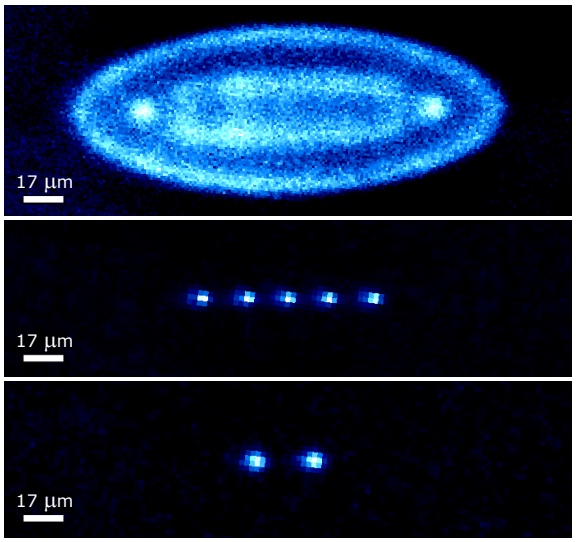

Figure 6.1: First ions in the superconducting Paul trap in Cryptex II. a) ion crystal consisting of several tens of ions. In b) and c) strings of 5 and 2 ions, respectively, are shown that are located at the trap axis. Figure from J. Stark [257].

low-vibration 4 K cryostat need to be moved to the container with the XUV comb. As briefly described in Section 3.3.3, the Paul trap will be mounted on the same laser table as the XUV comb, while the EBIT and cryostat, being the more noisy parts of the setup, will be placed outside the container. A differentially pumped vacuum beamline will then connect the vacuum chamber of the fsEC with the Paul trap. The harmonics, after being spatially filtered, will be focused on the HCI with a reflective curved optic under grazing incidence.

Since the linewidth of the comb is currently on the order of a few hundred kHz, it will be favorable to first look for a transition that has a similar natural linewidth and thus a sufficiently high excitation rate. For instance, the $^3P_1 \rightarrow {}^1S_0$ transition in Ca^{8+} could be used. At an energy of 17.9 eV, it falls within the bandwidth of the 15th harmonic of the comb (see Table 5.3) and has a suitable natural linewidth of roughly 220 kHz [258]. After the comb linewidth has been reduced by referencing to an ultra-stable cavity, also narrower lines could be probed. For example, the transition in $^3P_2 \rightarrow {}^1S_0$ in Sc^{9+} with an energy of 20.4 eV lies close to the 17th harmonic and has a linewidth of 86 mHz. Further down the road, particular transitions with a high sensitivity to α or μ could be probed, towards providing new limits of the time variation of these fundamental constants. Furthermore, the XUV comb could be employed to search for the nuclear transition in the thorium isomer, since the 7th harmonic, with a full-width half-maximum between 8.34 and 8.38 eV, overlaps with the currently most accurate energy determination of the isomer state, $E_m = 8.28 \pm 0.17$ eV [259]. Recent proposals for exciting the isomer by irradiating

a sample of ^{229}Th atoms deposited on a surface with an XUV comb [260] or through the electronic bridge mechanism in a highly charged ionic state [261] provide exciting prospects for the near future.

In summary, this work has resulted in a frequency-metrology capable XUV comb with long-term stability and a UHV residual gas purity level. The laser delivers sufficient flux for driving HCI transitions and is adapted for performing ultra-high precision spectroscopy due to its mechanical stability inside a low-noise environment. Furthermore, a novel VMI with unique features will enable low-intensity, high-precision measurements in the non-linear multi-photon regime. These results pave the road for the most accurate test of beyond the Standard Model physics and a novel generation of frequency standards running at XUV frequencies.

Appendix A

XUV outcoupling methods

While generating high harmonics inside a cavity brings the advantage of access to high repetition rates and high average power, it comes with an additional challenge of separating the XUV radiation from the resonant cavity beam. Since the latter is very sensitive to losses or dispersive effects, as discussed in the previous section, it is very important that the XUV optics minimally affect the circulating driving light. The generated harmonics are absorbed by almost any material, therefore standard beam-separation techniques such as using dichroic mirrors do not work, and a more sophisticated solution is needed. The ideal output coupler possesses the following properties [262, 263]:

- High XUV outcoupling efficiency.
- Broad outcoupling wavelength range.
- Small dispersion for the IR beam.
- Low thermal lensing (meaning high thermal conductivity and low thermal expansion).
- Low other losses (absorption, scattering, etc.) for the IR beam.
- High damage threshold.

In the following, an overview of various proposed and experimentally verified XUV outcoupling methods in literature is given.

Brewster Plate

The simplest and most widespread method to couple out XUV light from a cavity is the Brewster plate, which has been used in various intra-cavity HHG experiments [23, 24, 78, 85, 152, 264]. Usually, a thin sapphire or fused silica plate is used for minimal dispersion and non-linear effects. Typical outcoupling efficiencies are about 10%. However, the dispersion induced in the plate needs to be compensated by the cavity mirrors in some

way. A thin plate suffers from a bad heat dissipation in the vacuum and induces therefore some thermal lensing. Moreover, the delicate plate has a reduced damage threshold and the cavity beam suffers from nonlinearities inside the material. A study of different Brewster plate materials, thicknesses and their performance has been carried out by I. Pupeza *et al.* [265]. The authors conclude that a 100 μm fused silica plate gives the best results and can be used up to 4 kW intracavity power for 200 fs pulses without significant degradation.
Main limitations include:

- Low XUV outcoupling efficiency $<\lesssim$10 %.
- Low heat conductivity.
- Large dispersion.
- Low damage threshold.
- Poor optical quality due to the small thickness.

Main advantages:

- Low losses for the IR beam.
- Easy to implement.

Grazing incidence plate

The principle of the grazing incidence plate (GIP) is similar to a Brewster plate, except that the plate is placed under grazing incidence angle in the IR beam path. Because of the grazing angle, the reflection efficiency of the XUV light is large, while the plate can be anti-reflection (AR) coated to minimize the IR losses. The transmission of the IR beam can be optimized by designing a custom AR coating for the specific angle [263]. Depending on the coating complexity, losses can be below 0,1% for the IR beam using 100 fs pulses. Surface irregularities can reduce the XUV reflectivity but do not influence the reported performance significantly. The outcoupling efficiencies depend largely on the grazing angle and therefore on the complexity of the coating, but can be as large as 40% for SiO_2 at 40 nm and 75°AOI, increasing to $> 60\%$ for longer wavelengths. The thickness of the GIP is an important aspect and to minimize losses and dispersion, a thin plate is favorable. However, fabrication of the AR coatings puts limits on how thin the plate can be, and, similar to the Brewster plate, also thermal effects become stronger with a thinner plate. The GIP has been employed in a single-pass HHG system [266] but no application inside a fsEC has been reported.
Main limitations include:

- Damage threshold is low due to AR coating.
- Nonlinear and thermal effects in the thin plate.
- Plate requires minimum thickness due to mechanical tension during coating.
- Not demonstrated in enhancement cavity.

Main advantages:

- High XUV outoupling efficiency; $> 40\%$.
- Broad XUV wavelength range > 15 nm.

WOMOC

The wedge-on-mirror output coupler (WOMOC) is an improvement of the Brewster plate, which separates the XUV by reflection from a wedged top layer of multilayer coating under a different angle as the IR light [262]. The two main advantages of this method compared to a standard Brewster plate are better heat conduction and improved mechanical handling. Although these could overcome severe power scaling problems related to the Brewster plate, the $\sim$10 % outcoupling efficiency of the XUV light is still relatively low. On the other hand, dispersion and non-linear effects are claimed to be better controllable than in the case of a Brewster plate since the coating can be designed accordingly and the optical path length can be varied by changing the position of the WOMOC. The method has not yet been used for outcoupling XUV from a cavity.
Main limitations include:

- Low XUV outcoupling efficiency $\lesssim 10\%$.
- Damage threshold not investigated.

Main advantages:

- Robust mechanical handling.
- Low absorption and scattering of the IR beam.
- Low thermal lensing due to better heat conductivity.

Geometrical output coupling

Outcoupling of XUV light through a hole in the cavity mirror after the gas target has been shown to be feasible experimentally, especially for very high harmonic orders [83, 267]. Despite the on-axis hole with a radius of 80 μm an enhancement of the fundamental mode

of over 200 can be achieved. Depending on the focus size, an XUV outcoupling efficiency of ∼20% can be reached for 30 nm, increasing for shorter wavelengths. To decrease the IR losses through the outcoupling hole, it is possible to use a donut mode (a linear combination of TEM_{01} and TEM_{10}). It has been experimentally shown that an enhancement of 275 can be maintained for a hole of ∼100 μm diameter [268]. However, to efficiently produce the donut mode from the input beam, a phase mask has to be added in the beam path. Besides, the peak intensity at the focus for a donut mode is only 37% of that of a Gaussian mode, and the donut mode has a non-constant phase, which limits the HHG process even further. In more recent experiments [269–271] a single slit mode was used to couple out the XUV through a narrow slit in the mirror using a degenerate combination of Gauss-Hermite modes. The intensity at the position of the slit is minimal, but at the focus it is 64% of that of a Gaussian mode. Due to limited spectral and spatial overlapping of the incidence beam, the reported enhancement is limited to ∼50. An outcoupling efficiency of 30% at 60 nm was demonstrated, increasing with shorter wavelengths. Experimental realization is challenging due to the manufacturing of the slit and overlapping the incident beam with the cavity mode.
Main limitations include:

- Efficient XUV outcoupling range limited to shorter wavelengths ($\leq$25 nm).
- Manufactoring of the hole is challenging [267].
- Scattering and absorption losses for the IR beam.

Main advantages:

- High XUV outcoupling efficiency >50% for <20 nm.
- No dispersion or bandwidth limitations for the IR beam.

Diffraction grating

To couple the XUV out of the cavity using an IR reflective optic, a diffraction grating etched into the top layer of a dielectric mirror can be used [160]. The XUV radiation is diffracted by the shallow grating structure, while the IR light penetrates into the coating and is reflected in 0th order. In the reported experiment, a 420 nm SiO_2 grating period was used with a step height of 40 nm at an angle of ∼70°Ẇith an IR grating reflectivity of 0.99988 an enhancement factor of 260 is reached. Since the optic is purely reflective, no dispersion is added to the intra-cavity field and the damage threshold is as high as for other IR-coated optics. Although the outcoupling efficiency is only ∼10%, the harmonics are spectrally separated, mitigating the need of a grating further-on in the XUV beam path. The grating mirror has been used in several intra-cavity HHG experiments [80,

86, 154, 196]. An upgrade of the grating mirror using a blazed grating to increase the outcoupling efficiency has been proposed [272], but has not been reported to be used in a cavity.
Main limitations include:

- Low XUV outcoupling efficiency $\lesssim 10$ %.

Main advantages:

- Low losses for the IR beam.
- Low dispersion for the IR beam.
- Low absorption and scattering of the IR beam.
- High damage threshold.

Non-collinear HHG

To avoid any interaction of the XUV radiation with the cavity optics, high harmonics that emerge at a different angle as the fundamental field need to be generated. This is possible when two IR pulses meet under a small angle while interacting with the target gas. High harmonics appear along the bisector of the angle formed by the two IR beams, which do not need te be separated from the IR field anymore. Although non-collinear HHG in a single-pass geometry was shown several years ago [273], the experimental realization in a fsEC is a very recent development [156, 184, 268]. Owing to the high output coupling efficiency, a record power of 600 μW was coupled out of the cavity. The cavity design is however more complicated due to the two pulses that are circulating, which need to overlap in both space and time in the interaction region.
Main limitations include:

- Complicated cavity design.

Main advantages:

- High XUV outcoupling efficiency $\gtrsim 60$ %.
- Low losses for the IR beam.
- Low dispersion for the IR beam.
- Low absorption and scattering of the IR beam.
- High damage threshold.

Acknowledgements

When I came to Heidelberg for the first time to apply for a position, it was a rainy week and the city didn't seem very attractive. It was the warm welcome that I received from José and the people from the EBIT group that I remember the most. Together with the exciting proposal to extend the range of laser spectroscopy to the ultraviolet it made me decide to move to Germany for my PhD. Now, five years later, I can say that I have never regretted this decision ever since, and want to thanks all the people who have made my time in Heidelberg valuable and beautiful.

First of all, I would like to thank José and Thomas for accepting me as a PhD student and for supervising me over the past years. José, I very much appreciate your enthusiasm for physics and creative ideas to solve all sorts of experimental problems. From you I have learned a great deal about mechanical engineering and vacuum technology. You taught me critical thinking during numerous discussions on physics, and many other topics. Thanks for your guidance and ideas on crucial moments and for the freedom that I had while working on the project. I value your efforts and initiatives towards social cohesion within the EBIT group and I am also very grateful for the many opportunities that I have gotten to attend conferences and workshops. Thomas, many thanks for your interest and support of the project, your positive attitude has helped me a lot. Oscar, thanks for putting me in touch with José and starting this adventure.

I thank Prof. Andreas Wolf for assessing and reading my thesis and, together with Prof. Maurits Haverkort and Prof. Werner Aeschbach, for taking part in my thesis defense committee.

I would like to thank Jun Ye for allowing me to join his group at JILA for several weeks, and Gil, Stephen and Craig, from who I learned how to operate a femtosecond enhancement cavity.

Jan-Hendrik, José, Julian, Elwin, Fanni, Lukas, Hendrik, Patrick and Anna many thanks for proof-reading my thesis.

I thank Andrii for valuable ideas during the first phase of the project. Jan-Hendrik, thank you for joining the experiment, the many hours we spend together in the lab and your valuable ideas about everything that has to do with laser pulses. Our discussions have motivated me and made working in the lab so much more cheerful.

I also want to thank all the bachelor and master students that have contributed to the

experiment and made my time at the institute more lively. Fatima, Hans, Alex, Patrick, Ronja, Jakob, Anna, Nick and Valentin, thanks for your dedication.

Without the professional help from the mechanical workshops at the MPIK, this experiment would not have been possible. Many thanks for the skillful manufacturing of numerous parts to Christan Kaiser, Steffen Vogel, Lukas Dengel, Daniel Müller and the team of Thorsten Spranz from the central workshop. Also, many thanks to the technical design department of Frank Müller, especially to Yannick Steinhauser for modeling the complex differential pump system.

Next, I would like to thank my fellow (former) PhD students, with whom I spend a great deal of time over the last years. Julian, Steffen, Jan-Hendrik, Michael, Stepan, and Hendrik, thanks for the numerous barbecues, movie evenings, casual drinks and parties that made my time in Heidelberg so much more fun.

I thank all members of the EBIT-group for including me from the start. I appreciate their help whenever it was needed and have very much enjoyed the animated weekly group meetings, daily lunch breaks, the extraordinary EMBL rooftop coffee breaks without coffee, the occasional trip to Italy and frequent Stammtisches.

I would like to thank the HGSFP for providing funding and support and all the kind people that I met through its activities, ranging from trips to Vienna and Obergurgl to regular bouldering sessions at the Boulderhaus.

Many thanks to my international friends from Vuolukiventie: Markus, Peter, Miro and the others, with which I have spend many beautiful weekends throughout Europe.

Thanks also to my friends from Groningen, Frederik, Liesbeth and Laura, who despite the increased distance kept visiting me.

Many thanks to all the great people that I met via cycling and beach-volleyball. They, and especially you, Dimi, have driven my enthusiasm for these sports and made all the hours so much fun.

Moving to Heidelberg meant moving very far from everything that I knew. Therefore I am especially grateful that I found a place to live where I felt at home right from the start. Lukas, Lara, Bea, Fritz, Timo und Andy, vielen Dank für die wunderschöne Zeit in der Gutleutvilla. Nach mehr als drei Jahre in dem Gelben Haus fühlt es sich fast an, alsob wir eine Familie geworden sind. Lara, Lukas, Merlin, Sophie, Hendrik, Kathi und Fanni, ich hätte mich kein besseres Zuhause wünschen können, dankeschön.

Heit, mama, Dineke en Sietse, bedankt dat jullie er altijd voor me zijn, het is elke keer heerlijk om weer thuis te komen.

Als letztes, bedanke ich dir, Fanni, für dein Vertrauen, Unterstützung und Liebe.

List of publications

- J. Karhu, **J. Nauta**, M. Vainio, M. Metsälä, S. Hoekstra, and L. Halonen, Double resonant absorption measurement of acetylene symmetric vibrational states probed with cavity ring down spectroscopy. *Journal of Chemical Physics,* **144** 244201. `https://doi.org/10.1063/1.4954159` (2016).

- **J. Nauta**, A. Borodin, H. B. Ledwa, J. Stark, M. Schwarz, L. Schmöger, P. Micke, J. R. Crespo López-Urrutia and Thomas Pfeifer, Towards precision measurements on highly charged ions using a high harmonic generation frequency comb. *Nuclear Instruments and Methods in Physics Research Section B: Beam Interactions with Materials and Atoms* **408,** 285–288. `https://doi.org/10.1016/j.nimb.2017.04.077` (2017).

- J.-H. Oelmann, **J. Nauta**, A. Ackermann, P. Knauer, R. Pappenberger, S. Kühn, J. Stark, J. R. Crespo López-Urrutia and T. Pfeifer, Development of an XUV frequency comb for precision spectroscopy of highly charged ions. *2019 Conference on Lasers and Electro-Optics Europe and European Quantum Electronics Conference* ISBN: 978-1-7281-0469-0 (2019).

- **J. Nauta**, J.-H. Oelmann, A. Ackermann, P. Knauer, R. Pappenberger, A. Borodin, I. S. Muhammad, H. Ledwa, T. Pfeifer and J. R. Crespo López-Urrutia, 100 MHz frequency comb for low-intensity multi-photon studies: intra-cavity velocity-map imaging of xenon. *Optics Letters* **45,** 2156. `https://doi.org/10.1364/ol.389327` (2020).

- G. Brenner, S. Bernitt, S. Dobrodey, R. Steinbrügge, M. A. Blessenohl, A. Cieluch, Z. Hockenbery, S. Kühn **J. Nauta**, M. A. Sanchez, S. W. Epp and J. R. Crespo López-Urrutia, High-precision laser spectroscopy of the fine-structure transition $2s^2 s_{1/2} - 2p^2 p_{3/2}$ at 136 eV in lithiumlike Kr^{33+} using a free-electron laser. *Phys. Rev. A, in peer-review process* (2020).

- **J. Nauta**, J.-H. Oelmann, A. Ackermann, P. Knauer, R. Pappenberger, T. Pfeifer and J. R. Crespo López-Urrutia, An astigmatism-compensated femtosecond enhancement cavity for generating high-order harmonics, *in preparation* (2020).

Bibliography

1. M. Tanabashi *et al.* Review of Particle Physics. *Physical Review D* **98,** 030001. doi:10.1103/physrevd.98.030001 (2018).
2. A. Einstein. Die Feldgleichungen der Gravitation. *Sitzungsberichte der Königlich Preußischen Akademie der Wissenschaften (Berlin),* 844–847 (1915).
3. A. D. Sakharov. Violation of CP Invariance,Casymmetry, and baryon asymmetry of the universe. *Sov. Phys. Usp.* **34,** 392–393. doi:10.1070/pu1991v034n05abeh002497 (1991).
4. M. Dine & A. Kusenko. Origin of the matter-antimatter asymmetry. *Rev. Mod. Phys.* **76,** 1–30. doi:10.1103/revmodphys.76.1 (2003).
5. J. H. Oort. The force exerted by the stellar system in the direction perpendicular to the galactic plane and some related problems. *Bull. Astron. Inst. Netherlands* **6,** 249–287 (1932).
6. G. Bertone, D. Hooper & J. Silk. Particle dark matter: evidence, candidates and constraints. *Phys. Rep.* **405,** 279–390. doi:10.1016/j.physrep.2004.08.031 (2005).
7. R. Adam *et al.* Planck 2015 results. *Astron. Astrophys.* **594,** A1. doi:10.1051/0004-6361/201527101 (2016).
8. S. Perlmutter. Nobel Lecture: Measuring the acceleration of the cosmic expansion using supernovae. *Rev. Mod. Phys.* **84,** 1127–1149. doi:10.1103/revmodphys.84.1127 (2012).
9. D. DeMille, J. M. Doyle & A. O. Sushkov. Probing the frontiers of particle physics with tabletop-scale experiments. *Science* **357,** 990–994. doi:10.1126/science.aal3003 (2017).
10. M. S. Safronova *et al.* Search for new physics with atoms and molecules. *Rev. Mod. Phys.* **90,** 025008. doi:10.1103/revmodphys.90.025008 (2018).
11. V. A. Kostelecký & N. Russell. Data tables for Lorentz and CPT violation. *Rev. Mod. Phys.* **83,** 11–31. doi:10.1103/revmodphys.83.11 (2011).
12. V. Andreev *et al.* Improved limit on the electric dipole moment of the electron. *Nature* **562,** 355–360. doi:10.1038/s41586-018-0599-8 (2018).
13. C. Cesarotti, Q. Lu, Y. Nakai, A. Parikh & M. Reece. Interpreting the electron EDM constraint. *J. High Energy Phys.* **2019,** 59. doi:10.1007/jhep05(2019)059 (2019).
14. C. S. Wood. Measurement of Parity Nonconservation and an Anapole Moment in Cesium. *Science* **275,** 1759–1763. doi:10.1126/science.275.5307.1759 (1997).

15. M. A. Hohensee *et al.* Limits on Violations of Lorentz Symmetry and the Einstein Equivalence Principle using Radio-Frequency Spectroscopy of Atomic Dysprosium. *Phys. Rev. Lett.* **111,** 050401. doi:10.1103/physrevlett.111.050401 (2013).

16. T. Udem, R. Holzwarth & T. W. Hänsch. Optical frequency metrology. *Nature* **416,** 233. doi:10.1038/416233a (2002).

17. L Hollberg, S Diddams, A Bartels, T Fortier & K Kim. The measurement of optical frequencies. *Metrologia* **42,** S105–S124. doi:10.1088/0026-1394/42/3/s12 (2005).

18. J. N. Eckstein, A. I. Ferguson & T. W. Hänsch. High-resolution two-photon spectroscopy with picosecond light pulses. *Phys. Rev. Lett.* **40,** 847–850. doi:10.1103/physrevlett.40.847 (1978).

19. D. J. Jones. Carrier-Envelope Phase Control of Femtosecond Mode-Locked Lasers and Direct Optical Frequency Synthesis. *Science* **288,** 635–639. doi:10.1126/science.288.5466.635 (2000).

20. R. Holzwarth *et al.* Optical Frequency Synthesizer for Precision Spectroscopy. *Phys. Rev. Lett.* **85,** 2264–2267. doi:10.1103/physrevlett.85.2264 (2000).

21. T. W. Hänsch. Nobel Lecture: Passion for precision. *Rev. Mod. Phys.* **78,** 1297–1309. doi:10.1103/revmodphys.78.1297 (2006).

22. M. Zimmermann, C. Gohle, R. Holzwarth, T. Udem & T. W. Hänsch. Optical clockwork with an offset-free difference-frequency comb accuracy of sum- and difference-frequency generation. *Opt. Lett.* **29,** 310. doi:10.1364/ol.29.000310 (2004).

23. R. J. Jones, K. D. Moll, M. J. Thorpe & J. Ye. Phase-Coherent Frequency Combs in the Vacuum Ultraviolet via High-Harmonic Generation inside a Femtosecond Enhancement Cavity. *Phys. Rev. Lett.* **94,** 193201. doi:10.1103/PhysRevLett.94.193201 (19 2005).

24. C. Gohle *et al.* A frequency comb in the extreme ultraviolet. *Nature* **436,** 234–237. doi:10.1038/nature03851 (2005).

25. A. D. Ludlow, M. M. Boyd, J. Ye, E. Peik & P. Schmidt. Optical atomic clocks. *Rev. Mod. Phys.* **87,** 637–701. doi:10.1103/revmodphys.87.637 (2015).

26. N. Picqué & T. W. Hänsch. Frequency comb spectroscopy. *Nat. Photonics* **13,** 146–157. doi:10.1038/s41566-018-0347-5 (2019).

27. T. Wilken *et al.* A spectrograph for exoplanet observations calibrated at the centimetre-per-second level. *Nature* **485,** 611–614. doi:10.1038/nature11092 (2012).

28. A. Baltuška *et al.* Attosecond control of electronic processes by intense light fields. *Nature* **421,** 611–615. doi:10.1038/nature01414 (2003).

29. V. Torres-Company & A. M. Weiner. Optical frequency comb technology for ultra-broadband radio-frequency photonics. *Laser Photon. Rev.* **8,** 368–393. doi:10.1002/lpor.201300126 (2013).

30. D. B. Newell *et al.* The CODATA 2017 values of h,e,k, and N_A for the revision of the SI. *Metrologia* **55,** L13–L16. doi:10.1088/1681-7575/aa950a (2018).

31. J.-P. Uzan. Varying Constants, Gravitation and Cosmology. *Living Rev. Relativ.* **14,** 2. doi:10.12942/lrr-2011-2 (2011).

32. J. K. Webb *et al.* Indications of a Spatial Variation of the Fine Structure Constant. *Phys. Rev. Lett.* **107,** 191101. doi:10.1103/physrevlett.107.191101 (2011).

33. J. B. Whitmore & M. T. Murphy. Impact of instrumental systematic errors on fine-structure constant measurements with quasar spectra. *Mon. Not. R. Astron. Soc.* **447,** 446–462. doi:10.1093/mnras/stu2420 (2014).

34. V. Dumont & J. K. Webb. Modelling long-range wavelength distortions in quasar absorption echelle spectra. *Mon. Not. R. Astron. Soc.* **468,** 1568–1574. doi:10.1093/mnras/stx381 (2017).

35. V. A. Dzuba, V. V. Flambaum & J. K. Webb. Calculations of the relativistic effects in many-electron atoms and space-time variation of fundamental constants. *Phys. Rev. A* **59,** 230–237. doi:10.1103/physreva.59.230 (1999).

36. E. Dijck. *Spectroscopy of Trapped Ba+ Ions for Atomic Parity Violation and Optical Clocks* PhD thesis (University of Groningen, 2020). doi:10.33612/diss.108023683.

37. S. Brewer *et al.* Al+ 27 Quantum-Logic Clock with a Systematic Uncertainty below 10 $^{-18}$. *Phys. Rev. Lett.* **123,** 033201. doi:10.1103/physrevlett.123.033201 (2019).

38. J Terrien. News from the International Bureau of Weights and Measures. *Metrologia* **4,** 41–45. doi:10.1088/0026-1394/4/1/006 (1968).

39. F. Riehle. Towards a redefinition of the second based on optical atomic clocks. *C. R. Phys.* **16,** 506–515. doi:10.1016/j.crhy.2015.03.012 (2015).

40. T. E. Mehlstäubler, G. Grosche, C. Lisdat, P. O. Schmidt & H. Denker. Atomic clocks for geodesy. *Rep. Prog. Phys.* **81,** 064401. doi:10.1088/1361-6633/aab409 (2018).

41. A. Derevianko & M. Pospelov. Hunting for topological dark matter with atomic clocks. *Nat. Phys.* **10,** 933–936. doi:10.1038/nphys3137 (2014).

42. N. Huntemann *et al.* Improved Limit on a Temporal Variation of m_p/m_e from Comparisons of Yb+ and Cs Atomic Clocks. *Phys. Rev. Lett.* **113,** 210802. doi:10.1103/physrevlett.113.210802 (2014).

43. T. Rosenband *et al.* Frequency Ratio of Al+ and Hg+ Single-Ion Optical Clocks: Metrology at the 17th Decimal Place. *Science* **319,** 1808–1812. doi:10.1126/science.1154622 (2008).

44. R. Godun *et al.* Frequency Ratio of Two Optical Clock Transitions in Yb^+171 and Constraints on the Time Variation of Fundamental Constants. *Phys. Rev. Lett.* **113,** 210801. doi:10.1103/physrevlett.113.210801 (2014).

45. M. G. Kozlov, M. S. Safronova, J. R. Crespo López-Urrutia & P. O. Schmidt. Highly charged ions: Optical clocks and applications in fundamental physics. *Rev. Mod. Phys.* **90,** 045005. doi:10.1103/RevModPhys.90.045005 (4 2018).

46. J. C. Berengut, V. A. Dzuba, V. V. Flambaum & A. Ong. Highly charged ions withE1,M1, andE2 transitions within laser range. *Phys. Rev. A* **86,** 022517. doi:10.1103/physreva.86.022517 (2012).

47. J. C. Berengut, V. A. Dzuba & V. V. Flambaum. Enhanced Laboratory Sensitivity to Variation of the Fine-Structure Constant using Highly Charged Ions. *Phys. Rev. Lett.* **105,** 120801. doi:10.1103/physrevlett.105.120801 (2010).

48. J. C. Berengut, V. A. Dzuba, V. V. Flambaum & A. Ong. Optical Transitions in Highly Charged Californium Ions with High Sensitivity to Variation of the Fine-Structure Constant. *Phys. Rev. Lett.* **109,** 070802. doi:10.1103/physrevlett.109.070802 (2012).

49. M. S. Safronova *et al.* Highly Charged Ions for Atomic Clocks, Quantum Information, and Search for α variation. *Phys. Rev. Lett.* **113,** 030801. doi:10.1103/PhysRevLett.113.030801 (3 2014).

50. V. A. Dzuba & V. V. Flambaum. Highly charged ions for atomic clocks and search for variation of the fine structure constant. *Hyperfine Interact.* **236,** 79–86. doi:10.1007/s10751-015-1166-4 (2015).

51. A. Derevianko, V. A. Dzuba & V. V. Flambaum. Highly Charged Ions as a Basis of Optical Atomic Clockwork of Exceptional Accuracy. *Phys. Rev. Lett.* **109,** 180801. doi:10.1103/physrevlett.109.180801 (2012).

52. S. Schiller. Hydrogenlike Highly Charged Ions for Tests of the Time Independence of Fundamental Constants. *Phys. Rev. Lett.* **98,** 180801. doi:10.1103/physrevlett.98.180801 (2007).

53. I. Draganić *et al.* High Precision Wavelength Measurements of QED-Sensitive Forbidden Transitions in Highly Charged Argon Ions. *Phys. Rev. Lett.* **91,** 183001. doi:10.1103/physrevlett.91.183001 (2003).

54. R. Shaniv *et al.* New Methods for Testing Lorentz Invariance with Atomic Systems. *Phys. Rev. Lett.* **120,** 103202. doi:10.1103/physrevlett.120.103202 (2018).

55. H. Bekker *et al.* Detection of the 5p - 4f orbital crossing and its optical clock transition in Pr9+. *Nat. Commun.* **10,** 5651. doi:10.1038/s41467-019-13406-9 (2019).

56. S. Bernitt. *Resonante Anregung astrophysikalischer Röntgen-Übergänge in hochgeladenen Eisenionen mit dem Freie-Elektronen-Laser LCLS* PhD thesis (Ruprecht-Karls-Universität Heidelberg, 2013).

57. M. A. Levine, R. E. Marrs, J. R. Henderson, D. A. Knapp & M. B. Schneider. The Electron Beam Ion Trap: A New Instrument for Atomic Physics Measurements. *Phys. Scr.* **T22,** 157–163. doi:10.1088/0031-8949/1988/t22/024 (1988).

58. L. Schmöger *et al.* Coulomb crystallization of highly charged ions. *Science* **347,** 1233–1236. doi:10.1126/science.aaa2960 (2015).

59. P. Micke *et al.* Coherent laser spectroscopy of highly charged ions using quantum logic. *Nature* **578,** 60–65. doi:10.1038/s41586-020-1959-8 (2020).

60. P. O. Schmidt. Spectroscopy Using Quantum Logic. *Science* **309,** 749–752. doi:10.1126/science.1114375 (2005).

61. D. Allan. Statistics of atomic frequency standards. *Proc. IEEE* **54,** 221–230. doi:10.1109/proc.1966.4634 (1966).

62. T. Bothwell *et al.* JILA SrI optical lattice clock with uncertainty of 2.0×10^{-18}. *Metrologia* **56,** 065004. doi:10.1088/1681-7575/ab4089 (2019).

63. D. Matei *et al.* 1.5 μm Lasers with Sub-10 mHz Linewidth. *Phys. Rev. Lett.* **118,** 263202. doi:10.1103/physrevlett.118.263202 (2017).

64. V. A. Dzuba, A. Derevianko & V. V. Flambaum. High-precision atomic clocks with highly charged ions: Nuclear-spin-zero f^{12}-shell ions. *Phys. Rev. A* **86,** 054501. doi:10.1103/physreva.86.054501 (2012).

65. P. G. Thirolf, B Seiferle & L von der Wense. The 229-thorium isomer: doorway to the road from the atomic clock to the nuclear clock. *J. Phys. B: At., Mol. Opt. Phys.* **52,** 203001. doi:10.1088/1361-6455/ab29b8 (2019).

66. J. Berengut. Resonant Electronic-Bridge Excitation of the ^{235}U Nuclear Transition in Ions with Chaotic Spectra. *Phys. Rev. Lett.* **121,** 253002. doi:10.1103/physrevlett.121.253002 (2018).

67. S. Bernitt *et al.* An unexpectedly low oscillator strength as the origin of the Fe XVII emission problem. *Nature* **492,** 225. doi:10.1038/nature11627 (2012).

68. J. K. Rudolph *et al.* X-Ray Resonant Photoexcitation: Linewidths and Energies of $K\alpha$ Transitions in Highly Charged Fe Ions. *Phys. Rev. Lett.* **111,** 103002. doi:10.1103/PhysRevLett.111.103002 (10 2013).

69. S. Kühn. High resolution photoexcitation measurements exacerbate the long-standing Fe XVII oscillator strength problem. *Phys. Rev. Lett.* accepted (2020).

70. T. Nakazato *et al.* Phase-matched frequency conversion below 150 nm in $KBe_2BO_3F_2$. *Opt. Express* **24,** 17149. doi:10.1364/oe.24.017149 (2016).

71. J. M. Michan, G. Polovy, K. W. Madison, M. C. Fujiwara & T. Momose. Narrow-band solid state vuv coherent source for laser cooling of antihydrogen. *Hyperfine Interact.* **235,** 29–36. doi:10.1007/s10751-015-1186-0 (2015).

72. N. Bloembergen & P. S. Pershan. Light Waves at the Boundary of Nonlinear Media. *Phys. Rev.* **128,** 606–622. doi:10.1103/physrev.128.606 (1962).

73. A. McPherson *et al.* Studies of multiphoton production of vacuum-ultraviolet radiation in the rare gases. *J. Opt. Soc. Am. B.* **4,** 595. doi:10.1364/josab.4.000595 (1987).

74. M Ferray *et al.* Multiple-harmonic conversion of 1064 nm radiation in rare gases. *J. Phys. B: At., Mol. Opt. Phys.* **21,** L31–L35. doi:10.1088/0953-4075/21/3/001 (1988).

75. M.-C. Chen *et al. Efficient, phase matched keV high harmonic generation using mid-IR driving laser wavelengths* in *IEEE Photonics Conf. 2012* **10519** (IEEE, 2012). doi:10.1109/ipcon.2012.6358746.

76. K. S. E. Eikema, W. Ubachs, W. Vassen & W. Hogervorst. First laser excitation of ^{4}He 1^1S-2^1P resonance line at 58 nm. *Phys. Rev. Lett.* **71,** 1690–1692. doi:10.1103/physrevlett.71.1690 (1993).

77. S. D. Bergeson *et al.* Measurement of the He Ground State Lamb Shift via the Two-Photon1S1-2S1Transition. *Phys. Rev. Lett.* **80,** 3475–3478. doi:10.1103/physrevlett.80.3475 (1998).

78. J. Lee, D. R. Carlson & R. J. Jones. Optimizing intracavity high harmonic generation for XUV fs frequency combs. *Opt. Express* **19,** 23315–23326. doi:10.1364/OE.19.023315 (2011).

79. D. C. Yost *et al.* Power optimization of XUV frequency combs for spectroscopy applications (Invited). *Opt. Express* **19,** 23483–23493. doi:10.1364/OE.19.023483 (2011).

80. G. Porat *et al.* Phase-matched extreme-ultraviolet frequency-comb generation. *Nat. Photonics* **12,** 387–391. doi:10.1038/s41566-018-0199-z (2018).

81. A. Ruehl, A. Marcinkevicius, M. E. Fermann & I. Hartl. 80 W, 120 fs Yb-fiber frequency comb. *Opt. Lett.* **35,** 3015–3017. doi:10.1364/OL.35.003015 (2010).

82. A. K. Mills, T. J. Hammond, M. H. C. Lam & D. J. Jones. XUV frequency combs via femtosecond enhancement cavities. *J. Phys. B: At., Mol. Opt. Phys.* **45,** 142001 (2012).

83. I. Pupeza *et al.* Compact high-repetition-rate source of coherent 100 eV radiation. *Nat. Photonics* **7,** 608–612. doi:10.1038/nphoton.2013.156 (2013).

84. H. Carstens *et al.* High-harmonic generation at 250 MHz with photon energies exceeding 100 eV. *Optica* **3,** 366. doi:10.1364/optica.3.000366 (2016).

85. C. Benko *et al.* Extreme ultraviolet radiation with coherence time greater than 1 s. *Nat Photon* **8,** 530–536. doi:10.1038/nphoton.2014.132 (2014).

86. A. Cingöz *et al.* Direct frequency comb spectroscopy in the extreme ultraviolet. *Nature* **482,** 68–71. doi:10.1038/nature10711 (2012).

87. P. Micke *et al.* The Heidelberg compact electron beam ion traps. *Rev. Sci. Instrum.* **89,** 063109. doi:10.1063/1.5026961 (2018).

88. C. Lyu *et al. Interrogating temporal coherence of EUV frequency combs with highly charged ions* to be published. 2020.

89. A. M. Jayich, X. Long & W. C. Campbell. Direct Frequency Comb Laser Cooling and Trapping. *Phys. Rev. X* **6,** 041004. doi:10.1103/PhysRevX.6.041004 (4 2016).

90. M. L. Weichman *et al.* Broadband molecular spectroscopy with optical frequency combs. *J. Mol. Spectrosc.* **355,** 66–78. doi:10.1016/j.jms.2018.11.011 (2019).

91. L. Dreissen *et al.* High-Precision Ramsey-Comb Spectroscopy Based on High-Harmonic Generation. *Phys. Rev. Lett.* **123,** 143001. doi:10.1103/physrevlett.123.143001 (2019).

92. J.-C. Diels & W. Rudolph. *Ultrashort Laser Pulse Phenomena* ISBN: 978-0-12-215493-5. doi:10.1016/b978-0-12-215493-5.x5000-9 (Elsevier, 2006).

93. S. Witte. *Terawatt-intensity few-cycle laser pulses: Optical parametric chirped pulse amplification and frequency comb spectroscopy* PhD thesis (Vrije Universiteit Amsterdam, 2007).

94. S. T. Cundiff. Phase stabilization of ultrashort optical pulses. *J. Phys. D: Appl. Phys.* **35,** R43–R59. doi:10.1088/0022-3727/35/8/201 (2002).

95. N. Scharnhorst *et al.* High-bandwidth transfer of phase stability through a fiber frequency comb. *Opt. Express* **23,** 19771–19776. doi:10.1364/OE.23.019771 (2015).

96. E. Chae, K. Nakashima, T. Ikeda, K. Sugiyama & K. Yoshioka. Direct phase-locking of a Ti:Sapphire optical frequency comb to a remote optical frequency standard. *Opt. Express* **27,** 15649. doi:10.1364/oe.27.015649 (2019).

97. E. Oelker *et al.* Demonstration of 4.8×10^{-17} stability at 1 s for two independent optical clocks. *Nat. Photonics* **13,** 714–719. doi:10.1038/s41566-019-0493-4 (2019).

98. P. B. Corkum. Plasma perspective on strong field multiphoton ionization. *Phys. Rev. Lett.* **71,** 1994–1997. doi:10.1103/physrevlett.71.1994 (1993).

99. J. L. Krause, K. J. Schafer & K. C. Kulander. High-order harmonic generation from atoms and ions in the high intensity regime. *Phys. Rev. Lett.* **68,** 3535–3538. doi:10.1103/physrevlett.68.3535 (1992).

100. L. Keldysh. Ionization in field of a strong electromagnetic wave. *Sov. Phys. JETP* **20,** 1307 (1965).

101. X. M. Tong & C. D. Lin. Empirical formula for static field ionization rates of atoms and molecules by lasers in the barrier-suppression regime. *J. Phys. B: At., Mol. Opt. Phys.* **38,** 2593–2600. doi:10.1088/0953-4075/38/15/001 (2005).

102. C. Benko. *Numerical Code Repository, HHG Phase matching* https://github.com/c-benko.

103. A. M. Perelomov, V. S. Popov & M. V. Terentev. Ionization of atoms in an alternating electric field. *Sov. Phys. JETP* **23,** 924 (1966).

104. M. Ammosov, N. Delone & V. Krainov. Tunnel ionization of complex atoms and of atomic ions in an alternating electromagnetic field. *Sov. Phys. JETP* **64,** 1191 (1986).

105. K. L. Ishikawa. in *Advances in Solid State Lasers Development and Applications* (InTech, 2010). doi:10.5772/7961.

106. M. Lewenstein, P. Balcou, M. Y. Ivanov, A. L'Huillier & P. B. Corkum. Theory of high-harmonic generation by low-frequency laser fields. *Phys. Rev. A* **49,** 2117–2132. doi:10.1103/physreva.49.2117 (1994).

107. P. Balcou, P. Saliéres, A. L'Huillier & M. Lewenstein. Generalized phase-matching conditions for high harmonics: The role of field-gradient forces. *Phys. Rev. A* **55,** 3204–3210. doi:10.1103/physreva.55.3204 (1997).

108. M. B. Gaarde *et al.* Spatiotemporal separation of high harmonic radiation into two quantum path components. *Phys. Rev. A* **59,** 1367–1373. doi:10.1103/physreva.59.1367 (1999).

109. C. M. Heyl, C. L. Arnold, A Couairon & A L'Huillier. Introduction to macroscopic power scaling principles for high-order harmonic generation. *J. Phys. B: At., Mol. Opt. Phys.* **50,** 013001 (2017).

110. E. Constant *et al.* Optimizing High Harmonic Generation in Absorbing Gases: Model and Experiment. *Phys. Rev. Lett.* **82,** 1668–1671. doi:10.1103/physrevlett.82.1668 (1999).

111. P. D. Maker, R. W. Terhune, M. Nisenoff & C. M. Savage. Effects of Dispersion and Focusing on the Production of Optical Harmonics. *Phys. Rev. Lett.* **8,** 21–22. doi:10.1103/physrevlett.8.21 (1962).

112. S. Kazamias *et al.* Global Optimization of High Harmonic Generation. *Phys. Rev. Lett.* **90,** 193901. doi:10.1103/physrevlett.90.193901 (2003).

113. M. B. Gaarde, J. L. Tate & K. J. Schafer. Macroscopic aspects of attosecond pulse generation. *J. Phys. B: At., Mol. Opt. Phys.* **41,** 132001. doi:10.1088/0953-4075/41/13/132001 (2008).

114. C. M. Heyl, J Güdde, A L'Huillier & U Höfer. High-order harmonic generation with μJ laser pulses at high repetition rates. *J. Phys. B: At., Mol. Opt. Phys.* **45,** 074020. doi:10.1088/0953-4075/45/7/074020 (2012).

115. C. G. Durfee *et al.* Phase Matching of High-Order Harmonics in Hollow Waveguides. *Phys. Rev. Lett.* **83,** 2187–2190. doi:10.1103/physrevlett.83.2187 (1999).

116. B. Henke, E. Gullikson & J. Davis. X-Ray Interactions: Photoabsorption, Scattering, Transmission, and Reflection at E = 50-30,000 eV, Z = 1-92. *At. Data Nucl. Data Tables* **54,** 181–342. doi:10.1006/adnd.1993.1013 (1993).

117. A. Börzsönyi, Z. Heiner, M. P. Kalashnikov, A. P. Kovács & K. Osvay. Dispersion measurement of inert gases and gas mixtures at 800 nm. *Appl. Opt.* **47,** 4856. doi:10.1364/ao.47.004856 (2008).

118. C. Jin. in *Springer Theses* 1–23 (Springer International Publishing, 2013). doi:10.1007/978-3-319-01625-2_1.

119. T. Popmintchev *et al.* Phase matching of high harmonic generation in the soft and hard X-ray regions of the spectrum. *Proc. Natl. Acad. Sci. U. S. A.* **106,** 10516–10521. doi:10.1073/pnas.0903748106 (2009).

120. J. Rothhardt *et al.* Absorption-limited and phase-matched high harmonic generation in the tight focusing regime. *New J. Phys.* **16,** 033022. doi:10.1088/1367-2630/16/3/033022 (2014).

121. Y. Mairesse. Attosecond Synchronization of High-Harmonic Soft X-rays. *Science* **302,** 1540–1543. doi:10.1126/science.1090277 (2003).

122. M. D. Seaberg *et al.* Ultrahigh 22 nm resolution coherent diffractive imaging using a desktop 13 nm high harmonic source. *Opt. Express* **19,** 22470. doi:10.1364/oe.19.022470 (2011).

123. O. Chalus, P. K. Bates, M. Smolarski & J. Biegert. Mid-IR short-pulse OPCPA with micro-Joule energy at 100kHz. *Opt. Express* **17,** 3587. doi:10.1364/oe.17.003587 (2009).

124. F. J. Furch *et al.* Carrier-envelope phase stable few-cycle pulses at 400 kHz for electron-ion coincidence experiments. *Opt. Express* **21,** 22671. doi:10.1364/oe.21.022671 (2013).

125. J. Matyschok *et al.* Temporal and spatial effects inside a compact and CEP stabilized, few-cycle OPCPA system at high repetition rates. *Opt. Express* **21,** 29656. doi:10.1364/oe.21.029656 (2013).

126. J. Nauta. *The use of optical cavityeis in cold molecule trapping, laser cooling and acetylene spectroscopy* Master's thesis (University of Groningen, 2014).

127. H. Walther, B. T. H. Varcoe, B.-G. Englert & T. Becker. Cavity quantum electrodynamics. *Rep. Prog. Phys.* **69,** 1325–1382. doi:10.1088/0034-4885/69/5/r02 (Apr. 2006).

128. W. Nagourney. *Quantum Electronics for Atomic Physics and Telecommunication* ISBN: 9780199665488. doi:10.1093/acprof:oso/9780199665488.001.0001 (Oxford University Press, 2014).

129. E. A. Saleh & M. C. Teich. in *Fundamentals of Photonics* 310–341 (John Wiley & Sons, Inc., 1991). doi:10.1002/0471213748.ch9.

130. D. C. Yost. *Development of an Extreme Ultraviolet Frequency Comb for Precision Spectroscopy* PhD thesis (University of Colorado Boulder, 2011).

131. C. J. Hood, H. J. Kimble & J. Ye. Characterization of high-finesse mirrors: Loss, phase shifts, and mode structure in an optical cavity. *Phys. Rev. A* **64,** 033804. doi:10.1103/physreva.64.033804 (2001).

132. C. Benko. *Extreme ultraviolet frequency combs for precision measurement and strong-field physics* PhD thesis (University of Colorado Boulder, 2016).

133. A. E. Siegman. *Lasers* ISBN: 0935702113 (University Science Books, Mill Valley, California, 1986).

134. T. J. Hammond. *Intracavity Generation of High Order Harmonics* PhD thesis (University of British Columbia Vancouver, 2011).

135. T. Hammond, A. K. Mills & D. J. Jones. Simple method to determine dispersion of high-finesse optical cavities. *Opt. Express* **17,** 8998–9005. doi:10.1364/OE.17.008998 (2009).

136. A. Egl *et al.* Application of the Continuous Stern-Gerlach Effect for Laser Spectroscopy of the $^{40}Ar13^{+}$ Fine Structure in a Penning Trap. *Phys. Rev. Lett.* **123,** 123001. doi:10.1103/physrevlett.123.123001 (2019).

137. J. A. Armstrong. Measurement of picosecond laser pulse widths. *Appl. Phys. Lett.* **10,** 16–18. doi:10.1063/1.1754787 (1967).

138. A. Ackermann. *Development and characterization of a femtosecond-pulse compressor* Master's thesis (Ruprecht-Karls-Universität Heidelberg, 2019).

139. D. Kane & R. Trebino. Characterization of arbitrary femtosecond pulses using frequency-resolved optical gating. *IEEE J. Quantum Electron.* **29,** 571–579. doi:10.1109/3.199311 (1993).

140. K. W. DeLong, R. Trebino, J. Hunter & W. E. White. Frequency-resolved optical gating with the use of second-harmonic generation. *J. Opt. Soc. Am. B.* **11,** 2206. doi:10.1364/josab.11.002206 (1994).

141. K. W. DeLong, B. Kohler, K. Wilson, D. N. Fittinghoff & R. Trebino. Pulse retrieval in frequency-resolved optical gating based on the method of generalized projections. *Opt. Lett.* **19,** 2152. doi:10.1364/ol.19.002152 (1994).

142. R. Jafari, T. Jones & R. Trebino. 100% reliable algorithm for second-harmonic-generation frequency-resolved optical gating. *Opt. Express* **27,** 2112. doi:10.1364/oe.27.002112 (2019).

143. J. M. Dudley, C. Finot, D. J. Richardson & G. Millot. Self-similarity in ultrafast nonlinear optics. *Nat. Phys.* **3,** 597–603. doi:10.1038/nphys705 (2007).

144. J. Zhao, W. Li, C. Wang, Y. Liu & H. Zeng. Pre-chirping management of a self-similar Yb-fiber amplifier towards 80 W average power with sub-40 fs pulse generation. *Opt. Express* **22,** 32214. doi:10.1364/oe.22.032214 (2014).

145. X. Li *et al.* High-power ultrafast Yb:fiber laser frequency combs using commercially available components and basic fiber tools. *Rev. Sci. Instrum.* **87,** 093114. doi:10.1063/1.4962867 (2016).

146. T. Eidam *et al.* Femtosecond fiber CPA system emitting 830 W average output power. *Opt. Lett.* **35,** 94. doi:10.1364/ol.35.000094 (2010).

147. D. Luo *et al.* 130 W, 180 fs ultrafast Yb-doped fiber frequency comb based on chirped-pulse fiber amplification. *Opt. Express* **28,** 4817. doi:10.1364/oe.386211 (2020).

148. M. E. Fermann & I. Hartl. Ultrafast Fiber Laser Technology. *IEEE J. Sel. Top. Quantum. Electron.* **15,** 191–206. doi:10.1109/jstqe.2008.2010246 (2009).

149. R. Paschotta, J. Nilsson, A. Tropper & D. Hanna. Ytterbium-doped fiber amplifiers. *IEEE J. Quantum Electron.* **33,** 1049–1056. doi:10.1109/3.594865 (1997).

150. B. Wolter *et al.* Strong-Field Physics with Mid-IR Fields. *Phys. Rev. X* **5.** doi:10.1103/physrevx.5.021034 (2015).

151. F. Krausz & M. Ivanov. Attosecond physics. *Rev. Mod. Phys.* **81,** 163–234. doi:10.1103/revmodphys.81.163 (2009).

152. A. Ozawa *et al.* High Harmonic Frequency Combs for High Resolution Spectroscopy. *Phys. Rev. Lett.* **100,** 253901. doi:10.1103/PhysRevLett.100.253901 (25 2008).

153. T. J. Hammond, A. K. Mills & D. J. Jones. Near-threshold harmonics from a femtosecond enhancement cavity-based EUV source: effects of multiple quantum pathways on spatial profile and yield. *Opt. Express* **19,** 24871–24883. doi:10.1364/OE.19.024871 (2011).

154. A. K. Mills *et al.* Cavity-enhanced high harmonic generation for extreme ultraviolet time- and angle-resolved photoemission spectroscopy. *Rev. Sci. Instrum.* **90,** 083001. doi:10.1063/1.5090507 (2019).

155. T. K. Allison, A. Cingöz, D. C. Yost & J. Ye. Extreme Nonlinear Optics in a Femtosecond Enhancement Cavity. *Phys. Rev. Lett.* **107,** 183903. doi:10.1103/PhysRevLett.107.183903 (18 2011).

156. M. Högner *et al.* Cavity-enhanced noncollinear high-harmonic generation. *Opt. Express* **27,** 19675. doi:10.1364/oe.27.019675 (2019).

157. C. Corder *et al. Development of a tunable high repetition rate XUV source for time-resolved photoemission studies of ultrafast dynamics at surfaces* in *Laser Applications in Microelectronic and Optoelectronic Manufacturing (LAMOM) XXIII* **10519** (2018). doi:10.1117/12.2295232.

158. J. Weitenberg *et al.* Multi-pass-cell-based nonlinear pulse compression to 115 fs at 7.5 μJ pulse energy and 300 W average power. *Opt. Express* **25,** 20502–20510. doi:10.1364/OE.25.020502 (2017).

159. T. Saule *et al.* Cumulative plasma effects in cavity-enhanced high-order harmonic generation in gases. *APL Photonics* **3,** 101301. doi:10.1063/1.5037196 (2018).

160. D. C. Yost, T. R. Schibli & J. Ye. Efficient output coupling of intracavity high-harmonic generation. *Opt. Lett.* **33,** 1099–1101. doi:10.1364/OL.33.001099 (2008).

161. G. Winkler, J. Fellinger, J. Seres, E. Seres & T. Schumm. Non-planar femtosecond enhancement cavity for VUV frequency comb applications. *Opt. Express* **24,** 5253–5262. doi:10.1364/OE.24.005253 (2016).

162. H. Carstens *et al.* Large-mode enhancement cavities. *Opt. Express* **21,** 11606–11617. doi:10.1364/OE.21.011606 (2013).

163. K. Dupraz, K. Cassou, A. Martens & F. Zomer. The ABCD matrix for parabolic reflectors and its application to astigmatism free four-mirror cavities. *Opt. Commun.* **353,** 178–183. doi:10.1016/j.optcom.2015.05.021 (2015).

164. F. Bakhtawar. *Finding Waist at Focus of Femtosecond Enhancemnet Cavity for High Harmonic Generation* Technical report (Max-Planck-Institut für Kernphysik, 2017).

165. M. A. de Araújo, R. Silva, E. de Lima, D. P. Pereira & P. C. de Oliveira. Measurement of Gaussian laser beam radius using the knife-edge technique: improvement on data analysis. *Appl. Opt.* **48,** 393–396. doi:10.1364/AO.48.000393 (2009).

166. C. Lee. A first review of optical edge-diffraction technology for precision dimensional metrology. *Int. J. Adv. Manuf. Technol.* **102,** 2465–2480. doi:10.1007/s00170-019-03319-8 (2019).

167. R. W. P. Drever *et al.* Laser phase and frequency stabilization using an optical resonator. *Appl. Phys. B* **31,** 97–105. doi:10.1007/bf00702605 (1983).

168. T. Hansch & B. Couillaud. Laser frequency stabilization by polarization spectroscopy of a reflecting reference cavity. *Opt. Commun.* **35,** 441 –444. doi:10.1016/0030-4018(80)90069-3 (1980).

169. R. J. Jones & J.-C. Diels. Stabilization of Femtosecond Lasers for Optical Frequency Metrology and Direct Optical to Radio Frequency Synthesis. *Phys. Rev. Lett.* **86,** 3288–3291. doi:10.1103/physrevlett.86.3288 (2001).

170. S. Hannig *et al.* A highly stable monolithic enhancement cavity for second harmonic generation in the ultraviolet. *Rev. Sci. Instrum.* **89,** 013106. doi:10.1063/1.5005515 (2018).

171. T. C. Briles, D. C. Yost, A. Cingöz, J. Ye & T. R. Schibli. Simple piezoelectric-actuated mirror with 180 kHz servo bandwidth. *Opt. Express* **18,** 9739–9746. doi:10.1364/OE.18.009739 (2010).

172. P. Knauer. *Stabilisation of Thermal Drifts in a Femtosecond Enhancement Cavity* Bachelor's thesis (Department of Physics and Astronomy, University of Heidelberg, 2019).

173. J. Petersen & A. Luiten. Short pulses in optical resonators. *Opt. Express* **11,** 2975–2981. doi:10.1364/OE.11.002975 (2003).

174. S. Holzberger *et al.* Enhancement cavities for zero-offset-frequency pulse trains. *Opt. Lett.* **40,** 2165–2168. doi:10.1364/OL.40.002165 (2015).

175. N. Lilienfein *et al.* Enhancement cavities for few-cycle pulses. *Opt. Lett.* **42,** 271–274. doi:10.1364/OL.42.000271 (2017).

176. M. J. Thorpe, R. J. Jones, K. D. Moll, J. Ye & R. Lalezari. Precise measurements of optical cavity dispersion and mirror coating properties via femtosecond combs. *Opt. Express* **13,** 882–888. doi:10.1364/OPEX.13.000882 (2005).

177. A. Schliesser, C. Gohle, T. Udem & T. W. Hänsch. Complete characterization of a broadband high-finesse cavity using an optical frequency comb. *Opt. Express* **14,** 5975–5983. doi:10.1364/OE.14.005975 (2006).

178. T. Tamir & S. T. Peng. Analysis and design of grating couplers. *Appl. Phys.* **14,** 235–254. doi:10.1007/bf00882729 (1977).

179. J. Hollenshead & L. Klebanoff. Modeling radiation-induced carbon contamination of extreme ultraviolet optics. *J Vac Sci Technol B Nanotechnol Microelectron* **24,** 64. doi:10.1116/1.2140005 (2006).

180. C. Corder *et al.* Ultrafast extreme ultraviolet photoemission without space charge. *Struct. Dyn.* **5,** 054301. doi:10.1063/1.5045578 (2018).

181. D. Garzella *et al.* Mirror degradation and heating in storage ring FELs. *Nucl. Instrum. Methods Phys. Res., Sect. A* **358,** 387–391. doi:10.1016/0168-9002(94)01594-5 (1995).

182. R. A. Rosenberg & D. C. Mancini. Deposition of carbon on gold using synchrotron radiation. *Nucl. Instrum. Methods Phys. Res., Sect. A* **291,** 101–106. doi:10.1016/0168-9002(90)90041-4 (1990).

183. R. R. Kunz, V. Liberman & D. K. Downs. Experimentation and modeling of organic photocontamination on lithographic optics. *J. Vac. Sci. Technol. B. Nanotechnol. Microelectron.* **18,** 1306. doi:10.1116/1.591379 (2000).

184. C. Zhang *et al. A noncollinear enhancement cavity for record-high out-coupling efficiency of extreme-UV frequency comb* Mar. 5, 2020. arXiv: 2003.02429v1.

185. d. NIST Mass Spectrometry Data Center William E. Wallace. eng. in (eds P. J. Linstrom & W. Mallard) chap. Mass Spectra (National Institute of Standards and Technology, 2020). doi:10.18434/T4D303.

186. J. T. Herron & H. I. Schiff. Mass Spectrometry of Ozone. *J. Chem. Phys.* **24,** 1266–1267. doi:10.1063/1.1742773 (1956).

187. R. W. C. Hansen, M. Bissen, D. Wallace, J. Wolske & T. Miller. Ultraviolet/ozone cleaning of carbon-contaminated optics. *Appl. Opt.* **32,** 4114. doi:10.1364/ao.32.004114 (1993).

188. Q.-F. Chen *et al.* A compact, robust, and transportable ultra-stable laser with a fractional frequency instability of 1 × 10-15. *Rev. Sci. Instrum.* **85,** 113107. doi:10.1063/1.4898334 (2014).

189. T. Kessler *et al.* A sub-40-mHz-linewidth laser based on a silicon single-crystal optical cavity. *Nat. Photonics* **6,** 687–692. doi:10.1038/nphoton.2012.217 (2012).

190. J. Millo *et al. Ultra-stable optical cavities: Design and experiments at LNE-SYRTE* in *2008 IEEE International Frequency Control Symposium* (IEEE, 2008). doi:10.1109/freq.2008.4622968.

191. D. Świerad *et al.* Ultra-stable clock laser system development towards space applications. *Sci. Rep.* **6,** 33973. doi:10.1038/srep33973 (2016).

192. J. Nauta *et al.* Towards precision measurements on highly charged ions using a high harmonic generation frequency comb. *Nucl. Instrum. Methods Phys. Res., Sect. B* **408,** 285–288. doi:10.1016/j.nimb.2017.04.077 (2017).

193. S. Feuchtenbeiner. *Lasersysteme für die Präzisionsspektroskopie sympathetisch gekühlter hochgeladener Ionen* Master's thesis (Ruprecht-Karls-Universität Heidelberg, 2015).

194. A. Zadvornaya *et al.* Characterization of Supersonic Gas Jets for High-Resolution Laser Ionization Spectroscopy of Heavy Elements. *Phys. Rev. X* **8,** 041008. doi:10.1103/PhysRevX.8.041008 (4 2018).

195. R. Campargue. Progress in overexpanded supersonic jets and skimmed molecular beams in free-jet zones of silence. *J. Phys. Chem.* **88,** 4466–4474. doi:10.1021/j150664a004 (1984).

196. C. M. Heyl, S. B. Schoun, G. Porat, H. Green & J. Ye. A nozzle for high-density supersonic gas jets at elevated temperatures. *Rev. Sci. Instrum.* **89,** 113114. doi:10.1063/1.5051586 (2018).

197. B. Maté *et al.* Experimental and numerical investigation of an axisymmetric supersonic jet. *J. Fluid Mech.* **426,** 177–197. doi:10.1017/s0022112000002329 (2001).

198. R. Pappenberger. *Implementierung eines differentiellen Pumpsystems in einen optischen Resonator für einen Frequenzkamm im Ultravioletten* Master's thesis. Bachelor's thesis (Department of Physics and Astronomy, University of Heidelberg, 2019).

199. J. Nauta *et al.* 100 MHz frequency comb for low-intensity multi-photon studies: intra-cavity velocity-map imaging of xenon. *Opt. Lett.* **45,** 2156. doi:10.1364/ol.389327 (2020).

200. D. W. Chandler & P. L. Houston. Two-dimensional imaging of state-selected photodissociation products detected by multiphoton ionization. *J. Chem. Phys.* **87,** 1445–1447. doi:10.1063/1.453276 (1987).

201. A. T. J. B. Eppink & D. H. Parker. Velocity map imaging of ions and electrons using electrostatic lenses: Application in photoelectron and photofragment ion imaging of molecular oxygen. *Rev. Sci. Instrum.* **68,** 3477–3484. doi:10.1063/1.1148310 (1997).

202. N. H. Abel. Auflösung einer mechanischen Aufgabe. *Journal für die reine und angewandte Mathematik (Crelles Journal)* **1826,** 153–157. doi:10.1515/crll.1826.1.153 (1826).

203. D. D. Hickstein, S. T. Gibson, R. Yurchak, D. D. Das & M. Ryazanov. A direct comparison of high-speed methods for the numerical Abel transform. *Rev. Sci. Instrum.* **90,** 065115. doi:10.1063/1.5092635 (2019).

204. E. W. Hansen & P.-L. Law. Recursive methods for computing the Abel transform and its inverse. *J. Opt. Soc. Am. A.* **2,** 510. doi:10.1364/josaa.2.000510 (1985).

205. M. J. J. Vrakking. An iterative procedure for the inversion of two-dimensional ion/photoelectron imaging experiments. *Rev. Sci. Instrum.* **72,** 4084–4089. doi:10.1063/1.1406923 (2001).

206. V. Dribinski, A. Ossadtchi, V. A. Mandelshtam & H. Reisler. Reconstruction of Abel-transformable images: The Gaussian basis-set expansion Abel transform method. *Rev. Sci. Instrum.* **73,** 2634–2642. doi:10.1063/1.1482156 (2002).

207. B. Dick. Inverting ion images without Abel inversion: maximum entropy reconstruction of velocity maps. *Phys. Chem. Chem. Phys.* **16,** 570–580. doi:10.1039/c3cp53673d (2014).

208. K. Aron & P. M. Johnson. The multiphoton ionization spectrum of xenon: Interatomic effects in multiphoton transitions. *J. Chem. Phys.* **67,** 5099–5104. doi:10.1063/1.434737 (1977).

209. P. Agostini, F. Fabre, G. Mainfray, G. Petite & N. K. Rahman. Free-Free Transitions Following Six-Photon Ionization of Xenon Atoms. *Phys. Rev. Lett.* **42,** 1127–1130. doi:10.1103/physrevlett.42.1127 (1979).

210. D. Feldmann, D. Petring, G. Otto & K. H. Welge. Angular distribution of photo electrons from above-threshold-ionization (ATI) of xenon by 532 nm, 355 nm and 266 nm radiation. *Zeitschrift für Physik D Atoms, Molecules and Clusters* **6,** 35–42. doi:10.1007/bf01436995 (1987).

211. H. Rottke, B. Wolff, M. Tapernon, K. H. Welge & D. Feldmann. Resonant multiphoton ionization of xenon in intense sub-ps-laser pulses. *Zeitschrift für Physik D Atoms, Molecules and Clusters* **15,** 133–139. doi:10.1007/bf01437006 (1990).

212. R. R. Freeman *et al.* Above-threshold ionization with subpicosecond laser pulses. *Phys. Rev. Lett.* **59,** 1092–1095. doi:10.1103/physrevlett.59.1092 (1987).

213. H. Helm, N. Bjerre, M. J. Dyer, D. L. Huestis & M. Saeed. Images of photoelectrons formed in intense laser fields. *Phys. Rev. Lett.* **70,** 3221–3224. doi:10.1103/PhysRevLett.70.3221 (21 1993).

214. L. Zhang, Z. Miao, W. Zheng, X. Zhong & C. Wu. Nonresonant multiphoton ionization of xenon atoms by femtosecond laser pulses. *Chem. Phys.* **523,** 52–56. doi:10.1016/j.chemphys.2019.04.005 (2019).

215. P. Kaminski *et al.* Wavelength dependence of multiphoton ionization of xenon. *Phys. Rev. A* **70,** 053413. doi:10.1103/physreva.70.053413 (2004).

216. V. Schyja, T. Lang & H. Helm. Channel switching in above-threshold ionization of xenon. *Phys. Rev. A* **57,** 3692–3697. doi:10.1103/PhysRevA.57.3692 (5 1998).

217. M Goto & K Hansen. Branching ratio between resonant and non-resonant ionization of xenon evaluated from photoelectron angular distributions. *Phys. Scr.* **86,** 035303. doi:10.1088/0031-8949/86/03/035303 (2012).

218. G. G. Paulus, W. Nicklich, H. Xu, P. Lambropoulos & H. Walther. Plateau in above threshold ionization spectra. *Phys. Rev. Lett.* **72,** 2851–2854. doi:10.1103/physrevlett.72.2851 (1994).

219. M. J. Nandor, M. A. Walker & L. D. V. Woerkom. Angular distributions of high-intensity ATI and the onset of the plateau. *J. Phys. B: At., Mol. Opt. Phys.* **31,** 4617–4629. doi:10.1088/0953-4075/31/20/019 (1998).

220. T Marchenko, H. G. Muller, K. J. Schafer & M. J. J. Vrakking. Electron angular distributions in near-threshold atomic ionization. *J. Phys. B: At., Mol. Opt. Phys.* **43,** 095601. doi:10.1088/0953-4075/43/9/095601 (2010).

221. Y. Huismans *et al.* Time-Resolved Holography with Photoelectrons. *Science* **331,** 61–64. doi:10.1126/science.1198450 (2010).

222. B Bergues *et al.* Sub-cycle electron control in the photoionization of xenon using a few-cycle laser pulse in the mid-infrared. *New J. Phys.* **13,** 063010. doi:10.1088/1367-2630/13/6/063010 (2011).

223. S. Zherebtsov *et al.* Controlled near-field enhanced electron acceleration from dielectric nanospheres with intense few-cycle laser fields. *Nat. Phys.* **7,** 656–662. doi:10.1038/nphys1983 (2011).

224. P. A. Korneev *et al.* Interference Carpets in Above-Threshold Ionization: From the Coulomb-Free to the Coulomb-Dominated Regime. *Phys. Rev. Lett.* **108,** 223601. doi:10.1103/physrevlett.108.223601 (2012).

225. M. Li *et al.* Photoelectron angular distributions of low-order above-threshold ionization of Xe in the multiphoton regime. *Phys. Rev. A* **85,** 013414. doi:10.1103/physreva.85.013414 (2012).

226. M.-M. Liu *et al.* Energy- and Momentum-Resolved Photoelectron Spin Polarization in Multiphoton Ionization of Xe by Circularly Polarized Fields. *Phys. Rev. Lett.* **120,** 043201. doi:10.1103/physrevlett.120.043201 (2018).

227. C. Marceau, G. Gingras & B. Witzel. Excitation with Effective Subcycle Laser Pulses. *Phys. Rev. Lett.* **111,** 203005. doi:10.1103/physrevlett.111.203005 (2013).

228. M Kübel *et al.* Phase- and intensity-resolved measurements of above threshold ionization by few-cycle pulses. *J. Phys. B: At., Mol. Opt. Phys.* **51,** 134007. doi:10.1088/1361-6455/aac584 (2018).

229. P. Salières *et al.* Feynman's path-integral approach for intense-laser-atom interactions. *Science* **292,** 902–905. doi:10.1126/science.108836 (2001).

230. C. I. Blaga *et al.* Strong-field photoionization revisited. *Nat. Phys.* **5,** 335–338. doi:10.1038/nphys1228 (2009).

231. G. G. Paulus *et al.* Above-Threshold Ionization by an Elliptically Polarized Field: Interplay between Electronic Quantum Trajectories. *Phys. Rev. Lett.* **84,** 3791–3794. doi:10.1103/physrevlett.84.3791 (2000).

232. E Eremina *et al.* Laser-induced non-sequential double ionization investigated at and below the threshold for electron impact ionization. *J. Phys. B: At., Mol. Opt. Phys.* **36,** 3269–3280. doi:10.1088/0953-4075/36/15/308 (2003).

233. M. Baudisch, B. Wolter, M. Pullen, M. Hemmer & J. Biegert. High power multicolor OPCPA source with simultaneous femtosecond deep-UV to mid-IR outputs. *Opt. Lett.* **41,** 3583. doi:10.1364/ol.41.003583 (2016).

234. Y. Liu *et al.* Multiphoton Double Ionization of Ar and Ne Close to Threshold. *Phys. Rev. Lett.* **104,** 173002. doi:10.1103/physrevlett.104.173002 (2010).

235. X. Song *et al.* Attosecond Time Delay of Retrapped Resonant Ionization. *Phys. Rev. Lett.* **121,** 103201. doi:10.1103/physrevlett.121.103201 (2018).

236. M. Kübel *et al.* Streak Camera for Strong-Field Ionization. *Phys. Rev. Lett.* **119.** doi:10.1103/physrevlett.119.183201 (2017).

237. J. R. Gascooke, S. T. Gibson & W. D. Lawrance. A circularisation method to repair deformations and determine the centre of velocity map images. *J. Chem. Phys.* **147,** 013924. doi:10.1063/1.4981024 (2017).

238. L. V. Woerkom, R. Freeman, W. Cooke & T. McIlrath. Saturation Effects in the Spatial and Energy Distributions in Short-pulse High-intensity Multiphoton Ionization. *J. Mod. Opt.* **36,** 817–827. doi:10.1080/09500348914550931 (1989).

239. J. Cooper & R. N. Zare. Angular Distribution of Photoelectrons. *J. Chem. Phys.* **48,** 942–943. doi:10.1063/1.1668742 (1968).

240. H. L. Offerhaus *et al.* A magnifying lens for velocity map imaging of electrons and ions. *Rev. Sci. Instrum.* **72,** 3245–3248. doi:10.1063/1.1386909 (2001).

241. D. D. Hickstein *et al.* Direct Visualization of Laser-Driven Electron Multiple Scattering and Tunneling Distance in Strong-Field Ionization. *Phys. Rev. Lett.* **109,** 073004. doi:10.1103/physrevlett.109.073004 (2012).

242. J. Nauta *et al. An astigmatism-compensated femtosecond enhancement cavity for generating high-order harmonics* in preparation. 2020.

243. J. Samson. *Vacuum ultraviolet spectroscopy* ISBN: 9780126175608 (John Wiley & Sons, Inc., 1967).

244. D. C. Yost *et al.* Vacuum-ultraviolet frequency combs from below-threshold harmonics. *Nat. Phys.* **5,** 815–820. doi:10.1038/nphys1398 (2009).

245. A. L'Huillier, P. Balcou, S. Candel, K. J. Schafer & K. C. Kulander. Calculations of high-order harmonic-generation processes in xenon at 1064 nm. *Phys. Rev. A* **46,** 2778–2790. doi:10.1103/physreva.46.2778 (1992).

246. J. Krummeich. *Development of a cooling system for mirrors in an UHV chamber* Bachelor's thesis (Ruprecht-Karls-Universität Heidelberg, 2019).

247. S.-F. Zhao, A.-T. Le, C. Jin, X. Wang & C. D. Lin. Analytical model for calibrating laser intensity in strong-field-ionization experiments. *Phys. Rev. A* **93,** 023413. doi:10.1103/physreva.93.023413 (2016).

248. F. Emaury, A. Diebold, C. J. Saraceno & U. Keller. Compact extreme ultraviolet source at megahertz pulse repetition rate with a low-noise ultrafast thin-disk laser oscillator. *Optica* **2,** 980. doi:10.1364/optica.2.000980 (2015).

249. A. Vernaleken *et al.* Single-pass high-harmonic generation at 208 MHz repetition rate. *Opt. Lett.* **36,** 3428. doi:10.1364/ol.36.003428 (2011).

250. S. Hädrich *et al.* Exploring new avenues in high repetition rate table-top coherent extreme ultraviolet sources. *Light Sci. Appl.* **4,** e320–. doi:10.1038/lsa.2015.93 (2015).

251. T. Saule *et al.* High-flux ultrafast extreme-ultraviolet photoemission spectroscopy at 18.4 MHz pulse repetition rate. *Nat. Commun.* **10,** 458. doi:10.1038/s41467-019-08367-y (2019).

252. M. Wollenhaupt *et al.* Three-dimensional tomographic reconstruction of ultrashort free electron wave packets. *Appl. Phys. B* **95,** 647–651. doi:10.1007/s00340-009-3513-0 (2009).

253. M. Weyland *et al.* Novel method for state selective determination of electron-impact-excitation cross sections from 0° to 180°. *EPJ Tech. Instrum.* **1,** 6. doi:10.1140/epjti/s40485-014-0006-2 (2014).

254. G. Porat *et al.* Attosecond time-resolved photoelectron holography. *Nat. Commun.* **9,** 2805. doi:10.1038/s41467-018-05185-6 (2018).

255. M. Altarelli *et al. The European X-Ray Free-Electron Laser, Technical design report* tech. rep. (DESY, 200).

256. H. Leopardi *et al.* Single-branch Er:fiber frequency comb for precision optical metrology with 10ˆ-18 fractional instability. *Optica* **4,** 879. doi:10.1364/optica.4.000879 (July 2017).

257. J. Stark. *An ultralow-noise superconducting radio-frequency ion trap for frequency metrology with highly charged ions* PhD thesis (Ruprecht-Karls-Universität Heidelberg, 2020).

258. S. Gustafsson, P. Jönsson, C. F. Fischer & I. P. Grant. MCDHF and RCI calculations of energy levels, lifetimes and transition rates for 3l3l′,3l4l′, and 3s5l states in Ca IX - As XXII and Kr XXV. *Astron. Astrophys.* **597,** A76. doi:10.1051/0004-6361/201628768 (2017).

259. B. Seiferle *et al.* Energy of the 229th nuclear clock transition. *Nature* **573,** 243–246. doi:10.1038/s41586-019-1533-4 (2019).

260. L. von der Wense & C. Zhang. *Concepts for direct frequency-comb spectroscopy of ^{229m}Th and an internal-conversion-based solid-state nuclear clock* 2019. arXiv: 1905.08060 [physics.ins-det].

261. P. V. Bilous *et al.* Electronic Bridge Excitation in Highly Charged Th229 Ions. *Phys. Rev. Lett.* **124,** 192502. doi:10.1103/physrevlett.124.192502 (May 2020).

262. I. Pupeza, E. E. Fill & F. Krausz. Low-loss VIS/IR-XUV beam splitter for high-power applications. *Opt. Express* **19,** 12108–12118. doi:10.1364/OE.19.012108 (2011).

263. O. Pronin *et al.* Ultrabroadband efficient intracavity XUV output coupler. *Opt. Express* **19,** 10232–10240. doi:10.1364/OE.19.010232 (2011).

264. A. Ozawa, Z. Zhao, M. Kuwata-Gonokami & Y. Kobayashi. High average power coherent vuv generation at 10 MHz repetition frequency by intracavity high harmonic generation. *Opt. Express* **23,** 15107–15118. doi:10.1364/OE.23.015107 (2015).

265. I. Pupeza. *Power scaling of enhancement cavities for non-linear optics* PhD thesis (Ludwig-Maximilians-Universität München, 2011).

266. S. Hädrich *et al.* High photon flux table-top coherent extreme-ultraviolet source. *Nat. Photonics* **8,** 779–783. doi:10.1038/nphoton.2014.214 (2014).

267. D. Esser *et al.* Laser-manufactured mirrors for geometrical output coupling of intracavity-generated high harmonics. *Opt. Express* **21,** 26797–26805. doi:10.1364/OE.21.026797 (2013).

268. K. D. Moll, R. J. Jones & J. Ye. Output coupling methods for cavity-based high-harmonic generation. *Opt. Express* **14,** 8189–8197. doi:10.1364/OE.14.008189 (2006).

269. I. Pupeza *et al.* Cavity-Enhanced High-Harmonic Generation with Spatially Tailored Driving Fields. *Phys. Rev. Lett.* **112,** 103902. doi:10.1103/PhysRevLett.112.103902 (10 2014).

270. J. Weitenberg, P. Rußbüldt, T. Eidam & I. Pupeza. Transverse mode tailoring in a quasi-imaging high-finesse femtosecond enhancement cavity. *Opt. Express* **19,** 9551–9561. doi:10.1364/OE.19.009551 (2011).

271. J Weitenberg *et al.* Geometrical on-axis access to high-finesse resonators by quasi-imaging: a theoretical description. *J. Opt.* **17,** 025609. doi:10.1088/2040-8978/17/2/025609 (2015).

272. Y.-Y. Yang *et al.* Optimization and characterization of a highly-efficient diffraction nanograting for MHz XUV pulses. *Opt. Express* **19,** 1954–1962. doi:10.1364/OE.19.001954 (2011).

273. A. Ozawa *et al.* Non-collinear high harmonic generation: a promising outcoupling method for cavity-assisted XUV generation. *Opt. Express* **16,** 6233–6239. doi:10.1364/OE.16.006233 (2008).